Microscopic baryon-baryon interactions at finite density and hypernuclear structure

vorgelegt von
Christoph Marcus Keil
aus Linden

Gießen, 2004

Contents

Contents

iv

Introduction

The interaction between baryons, of which protons and the neutrons are the lightest and best known, is very strong. This does not only provide a variety of very interesting phenomena, but requires also an elaborate framework to describe it. The interaction between baryons in a baryonic medium is a special challenge, it changes dramatically, depending on the density and composition of the medium. From a modern point of view these interactions observed at finite density or between baryons in free space are only effective interactions, different facets of a more fundamental interaction between the particles, from which the effective interactions can be derived in one consistent formalism. The underlying bare or microscopic interaction, gouverned by quantum chromodynamics (QCD), cannot be accessed directly, but has to be traced back using its various appearences. In this work we are going to develop a microscopic model, describing baryon-baryon interactions in free space, in infinite, homogeneous systems of finite density and in small, nuclear systems.

The interaction between baryons is not only very strong, but also of very short range, about a few of $10^{-15}m$. It is, however, in large parts responsible for the structure of the matter surrounding us – at all scales from close by, in our environment to far away, in the whole visible universe. Baryon-baryon interactions connect very large and very small scales. To get a taste of where these are at work all around us and to see their relevance in our world, let us start with a short look into the history of baryons in the universe and point out the places in which their interactions are of importance.

Baryons – the constituents of the matter surrounding us

Baryons are as old as the universe itself, they were created already 100 seconds after the big-bang, when the hot soup of quarks and gluons, from which baryons are made, cooled down so far that they started sticking together in tiny lumps of quarks [Kolb90]. Due to the confining character of the quark-quark interaction only baryons, bags containing three valence quarks, were left. And maybe also heavier quark bags, the strangelets, which, however, would interact very weakly and have so far not been observed. Due to processes violating CP symmetry, which regulates the balance between matter and antimatter, a tiny amount of baryons was left after the antibaryons had annihilated with baryons into eadiation. Baryonic matter is responsible for only about 4% of the total cosmic energy, while the unknown components dark matter ($\approx 29\%$) and dark energy ($\approx 67\%$) contribute most. Although negligible from the cosmological point of view, baryons and their interactions are the physical basis of our lives.

The initially formed baryons very quickly converted into protons, combining with electrons to the primordial hydrogen. Also a sizable amount of helium was synthesized by the first reaction shown in fig. I. After some 100,000 years the hot gas of very light

$$4\,{}^{1}\mathrm{H} \longrightarrow {}^{4}\mathrm{He} \qquad 3\,{}^{4}\mathrm{He} \longrightarrow {}^{12}\mathrm{C} \qquad {}^{12}\mathrm{C} + {}^{4}\mathrm{He} \longrightarrow {}^{16}\mathrm{O}$$
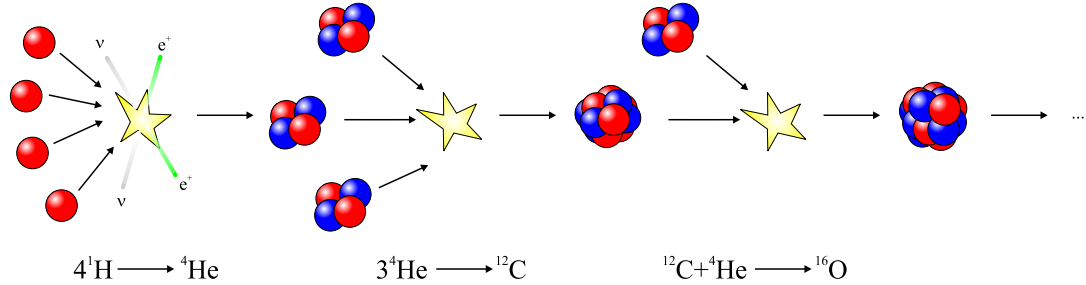
Figure I.: Fusion processes generating the light chemical elements.

nuclei up to ^{4}He and electrons had cooled sufficiently so that atoms could form and for the next 10^{9} years nuclear physics was of no relevance any more in the formation of the universe.

Then first stars formed, starting to burn hydrogen to helium, helium to carbon, and so on (see fig. I). Nucleosynthesis had started. The heavier a star is, the heavier are the elements it can fuse. However, only elements up to iron are be synthesized in stars, the fusion of heavier elements would cost instead of revealing energy and the stellar fire is extinguished. For the formation of heavy elements there are two main processes. The slow neutron capture (*s-process*), happening in red giant stars[1], old light stars, takes several ten thousands of years. It goes along a path in the well known region of the nuclear chart, close to the stable isotopes, see fig. II. Since the lighter stars burn a lot slower than their heavier brothers there is plenty of time to achieve a substantial amount of heavy elements even by such a slow process. The rapid neutron capture or *r-process* appears in the violent explosions at the end of a massive star's life. Those heavy stars with a mass larger than $6m_{\odot}$, fusing nuclei up to iron, will collapse after the stabilizing pressure due to the fusion processes ceases and finally blast in a violent *supernova explosion*. This not only distributes the synthesized elements up to the weight of iron into the interstellar space, but by providing a high flux of neutrons it starts the r-process. By successive neutron captures and β decays of heavier and heavier nuclei, the heavy element are formed. In the nuclear chart this process goes along a path in the very neutron rich region as shown in fig. II. This whole process happens on the time scale of only a few seconds.

The final stage of a massive star's life (but not heavier than $8m_{\odot}$) is a neutron star. This forms from the leftover part of the iron core after a supernova explosion. The newly formed proto neutron star is a hot object built from protons and neutrons. Cooling down the density rises. Due to the fermionic character of the nucleons very high kinetic energies keep the total energy of the neutron star up. This kinetic energy is so high, that it is favorable to convert a part of the nucleons into hyperons, which lowers the total

---

[1]A red giant denotes a star with a mass up to $6m_{\odot}$ which has burnt already more than 30% of its hydrogen. Due to changes in the fusion process its radius has grown by several orders of magnitude.
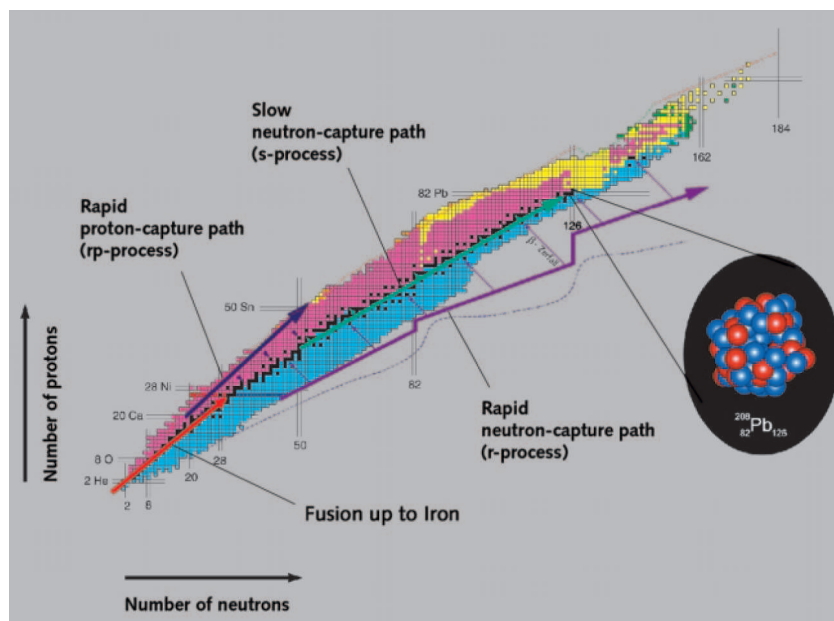
Figure II.: The chart of nuclei contains about 2500 known elements [GSI01].

energy of the neutron star drastically by opening new Fermi seas. In the end a cold lump of nucleons and hyperons, having a radius of about 15 km, is left.

About $5 \cdot 10^9$ years after the big bang enough inter stellar debris has been produced by all these processes, that our solar system could form from it and provide a planet which contains a mixture of light and heavy elements nicely suited to support life. The abundancies of different elements in the universe, as shown in fig. III, provide a fingerprint of all the processes at work in nucleosynthesis that enables us to reconstruct the stellar evolution in the universe.

To understand these large scale processes, an understanding of the processes at very small scales, the interaction of two baryons with each other, in free space and at finite density, has to be gained. This is the physics of hadrons and nuclei.

Hadron and nuclear physics

To understand the above described processes the mechanisms of hadron physics and especially nuclear and hypernuclear physics have to be understood. As the fundamental theory of strongly interacting particles, QCD, does not allow for free quarks since about $15 \cdot 10^9$ years, the degrees of freedom to describe our world are the *hadrons*, strongly interacting particles, subsummized in *baryons* and *mesons*. In a simplified picture baryons may be viewed as bags built from three quarks and mesons as containing a quark and an antiquark. In normal nuclei only baryons with up (u) and down (d) quark content exist, the proton and the neutron. In neutron stars and hypernuclei also the strange (s) quark, which appears in hyperons, is involved. A sketch of some hadrons is shown in fig. IV.

To understand the fusion processes in stars as well as the production mechanisms of heavy isotopes a detailed knowledge about the excitation spectrum of all the involved

3
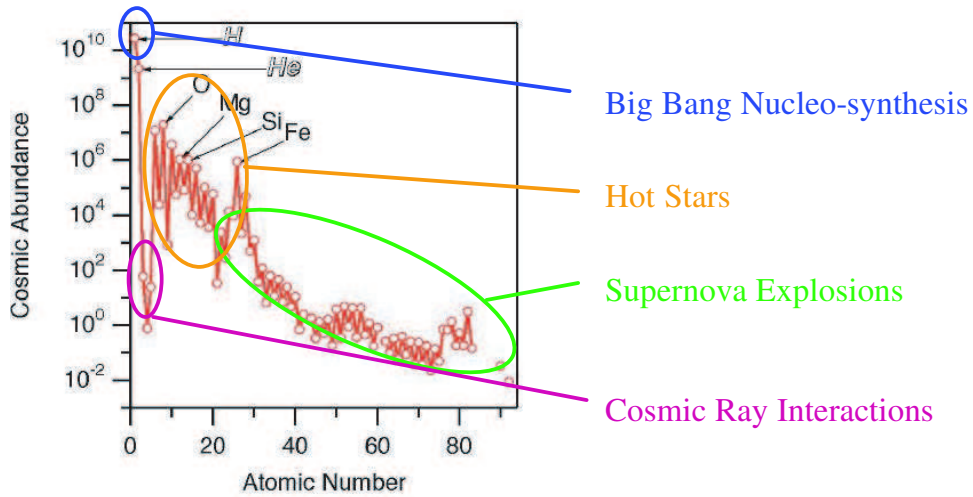
Figure III.: This figure shows the abundance of nuclear isotopes in the universe. The structure carries the fingerprints of all processes synthesizing our chemical elements [Zuber02].
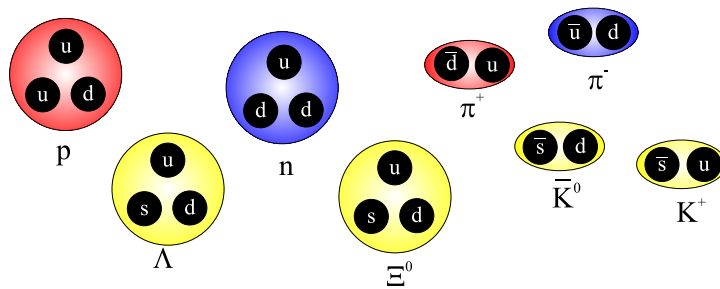
Figure IV.: Hadrons can be described in a simplified picture as being bags of three quarks (baryons) or quarks and antiquarks (mesons).

isotopes is needed. Especially for stable and long-lived isotopes very accurate experiments can be performed and have found many important resonances in the nuclear excitation spectra that greatly changed the picture of the involved fusion processes, based mostly on theoretical nuclear models.

For the s-process all necessary information to understand it can be obtained by experiments – at least in principle. However, most nuclei participating in the r- and rp-process will probably never be accessible by experiment, although future radioactive beam facilities, as, e.g., FAIR and RIA, may come close to that region. Modeling becomes very important here, but one has to be aware, that this needs to be extremely accurate. The state of the art nuclear structure calculations for astrophysical processes are non-relativistic shell-model calculations, which on an empirical level provide an excellent description of basically all known nuclei. Especially in the heavy mass region they, however, bear two great disadvantages. The first concern is the interaction used. In high accuracy calculations, the model parameters have to be fixed for every mass region, in which the calculations are done, making an extrapolation to very exotic nuclei rather unreliable. Since parameters can be fixed only for long lived isotopes, for which experimental spectra exist, especially the isospin dependence of the interaction, i.e., the dependence on $(N - Z)$, is ambiguous. For the description of strongly isospin asymmetric nuclei as they appear in the r- and rp-process, this is a clear problem. Non-relativistic Microscopic interactions, derived from the well known interactions between two nucleons, yield The correct saturation properties of nuclear matter only with additional phenomenological density dependent interactions. The second concern is related to the structure of dripline nuclei. Due to their very weak binding, the shell structure has almost dissolved and continuum caouling plays a major role. For a realistic shell-model calculation an incredibly large amount of configurations has to be taken into account already for light exotic nuclei, which is even for nowadays's computers not tractable.

Since a substantial fraction of hyperons is contained in neutron stars a lot less experimental input is available for the modeling. Microscopic models which contain already in their structure as many physical constraints as possible, i.e. systematics of the interactions and relations between the interactions of different baryons, are even more required. Especially the fact, that in experiments one always deals with very small objects, implying all sorts of finite size effects that do not appear in neutron stars, points at the necessity of microscopic models that are able to describe all systems built from baryons with a limited set of parameters. Furthermore the study of hypernuclei is interesting by itself, since hypernuclei are excellent laboratories to study all kinds of nuclear and hadron physics. Pictorially spoken, it opens up the third dimension of the nuclear chart, revealing new systematics in hadron many-body systems.

A very promising class of models are relativistic meson exchange models, quantum field theories which contain baryons as matter fields and mesons as mediators of the interaction. Their relativistic structure poses already strong constraints on the dynamics. The requirement that the Lagrangian has to be invariant under Lorentz transformations constrains very tightly for example interactions due to the particle spin which are completely unconstrained in non-relativistic models. Besides that, the formulation as Lagrangian field theory makes it very easy to impose symmetries on the model, flavor symmetries as isospin or SU(3), for example. Within these field theories there is a well defined pro-

cedure to calculate interactions in a surrounding medium from free interactions, which makes them an ideal basis for microscopic models. Actual calculations of nuclear structure within this formalism show, that not only the formal requirements on a theory for baryon-baryon interactions are well fulfilled, but also the results are impressive. Such calculations of nuclear interactions at finite density, Dirac-Brueckner calculations, show as compared to non-relativistic models a by far better agreement with observed nuclear matter ground state properties. In finite nuclei the dynamical constraints due to the relativistic formulation yield a very good agreement with the observed spin-orbit splitting in nuclei, which is part of the fine structure in the nuclear spectrum. The application of systematically derived effective interactions in addition opens the possibility for controlled extensions beyond the mean-field level. These models provide a well suited basis for an ab-initio description of many types of baryonic systems like nuclei and hypernuclei.

Relativistic nuclear structure models using microscopic interactions are still in their early stages. In recent years they could proof their power already in very successful mean-field calculations of whole isotopic chains. Processes beyond the mean-field in these models have not even been touched in actual calculations. This shows that there is a huge potential still hidden in this class of models.

Overview of the thesis

In this work we develop a complete ab-initio framework for the calculation of microscopic baryon-baryon interactions between the lowest flavor-SU(3) octet states and their application in finite nuclei and hypernuclei. The described formalism includes all the basic concepts discussed above. We start from the Bonn meson exchange potential model, which is extended to include also hyperons. On top of that a Dirac-Brueckner-Hartree-Fock formalism is developed, which can deal as well with symmetric and asymmetric nuclear matter as with hypermatter. The microscopic interactions are then applied in a low density approximation to the calculation of finite nuclei within a relativistic mean-field approximation of the density dependent relativistic hadron field theory.

The work is split in two parts. In the first part we develop the formalism of a relativistic framework for ab-initio calculations of finite baryonic objects as nuclei and hypernuclei. In the the second part calculations of hypernuclear properties are presented.

In chapter 1 we introduce the the formalism of relativistic scattering theory. In the discussion the relativistic integral equation for two body scattering, the Bethe-Salpeter (BS) equation is derived. After discussing the formal structure of the T-matrix, approximations to the BS equation are introduced, which are necessary to perform actual calculations. The full integral kernel is truncated to contain only the lowest order interactions and the full two baryon propagator is fixed to positive energy states and modified such in a covariant way, that retardation effects are suppressed in effective interactions. For the resulting equations the K-matrix approximation and the formalism of scattering phase shifts are explained. Chapter 2 develops then on the basis of the previous one the general formalism of meson-exchange models and its application to interactions between the members of the lowest baryon octet. This is extended in chapter 3 to the relativistic in-medium scattering theory. In this so-called Dirac-Brueckner-Hartree-Fock (DBHF)

formalism, the one-body self-energies and Pauli blocking are taken into account. The structure of the Pauli operator and the self-energies are discussed in detail. In the calculation of self-energies ambiguities arise due to the neglection of negative energy states in the whole formalism. Recipes to cure this partly are discussed. The following section formulates the part of our microscopic framework to describe finite systems of baryons, the density dependent relativistic hadron field theory. The in-medium interactions obtained from DBHF calculations are mapped onto density dependent vertex functionals in DDRH theory, which account for the change of the effective interaction in the medium due to correlations. The mapping procedure and specialties arising due to the density dependent interaction are discussed. Concluding the part of the work presenting our ab-initio approach in chapter 5 we study the dynamics of baryon-baryon interactions. It is investigated how the effective interactions depend on changes in the coupling constants and masses. It is determined how well SU(3) relations are fulfilled for effective interactions as used, for example, in the standard phenomenological calculations of hypernuclei and neutron star matter. In chapter 6 a new concept for solving the BS equation in free space and at finite density is developed. The basic idea is to map the full effective interaction onto a meson exchange kernel. This amounts to a rescaling of the vertices which obtain a dependence on the Mandelstam variables and the Fermi momenta. This treatment simplifies the solution of BS equations dramatically while producing qualitatively and quantitatively similar results.

In the next part of this work hypernuclear structure calculations are presented. After a short introduction to hypernuclear physics, given in chap. 7, we continue in chap. 8 with a discussion of single particle spectra of hypernuclei with large ground state spins. The first experimental indication of a spin-orbit splitting in intermediate mass hypernuclei are analyzed and discussed. In chap. 9 we present our calculations on the hypernuclear Auger effect, which provides an alternative method of spectroscopy in intermediate and heavy mass hypernuclei.

The work closes with a summary and an outlook given in chapter 10.

Contents

Part I.

Relativistic ab-initio Calculations

1. Relativistic Scattering Theory

1.1. Formalism

The quantum mechanical scattering problem is always connected to the so called *S-matrix* or scattering matrix S_{fi}. This object contains all the information about the system of n particles coming in and m particles coming out after their interaction. Formally it is the probability amplitude that the states $\Phi_i = |\phi_1\phi_2...\phi_n\rangle$ coming from the time $t = -\infty$ end up as $\Phi_f = \langle\phi'_1\phi'_2...\phi'_m|$ at $t = +\infty$.

$$S_{fi} \equiv \left\langle \tilde{\Phi}_f | \tilde{\Phi}_i \right\rangle = \langle\Phi_f| \hat{S} |\Phi_i\rangle \tag{1.1}$$

$\hat{S}$ denotes here the time evolution operator connecting the asymptotic states at $T = \pm\infty$. The S-matrix is most conveniently split up into its trivial and an interaction part

$$S_{fi} = \langle\Phi_{out}|\Phi_{in}\rangle + 2\pi i\delta^{(4)}(P_f - P_i) \langle\Phi_f| \hat{T} |\Phi_i\rangle \tag{1.2}$$

This defines the *T-matrix*.
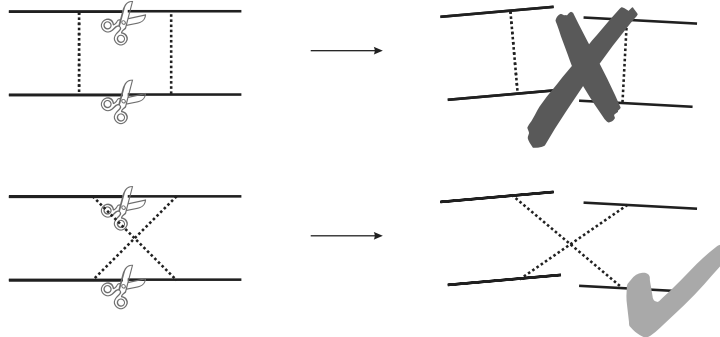
Figure 1.1.: The two particle irreducible (2PI) diagrams are defined such, that they do not fall apart when cutting two arbitrary particle lines.

We will now focus on elastic two-particle scattering which is the relevant amplitude for modeling effective interactions and consider here the T-matrix part only. Formally this is the theory of *four point functions*. The whole four pint function can be generated by so called two particle irreducible (2PI) diagrams which are defined such that cutting two arbitrary particle lines in the diagram it will not fall apart, see fig. 1.1. Let us call this set of 2PI diagrams $\{t_i\}$. As sketched in fig. 1.2, the infinite diagrammatic expansion of the T-matrix may then be written symbolically as

$$T = \sum_i t_i + \sum_{i,j} t_i G^{(2)} t_j + \sum_{i,j,k} t_i G^{(2)} t_j G^{(2)} t_k + \cdots, \tag{1.3}$$

where the integrals over the loop momenta are suppressed. $G^{(2)}$ is the two baryon propagator. Since all the sums are infinite this is not a perturbative expansion but an exact representation of the T-matrix. Defining the kernel $V \equiv \sum_i t_i$ one can rewrite eq.(1.3) as

$$T = V + \int VG^{(2)}V + \int \int VG^{(2)}VG^{(2)}V + \cdots = V + \int VG^{(2)}T \qquad (1.4)$$

This is the famous Bethe-Salpeter (BS) integral equation which governs all quantum mechanical scattering problems.

Figure 1.2.: The full T-matrix can be expressed in terms of a 2PI Kernel and the two particle propagator.

The most appropriate reference frame for scattering problems is the center of momentum (c.m.) frame. In the c.m. frame the three independent Lorentz vectors are the (conserved) total momentum $P = (\sqrt{s}, \mathbf{0})$ and the relative incoming and outgoing momenta q, q', respectively. The full formal structure of the BS equation is thus given by

$$T(q', q, \sqrt{s}) = V(q', q, \sqrt{s}) + \int \frac{d^4\tilde{q}}{(2\pi)^4} \, V(q', \tilde{q}, \sqrt{s}) G^{[2]}(\sqrt{s}, \tilde{q}) T(\tilde{q}, q, \sqrt{s}) \qquad (1.5)$$

The part of the T-matrix, which is physically relevant, the *on-shell T-matrix*, depends only on two parameters in the c.m. frame, the total energy $\sqrt{s}$ and the scattering angle $\sphericalangle(\mathbf{q'}, \mathbf{q})$. Due to energy and momentum conservation $q_0 = q_0' = 0$ and $|\mathbf{q}| = |\mathbf{q'}| = q_s$. The T-matrix inside the correlation integral is often referred to as *half off-shell T-matrix*. As can be seen from eq.(1.5), the incoming momentum q is the same as for the physical T-matrix, fulfilling the on-shell conditions, while the outgoing momentum $\tilde{q}$ is an integration parameter, which is not constrained by any on-shell conditions.

Since the kernel V itself is an infinite sum containing diagrams with infinitely many loops not even this central quantity, the starting point for a calculation of scattering observables in the BS formalism, can be calculated. For practical calculations so called *truncation schemes* of the kernel are used. This means that only specific classes of diagrams, e.g. Born or Born and crossed box, are included in V. The probably most popular truncation scheme is the *ladder approximation*. Here only the most simple 2PI kernel is taken into account, namely the Born graphs of the perturbation series. This generates the whole infinite sum of planar diagrams. The ladder (+ crossed ladder, depending on the two-particle propagator used, see further down) resummation turned out to be the most important class of diagrams and has been used for almost all the meson exchange models of the nuclear forces.

1.2. Symmetries and systematics of the T-matrix

1.2.1. Partial wave decomposition
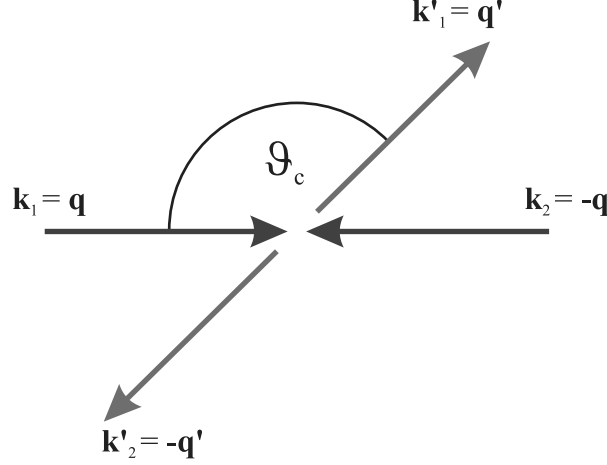
Figure 1.3.: Kinematics of the center of mass frame. The half off-shell scattering matrix depends only on four variables in that frame: the absolute values of the incoming and outgoing momenta $|\boldsymbol{q}|$ and $|\boldsymbol{q}'|$, respectively, the scattering angle ϑ_c and $\sqrt{s}$.

The easiest way to discuss the structure and symmetries of the T-matrix is by first decomposing it into the partial wave basis [Jacob59]. This is a very convenient way of describing two body scattering in the c.m. frame, since it exploits the kinematical symmetries of this process. The physical scattering matrix depends only on three kinematical variables, the absolute value of the relative momentum and the scattering angle, i.e., the angle between incoming and outgoing relative momentum. Solving the BS equation also the half off-shell scattering matrix is needed, which introduces the fourth kinematic variable. In addition the amplitudes depend on polarization observables, the helicities of incoming and outgoing particles.

The dependence on only one angle leads to an azimuthal symmetry and makes a formulation in terms of spherical basis functions favorable. The Wigner d functions, which are expectation values of the rotation operator

$$d^J_{\lambda'\lambda}(\vartheta) = \langle J\lambda' | \exp[-i\vartheta \hat{J}_y] | J\lambda \rangle \,, \tag{1.6}$$

form a basis, in which the angular part of scattering amplitudes in the c.m. frame may be expanded with respect to total angular momentum J. $\lambda = \lambda_1 - \lambda_2$ and $\lambda' = \lambda'_1 - \lambda'_2$ are the relative helicities of the incoming and outgoing particles, respectively. These are equivalent to the z directions of the total spins, since the momenta are back-to-back in the c.m. frame along the z axis. The T-matrix expanded into the partial wave basis is then given by

$$\langle q'\lambda'_1\lambda'_2 | T | q\lambda_1\lambda_2 \rangle = \frac{1}{4\pi} \sum_J (2J+1) d^J_{\lambda'\lambda}(\theta) \langle \lambda'_1\lambda'_2 | T^J(\boldsymbol{q}',\boldsymbol{q}) | \lambda_1\lambda_2 \rangle \,. \tag{1.7}$$

13

Due to orthogonality of the D functions, see app. B.2, the different angular momentum components of the T-matrix are obtained by

$$\langle\lambda_1'\lambda_2'|\,T^J(\boldsymbol{q}',\boldsymbol{q})\,|\lambda_1\lambda_2\rangle = 2\pi \int_{-1}^{1} d\cos(\theta)d_{\lambda\lambda'}^J(\theta)\,\langle q'\lambda_1'\lambda_2'|\,T\,|q\lambda_1\lambda_2\rangle \tag{1.8}$$

More details about the partial wave decomposition and a derivation of the partial wave decomposed BS equation is given in app. B.2.

1.2.2. The structure of the T-matrix

There are several exact and approximate symmetries obeyed by the baryon-baryon interaction which help to understand the structure of the very complex T-matrix equations and to simplify the numerical work. The approximate symmetries are the almost exactly realized *isospin symmetry* (broken by electromagnetic and weak interaction) and the slightly broken *SU(3) symmetry* (broken by the mass difference between up, down and strange quark). The exact symmetries are

- *parity invariance*

- *time reversal invariance*

- *identical particle symmetry*

The appropriate framework for the further discussion is the partial wave decomposed helicity state basis, defined in the c.m. frame. The basis states $|\lambda_1\lambda_2\rangle$ are eigenstates of the helicity operator

$$\hat{h}_i = \frac{\frac{1}{2}\boldsymbol{\sigma}_{(i)}\boldsymbol{p}_{(i)}}{|\boldsymbol{p}_{(i)}|}, \tag{1.9}$$

with eigenvalues λ_i. i is the index of the respective particle; $\lambda = \pm\frac{1}{2}$ and will be abbreviated $+/-$. There are in total four basis states, $|++\rangle$, $|+-\rangle$, $|-+\rangle$ and $|--\rangle$, leading to in total 16 helicity matrix elements.

The **parity** transformation acts on space-like 3-vectors. It flips the sign of vectors, like $\boldsymbol{x}$ and $\boldsymbol{p}$, but leaves pseudovectors, like, e.g., angular momenta, untouched. Thus, see eq.(1.9), the helicity flips sign under parity.

The helicity state basis is not an eigenbasis of parity which is, however, a symmetry of the strong interaction. To find a set of parity conserving matrix elements which will decouple the BS equation and thereby reduce its complexity, we expand the helicity basis states in terms of parity eigenstates. The LSJ basis is an equivalent basis for the two particle system and consists of parity eigenstates. The transformation rule between helicity and LSJ-states is given by a recoupling of the two particles' angular momenta

$$|JM\lambda_1\lambda_2\rangle = \sum_{LS}\sqrt{\frac{2L+1}{2J+1}}\,\langle L0S\lambda|J\lambda\rangle\,\langle s_1\lambda_1 s_2 - \lambda_2|S\lambda\rangle\,|JMLS\rangle \tag{1.10}$$

s_1 and s_2 are the spins of the two particles, λ_1 and λ_2 the respective helicity, $\lambda \equiv \lambda_1 - \lambda_2$ and S is the total spin. The parity eigenvalue of $|JMLS\rangle$ is the product of two particles' intrinsic parities η_1 and η_2 and the parity factor due to orbital angular momentum:

$$P\,|JMLS\rangle = \eta_1\eta_2(-)^L\,|JMLS\rangle \tag{1.11}$$

The intrinsic parity $\eta = 1$ for the baryons of the lowest octet so that the product also equals 1. Thus the parity operation on the helicity state basis yields

$$P\,|JM\lambda_1\lambda_2\rangle = \sum_{LS}\sqrt{\frac{2L+1}{2J+1}}\,\langle L0S\lambda|J\lambda\rangle\,\langle s_1\lambda_1 s_2 - \lambda_2|S\lambda\rangle\,(-)^L\,|JMLS\rangle \tag{1.12}$$

On the other hand

$$
\begin{aligned}
|JM - \lambda_1 - \lambda_2\rangle &= \sum_{LS}\sqrt{\frac{2L+1}{2J+1}}\,\langle L0S - \lambda|J - \lambda\rangle\,\langle s_1 - \lambda_1 s_2\lambda_2|S - \lambda\rangle\,|JMLS\rangle \\
&= \sum_{LS}\sqrt{\frac{2L+1}{2J+1}}(-)^{L+S-J}\,\langle L0S\lambda|J\lambda\rangle\,\times \\
&\qquad (-)^{s_1+s_2-S}\,\langle s_1\lambda_1 s_2 - \lambda_2|S\lambda\rangle\,|JMLS\rangle
\end{aligned}
\tag{1.13}
$$

where we used the property of the Clebsch-Gordan coefficients that

$$\langle J_1 M_1 J_2 M_2|JM\rangle = (-)^{J_1+J_2-J}\,\langle J_1 - M_1 J_2 - M_2|J - M\rangle, \tag{1.14}$$

Since we deal with baryons of the lowest octet $s_1 = s_2 = \frac{1}{2}$. Linking all this together one finds

$$P\,|JM\lambda_1\lambda_2\rangle = (-)^{J+1}\,|JM - \lambda_1 - \lambda_2\rangle \tag{1.15}$$

Out of the four helicity basis elements two pairs can be grouped which are connected through the parity operation:

$$
\begin{array}{ccc}
 & P & \\
|{+}{+}\rangle & \leftrightarrow & |{-}{-}\rangle \\
|{+}{-}\rangle & \leftrightarrow & |{-}{+}\rangle
\end{array}
\tag{1.16}
$$

Using eq.(1.15) we can reduce the 16 helicity amplitudes to 8 independent ones. We chose this basis set to be

$$
\begin{aligned}
T_1^J &= \langle{+}{+}|\,T^J(q',q)\,|{+}{+}\rangle, & T_5^J &= \langle{+}{+}|\,T^J(q',q)\,|{+}{-}\rangle, \\
T_2^J &= \langle{+}{+}|\,T^J(q',q)\,|{-}{-}\rangle, & T_6^J &= \langle{+}{-}|\,T^J(q',q)\,|{+}{+}\rangle, \\
T_3^J &= \langle{+}{-}|\,T^J(q',q)\,|{+}{-}\rangle, & T_7^J &= \langle{+}{+}|\,T^J(q',q)\,|{-}{+}\rangle, \\
T_4^J &= \langle{+}{-}|\,T^J(q',q)\,|{-}{+}\rangle, & T_8^J &= \langle{-}{+}|\,T^J(q',q)\,|{+}{+}\rangle.
\end{aligned}
\tag{1.17}
$$

Through summing and subtracting the states given in eq.(1.15) pairwise parity eigenstates are found which have the same parity for every other J:

$$
\begin{aligned}
P\left(|\lambda_1\lambda_2\rangle + |{-}\lambda_! - \lambda_2\rangle\right) &= (-)^{J+1}\left(|\lambda_1\lambda_2\rangle + |{-}\lambda_1 - \lambda_2\rangle\right) \\
P\left(|\lambda_1\lambda_2\rangle - |{-}\lambda_! - \lambda_2\rangle\right) &= (-)^{J}\left(|\lambda_1\lambda_2\rangle - |{-}\lambda_1 - \lambda_2\rangle\right)
\end{aligned}
\tag{1.18}
$$

Symmetries of the helicity amplitudes

•identical particles $\quad \langle \lambda_1' \lambda_2' | T^J(\boldsymbol{q'}, \boldsymbol{q}) | \lambda_1 \lambda_2 \rangle = \langle \lambda_2' \lambda_1' | T^J(\boldsymbol{q'}, \boldsymbol{q}) | \lambda_2 \lambda_1 \rangle$ ⓘp

•time reversal $\quad \langle \lambda_1' \lambda_2' | T^J(\boldsymbol{q'}, \boldsymbol{q}) | \lambda_1 \lambda_2 \rangle = \langle \lambda_1 \lambda_2 | T^J(\boldsymbol{q}, \boldsymbol{q'}) | \lambda_1' \lambda_2' \rangle$ Ⓣ

Figure 1.4.: Symmetry connections between the different helicity amplitudes.

This decouples the original 8×8 system into two separate 2×2 systems of opposite parity

$$
\begin{array}{ll}
\pi = (-)^{J+1} & \pi = (-)^J \\[4pt]
{}^0T^J = T_1^J - T_2^J & {}^{12}T^J = T_1^J + T_2^J \\
{}^1T^J = T_3^J - T_4^J & {}^{34}T^J = T_3^J + T_4^J \\
{}^2T^J = T_5^J - T_7^J & {}^{57}T^J = T_5^J + T_7^J \\
{}^3T^J = T_6^J - T_8^J & {}^{68}T^J = T_6^J + T_8^J
\end{array}
\tag{1.19}
$$

The explicit form of the BS equation in terms of these matrix elements is given in sec. 2.2, where technical details are discussed (additional operations have to be performed to transform it into an equation for helicity matrix elements).

The **identical particle symmetry** (or total spin symmetry, as it is also frequently called in the literature, e.g. [Erkelenz74]) applies, as one may conjest from the name, to the scattering of identical particles. Identical in this framework means: *i*) they are in the same isospin multiplet (since exact isospin symmetry will be assumed for the free particles); *ii*) they have the same mass (this is in asymmetric matter not the case, even for an exactly isospin symmetric free theory). The identical particle symmetry relates under the given condition the following matrix elements:

$$
\langle \lambda_1' \lambda_2' | T^J(\boldsymbol{q'}, \boldsymbol{q}) | \lambda_1 \lambda_2 \rangle = \langle \lambda_2' \lambda_1' | T^J(\boldsymbol{q'}, \boldsymbol{q}) | \lambda_2 \lambda_1 \rangle
\tag{1.20}
$$

This symmetry leads to an equality of T_5^J and T_7^J as well as T_6^J and T_8^J. Then $^2T^J$ and $^3T^J$ will be zero. Since they are responsible for the mixing of the $J^\pi = (-)^{J+1}$ system, this is uncoupled for the scattering of identical particles. $^0T^J$ and $^1T^J$ are thus traditionally referred to as uncoupled singlet and triplet, respectively, in the NN scattering, whereas the other parity block is called the coupled triplet. Singlet and triplet refers to the spin states $S = 0$ and $S = 1$, respectively.

The last symmetry, which is irrelevant for simplifying the scattering matrix, but is of great importance in their decomposition for the calculation of the self-energy in the G-matrix, see sec. 3.1.3, is **time reversal**. It applies as a reduction of dependent matrix elements only for those diagonal in momentum:

$$\langle \lambda_1' \lambda_2' | \, T^J(\boldsymbol{q'}, \boldsymbol{q}) \, | \lambda_1 \lambda_2 \rangle = \langle \lambda_1' \lambda_2' | \, T^J(\boldsymbol{q}, \boldsymbol{q'}) \, | \lambda_1 \lambda_2 \rangle \tag{1.21}$$

This yields an equivalence of each of the pairs T_5^J, T_6^J and T_7^J, T_8^J for $|\boldsymbol{q}| = |\boldsymbol{q'}|$ and in turn leads to an equivalence of the parity basis matrix elements $^2T^J$, $^3T^J$ and $^{57}T^J$, $^{68}T^J$.

All the relations between the different matrix elements due to identical particle and time reversal symmetry are displayed in fig. 1.4. Scattering identical particles, one has 5 independent matrix elements for $|\boldsymbol{q}| = |\boldsymbol{q'}|$, i.e., especially when considering on-shell matrix elements, and 6 independent off-diagonal matrix elements. For the scattering of different particles there are either 6 independent matrix elements which are diagonal in momentum or 8 off-diagonal ones.

1.2.3. Scattering of identical particles

Describing the scattering of identical particles leads to special constraints on the wave functions. In the case of fermions, the Pauli principle requires a fully antisymmetric wave function with respect to the exchange of all the particle variables. Working with a T-matrix decomposed into partial waves, selection rules for the matrix elements can be very easily deduced. When scattering nucleons, in addition to the angular momentum we have the isospin quantum number. The isospin part of the wave function just multiplies the space part.

Normally in relativistic systems it is impossible to separate orbital angular momentum and spin, since relativistic dynamics only conserves total angular momentum. Investigating, however, nuclear interactions, the situation is different. As discussed in sec. 1.2.2, parity is a conserved quantity in the two nucleon system. Due to its intimate connection to the orbital angular momentum, as well total spin as orbital angular momentum are good quantum numbers themselves. For this reason also the old labeling of amplitudes by spin, orbital and total angular momentum is kept as it was used in non-relativistic approaches:

$$^{2S+1}L_J, \tag{1.22}$$

where for L the corresponding letters $(S, P, D, ...)$ are used.

In the c.m. frame the two particles sit at $\pm x$, so that an exchange is equivalent to the parity operation. Parity of the wave function's space part, in turn, is fixed by the orbital angular momentum $\pi = (-)^L$. For a given J the following combinations of spin

and orbital angular momentum are possible:

orbit	spin	parity
$L = J+1$	1	$-\pi$
$L = J$	$0, 1$	$\pi = (-)^L$
$L = J-1$	1	$-\pi$

$$(1.23)$$

The total spin defines the symmetry character of the spin wave function, a singlet state is odd and a triplet state is even under exchange of particle spins. Combining the symmetries of the wave function's space and spin parts, which are linked, as we just have seen, one obtains

$$|x, x', \lambda, \lambda'\rangle = (-)^{L+S+1} |x', x, \lambda', \lambda\rangle \tag{1.24}$$

J	$T = 0$	$T = 1$
0	$^3S_0$	$^1S_0, \, ^3P_0$
1	$^1P_1, ^3S_1-^3D_1$	$^3P_1$
2	$^3D_2$	$^1D_2, \, ^3P_2-^3F_2$
3	$^1F_3. \; ^3D_3-^3G_3$	$^3F_3$

Table 1.1.: The partial wave amplitudes in NN scattering with their corresponding isospin quantum numbers. Mixing states are linked by a "–".

The isospin part adds another factor of $(-)^{T+1}$. The requirement of an antisymmetric wave function can therefore be coded

$$(-)^{L+S+T} \overset{!}{=} -.1 \tag{1.25}$$

Knowing that the isospin wave function has opposite parity for $T = 0$ and $T = 1$, we can read off eq.(1.23), that we will have a mixing between the $L = J \pm 1$ states, since all their quantum numbers are identical, while the two $L = J$ states will remain uncoupled. From this the notion "uncoupled singlet", "uncoupled triplet" and "coupled triplet" arise. Singlet and triplet refers to the respective spin states. The partial wave amplitudes with their corresponding isospin and mixing are listed in tab. 1.1. If scattering non-identical particles, the restriction of defined symmetry is gone and two 2×2 coupled systems of opposite parity are obtained.

For the general baryon-baryon interaction one may treat hyperons and nucleons also as identical particles with respect to the interaction (as it is done, e.g., in the Nijmegen models [Rijken99, Stoks99]). Instead of coupling the particles to irreducible representations of the isospin group SU(2), the isospin multiplets, they are coupled to irreducible SU(3) representations. As the isospin multiplets, these also behave either symmetric or antisymmetric when interchanging two particles. The SU(3) multiplets are labelled by their multiplicity n and $[n]$, the adjoint representation is denoted by an additional bar. For the octet [8] an additional index, either a or s, is needed to distinct between antisymmetric and symmetric octet, respectively. The selection rule for the scattering of SU(3) multiplts is then obtained by replacing the isospin factor $(-)^{T+1}$ in eq.(1.25) by the respective SU(3) symmetry factor, which can be found in tab. 1.2 and tab. 1.3.

strangeness	T	channels	SU(3) ir.rep.
0	0	NN	$[\overline{10}]$
-1	$\frac{1}{2}$	$\Lambda N,\ \Sigma N$	$[\overline{10}],\ [8]_a$
	$\frac{3}{2}$	ΣN	$[10]$
-2	0	ΞN	$[8]_a$
	1	$\Xi N,\ \Sigma\Sigma$	$[10],\ [\overline{10}],\ [8]_a$
		$\Sigma\Lambda$	$[10],\ [\overline{10}]$
-3	$\frac{1}{2}$	$\Xi\Lambda,\ \Xi\Sigma$	$[10],\ [8]_a$
	$\frac{3}{2}$	$\Xi\Sigma$	$[\overline{10}]$
-4	0	$\Xi\Xi$	$[10]$

Table 1.2.: Symmetry of the flavor part for space-spin symmetric two baryon wave functions [Stoks99].

strangeness	T	channels	SU(3) ir.reps.
0	1	NN	$[27]$
-1	$\frac{1}{2}$	$\Lambda N,\ \Sigma N$	$[27],\ [8]_s$
	$\frac{3}{2}$	ΣN	$[27]$
-2	0	$\Lambda\Lambda,\ \Xi N,\ \Sigma\Sigma$	$[27],\ [8]_s,\ [1]$
	1	$\Xi N,\ \Sigma\Lambda$	$[27],\ [8]_s$
	2	$\Sigma\Sigma$	$[27]$
-3	$\frac{1}{2}$	$\Xi\Lambda,\ \Xi\Sigma$	$[27],\ [8]_s$
	$\frac{3}{2}$	$\Xi\Sigma$	$[27]$
-4	1	$\Xi\Xi$	$[27]$

Table 1.3.: Symmetry of the flavor part for space-spin antisymmetric two baryon wave functions [Stoks99].

Imposing the just discussed projection on the kernel of the BS equation, one immediately obtains the physical, antisymmetrized T-matrix. Then Hartree and Fock terms are implicitly generated. It is, however, also possible, to calculate the direct terms only by ignoring antisymmetrization and afterward account for the identical particle nature by subtracting the exchange amplitude. Therefore the calculated T-matrix has to be decomposed into Lorentz covariants, from which the exchange parts may then be calculated and subtracted from the unphysical amplitude. This procedure is described in detail in sec. 3.1.3.

In fig. 1.2.3 we show as an example the behavior with respect to q_s of the scalar invariant of the Bonn A potential, which corresponds, loosely spoken, to the tree-level graph of an effective scalar exchange meson. Panel a) displays the comparison between the physical, antisymmetrized, and unphysical, not antisymmetrized, scalar amplitudes[1]. The effect of the implicit inclusion of exchange diagrams in the antisymmetrized amplitudes in nicely visible as a strong momentum dependence, which is absent for the unphysical, direct term. Panel b) illustrates the cancellation of large, momentum dependent contributions in the partial wave expansion, which in the end restores the $\sqrt{s}$ independent behavior of the Born diagrams. Leaving out every second partial wave, as the antisymmetrization technically does, leads to the strong momentum dependence of the physical amplitudes displayed in panel a), which can be attributed to the inclusion of exchange amplitudes.

1.3. 3D-reduced two baryon propagators

In typical nuclear interaction models the full two baryon propagator is for technical reasons replaced by a tree dimensional reduced propagator (3D propagator). This is, however, done covariantly. The 3D propagator fixes the time-like momentum component by a δ function and thus eliminates one of the four loop integrations. The leftover three integrations over the space-like momentum components can then later on be transformed in angular momentum projected one dimensional integrals which are a lot easier to solve.

1.3.1. Reference frames in two particle scattering

To derive the expressions for the 3D propagators we will first define relative and total c.m. four momenta that are orthogonal in space and time component. An arbitrary set of four-momenta in the c.m. frame, which needs not to fulfill the mass-shell relation is given by

$$k^{(1)} = \left(k_0^{(1)}, \boldsymbol{q}\right), \quad k^{(2)} = \left(k_0^{(2)}, -\boldsymbol{q}\right) \tag{1.26}$$

The total four momentum is straightforwardly constructed by adding both and obtaining the purely time-like

$$P \equiv k^{(1)} + k^{(2)} = \left(k_0^{(1)} + k_0^{(2)}, \boldsymbol{0}\right) \tag{1.27}$$

---

[1]The amplitudes displayed there are obtained from a partial wave decomposition and include partial waves up to $J = 15$. The high momentum part is thus not quite converged.
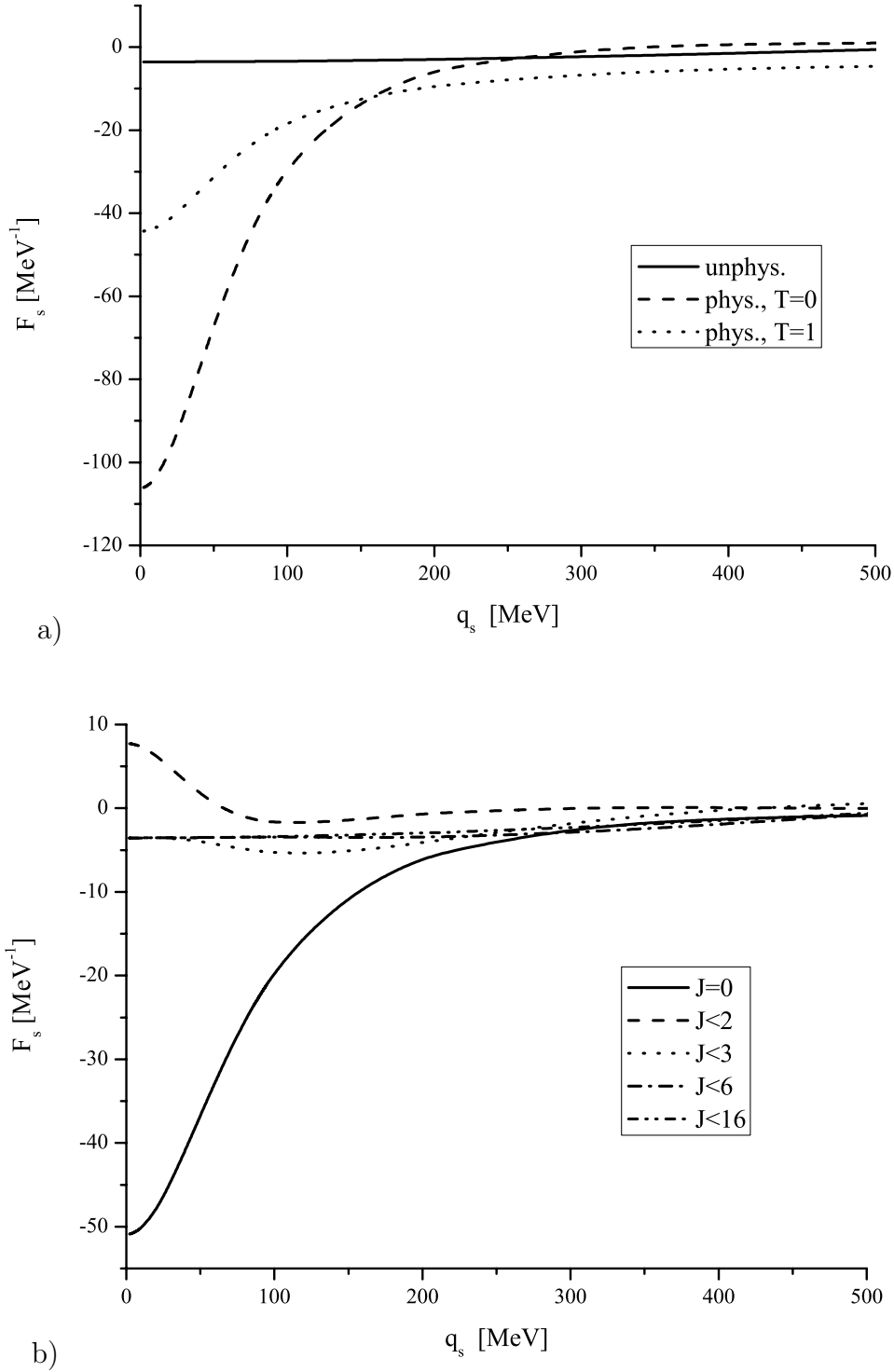
Figure 1.5.: The panels show scalar invariants of the Bonn A Born diagrams. Antisymmetrization, which is an implicit inclusion of exchange diagrams, leads to a strong momentum dependence as shown in panel a). Panel b) shows the not antisymmetrized partial wave decomposed amplitudes summed up to a given J. The cancellation between contributions of different partial waves restores the $\sqrt{s}$ independence of the original Born diagram.

To construct a relative four momentum which is orthogonal to P, i.e. purely space-like, we need to take a weighted difference of $k^{(1)}$ and $k^{(2)}$

$$q \equiv x_1 k^{(1)} - x_2 k^{(2)} \overset{!}{=} (0, \boldsymbol{q}) \tag{1.28}$$

$$\Rightarrow \quad \left.\begin{array}{l} x_1 + x_2 = 1 \\ x_1 k_0^{(1)} - x_2 k_0^{(2)} = 0 \end{array}\right\} \quad \Rightarrow \quad x_{1,2} = \frac{k_0^{(2,1)}}{P_0} \tag{1.29}$$

In the relative coordinates $k^{(1)}$ and $k^{(2)}$ are

$$k^{(1)} = x_2 P + q, \quad k^{(2)} = x_1 P - q \tag{1.30}$$

As needed in the loop integration of the BS equation, both particle four momenta can be independently arbitrarily far off shell, as long as P_0 is a free parameter. For the 3D reduction P_0 is fixed to a specific energy. Choosing P_0 to be the total energy, the two particles are bound to be *symmetrically off shell* and therefore on-shell simultaneously (with respect to $\boldsymbol{q}$). One could as well imagine to fix P_0 to some other energy which would make the two particles asymmetrically off-shell by a fixed value. Having $P_0 = \sqrt{s(\boldsymbol{q})}$, which is the on-shell case, x_1 and x_2 can be expressed in terms of the total energy and the masses:

$$x_1 = \frac{1}{2}\left(\frac{M_2^2 - M_1^2}{s} + 1\right), \quad x_2 = \frac{1}{2}\left(\frac{M_1^2 - M_2^2}{s} + 1\right) \tag{1.31}$$

For the c.m. frame this is also the most reasonable choice since the incoming physical particles correspond to asymptotic, on-shell states. In the framework of the BS equation they can only go symmetrically off-shell, which preserves the orthogonality of the total and relative momentum. Two prescriptions of symmetrically off-shell 3D propagators, the Blankenbecler-Sugar (BbS) and the Thompson (Th) propagator, will be described below.

The relative c.m. momentum, q_c may be expressed in terms of Lorentz invariants, so it may be calculated very easily from momenta in arbitrary reference frames. Solving $s = (E_1(q_s) + E_2(q_s))^2$ for q_c we obtain

$$q_s{}^2 = \frac{(s - M_1{}^2 - M_2{}^2)^2 - 4M_1{}^2 M_2{}^2}{4s} \tag{1.32}$$

Another common variable in two particle scattering formalisms is the *laboratory energy* T_{lab}. To derive it, we need the notion of laboratory frame. The laboratory frame is defined such, that the target particle is at rest, $p_1 = (M_1, \boldsymbol{0})$, while the projectile moves with three momentum $\boldsymbol{q}_l$, $p_2 = (E_2(\boldsymbol{q}_l), \boldsymbol{q}_l)$, $E_i(\boldsymbol{k}) = \sqrt{M_i^2 + \boldsymbol{k}^2}$. By the Lorentz invariant $s = (p_1 + p_2)^2$ we can relate this to the relative momentum in c.m. frame, where $q_{1,2} = (E_{1,2}(\boldsymbol{q}), \pm\boldsymbol{q})$. The laboratory energy is then defined as

$$T_{lab} \equiv E_2(\boldsymbol{q}_l) - M_2 = \frac{\boldsymbol{q}^2 - E_1(\boldsymbol{q})E_2(\boldsymbol{q})}{M_1} - M_2 \overset{M_1 = M_2}{\longrightarrow} \frac{2\boldsymbol{q}^2}{M} \tag{1.33}$$

1.3.2. The pseudo-potential equation

The 3D reduced ladder approximation can be formally deduced as an expansion of the full kernel with respect to the difference between full and 3D propagator. The full propagator G (the index $^{(2)}$ will be suppressed) is rewritten as $G = g + (G - g)$, where g is three dimensional and has the same elastic unitarity cut as G. The BS equation may then be transformed into a coupled system

$$T = W + WgT \tag{1.34}$$
$$W = V + V(G - g)W \tag{1.35}$$

which is equivalent to eq.(1.4). Eq.(1.34) is now the easier to solve 3D equation, but eq.(1.35) is at least as hard to solve as eq.(1.4). One should note, that V is still the full kernel. The pseudo potential W is now expanded in orders of the coupling constants denoted by the superscript of V and W:

$$W^{(2)} = V^{(2)} \tag{1.36}$$
$$W^{(4)} = V^{(4)} + V^{(2)}(G - g)V^{(2)}) \tag{1.37}$$
$$\vdots$$

The full kernel V is reduced such, that $V^{(n)} \sim \mathcal{O}(g^n)$. The first order of the pseudopotential, $W^{(2)}$, is then proportional to g^2, the second order, $W^{(4)}$, is proportional to g^4, etc..

The combined ladder + 3D approximation is then obtained quite naturally by truncating this expansion after eq.(1.36), i.e., keeping only kernel elements up to second order in the couplings.

1.3.3. The Blankenbecler-Sugar propagator
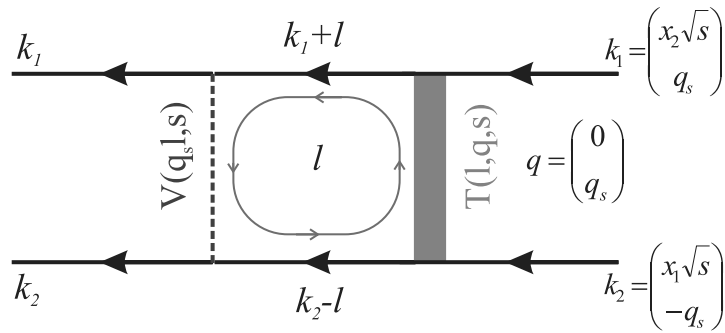
Figure 1.6.: In the physically relevant on-shell T-matrix the intermediate two baryon propagator of the loop transports the particle momenta $k_1 + l$ and $k_2 - l$, where k_1 and k_2 are the incident on-shell momenta.

The definition of the Blankenbecler-Sugar (BbS) propagator [Blankenbecler66] is made with respect to the physically relevant on-shell T-matrix, i.e., the T-matrix for in- and

outgoing states, which are on their mass shell. As illustrated in fig. 1.6, the incoming and also outgoing particle momenta are given by

$$k_{1,2} = \begin{pmatrix} x_{2,1}\sqrt{s_0} \\ \pm\boldsymbol{q}_s \end{pmatrix} = x_{2,1}P_\mu \pm q_{s\mu}, \quad \text{where } P_\mu = (\sqrt{s_0}, 0). \tag{1.38}$$

As the on-shell relation is fullfilled for these four-momenta, eq.(1.31) hols for x_1 and x_2. The momenta propagated in the intermediate state contain an additional loop momentum l^μ,

$$k_1'^{\,\mu} = (k_1 + l)^\mu, \qquad k_2'^{\,\mu} = (k_2 - l)^\mu, \tag{1.39}$$

with the respective c.m. variables

$$P'^\mu = (k_1' + k_2')^\mu = P^\mu, \qquad q'^\mu = x_1' k_1' - x_2' k_2' = q^\mu + l^\mu \tag{1.40}$$

The complete two fermion propagator of the intermediate state in the BS equation is then, in the c.m. frame and with the momenta just defined, given by

$$\frac{[\gamma_\mu(k_1 + l)^\mu + M_1]_{(1)}}{(k_1 + l)_\mu^2 - M_1^2 + i\epsilon} \frac{[\gamma_\mu(k_2 - l)^\mu + M_2]_{(2)}}{(k_2 - l)_\mu^2 - M_2^2 + i\epsilon}. \tag{1.41}$$

The 3D reduced propagators have the aim to simplify the BS equation. Their merits are

1. removing the integration over l^0 by introducing a $\delta(f(l^0))$ in the reduced propagator;

2. converting the numerator of the full two particle propagator into a positive energy projection operator, leading to a formulation of the BS equation in terms of positive energy matrix elements.

This sounds rather restrictive at first but is done in an elegant and also covariant way. The new propagator needs to fulfill at least the most important analytic properties of the full one. The most prominent analytic structures of the two particle propagator are the one- and two-particle cuts. In the 3D reduction only one of both can be realized, leading to a whole variety of different 3D propagators that may be constructed. In the BbS propagator, as well as in the Thompson propagator, which is derived further down, the two-particle cut is included. Having a two-particle cut only, both baryons can only go an-shell simultaneously, i.e., for the same q. This implies, that they have to be equally far off-shell. Other prescriptions, which only conserve the single particle cuts are discussed in sec. 1.3.5.

We will now first sketch and motivate the procedure of deriving the BbS propagator before actually duing the algebra. Instead of a denominator which becomes zero when either the particle goes on its mass shell, as in eq.(1.41), a total energy denominator $(s_0 - s')^{-1}$ is chosen with $s_0 = P_\mu P^\mu$. s_0 is a constant in this context, fixed from outside. To obtain a two-particle cut, s' has to be a function of $(q+l)^\mu$, which equals s for $l^\mu = 0$. The delta function

$$\delta^{(+)}((x_2'P' + q_s + l)_\mu^2 - M_1^2)\delta^{(+)}((x_1'P' - q_s - l)_\mu^2 - M_2^2), \qquad P' = (\sqrt{s'}, \boldsymbol{0}), \tag{1.42}$$

together with an integral over s' produces exactly this behavior, where $^{(+)}$ indicates, that only the positive energy root contributes. The factors x'_1 and x'_2 are chosen in analogy to eq.(1.31) where s is replaced by s'. This leads to a symmetric off-shellness as was discussed earlier. Comparing this to eq.(1.38), it is obvious, that the delta functions imply $s' = E_1(\boldsymbol{q_s} + \boldsymbol{l}) + E_2(\boldsymbol{q_s} + \boldsymbol{l})$, i.e., the newly constructed propagator will have the two-particle cut for $\boldsymbol{l} = 0$.

The pole is thus translated from being a *mass-shell pole* into being a *momentum-shell pole*. The singularity appears when $\boldsymbol{l} = \boldsymbol{0}$ so that the propagated momentum equals the incident on-shell 3-momentum. Although it is equivalent in the exact treatment, the reduction leads to a subtle difference: As we will see, the total energy of the intermediate two nucleons, i.e. $k_1'^{\,0} + k_1'^{\,0}$, is kept fixed to $E_1(\boldsymbol{q_s}) + E_2(\boldsymbol{q_s})$ in this approximation, only the three-momentum loop integral will be left. So the propagated baryons are always on their *energy* shell. The new propagator gets "on-shell" when it goes onto its momentum shell, i.e., $\boldsymbol{l} = 0$.

In analogy to the arguments of the delta functions the numerator is chosen as

$$[\gamma_\mu (x'_2 P' + q_s + l)^\mu + M_1]_{(1)}\,[\gamma_\mu (x'_1 P' - q_s - l)^\mu + M_2]_{(2)}, \tag{1.43}$$

which produces the desired residue of the propagator. Since the delta functions lead to $s' = E_1(\boldsymbol{q_s} + \boldsymbol{l}) + E_2(\boldsymbol{q_s} + \boldsymbol{l})$, This expression becomes a positive energy projection operator for the two intermediate states.

The above discussion can be collected in the following integral representation of th fermionic[2] BbS propagator:

$$G_{BbS}^{(2)}(q,s) \equiv \int_{(M_1+M_2)^2}^{\infty} ds' \frac{[\gamma_\mu (x'_2 P' + q)^\mu + M_1]_{(1)}\,[\gamma_\mu (x'_1 P' - q)^\mu + M_2]_{(2)}}{s' - s_0 + i\epsilon} \\ \delta^{(+)}((x'_2 P' + q)_\mu^2 - M_1^2)\delta^{(+)}((x'_1 P' - q)_\mu^2 - M_2^2) \tag{1.44}$$

(q_μ must not be confused with $q_{s\,\mu}$ from above; $q_\mu = (q_s + l)_\mu$ and thus contains, unlike $q_{s\,\mu}$, a time-like component as well.) Restricting our formalism to the scattering of positive energy states, also in the intermediate ones, we will only use the positive energy root of the delta function, symbolized by $\delta^{(+)}$ [3]. Since we would like the energy to be symmetrically off-shell in the delta functions, we have, as discussed above:

$$x'_{1,2} = \frac{E_{2,1}(\boldsymbol{q})}{\sqrt{s(\boldsymbol{q})}} \tag{1.45}$$

In the c.m. frame we can now explicitly derive the expression for G_{BbS}. Let us begin by evaluating the first delta function with the s' integration. The root of its argument with respect to s' is

$$\sqrt{s'} = \frac{E_1(\boldsymbol{q}) - q^0}{x'_2} \tag{1.46}$$

---

[2]In the original work [Blankenbecler66] Blankenbecler and Sugar set up a covariant reduced scattering equation for a two meson system.

[3]Positive energy means here that $x'_{2,1} P'_0 \pm q_0 > 0$.

$E_i(\boldsymbol{q})$ will be abbreviated by E_i in the following since there is only $\boldsymbol{q}$ appearing as argument. The derivative of the delta function's argument is given by

$$d_1(s') \equiv \frac{\partial}{\partial s'} \left[(x_2' P' + q)^2 - M_1^2 \right] = x_2'(x_2' + \frac{q^0}{\sqrt{s'}}) \tag{1.47}$$

The first delta function thus becomes

$$\delta^{(+)}((x_2' P' + q)^2 - M_1^2) = \left| \frac{E_1 - q^0}{x_2'^2 E_1} \right| \delta^{(+)} \left(s' - \left[\frac{E_1 - q^0}{x_2'} \right]^2 \right) \tag{1.48}$$

Performing the s' integration now, the argument of the second delta function becomes

$$(x_1' \sqrt{s'} - q^0)^2 - E_2^2 \xrightarrow{\sqrt{s'} = \frac{E_1(q) - q^0}{x_2'}} \left(\frac{x_1'}{x_2'} E_1 - \left(1 + \frac{x_1'}{x_2'} \right) q^0 \right)^2 - E_2^2 \tag{1.49}$$

Using eq. (1.45) it directly follows that the *positive energy root* is $q^0 = 0$. To rewrite this delta function for being evaluated directly in the q^0 integral of the BS equation we need the argument's derivative at $q^0 = 0$ which is easily calculated to be

$$d_2(q^0 = 0) = -2\frac{E_2}{x_2'} \tag{1.50}$$

So the second delta function becomes

$$\delta^{(+)} \left(\left[\frac{x_1'}{x_2'} E_1 - \left(1 + \frac{x_1'}{x_2'} \right) q^0 \right]^2 - E_2^2 \right) = \frac{x_2'}{2E_2} \delta^{(+)}(q^0) \tag{1.51}$$

To collect the whole expression for the BbS propagator we will at those places where q^0 appears assume, that the remaining delta function is already evaluated, i.e. setting q^0 to zero, since it will contribute anyway only then and simplifies the expression. Furthermore we define the positive energy projection operators

$$\Lambda_i^{(+)}(\boldsymbol{q}) = \frac{1}{2M_i}(\gamma^0 E_i - \boldsymbol{\gamma}\boldsymbol{q} + M_i) \tag{1.52}$$

into which the numerator of eq. (1.44) is turned by the first delta function and the condition $q^0 = 0$ implied by the second one. The final expression is then

$$g_{BbS}(\boldsymbol{q}, s) = \frac{\Lambda_1^{(+)}(\boldsymbol{q}) \Lambda_2^{(+)}(\boldsymbol{q})}{s(\boldsymbol{q}) - s_0 + i\epsilon} \frac{2M_1 M_2 \sqrt{s(\boldsymbol{q})}}{E_1 E_2} \tag{1.53}$$

where $G_{BbS}(q, s) = g_{BbS}(\boldsymbol{q}, s)\delta^{(+)}(q^0)$.

1.3.4. The Thompson propagator

The Thompson (Th) propagator [Thompson70] is very similar to the BbS propagator, so it will be sufficient to sketch here the differences and state the final result. The ansatz for the Th propagator uses $\sqrt{s'}$ in place of s':

$$G^{(2)}_{Th}(q,s) \equiv \int_{(M_1+M_2)}^{\infty} d\sqrt{s'} \frac{[\gamma_\mu(x'_2 P' + q)^\mu + M_1]_{(1)} [\gamma_\mu(x'_1 P' - q)^\mu + M_2]_{(2)}}{\sqrt{s'} - \sqrt{s_0} + i\epsilon}$$
$$\delta^{(+)}((x'_2 P' + q)^2_\mu - M_1^2)\delta^{(+)}((x'_1 P' - q)^2_\mu - M_2^2) \tag{1.54}$$

The evaluation proceeds similar to the BbS case and yields

$$g_{Th}(\boldsymbol{q},s) = \frac{\Lambda_1^{(+)}(\boldsymbol{q})\Lambda_2^{(+)}(\boldsymbol{q})}{\sqrt{s(\boldsymbol{q})} - \sqrt{s_0} + i\epsilon} \frac{M_1 M_2}{E_1 E_2} \tag{1.55}$$

Both propagators are related by a very simple transformation

$$g_{Th} = \frac{\sqrt{s(\boldsymbol{q})} + \sqrt{s_0}}{2\sqrt{s(\boldsymbol{q})}} g_{BbS} \tag{1.56}$$

1.3.5. Discussion of 3D propagators

The 3D propagators presented in the last section are all constructed such that they put the baryons equally far off-shell. This is by no means a unique, nor a supreme choice. There exist many different families of such reduced propagators which may even depend on a continuous parameter [Woloshyn73, Gross82].

Physically, the reduction of the two baryon propagator – interpreted in the meson exchange framework – means a modification of the retardation compared to the full BS equation, since the $0th$ component of the loop momentum is set to a fixed value. The symmetric choice which we will use throughout this work implies that all retardation effects are neglected due to the $\delta(k_0)$. This leads to a modification of pole structure in the exchange meson's propagator. In the symmetrically off-shell case it completely removes the pole. At low energies, as they are needed for baryon interactions in nuclear structure theory, neglecting retardation effects seems to be a reasonable assumption, which is consistent with data in present day models. As is well known, the integrated strength of the exchange particle's propagator is by far more important for the scattering amplitude than the exact pole structure.

In the literature many investigations on what would be the best 3D equation for nuclear physics can be found, the most detailed ones are [Woloshyn73, Gross82]. There are two main focuses in the discussions: (1) which 3D equation is closest to the full BS equation using the same kernel, and (2) which one has the best characteristics in terms of an expansion in orders of the coupling squared. As pointed out by [Gross82], the first point does not make sense, since the full four dimensional equation using a ladder kernel has an incorrect single particle limit, whereas all the 3D equations show the correct behavior. The second point is more a "would be" criterion since an expansion beyond coupling constant to the fourth power, which is only second order (!), is technically far too involved. From our point of view the choice of the 3D propagator is a free model parameter like the couplings are and is intimately connected with them.

1.4. The K-matrix approximation and scattering phase shifts

Below the threshold for particle production the real valued reaction or K-matrix is equivalent to the 3D reduced T-matrix (and non relativistic T-matrix, respectively). The K-matrix operator is almost identical to the T-matrix operator, only that the loop integral part contains a principal value:

$$K = V + \mathcal{P}VG^{(2)}K \tag{1.57}$$

Both scattering matrices are connected through the Heitler integral equation [Joachain75]

$$T(q', q, \sqrt{s}) = K(q', q, \sqrt{s}) - i\pi \int d^3k \, K(q', k, \sqrt{s})\delta(s - s_k)T(k, q, \sqrt{s}) \tag{1.58}$$

Please note, that the factor of $(2\pi)^{-3}$, belonging to the integral measure, is absorbed in the scattering matrices in this definition. The k integral of eq.(1.58) can be easily solved using

$$dk = \frac{E_1(k)E_2(k)}{k\sqrt{s_k}}d\sqrt{s_k} \equiv \frac{\rho(s_k)}{k^2} \, d\sqrt{s_k}, \tag{1.59}$$

In the context of baryon-baryon scattering, where incident, intermediate and outgoing states may be of different mass, one usually uses an equivalent expression which is symmetric in the energies of the incoming and outgoing states, labelled by i, o, respectively:

$$\rho(s) = \sqrt{\rho_o(s)\rho_i(s)} = \sqrt{\frac{q_s E_{1,o}(q_s)E_{2,o}(q_s)}{\sqrt{s}} \frac{q_s E_{1,i}(q_s)E_{i,o}(q_s)}{\sqrt{s}}} \tag{1.60}$$

$$T(q', q, \sqrt{s}) = V(q', q, \sqrt{s}) - i\pi\rho(s) \int d\Omega \, V(q', q_s, \sqrt{s})T(q_s, q, \sqrt{s}) \tag{1.61}$$

Performing a partial wave decomposition now yields an algebraic equation which may be trivially solved for the full on-shell matrices in the uncoupled scattering channels:

$$T^{(J)}(s) = \frac{K^{(J)}(s)}{1 + i\pi\rho(s)K^{(J)}(s)} \tag{1.62}$$

$$K^{(J)}(s) = \frac{T^{(J)}(s)}{1 - i\pi\rho(s)T^{(J)}(s)} \tag{1.63}$$

Since angular momentum is conserved and we are considering elastic scattering, flux conservation tells us that the scattering matrix needs to be unitary. This means for the so far discussed single channel problem, that it may only depend on a single parameter, a real scattering phase $\delta_J(s)$. The reaction matrix K can therefore also be parametrized in terms of that scattering phase [Joachain75]

$$K^{(J)} = -\frac{1}{\pi\rho(s)} \tan\left(\delta_J(s)\right) \tag{1.64}$$

Due to the general definition of ρ, eq.(1.60), this applies as well for identical particles as for particles of different mass. Using eqs.(1.62) and (1.64) the respective parametrization for the T-matrix is

$$T^{(J)} = -\frac{1}{\pi\rho(s)}\exp\left[i\delta_J(s)\right]\sin\left(\delta_J(s)\right) \tag{1.65}$$

As a characteristic measure for an interaction one often uses the *effective range* parameters, which describe the behavior of the scattering amplitude at very low energy. They are defined as coefficients in the expansion of

$$\frac{q}{\tan(\delta)} = q(-\pi\rho(q_s)K(q_s))^{-1} \approx -\frac{1}{a} + \frac{1}{2}rq_s^2. \tag{1.66}$$

a is usually referred to as *scattering length* and r is called *effective range*.

1.4.1. Scattering Phase shifts in multi-channel systems

In the general case, the two body scattering problem involves multiple interacting channels. In the coupled channel problem we only have conservation of total current, not of each current in the individual channels. For this case there are parameters in addition to the scattering phase which characterize the mixing of the channels. We will discuss here in detail the mixing of different orbital angular momenta and follow closely the prescription of Blatt and Biedenharn [Blatt52].

As described in sec. 1.2, there are two coupled sets of amplitudes of different angular momentum structure that belong to opposite parity. We will focus here on the coupled triplet, having $S = 1$ and $m_S = \pm 1$. Thus the orbital angular momentum ℓ is given by $\ell = J \pm 1$. Since all four states have the same conserved J and π quantum numbers they will mix. The S-matrix has then the following structure

$$S = \begin{pmatrix} \langle J-1|\, S_{11}^{(J)}\, |J-1\rangle & \langle J-1|\, S_{12}^{(J)}\, |J+1\rangle \\ \langle J+1|\, S_{21}^{(J)}\, |J-1\rangle & \langle J+1|\, S_{22}^{(J)}\, |J+1\rangle \end{pmatrix} \tag{1.67}$$

Although the S-matrix in total is unitary, the individual components are not. This observation leads us to a natural extension of the single channel S-matrix parametrization $S^{(J)} = \exp(i2\delta_J)$, namely

$$S = U^{-1}(\epsilon)\exp(i2\Delta)U(\epsilon), \tag{1.68}$$

where Δ is a diagonal matrix containing the eigenphases

$$\begin{pmatrix} \delta_J^- & 0 \\ 0 & \delta_J^+ \end{pmatrix} \tag{1.69}$$

and $U(\epsilon)$ is the unitary 2-dimensional rotation matrix

$$U(\epsilon) = \begin{pmatrix} \cos(\epsilon) & \sin(\epsilon) \\ -\sin(\epsilon) & \cos(\epsilon) \end{pmatrix}. \tag{1.70}$$

In general the states $A_1\,|J-1\rangle + A_2\,|J+1\rangle$ are no eigenstates of S and the ratio of the coefficients A_1/A_2 for the incoming and outgoing wave will differ. Channel $+$ and $-$ mix,

ϵ is the measure of this mixing of both states and strongly depends on $\sqrt{s}$. For $q_s \to 0$, ϵ vanishes and $|J \pm 1\rangle$ really do become eigenstates of S. This defines the assignment of the eigenphases $\delta_J^{\pm}$.

The K-matrix is of the same structure as the S-matrix and can therefore be parametrized in a similar fashion. The Blatt-Biedenharn phase-shifts in terms of the K-matrix elements

$$K_{\pm\mp}^J \equiv \langle J \pm 1| K^J |J \mp 1\rangle \tag{1.71}$$

are then given by

$$\tan\left(\delta_J^{\mp}(\sqrt{s})\right) \;=\; -\frac{\pi}{2}\rho(\sqrt{s})\left(K_{--}^J + K_{++}^J \pm \frac{K_{--}^J - K_{++}^J}{\cos(2\epsilon_J)}\right) \tag{1.72}$$

$$\tan(2\epsilon_J) \;=\; \frac{2K_{+-}^J}{K_{--}^J + K_{++}^J} \tag{1.73}$$

In the case of identical particles this one is uncoupled, see fig. 1.4, so that $\epsilon = 0$ and $^{0,1}\delta_J$ are of particularly simple form as can be read off eq.(1.72).

Similar considerations will lead to a parametrization of coupled channel systems involving different particles and thus also a threshold. A nice description on that is given in [Bryan81, Bryan84]. When displaying phase shifts in the YN sector, we will, however stick to those below thresholds and will use the phase shift conventions elaborated above.

2. Relativistic Meson-Exchange Models

As the foundation of our interaction modeling we chose the relativistic meson-exchange models, since they have very appealing features in terms of their universality:

- It is a covariant quantum field theory which ensures that all relevant kinematical and dynamical constraints are consistently implemented.

- It uses the same degrees of freedom as hadron physics does and is thereby able to provide a link between hadron and nuclear physics. Both fields should be described in a consistent way since they are just two sides of the same story.

- It provides a microscopic starting point for many-body calculations and a basis for systematically improvable finite density effective interactions (see chap. 3).

In our developments we will stick closely to the one boson exchange (OBE) models of the Bonn group [Erkelenz74, Machleidt87, Machleidt89] and basically extend the formalism to also include hyperonic degrees of freedom.

Meson exchange models are quantum field theories defined by a Lagrangian which involves baryons and mesons as degrees of freedom. The mesons, usually pseudoscalar, vector and scalar isospin singlets and multiplets, are taken to be stable particles of a fixed mass, as the baryons are. The coupling constants are fixed by performing relativistic or non-relativistic T-matrix calculations and matching the calculated phase shifts to the experimental ones by adjusting coupling constants. Similar models to the one we develop in this work have been developed by the Jülich group [Holzenkamp89, Reuber94], as well as by the Nijmegen group [Nagels78, Maessen89, Rijken99, Stoks99]. The Jülich model is as well as ours an extension of the Bonn model. They, however use the so called full model which involves time ordered perturbation theory and correlated meson exchanges. In the Bonn OBE model, as well as in ours, the latter are included effectively through the Lorentz scalar mesons. In their model there is also no 3D reduction applied. The Nijmegen model is a non-relativistic meson-exchange model and constitutes a kind of reference case hyperon nucleon interaction used in all the most recent non-relativistic hypernuclear calculations. In addition to the scalar nonet they introduce also scalar reggions to cure some deficiencies in the reproduction of phase shifts.

Most of the meson exchange models have an exact isospin symmetry, i.e., the baryon and meson isospin multiplets are mass degenerated and the interaction terms in the Lagrangian are invariant under isospin transformations. The high precision CD-Bonn potential [Machleidt01] is a counter example, breaking explicitly isospin invariance. Here the π mesons and the nucleons are given different masses which significantly improves the reproduction of NN phase shifts.

As seen from tab. 2.1, in models including hyperons the baryon masses among the flavor sub-multiplets are always split and an average mass is assigned to each isospin multiplet. The coupling constants of the pseudoscalar and vector mesons to the baryons obey strict SU(3) invariance, while the couplings of the scalar mesons are left as free parameters since they are considered as composite objects, i.e., resonances in scattering amplitudes between the mesons of the pseudoscalar and vector sector. The meson masses are treated identically to the baryon masses. The assumption of SU(3) invariance of the couplings is justified since the SU(3) charges are exactly conserved despite the mass splitting within the multiplets. In view of the scarce hyperon scattering data small SU(3) breaking effects are not accessible anyway at present.

2.1. Invariant Lagrangians

particle type	filed	isospin (T)	strangeness (S)	physical mass [MeV]
baryons	N	$\frac{1}{2}$	0	939
	Λ	0	-1	1115
	Σ	1	-1	1193
	Ξ	$\frac{1}{2}$	-2	1318
pseudoscalar mesons	π	1	0	137
	η, η'	0	0	547, 958
	K	$\frac{1}{2}$	± 1	494
vector mesons	ρ	1	0	769
	ω, ϕ	0	0	783, 1019
	$K*$	$\frac{1}{2}$	± 1	893
scalar mesons	δ	1	0	–
	σ, σ_s	0	0	–
	κ	$\frac{1}{2}$	± 1	–

Table 2.1.: Particle spectrum of our model

The model applied in this work unless otherwise stated is constructed in this section. The particle spectrum consists of the SU(3) baryon octet and the pseudoscalar, vector and scalar meson nonets as displayed in tab. 2.1 and fig. 2.1. In the interaction terms of the Lagrangian mesons and baryons are coupled in a minimal, i.e., simplest and most natural, covariant and SU(3) invariant fashion. For the pseudoscalar mesons there is the constraint arising from their nature of being a Goldstone boson, that for vanishing
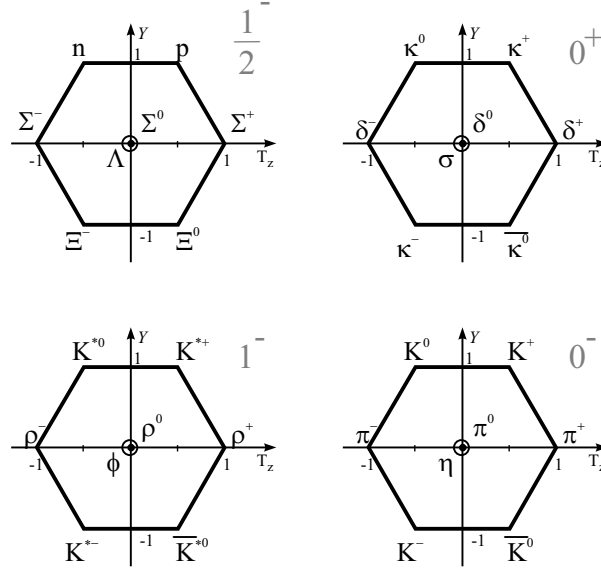
Figure 2.1.: The baryon and meson octets labeled by their quantum numbers J^π. This is the particle spectrum appearing in our meson exchange model.

momentum transfer they have to decouple. Therefore the pseudovector coupling is chosen for them. This leads to the following Lorentz invariant structures of the vertices:

$$\alpha(0^-)NN \qquad f_{BB'\alpha}\overline{\psi}_{B'}\gamma_5\gamma_\mu\psi_B\partial^\mu\phi \tag{2.1}$$

$$\alpha(1^-)NN \qquad g_{BB'\alpha}\overline{\psi}_{B'}\gamma_\mu\psi_B\phi^\mu + \frac{f_{BB'\alpha}}{2(M_B + M_{B'})}\overline{\psi}_{B'}\sigma_{\mu\nu}\psi_B F_\alpha^{\mu\nu} \tag{2.2}$$

$$\alpha(0^+)NN \qquad g_{BB'\alpha}\overline{\psi}_{B'}\psi_B\phi \tag{2.3}$$

where g and f are the electric and magnetic or normal and tensor couplings of meson α, respectively, $F^{\mu\nu}$ is the field strength tensor and M_B the mass of baryon B.

The next step is to couple the flavor structure of the vertices to SU(3) singlets. Each vertex contains an element of each of the three octets B, $\overline{B}$ and ϕ. Group theoretically we are looking for a singlet representation contained in the decomposition of the direct product $[8]\otimes[8]\otimes[8]$ ($[\overline{8}] = [8]$) into its irreducible representations. The first step is the decomposition of the direct product of two octets

$$[8] \otimes [8] = [1] \oplus [8^1] \oplus [8^2] \oplus [\overline{10}] \oplus [27] \tag{2.4}$$

The $[\overline{n}]$ denotes the adjoint to $[n]$ which is not necessarily identical in SU(3). $[8^1]$ and $[8^2]$, which are of mixed symmetry, can be rewritten into $[8^s]$ and $[8^a]$, a symmetric and an antisymmetric octet representation. Next a singlet from the decomposition of the direct product of $[8]$ and eq.(2.4) has to be found. Only $[8^{a,s}]\otimes[8]$ contain a singlet. The singlet in the direct product of two octets is given through the full contraction, i.e. the trace of two octets, $\mathrm{Tr}([8][8])$.

In analogy to the well known coupling of angular momenta, also the coupling of SU(3) octets to a singlet can be done using (SU(3)) Clebsch-Gordan coefficients. The prime reference in which all the required SU(3) Clebsch-Gordan coefficients are worked out is

[deSwart63], which is, however, somewhat hard to access. A nice and understandable presentation of coupling SU(3) representations is given in [Holzenkamp88].

Here we will set up the couplings with the help of the SU(3) matrix representation, which coincides with the octets (the 3 dimensional matrix representation of SU(3) also spans an 8 dimensional space). An introduction to that formalism frequently applied in constructing effective Lagrangians can be found, e.g., in [Donoghue92]. The baryon and the meson fields can be expressed in matrix form as follows:

$$B = \frac{1}{\sqrt{2}} \sum_{a=1}^{8} \lambda^a B^a = \begin{pmatrix} \frac{\Sigma^0}{\sqrt{2}} + \frac{\Lambda}{\sqrt{6}} & \Sigma^+ & p \\ \Sigma^- & -\frac{\Sigma^0}{\sqrt{2}} + \frac{\Lambda}{\sqrt{6}} & n \\ \Xi^- & \Xi^0 & -\frac{2\Lambda}{\sqrt{6}} \end{pmatrix} \tag{2.5}$$

$$\phi = \frac{1}{\sqrt{2}} \sum_{a=1}^{8} \lambda^a \phi^a = \begin{pmatrix} \frac{\pi^0}{\sqrt{2}} + \frac{\eta_8}{\sqrt{6}} & \pi^+ & K^+ \\ \pi^- & -\frac{\pi^0}{\sqrt{2}} + \frac{\eta_8}{\sqrt{6}} & K^0 \\ K^- & \overline{K}^0 & -\frac{2\eta}{\sqrt{6}} \end{pmatrix} \tag{2.6}$$

For the mesons we representatively took the pseudoscalar octet. λ^a are the Gell-Mann matrices. To follow the above described construction of a singlet we need the symmetric and antisymmetric representation of the octet in matrix form, which are given by the commutator and anticommutator of two octets, respectively:

$$[8^s] = [[8], [8]] \quad \text{and} \quad [8^a] = \{[8], [8]\} \tag{2.7}$$

And therefore

$$[1] = \text{Tr}([8^s][8]) = \text{Tr}([[8], [8]] [8]), \text{and} \tag{2.8}$$

$$[1] = \text{Tr}([8^a][8]) = \text{Tr}(\{[8], [8]\} [8]) \tag{2.9}$$

The formal structure of the SU(3) invariant Lagrangian's interaction part is then

$$\mathcal{L}_{\text{int}} = -g \, \alpha \, \text{Tr}(\left[\overline{B}, B\right] \phi) + g \, (1 - \alpha) \, \text{Tr}(\{\overline{B}, B\} \phi) \tag{2.10}$$

g is now the universal octet coupling and α, the so called $F/(F+D)$ ratio, fixes the relative strength of symmetric and antisymmetric part. For the actual interaction Lagrangian the respective Lorentz structures need to be added. There is a distinct g and α for each of the three meson octets. The coupling strengths of the physical particles in terms of the octet couplings are given in tab. 2.2 and tab. 2.3. To get the hadron physics completely right the mixing between η_8 (which is the one included so far) and η_1 has to be incorporated. The same numbers also hold for the vector mesons, where the ω-ϕ mixing has to be taken into account.

Including also model predictions of the SU(6) quark model, which incorporates in addition to the flavor structure the quark spin structure of the baryons, additional constraints appear:

- for the pseudoscalar octet $\alpha_{ps} = \frac{2}{5}$

- for the electric couplings in the vector octet $\alpha_{v,g} = 1$

$\boldsymbol{g_{BB'\phi}}$	NN	$\Lambda\Lambda$	$\Sigma\Sigma$	$\Xi\Xi$	$\Lambda\Sigma$
π	g	0	$2\alpha g$	$-(1-2\alpha))g$	$\frac{2}{\sqrt{3}}(1-\alpha)g$
η	$-\frac{1}{\sqrt{3}}(1-4\alpha)g$	$-\frac{2}{\sqrt{3}}(1-\alpha)g$	$\frac{2}{\sqrt{3}}(1-\alpha)g$	$-\frac{1}{\sqrt{3}}(1+2\alpha)g$	0

Table 2.2.: SU(3) relations between the octet couplings and the physical particle couplings for $S = 0$ interactions.

$\boldsymbol{g_{BB'\phi}}$	$N\Lambda$	$N\Sigma$	$\Xi\Lambda$	$\Xi\Sigma$
K	$-\frac{1}{\sqrt{3}}(1+2\alpha)g$	$(1-2\alpha)g$	$-\frac{1}{\sqrt{3}}(1-4\alpha)g$	$-g$

Table 2.3.: SU(3) relations between the octet couplings and the physical particle couplings for strangeness changing interactions.

- for the sum of the electric and the magnetic coupling $G = g + f$ in the vector octet $\alpha_{v,G} = \frac{2}{5}$

Additionally, the values for G can be calculated. They are listed in table tab. 2.4.

2.2. Calculation of effective interactions

For actual calculations in meson exchange models the whole formalism developed in sec. 1 is applied. First the truncation in the pseudopotential expansion after the first term is done, leading to a 3D reduced propagator

$$G^{(2)}(|\boldsymbol{q}|, s) = g(|\boldsymbol{q}|, s)\Lambda_1^{(+)}(\boldsymbol{q})\Lambda_2^{(+)}(\boldsymbol{q})\delta^{(+)}(q^0), \tag{2.11}$$

and a kernel $V(\boldsymbol{q'}, \boldsymbol{q})$ that only contains one meson exchange diagrams. Due to the delta function in the 3D propagator, the time like components stay fixed to $E_i(\boldsymbol{q_s})$. This is not altered by the loop integrations and therefore no time-like component in the momentum transfer through the kernel will contribute. V only depends on the relative three momenta. The BS equation is then

$$T(\boldsymbol{q'}, \boldsymbol{q}, s) = V(\boldsymbol{q'}, \boldsymbol{q}) + \int d^3\tilde{q}\, V(\boldsymbol{q'}, \tilde{\boldsymbol{q}})g(|\tilde{\boldsymbol{q}}|, s)\Lambda_1^{(+)}(\tilde{\boldsymbol{q}})\Lambda_2^{(+)}(\tilde{\boldsymbol{q}}`)T(\tilde{\boldsymbol{q}}, \boldsymbol{q}, s). \tag{2.12}$$

(For clarity of the formulas we have absorbed the factor $(2\pi)^{-3}$ of the integral into V and T by dividing the whole equation by $(2\pi)^3$ and replacing $V/(2\pi)^3, T/(2\pi)^3 \to V, T$.) One

$\boldsymbol{G_{BB'\phi}}$	N	Λ	Σ	Ξ
ρ	1	$0, 2\frac{\sqrt{3}}{5}\ (\Sigma)$	$\frac{4}{5}$	$-\frac{1}{5}$
ω	$\frac{3}{5}$	0	$\frac{4}{5}$	$-\frac{1}{5}$
ϕ	0	$-3\frac{\sqrt{2}}{5}$	$\frac{\sqrt{2}}{5}$	$-4\frac{\sqrt{2}}{5}$
K^*	$-3\frac{\sqrt{3}}{5}\ (\Lambda)$	$\frac{\sqrt{3}}{5}\ (\Xi)$	$\frac{1}{5}\ (N)$	$-1\ (\Sigma)$

Table 2.4.: SU(6) couplings for the vector meson octet.

clearly sees, that the s dependence arises in this approximation only from the reduced propagator. In a full BS equation already the kernel itself depends on s. By rewriting the positive energy projectors into

$$\Lambda_i^{(+)}(\tilde{\boldsymbol{q}}) = \sum_{\tilde{\lambda}_i} \left|\tilde{\lambda}_i\right\rangle \overline{u}_{\tilde{\lambda}_i}(\tilde{\boldsymbol{q}}) u_{\tilde{\lambda}_i}(\tilde{\boldsymbol{q}}) \left\langle\tilde{\lambda}_i\right| \tag{2.13}$$

($\tilde{\lambda}_i$ labels the helicities) and taking matrix elements of eq.(2.12) with respect to helicity states, we arrive at a BS equation for helicity matrix elements

$$\langle\lambda_1'\lambda_2'|\, T(\boldsymbol{q}', \boldsymbol{q}, s)\,|\lambda_1\lambda_2\rangle = \langle\lambda_1'\lambda_2'|\, V(\boldsymbol{q}', \boldsymbol{q})\,|\lambda_1\lambda_2\rangle$$
$$+ \sum_{\tilde{\lambda}_1\tilde{\lambda}_2}\int d^3\tilde{q}\,\langle\lambda_1'\lambda_2'|\, V(\boldsymbol{q}', \tilde{\boldsymbol{q}})\left|\tilde{\lambda}_1\tilde{\lambda}_2\right\rangle g(|\tilde{\boldsymbol{q}}|, s) \left\langle\tilde{\lambda}_1'\tilde{\lambda}_2'\right|\, T(\tilde{\boldsymbol{q}}', \boldsymbol{q}, s)\,|\lambda_1\lambda_2\rangle \tag{2.14}$$

In the next step the matrix elements are expanded in a partial wave basis, see app. B.2, so that we can project out independent BS equations for all values of J

$$\langle\lambda_1'\lambda_2'|\, T^J(|\boldsymbol{q}'|, |\boldsymbol{q}|, s)\,|\lambda_1\lambda_2\rangle = \langle\lambda_1'\lambda_2'|\, V^J(|\boldsymbol{q}'|, |\boldsymbol{q}|)\,|\lambda_1\lambda_2\rangle$$
$$+ \sum_{\tilde{\lambda}_1\tilde{\lambda}_2}\int d|\tilde{\boldsymbol{q}}|\tilde{\boldsymbol{q}}^2\,\langle\lambda_1'\lambda_2'|\, V^J(|\boldsymbol{q}'|, |\tilde{\boldsymbol{q}}|)\left|\tilde{\lambda}_1\tilde{\lambda}_2\right\rangle g(|\tilde{\boldsymbol{q}}|, s) \left\langle\tilde{\lambda}_1'\tilde{\lambda}_2'\right|\, T^J(|\tilde{\boldsymbol{q}}'|, |\boldsymbol{q}|, s)\,|\lambda_1\lambda_2\rangle$$
$$\tag{2.15}$$

For the following developments let us define $q = |\boldsymbol{q}|$. All helicity matrix elements of the Born diagrams arising from the vertices given in eq.(2.1)– (2.3) are evaluated for the scattering of non identical particles using 3D propagators in app. B.1.

Next we will apply the K-matrix formulation, eq.(1.57). This results in an equation which is in structure almost identical to eq.(2.15), only the integral is replaced by a principal value integral

$$\langle\lambda_1'\lambda_2'|\, T^J(q', q, s)\,|\lambda_1\lambda_2\rangle = \langle\lambda_1'\lambda_2'|\, V^J(q', q)\,|\lambda_1\lambda_2\rangle$$
$$+ \sum_{\tilde{\lambda}_1\tilde{\lambda}_2}\mathcal{P}\int d\tilde{q}\tilde{q}^2\,\langle\lambda_1'\lambda_2'|\, V^J(q', q)\left|\tilde{\lambda}_1\tilde{\lambda}_2\right\rangle g(\tilde{q}, s) \left\langle\tilde{\lambda}_1'\tilde{\lambda}_2'\right|\, T^J(q', q, s)\,|\lambda_1\lambda_2\rangle \tag{2.16}$$

As we worked out in sec. 1.2.2, the helicity matrix elements are not independent. Choosing the parity eigenbasis constructed there, we find two independent 2×2 systems of BS equations, which can then be written in the following matrix form

$$\left(T^J(q', q, s)\right)_{ij} = \left(V^J(q', q)\right)_{ij} + \tag{2.17}$$
$$\sum_l \mathcal{P}\int d\tilde{q}\tilde{q}^2\left(V^J(q', \tilde{q})\right)_{il} g(\tilde{q}, s)\left(T^J(\tilde{q}, q, s)\right)_{lj}$$

The components of the matrices are defined in terms of the parity basis, eq.(1.19), as

$$\begin{aligned}
(T^J)_{11} &\doteq T_1^J, & T_{12}^J \\
(T^J)_{22} &\doteq T_2^J, & T_{34}^J \\
(T^J)_{12} &\doteq T_3^J, & T_{55}^J \\
(T^J)_{21} &\doteq T_4^J, & T_{66}^J
\end{aligned}$$

The coupled equations (2.17) are solved numerically by converting the discretized integral equations into matrix equations and inverting them, as is described in app. F.1 in detail.

2.2.1. Regularization of the loop integrals

Being a low energy effective theory, the interaction is only under good control for the low momentum region. Going higher in momentum many other degrees of freedom enter which would make it necessary to also include them in the Lagrangian. The T-matrix should therefore only be considered as an appropriate interaction for momenta smaller then the threshold momentum for particle production. For this reason also the loop integrations in the BS equation needs to be regularized. The appropriate covariant method which is suitable for numerical calculations, also, is to use *form factors*. The most popular cutoff functions are either multipole or Gauss shaped form factors. Here we attach to each meson-baryon vertexthe multipole form

$$\mathcal{F}\left[(q - q')^2\right] = \left(\frac{\Lambda^2 - m^2}{\Lambda^2 - (q - q')^2_\mu - \delta q^0}\right)^n \tag{2.18}$$

δq^0 fixes the possibly destroyed symmetric off-shellness due to different in and out channels, see sec. 2.2.2. q and q' are four-vectors and m is the mass of the exchange meson corresponding to the vertex the cutoff is attached to. Λ is the so called cutoff mass, it sets the scale from which on the vertex will be suppressed. The momentum structure is constructed such that the cutoff equals one when the exchanged meson goes on-shell.

There is a different cutoff for each vertex. As a justification for that the different substructures of the mesons are often given. This is, however not a relevant scale in effective baryon interactions. Restricting the potentials to their low momentum part, it should better be a universal cutoff for the whole model, separating soft and hard physics. In actual constructions of meson-exchange models it yet turns out, that the form factors need to be kept differently at each vertex to obtain an adequate description of scattering data. Since the multipole form-factors can be decomposed in a sum of Yukawa propagators for the original and heavier mesons with the mass Λ, it may also be interpreted as adding additional, heavy exchange particles. The cutoffs obtain a modified structure in the time-like component due to 3D reduction. Their actual functional form is derived in app. B.1.2.

2.2.2. Multi baryon coupled channel calculations

When scattering different particle species two additional subtleties enter the procedure of solving the BS equation:

- coupling between scattering amplitudes of different initial states and
- thresholds of heavier particle species in the coupled system.

The treatment of both will be discussed in this section.

Let us start with the discussion of coupling between different channels. To calculate, e.g., the scattering between nucleon and Λ, the following scattering equation has to be solved

$$
\begin{aligned}
\langle \Lambda N | T | \Lambda N \rangle = \langle \Lambda N | V | \Lambda N \rangle + \int \langle \Lambda N | V | \Lambda N \rangle \, g_{\Lambda N} \, \langle \Lambda N | T | \Lambda N \rangle + \\
\int \langle \Lambda N | V | \Sigma N \rangle \, g_{\Sigma N} \, \langle \Sigma N | T | \Lambda N \rangle + \\
\int \langle \Lambda N | V | N \Lambda \rangle \, g_{N \Lambda} \, \langle N \Lambda | T | \Lambda N \rangle + \\
\int \langle \Lambda N | V | N \Sigma \rangle \, g_{N \Sigma} \, \langle N \Sigma | T | \Lambda N \rangle
\end{aligned}
\tag{2.19}
$$

Due to the exchange of mesons carrying explicitly isospin or strangeness other intermediate states are mixed in, so that T-matrices with those out channels also appear in the equation. Thus, one needs to also solve the BS equations for $\langle \Sigma N | T | \Lambda N \rangle$, $\langle N \Lambda | T | \Lambda N \rangle$ and $\langle N \Sigma | T | \Lambda N \rangle$. The whole coupled system can be written in a compact matrix form. Defining the matrices of matrix elements as

$$
\mathbb{A} \equiv
\begin{pmatrix}
\langle \Lambda N | \mathbb{A} | \Lambda N \rangle & \langle \Lambda N | \mathbb{A} | \Sigma N \rangle & \langle \Lambda N | \mathbb{A} | N \Lambda \rangle & \langle \Lambda N | \mathbb{A} | N \Sigma \rangle \\
\langle \Sigma N | \mathbb{A} | \Sigma N \rangle & \langle \Sigma N | \mathbb{A} | \Sigma N \rangle & \langle \Sigma N | \mathbb{A} | N \Lambda \rangle & \langle \Sigma N | \mathbb{A} | N \Sigma \rangle \\
\langle N \Lambda | \mathbb{A} | N \Lambda \rangle & \langle N \Lambda | \mathbb{A} | \Sigma N \rangle & \langle N \Lambda | \mathbb{A} | N \Lambda \rangle & \langle N \Lambda | \mathbb{A} | N \Sigma \rangle \\
\langle N \Sigma | \mathbb{A} | N \Sigma \rangle & \langle N \Sigma | \mathbb{A} | \Sigma N \rangle & \langle N \Sigma | \mathbb{A} | N \Lambda \rangle & \langle N \Sigma | \mathbb{A} | N \Sigma \rangle
\end{pmatrix}
\tag{2.20}
$$

and the propagator matrix

$$
\mathbb{G} =
\begin{pmatrix}
g_{\Lambda N} & 0 & 0 & 0 \\
0 & g_{\Sigma N} & 0 & 0 \\
0 & 0 & g_{N \Lambda} & 0 \\
0 & 0 & 0 & g_{N \Sigma}
\end{pmatrix},
\tag{2.21}
$$

the coupled set of BS equations can be formally expressed as

$$
\mathbb{T} = \mathbb{V} + \int \mathbb{V} \mathbb{G} \mathbb{T}.
\tag{2.22}
$$

A closer inspection in fact shows, this is only half as complex as it seems. Because $\mathbb{G}$ is diagonal, only the elements of each column in $\mathbb{T}$ are coupled, i.e., there is one coupled set of equations for the first, one for the second, etc. .

Having particles of different mass in incoming and outgoing channel, one has to take care of the correctness of the kernel matrix elements with respect to the 3D recipe used. In our case, the 3D propagators are defined such, that both particles are equally far off-shell, which implies, that both have to be on-shell for the same relative momentum $\boldsymbol{q}$ (see the discussion in sec. 1.3.1). Therefore a momentum transfer in the time-like component, which balances the time-like component of the particles' four momenta again, is necessary in the kernel matrix elements, with $M_1/M_2 \neq M_1'/M_2'$. Using the definitions of $x_{1,2}$ in

eq.(1.31),which assures a symmetric off-shellness in incoming and outgoing channel we find that balancing energy transfer is obtained by

$$q^0 = k_1{}^0 - k_1'{}^0 = (|x_2| - |x_2'|)\sqrt{s}. \tag{2.23}$$

This energy transfer may actually cause a pole in the meson propagator. However, especially for the free masses, there is no danger: processes involving pion exchange have $q^0 < 44\ MeV$ and those involving kaon exchange have $q^0 < 190\ MeV$. This is far below the masses of the respective exchange mesons (see tab. 2.1). Going into medium the situation may be different. Decreasing the nucleon mass for simulating a nuclear matter situation shows, that the processes coming closest to a pole in the exchange meson propagators are $N\Xi \rightarrow \Lambda\Lambda, \Sigma\Sigma, \Sigma\Lambda$. There, however, the nucleon mass has to drop down to $1/3$ until a pole appears. Nevertheless, these channels will be enhanced due to that effect and may play an important role then in double Λ hypernuclei, for example.

In these coupled channel systems which involve particles of different mass one has to keep an eye also on the meaning of the relative c.m. momentum q_s. According to eq.(1.32), the c.m. momentum depends besides the total energy s_0 on the mass of the involved particles, so that for different incident and outgoing states $q_s(M_1, M_2) \neq q_S(M_1', M_2')$. The formulation of the T-matrix in terms of relative three momenta is thus a bit unfavorable for a transparent interpretation. The on-shell matrix elements which have different masses in the in and out channels are not diagonal in momentum! In fact this is an immediate and measurable consequence from using a realistic mass spectrum for the baryonic isospin multiplets.
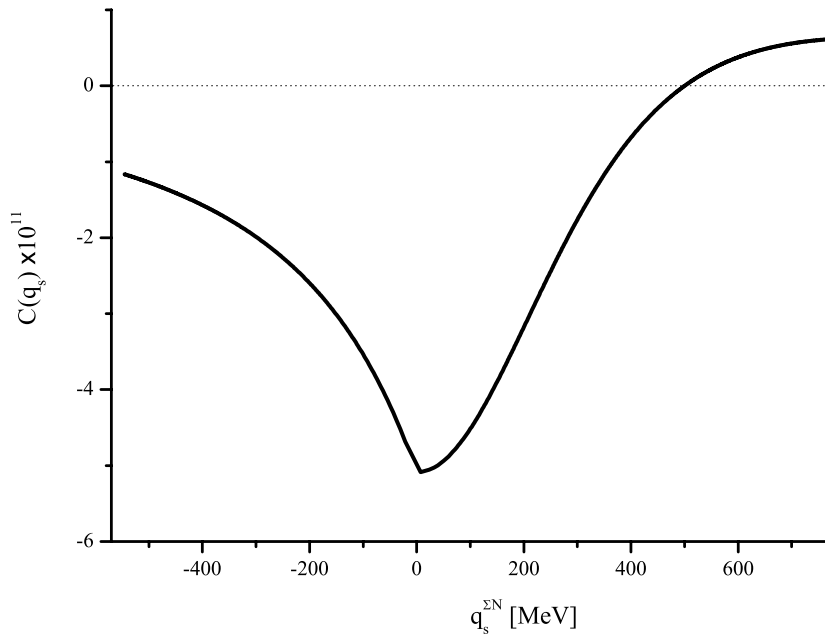
Figure 2.2.: The correlation integral of the BS equation for $N\Lambda$ scattering with intermediate $N\Sigma$ states. The x-axis is the c.m. momentum of the $N\Sigma$ state.

An interesting effect arises from opening thresholds of intermediate states of higher mass as compared the incoming ones. Let us consider an example now of the process

$12 \rightarrow 12$ which involves an intermediate state $\tilde{1}\tilde{2}$, where $M_1 + M_2 < M_{\tilde{1}} + M_{\tilde{2}}$. As long as $s < (M_{\tilde{1}} + M_{\tilde{2}})^2$ the intermediate state is propagated sub-threshold. According to eq.(1.32) we find the – at first sight surprising – effect, that then $\boldsymbol{q}_s(M_{\tilde{1}}, M_{\tilde{2}})^2 < 0$. The behavior of the correlation integral involving an intermediate state sub-threshold can be sketched in a very schematic model. Taking the meson exchange potential to be

$$V(q) = \frac{g^2}{q^2 + m^2}, \tag{2.24}$$

and the 3D reduced propagator being defined as

$$g(q, q_s) = \frac{1}{q_s^2 - q^2} \tag{2.25}$$

(this is the actual pole structure of the propagator, as derived in app. F.1.1), we are able to calculate the (second order) correlation integral analytically

$$C(q_s) = \mathcal{P} \int_0^\infty dq \, q^2 V(q) g(q, q_s) V(q). \tag{2.26}$$

$C(q_s)$ mimics the behavior of a loop integration in the full BS equation. For the numerical evaluation we chose as in and out channel ΛN and as intermediate channel ΣN, obtaining $C(q_s)$ as presented in fig. 2.2 (in arbitrary units). The clear bump, which reminds of a resonant structure, is the typical threshold behavior, appearing in scattering amplitudes, a so called *cusp*.

3. Microscopic In-Medium Interaction

In this chapter we will describe the Dirac-Brueckner-Hartree-Fock (DBHF) theory which we will use to calculate our effective in-medium interactions [Horowitz87, Ter Haar87, Brockmann90]. The approach is a straightforward extension to the finite density regime of the relativistic meson-exchange theory developed in chap. 2.
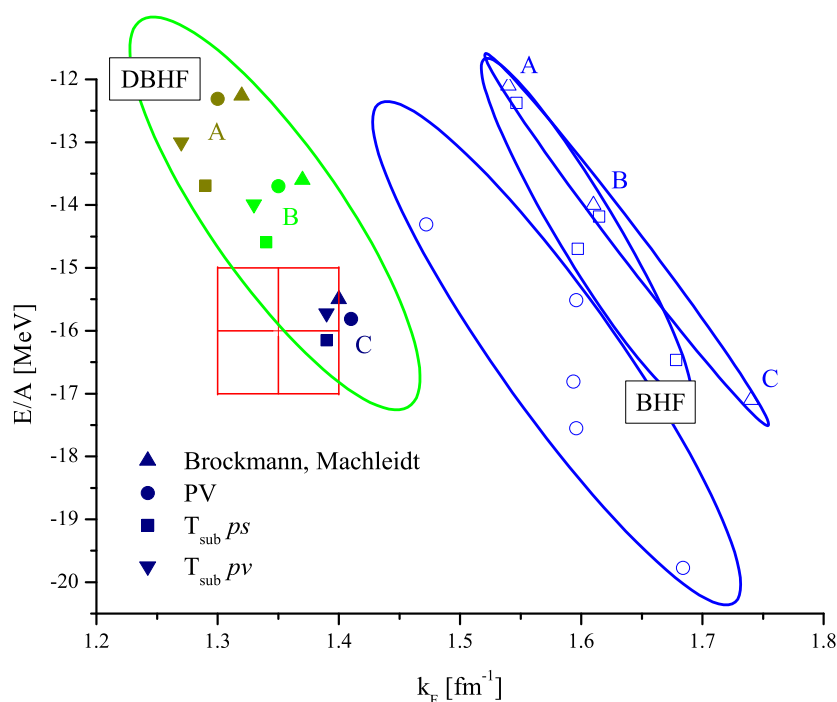
Figure 3.1.: The Coester lines of BHF (open symbols; triangles are calculations using the Bonn potentials [Machleidt89], others are from misc. non-relativistic potentials [Muther00]) and DBHF (for Bonn potentials; triangles are from [Brockmann90], others are [Gross-Boelting99]) in comparison to the empirical saturation point. Both, relativistic and non-relativistic Brueckner calculations lead to Coester bands when using free space interactions. The relativistic calculations, however, seem to include more of the relevant physics, being much closer to or even inside the error bands of the empirical saturation point.

DBHF theory is a many-body framework for the calculation of effective two-body interactions at finite density based on the T-matrix formalism. The medium modifications of the interaction enter through changes in the two baryon propagator, which is dressed by mean-field single particle self-energies (sec. 3.1.3) and includes a Pauli

projector for each of the two baryons (sec. 3.1.1). The coupled set of scattering equations, self-energy integral and Dyson equation has to be solved self-consistently. An illustration is given in fig. 3.3. The introduction of relativistic Brueckner theory by [Horowitz87, Ter Haar87] was a big step forward. The saturation points of all non-relativistic DBHF calculations using microscopic potentials fall on a so-called Coester line in the E/A *vs.* k_F-plane [Coester70] which misses the empirical saturation point $k_F = 1.35 \pm 0.05 \ fm^{-1}$, $E/A = -16 \pm 1 \ MeV$. The relativistic DBHF calculations with realistic interactions reveal a new Coester band, which, however, meets the empirical saturation point [Brockmann90]. Both, relativistic and non-relativistic Coester bands are shown for a set of NN interactions in fig. 3.1. The superior description of nuclear matter saturation properties by a relativistic description points, as do the very successful relativistic mean-field calculations of nuclear structure, to the fact, that relativistic dynamics might be an indispensable ingredient in nuclear modeling although relativistic kinematics by itself is obviously not a necessity.

Relativistic Brueckner theory is despite its successes not settled yet. As a consequence of confining the intermediate baryon states to positive energy the decomposed representation of the G-matrix into Lorentz invariants is not unique. This decomposition will be addressed in detail in sec. 3.1.2. In recent years quite some effort has been put in this topic, see, e.g., [Fuchs04, Gross-Boelting99, Sehn97]. In asymmetric matter the decomposition is even more crucial as discussed in [deJong98, Ulrych97]. We will encounter similar problems in sec. 3.1.2 when describing hypermatter.

Another problem of DBHF theory is the thermodynamical consistency or violation of the Hugenholtz-van Hove theorem [Hugenholtz58]. This states, in simple words, that when adding an additional particle to the filled Fermi sea with an average energy per particle E/A, the gained energy, which defines the Fermi energy E_F, has to coincide with E/A. This links a single particle property, the Fermi energy, to a bulk or thermodynamic property, the energy per particle and assures thereby a consistency of microscopic and macroscopic properties of the system. The Hugenholtz-van Hove theorem can be rigorously derived. At vanishing temperature $T = 0$ it leads to an equality between the thermodynamical pressure, given in terms of the energy density ϵ and baryon density ρ, and the field pressure, as derived from the energy momentum tensor $T_{\mu\nu}$:

$$\rho^2 \partial_\rho \left(\frac{\epsilon}{\rho} \right) = \frac{1}{3} \sum_{i=1}^{3} T^{ii} \tag{3.1}$$

The violation of this consistency by DBHF theory is due to the truncation scheme of the self-energies in DBHF theory. A detailed study of this topic has been performed, e.g., by de Jong [deJong91].

3.1. In-medium scattering theory

The DBHF theory is a many-body framework in which an effective in-medium interaction, the in-medium T-matrix or G-matrix, is calculated starting from the interaction kernel of the free T-matrix. At finite density there are two additional effects entering the scattering problem:

1. self-energies and

2. the Pauli exclusion principle

The Pauli principle is included by by a straightforward modification of the baryon Green's functions. To the numerator a theta function is multiplied, setting the propagator to zero as long as the relative momentum of the intermediate state obeys $|\boldsymbol{k}| \leq |\boldsymbol{k_F}|$ in the n.m. frame. This procedure is described in detail in sec. 3.1.1.
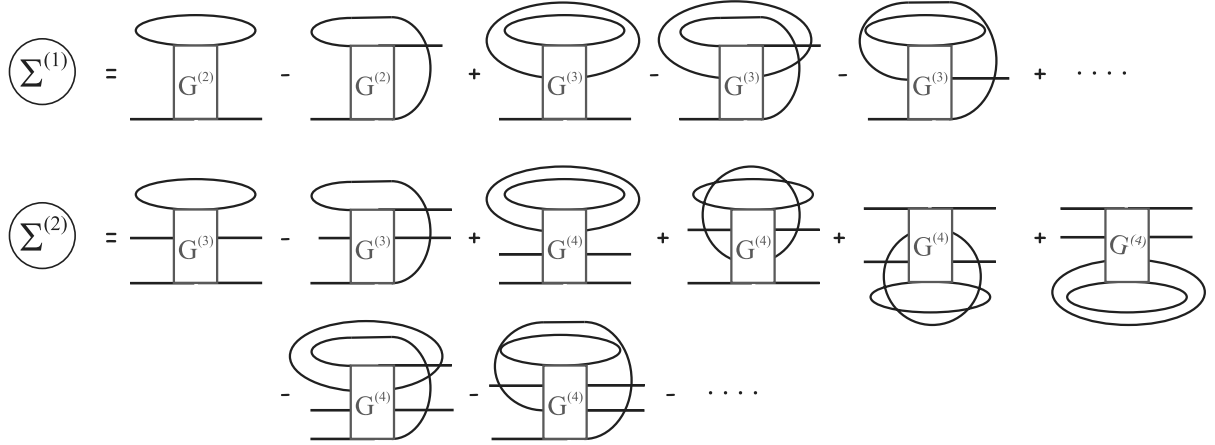
Figure 3.2.: The infinite series of the one-body and two body self-energies. In actual calculations these series have to be truncated since N-point functions of all orders are needed for the full self-energies.

The inclusion of the self-energies is a lot more subtle, since these couple n-point functions of arbitrary order. For the two-particle interaction which we are considering here, the Dyson equations for the one-particle Green's function $g^{(1)}$ and for the two-particle Green's function $g^{(2)}$ have to be solved

$$g^{(1)} = g_0^{(1)} + g_0^{(1)} \Sigma^{(1)} g^{(1)} \tag{3.2}$$
$$g^{(2)} = g_0^{(2)} + g_0^{(2)} \Sigma^{(2)} g^{(2)}, \tag{3.3}$$

where $g_0^{(i)}$ denotes the free i-particle propagator. This may be solved algebraically. The one- and two-particle self-energies, however consist of infinite series involving all orders of n-point functions. In fig. 3.2 we depict the first elements of these series. It is clear, that these have to be truncated. In a pictorial view one may expect that n-body interactions with larger n become only relevant at higher densities, since n particles need to come into contact almost simultaneously, which is less likely at lower density where the average distance of the particles increases. The argument can also be made more quantitative by a little estimate: In fig. 3.2 one sees, that going from n- to $n+1$-body interactions one gets an additional loop, corresponding approximately to an additional factor of $Vg\rho$, i.e., potential, baryon-propagator and density. As a rough estimate we chose an additional factor of the bare two-body potential V for the next order in th n-body potential. Taking the σ-potential at zero momentum transfer, $V = (500 MeV)^{-2}$, the in-medium propagator eq.(3.68), $g = E^{-1} < (1000 MeV)^{-1}$ and $\rho = x fm^{-3}$, we get a suppression factor of

x ($3\ 10^{-2}$) as compared to the previous order. When including such an additional order a 10% effect would only arise at $x \approx 3$, which is way above nuclear matter saturation density ($x = 0.16$).

Considering the above arguments, a truncation scheme that includes only two-body interactions is a reasonable choice. Also the two-particle self-energies, eq.(3.3), will be neglected since these require at least three-body interactions. The evaluation of self-energies is discussed in detail in sec. 3.1.3. This leaves us with the dressed one-baryon Green's function which can be found from eq.(3.2) to be

$$\left(g^{(1)}\right)^{-1} = \left[\left(g_0^{(1)}\right)^{-1} - \Sigma^{(1)}\right] \hat{P} \tag{3.4}$$

where $\hat{P}$ is the Pauli operator. The self-energy is evaluated from the antisymmetrized G-matrix T_A

$$\Sigma = \int \mathrm{Tr}(T_A g^{(1)}) \tag{3.5}$$

and finally T_A is obtained from the BS equation

$$T_A = V_A + \int V_A\ g^{(1)} g^{(1)}\ T_A \tag{3.6}$$

Eqs.(3.4), (3.5), and (3.6) define the coupled system of DBHF equations which have to be solved self-consistently. They are diagrammatically displayed in fig. 3.3.
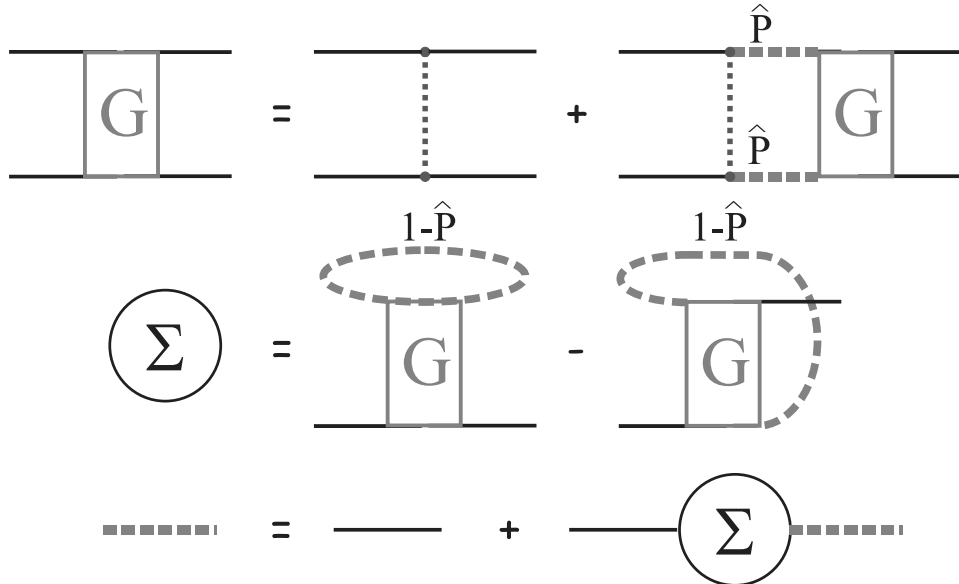
Figure 3.3.: The self-consistency scheme of Dirac-Brueckner-Hartree-Fock theory. $\hat{P}$ is the Pauli projection operator.

3.1.1. The Pauli operator

The first detail of the DBHF scheme which we will discuss is the most important modification of the scattering equation of identical particles, the Pauli operator. Working at zero temperature, it has to take care that in the loop integrations only n.m. frame momenta larger than k_F contribute. The two baryon Pauli projector can be represented by a simple product of two theta functions in the n.m. frame

$$Q(k_F^{(1)}, \; k_F^{(2)}, \; \boldsymbol{k}_1, \; \boldsymbol{k}_2) = \theta(k_F^{(1)2} - |\boldsymbol{k}_1|^2)\theta(k_F^{(2)2} - |\boldsymbol{k}_2|^2) \tag{3.7}$$

The evaluation of the BS equation is, however, for reasons of convenience, done in the c.m. frame. The Pauli operator, eq.(3.7), thus needs to be boosted or reformulated, if possible, in a boost invariant way.
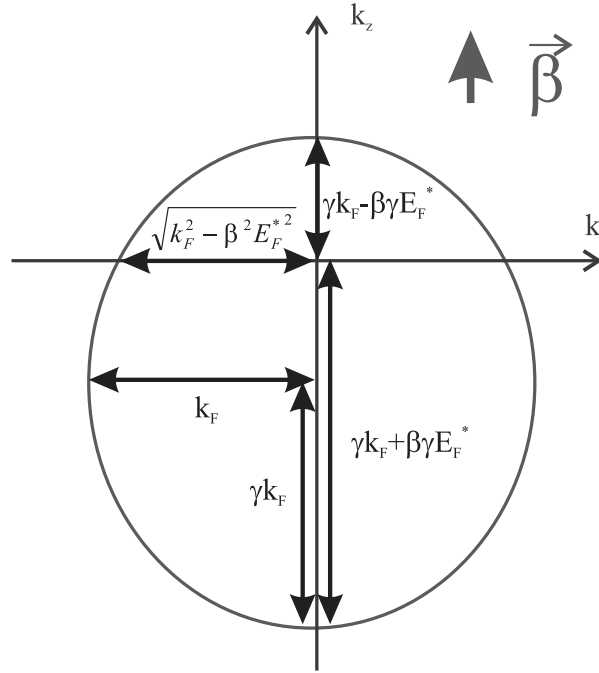
Figure 3.4.: The Fermi sphere, as seen in the c.m. frame, is deformed into an ellipsoid.

The argument of the Pauli theta functions $\theta(k_F - |\boldsymbol{k}|)$ can be rewritten in a covariant way. k_F is a Lorentz scalar defined through the norm of the baryon current B_μ, which is the n.m. frame baryon density

$$\sqrt{B_\mu B^\mu} = \rho_B = \frac{1}{2\pi^2}k_F{}^3 \quad \text{(for each degree of freedom).} \tag{3.8}$$

One can then rewrite eq.(3.8)

$$
\begin{aligned}
\theta(|\boldsymbol{k}| - k_F) &= \theta(\boldsymbol{k}^2 - k_F^2) \\
&= \theta(k_0^{*2} - M^{*2} - k_F^2) \\
&= \theta\left(\frac{(k_\mu^* B^\mu)^2}{B_\mu B^\mu} - (k_F^2 + M^{*2})\right) \\
&= \theta\left(\frac{(k_\mu^* B^\mu)^2}{B_\mu B^\mu} - E_F^{*\,2}\right)
\end{aligned}
\tag{3.9}
$$

The third row is only a complicated rewriting of k_0^{*2} in the n.m. rest frame, which is, however, leading to a covariant generalization of the Fermi sphere. The argument in eq. (3.9) can be further rewritten as:

$$
\frac{(k_\mu^* B^\mu)^2}{B_\mu B^\mu} - E_F^{*\,2} = \left(\frac{k_\mu B^\mu}{\rho_B} - E_F^*\right) \underbrace{\left(\frac{k_\mu B^\mu}{\rho_B} + E_F^*\right)}_{>0}
\tag{3.10}
$$

Since this expression is Lorentz invariant we may easily evaluate it in any reference frame. For the BS equation we need the Pauli operator in the c.m. frame, i.e., $k_\mu = (E(\boldsymbol{q}), \boldsymbol{q})$ and $B_\mu = (B^0, \boldsymbol{j})$. Applying the relations of eq.(3.76) the θ function becomes

$$
\theta\left(E^*(\boldsymbol{q})\frac{B^0}{\rho_B} - \boldsymbol{q} \cdot \frac{\boldsymbol{j}}{\rho_B} - E_F^*\right) = \theta(\gamma E^*(\boldsymbol{q}) + \gamma\boldsymbol{\beta} \cdot \boldsymbol{q} - E_F^*)
\tag{3.11}
$$

This can immediately be identified as the equation of an ellipsoid. Thus boosting the Fermi sphere out of the n.m. frame deforms it to an ellipsoid. This is shown for arbitrary β in fig. 3.4. The lengths of the axes can be determined analytically by setting $\boldsymbol{q}$ parallel or orthogonal to $\boldsymbol{\beta}$. The results are given in fig. 3.4.

The full covariant Pauli projection operator for a two fermion system is then given by

$$
Q(\boldsymbol{q}, k_F^{(1)}, k_F^{(2)}, \boldsymbol{\beta}) = \theta(\gamma E^{(1)*}(\boldsymbol{q}) + \gamma\boldsymbol{\beta} \cdot \boldsymbol{q} - E_F^{(1)*}) \, \theta(\gamma E^{(2)*}(\boldsymbol{q}) - \gamma\boldsymbol{\beta} \cdot \boldsymbol{q} - E_F^{(2)*})
\tag{3.12}
$$

Its effect is, that it allows for a given relative momentum $\boldsymbol{q}$ a distinct angular range between $\boldsymbol{q}$ and $\boldsymbol{\beta}$ in which both, $\boldsymbol{q}$ and $-\boldsymbol{q}$ are outside the Fermi ellipsoid. This is shown in fig. 3.5. For a single particle species, e.g. symmetric nuclear matter, the angle range is forward-backward symmetric as shown in panel a). In panel b) the situation of different particle species at unequal densities is displayed. Here the center of the angle range is tilted compared to the case of identical particles.

The angle averaged Pauli projector

When solving the scattering equation in partial wave decomposition, as we do, the additional angular dependence of the two baryon propagator which is introduced by the Pauli operator, will mix between partial waves and thereby destroy the advantages gained by the decomposition. For this reason an angle average is performed on the Pauli operator.
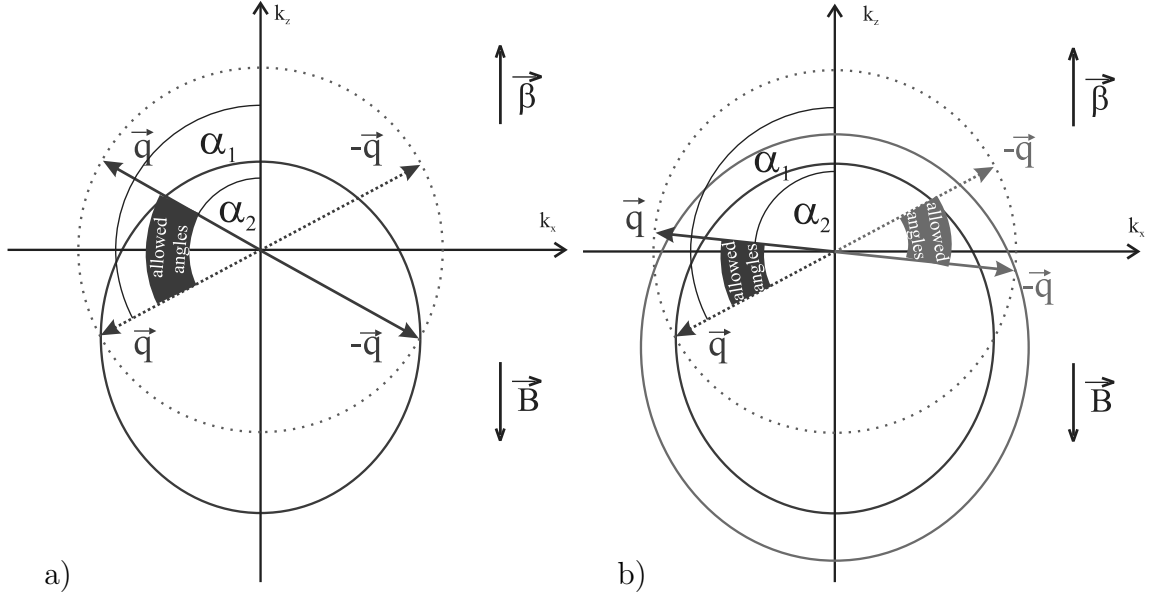
Figure 3.5.: Allowed angle range of the Pauli operator for a given relative momentum $|\boldsymbol{q}|$. Figures a) and b) depict the situation for one particle species and different particle species with different densities, respectively. The solid and dashed pairs of back-to-back arrows mark the two extremes of the allowed angle range, in which both, $\boldsymbol{q}$ and $-\boldsymbol{q}$, are outside the Fermi sea.

It is possible to split the absolute values of the relative momentum in three regimes with respect to the angle between $\boldsymbol{\beta}$ and $\boldsymbol{q}$: 1) either $\boldsymbol{q}$ or $-\boldsymbol{q}$ is inside the ellipsoid for all angles and thus the projector $Q = 0$, 2) both, $\boldsymbol{q}$ and $-\boldsymbol{q}$ are outside for all angles and therefore $Q = 1$ and 3) depending on the angle $Q = 0$ or $Q = 1$ (this is the situation shown in fig. 3.5). The third case is the one which needs to be considered here in the averaging. The Pauli projector, eq.(3.12), can be formally rewritten as a function of θ, which is the angle between $\boldsymbol{\beta}$ and $\boldsymbol{q}$. From fig. 3.5 we can read off that there are two angles, $\alpha_1(\boldsymbol{q})$ and $\alpha_2(\boldsymbol{q})$, which define the allowed angular region. Between these angles $Q = 1$ and outside the region $Q = 0$. Both angles depend on the relative momentum variable $\boldsymbol{q}$. If $\vartheta > \alpha_2$, $-\boldsymbol{q}$ exits the region inside the Fermi ellipsoid, if $\vartheta > \alpha_1$, $\boldsymbol{q}$ enters the region. The cosines of $\alpha_{1,2}$ are obtained by setting the arguments of the θ functions in eq.(3.12) to zero:

$$\cos(\alpha_1) = \frac{1}{\gamma|\boldsymbol{\beta}||\boldsymbol{q}|} \left(E_1^*(k_{F,1}) - \gamma E_1^*(\boldsymbol{q}) \right) \tag{3.13}$$

$$\cos(\alpha_2) = -\frac{1}{\gamma|\boldsymbol{\beta}||\boldsymbol{q}|} \left(E_2^*(k_{F,2}) - \gamma E_2^*(\boldsymbol{q}) \right) \tag{3.14}$$

These relations are clearly only valid if the cosines are between -1 and 1. We rewrite eq.(3.12)

$$Q(\boldsymbol{q}, k_F^{(1)}, k_F^{(2)}, \boldsymbol{\beta}) = \theta(\alpha_1(\boldsymbol{q}) - \vartheta)\, \theta(\vartheta - \alpha_2(\boldsymbol{q})) \tag{3.15}$$

The dependence of $\alpha_{1,2}$ on the other arguments of Q has been suppressed. This form of

the Pauli operator can now be easily averaged over the spherical angles

$$
\begin{aligned}
Q_{av}(|\boldsymbol{q}|, k_F^{(1)}, k_F^{(2)}, |\boldsymbol{\beta}|) =& \frac{1}{4\pi} \int d\Omega\ \theta(\alpha_1(\boldsymbol{q}) - \vartheta)\ \theta(\vartheta - \alpha_2(\boldsymbol{q})) \\
=& \frac{1}{2} \int_{\alpha_2}^{\alpha_1} d\vartheta\ \sin(\vartheta)\ \theta(\alpha_1(\boldsymbol{q}) - \vartheta)\ \theta(\vartheta - \alpha_2(\boldsymbol{q})) \\
& \text{(where } \alpha_1 \text{ has to be larger than } \alpha_2) \\
=& \frac{1}{2} \left(\cos(\alpha_2) - \cos(\alpha_1)\right) \theta(\alpha_1 - \alpha_2) \\
=& \frac{1}{\gamma|\boldsymbol{\beta}||\boldsymbol{q}|}\{\gamma\sqrt{s_{\boldsymbol{q}}^*} - \sqrt{s_F^*}\}\theta\left(\sqrt{s_{\boldsymbol{q}}^*} - \sqrt{s_F^*}\right)
\end{aligned}
\tag{3.16}
$$

with

$$
\sqrt{s_{\boldsymbol{q}}^*} \equiv E_1^*(\boldsymbol{q}) + E_2^*(\boldsymbol{q}), \qquad \sqrt{s_F^*} \equiv E_1^*(k_{F,1}) + E_2^*(k_{F,2}) \tag{3.17}
$$

Since $\alpha_1 > \alpha_2 \Leftrightarrow \cos(\alpha_2) > \cos(\alpha_1)$, $\theta(\alpha_1 - \alpha_2)$ makes sure that Q_{av} is alway larger than zero. In addition one has to obey that eq.(3.13) and eq.(3.14) are only defined between -1 and 1, keeping $Q_{av} \leq 1$. We therefore finally obtain

$$
Q_{av}(|\boldsymbol{q}|, k_F^{(1)}, k_F^{(2)}, |\boldsymbol{\beta}|) = \begin{cases} 0 & \text{for } \gamma\sqrt{s_{\boldsymbol{q}}^*} \leq \sqrt{s_F^*} \\ 1 & \text{for } \gamma\sqrt{s_{\boldsymbol{q}}^*} \geq \gamma|\boldsymbol{\beta}||\boldsymbol{q}| + \sqrt{s_F^*} \\ \frac{1}{\gamma|\boldsymbol{\beta}||\boldsymbol{q}|}\{\gamma\sqrt{s_{\boldsymbol{q}}^*} - \sqrt{s_F^*}\} & \text{else} \end{cases}
\tag{3.18}
$$

In fig. 3.6 we display the behavior of the angle averaged Pauli operator when the parameters it depends on are varied. Panel a) shows the density dependence of Q_{av} for a fixed $\beta = 0.1$ and two identical particles of mass $M = 939\ MeV$ and therefore also identical k_F. The washed-out step function moves to higher momenta as the Fermi momentum increases. The center of the step is located at $q \approx k_F$. In panel b) the angle averaged Pauli operator for identical particles ($M = 939\ MeV$, $k_F = 300\ MeV$) is displayed for different β. For $\beta = 0$, i.e., in the n.m. frame we obtain the expected step which gets washed out more at higher values of β. If beta gets so large that $|\boldsymbol{P}_{cm}| > k_F$ a curious effect appears: Instead of a suppression at low $\boldsymbol{q}$ a dip at higher relative momenta appears. In this case the c.m. motion is so fast, that for low relative momenta the particles still move above the Fermi-sea and only at higher relative momenta the effect of the Fermi-sea appears. This is, however out of focus in our calculations since only particle momenta up to the Fermi-momentum will have to be considered for the calculation of self-energies and effective interactions for a particle inside the Fermi-sphere. In panel c) the effect of variations of M_2 is studied at fixed $\beta = 0.2$ and $k_{F,1} = k_{F,2} = 300\ MeV$. Variations of M_2 are obviously of minor importance, leading to a further dissolution of the step for higher masses. A fully asymmetric system in which as well M_2 as $k_{F,2}$ are varied is shown in panel d). Starting with $k_{F,2} = 0\ MeV$ the very smooth step gets cut off at the lower end as $k_{F,2}$ is raised. The cutting point rises with $k_{F,2}$ until at $k_{F,1} = k_{F,2}$ the step gets a continuous slope. For $k_{F,2}$ growing further the scenario continues with inverted roles.

To illustrate the structure of the angle averaged Pauli projector in a broader context, in fig. 3.7 we show surface plots of Q as function of $(\boldsymbol{q}, k_F)$ and $(\boldsymbol{q}, \beta)$. In addition to the
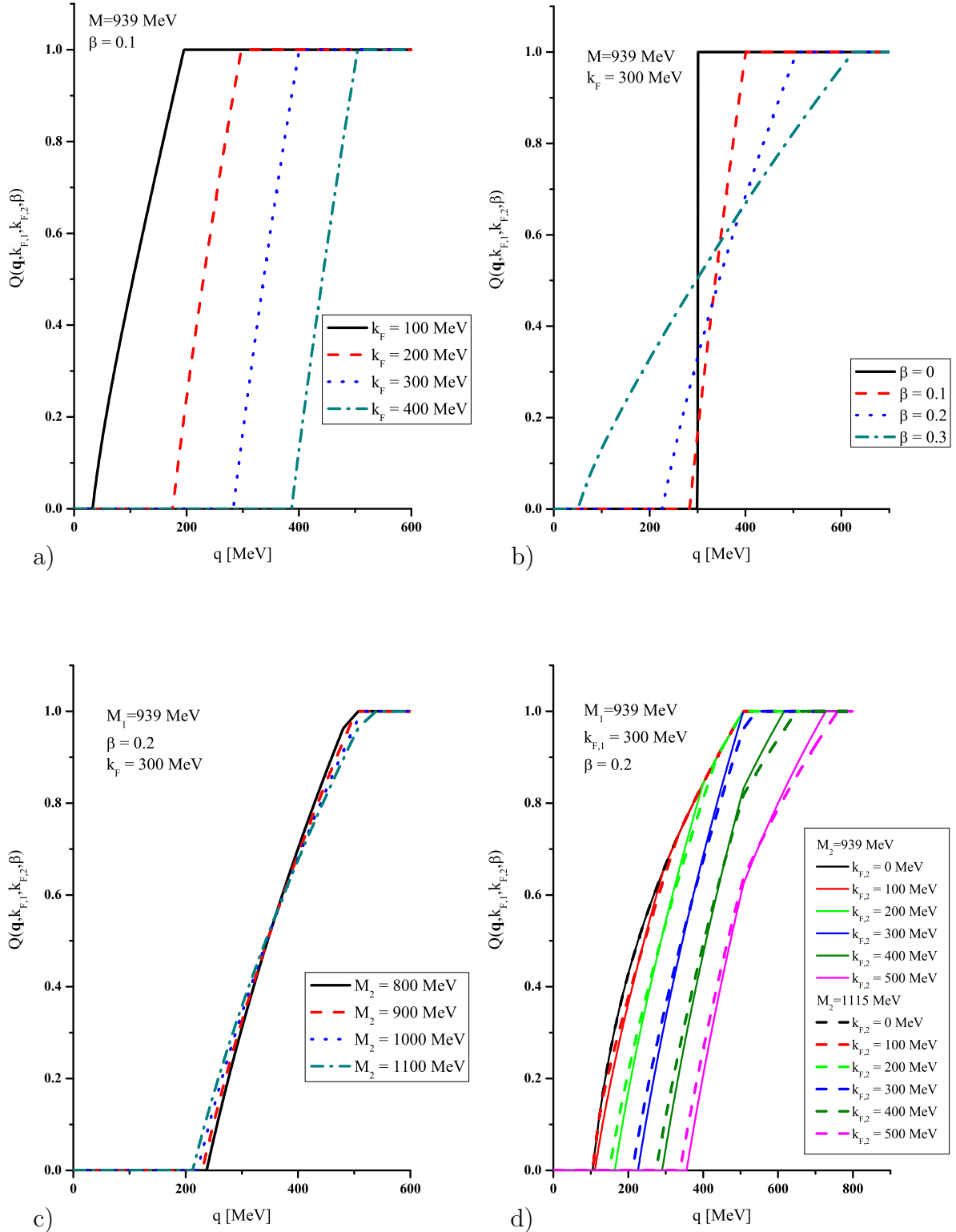
Figure 3.6.: Behavior of the angle averaged Pauli operator with respect to the different variables it depends on.

a)

b)
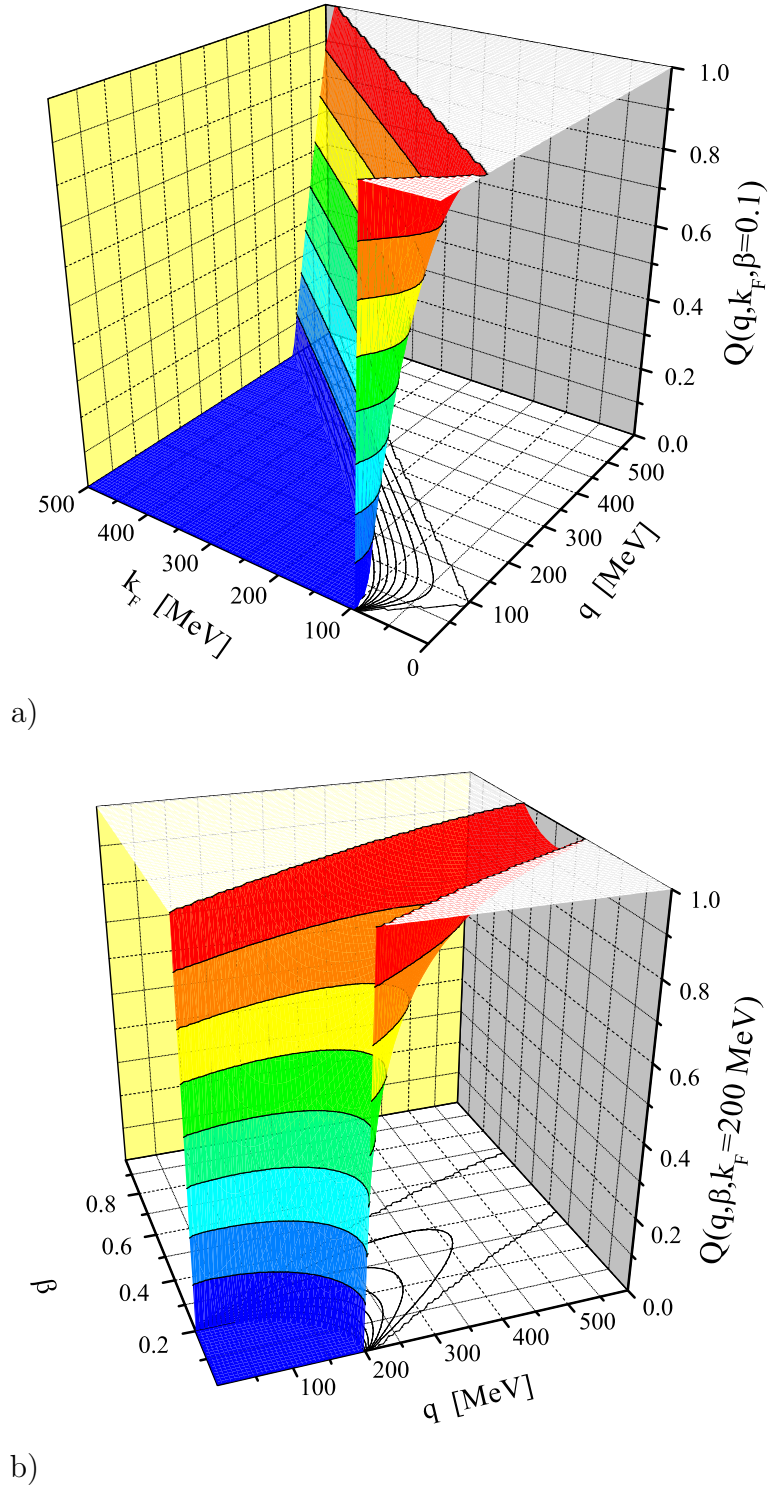
Figure 3.7.: The surface plots show the **q** dependence of the angle averaged Pauli operator
Q, in panel a) for $\beta = 0.1$ fixed and varying k_F, in panel b) for $k_F = 200$ fm
and varying β. The effect of a boost larger than the velocity corresponding
to k_F can nicely be seen as a dip in **q** direction. As described in the text,
this happens, if the c.m. movement of the particle pair is si high, that for
low relative momenta the particle momenta are still above the Fermi-sphere.

behavior already shown in fig. 3.6 a) and b), the effect of a boost outside the Fermi-sphere can be nicely seen as dips in the surface.

3.1.2. The relativistic structure of the T-matrix

Prior to describing the evaluation of self-energies we will analyze the Lorentz structure of the T-matrix, which is essential to calculate the self-energies. The relativistic scattering matrix is in spinor space a direct product of two 4×4 matrices, so it can be expanded in terms of direct products from elements of the Clifford basis

$$\{\mathcal{C}_i\} = \{1, \gamma_5, \{\gamma_\mu\}, \{\gamma_5\gamma_\mu\}, \{\sigma_{\mu\nu}\}\} \tag{3.19}$$

as

$$T = \sum_{i,j} c_{ij}\mathcal{C}_i\mathcal{C}_j. \tag{3.20}$$

As discussed in [Tjon85] there are only eight independent Lorentz covariants, i.e., the products $\mathcal{C}_i\mathcal{C}_j$. Defining

$$S = 1^{(1)} \otimes 1^{(2)}, \quad V = \gamma_\mu^{(1)} \otimes \gamma^{(2)\mu}, \quad T = \sigma_{\mu\nu}^{(1)} \otimes \sigma^{(2)\mu\nu},$$
$$P = \gamma_5^{(1)} \otimes \gamma_5^{(2)}, \quad A = \gamma_5\gamma_\mu^{(1)} \otimes \gamma_5\gamma^{(2)\mu} \tag{3.21}$$

and the normalized 4-momenta

$$Q^{(i)\mu} = \frac{1}{M_i + M_i'}(p_i + p_i')^\mu, \tag{3.22}$$

where $p_i^{(')}$ are the particle momenta, nine covariants are obtained, from which only eight are linearly independent

$$\{\mathcal{K}_n\} = \left\{ S, V, T, P, A, \gamma^{(2)}{}_\mu Q^{(1)\mu}, \gamma^{(1)}{}_\mu Q^{(2)\mu}, P\gamma^{(2)}{}_\mu Q^{(1)\mu}, P\gamma^{(1)}{}_\mu Q^{(2)\mu} \right\} \tag{3.23}$$

The T-matrix expanded in this basis reads

$$T = \sum_{i=1}^{9} F_i\mathcal{K}_i. \tag{3.24}$$

It can now be shown that the linear dependence of the nine covariants leads to $F_6 = -F_7$ for the T-matrix involving incoming and outgoing states of positive energy only [Tjon85].

In the scattering off identical particles, as in NN scattering , the T-matrix has to be antisymmetric under exchange of particles in the in or out channel. There is an equivalent basis of covariants which incorporates this in a transparent way. When the operator $\hat{X}$ exchanges particle 1 and 2, the covariants with two exchanged particles are denoted by

$$\tilde{\mathcal{C}}_{\alpha\beta\gamma\delta} \equiv a_{\alpha\beta}^{(1)}b_{\gamma\delta}^{(2)} = \hat{X}a_{\alpha\delta}^{(1)}b_{\gamma\beta}^{(2)}. \tag{3.25}$$

The greek letters are spinor space indices. The equivalent antisymmetrized basis is given by

$$
\begin{aligned}
\{\kappa_n\} = \Big\{ & S - \tilde{S}, T + \tilde{T}, -(A - \tilde{A}), V + \tilde{V}, P - \tilde{P}, \\
& \gamma^{(2)}{}_\mu Q^{(1)\mu} - \gamma^{(1)}{}_\mu Q^{(2)\mu}, \gamma^{(2)}{}_\mu Q^{(1)\mu} + \gamma^{(1)}{}_\mu Q^{(2)\mu}, \\
& P\gamma^{(2)}{}_\mu Q^{(1)\mu} - P\gamma^{(1)}{}_\mu Q^{(2)\mu}, P\gamma^{(2)}{}_\mu Q^{(1)\mu} + P\gamma^{(1)}{}_\mu Q^{(2)\mu} \Big\}
\end{aligned}
\tag{3.26}
$$

and the T-matrix is thus the sum

$$
T = \sum_{i=1}^{9} f_i \kappa_i. \tag{3.27}
$$

Because of the linear dependence of the nine covariants we are allowed to choose $f_7 = 0$. By the Fierz transformation direct and exchange covariants can be algebraically related [Sehn97] through

$$
\begin{pmatrix} \tilde{S} \\ \tilde{V} \\ \tilde{T} \\ \tilde{A} \\ \tilde{P} \end{pmatrix} = \frac{1}{4} \begin{pmatrix} 1 & 1 & \frac{1}{2} & -1 & 1 \\ 4 & -2 & 0 & -2 & -4 \\ 12 & 0 & -2 & 0 & 12 \\ -4 & -2 & 0 & -2 & 4 \\ 1 & -1 & \frac{1}{2} & 1 & 1 \end{pmatrix} \begin{pmatrix} S \\ V \\ T \\ A \\ P \end{pmatrix} \tag{3.28}
$$

This results in the following relation of the amplitudes F_i and f_i as given in [Sehn97]:

$$
\begin{pmatrix} f_1 \\ f_2 \\ f_3 \\ f_4 \\ f_5 \end{pmatrix} = \frac{1}{4} \begin{pmatrix} 2 & -4 & 12 & 0 & 0 \\ 1 & 0 & 4 & 0 & 1 \\ 0 & -2 & 0 & -2 & 0 \\ 1 & 2 & 0 & -2 & -1 \\ 0 & 4 & -12 & 0 & 2 \end{pmatrix} \begin{pmatrix} F_1 \\ F_2 \\ F_3 \\ F_4 \\ F_5 \end{pmatrix} \tag{3.29}
$$

For the calculation of self-energies the helicity state amplitudes which are obtained in the BS equation have to be mapped onto the Lorentz covariants. Having, at least in principle, eight helicity state amplitudes (four of each parity) and eight linearly independent covariants, a mapping is performed by a simple linear transformation

$$
\langle T \rangle_h = \sum_{i=1}^{8} F_i \langle \mathcal{C}_i \rangle_h, \quad h = 1, ...8 \tag{3.30}
$$

The $\mathcal{C}_i$ are a set of covariants and h denotes the helicity matrix element. Taking helicity matrix elements of eq.(3.24), e.g., and applying the constraint to eliminate the linear dependency of the nine covariants, is an example.

In practice, however, one finds several difficulties arising from this procedure. One may already expect problems from the fact, that for identical particleson-shell there are five independent helicity amplitudes and five independent matrix elements of covariants, whereas off-shell there are seven independent matrix elements of the covariants, but only six of the T-matrix, see app. C.1.2. The origin and effect on DBHF calculations of these ambiguities will be discussed at the end of the following section. The numerical procedure of inverting eq.(3.30) is described in detail in app. C.1.

3.1.3. Self-energies
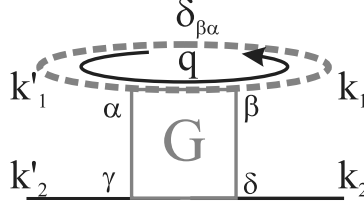
Figure 3.8.: The direct part of the self-energy. Due to conservation of four-momentum $k_1 = k'_1$ and $k_2 = k'_2$, thus $k_1 - k_2 = k'_1 - k'_2$. This leads to a scattering angle $\vartheta_c = 0$.

To obtain the direct part of the self-energy – let us consider here the self-energy of particle 2 – particle 1 in the G-matrix is integrated out as shown in fig. 3.8. Obviously this only makes sense, if $1 = 1'$ and $2 = 2'$ as far as the particle species are concerned. The loop integration fixes the kinematics such that $k_1 = k'_1$ and thus also $k_2 = k'_2$. As we therefore have $k_1 - k_2 = k'_1 - k'_2$, which translates by a Lorentz boost to the c.m. frame also into an equivalence of the relative momenta there, the scattering angle $\vartheta_c = 0$. This implies, that we only need fully on-shell elements of the G-matrix. Being only interested in its real part (the self-energy is defined with an i), we need the imaginary part of the in-medium propagator, eq.(3.67):

$$\Im(G^0(k)_{\alpha\beta}) = \frac{1}{i} G_D^0(k)_{\alpha\beta} = \frac{\pi}{E} (\gamma_\mu k^\mu + M)_{\alpha\beta} \underbrace{\delta(k_0 - E(\mathbf{k}))\theta(\mathbf{k_F} - |\mathbf{k}|)}_{f(\mathbf{k})} \tag{3.31}$$

The delta function in the medium propagator sets the baryon loop on-shell. For mean-field theory, as DBHF theory is, only the on-shell self-energies are needed, i.e., also the four-momentum of particle 2 has to obey the mass-shell relation. Therefore only the physical, full on-shell G-matrix at $\vartheta_c = 0$ is needed in evaluating the direct self-energy. In a medium containing several baryon specied all there contributions are summed up. Mean-field self-energies may reasonably only be calculated from G-matrices with $B_1 B_2 = B'_1 B'_2$, denoted in the following by $T^{B_1 B_2}$. To clarify the spinor-space structure of the self-energy we will furthermore explicitly denote these indices by greek letters. A sum over identical indices is implied here. Since the G-matrix is a direct product of two spinor-space matrices, corresponding to baryon 1 and 2, the respective indices are gouped in parentheses as $T_{(1)(2)}$. The the full structure of the self-energy is given by

$$\Sigma_{B_2}(\boldsymbol{k}_2) = -i \sum_{B_1} \int \frac{d^4 k_1}{(2\pi)^4} G_{\beta\alpha}^{B_1} T_{(\alpha\beta)(\gamma\delta)}^{B_1 B_2}(\sqrt{s}(\boldsymbol{k}_1, \boldsymbol{k}_2), \vartheta_c = 0). \tag{3.32}$$

The real part of the direct self-energy is obtained by inserting eq.(3.31):

$$\Sigma_{B_2} = \sum_{B_1} \int \frac{d^4 k_1}{(2\pi)^4} \frac{\pi}{E(\boldsymbol{k}_1)} f_{B_1}(\boldsymbol{k}_1) \mathrm{Tr}_1 \left[(\gamma_\mu^{(1)} k_1^\mu + M_1) T^{B_1 B_2}(\sqrt{s(\boldsymbol{k}_1, \boldsymbol{k}_2)}) \right]. \tag{3.33}$$

Tr_1 denotes a trace over the spinor indices corresponding to baryon 1. This structure can be read off eq.(3.32).

Using the representation for the T-matrix given in eq.(3.24) and applying the trace rules, which can be found in sec. A.2.1, one finds that only the scalar and the vector parts of the T-matrix survive,

$$\mathrm{Tr}\left[(\gamma_m u k^\mu + M)1\right] = 4M \tag{3.34}$$

$$\mathrm{Tr}\left[(\gamma_m u k^\mu + M)\gamma_\mu\right] = 4k_\mu, \tag{3.35}$$

all other traces are 0. Inserting this into the expression for the direct self-energy, we finally obtain

$$\Sigma_{B_2}(\boldsymbol{k}) = \sum_{B_1} \int \frac{d^3 k_1}{(2\pi)^3} \frac{2}{E(\boldsymbol{k}_1)} f_{B_1}(\boldsymbol{k}_1) \left[M_{B_1} F_S^{B_1 B_2}(\sqrt{s}(\boldsymbol{k}_1, \boldsymbol{k}), \vartheta_c = 0) \right. \tag{3.36}$$
$$\left. + k_{1\mu} \gamma^{(2)\mu} F_V^{B_1 B_2}(\sqrt{s}(\boldsymbol{k}_1, \boldsymbol{k}), \vartheta_c = 0) \right].$$

Thus the form of the self-energy in the rest frame of homogeneous and isotropic baryonic matter is given by

$$\Sigma = \Sigma^s - \gamma_\mu \Sigma^\mu = \Sigma^s - \gamma_0 \Sigma^0 + \boldsymbol{\gamma} \boldsymbol{k} \Sigma^v \tag{3.37}$$

By applying again the trace rules, eq.(A.19)–(A.26), we are able to project out the scalar functions Σ^s, Σ^0 and Σ^v from the matrix-valued self-energy expression, eq.(3.36):

$$
\begin{aligned}
\Sigma_B^s(\boldsymbol{k}) &= \frac{1}{4} \mathrm{Tr}_2 \left[\Sigma_B(\boldsymbol{k}) \right] \\
&= \sum_{B_1} \int \frac{d^3 k_1}{(2\pi)^3} 2 f_{B_1}(\boldsymbol{k}_1) \frac{M_{B_1}}{E_1(\boldsymbol{k}_1)} F_S^{B_1 B_2}(\sqrt{s}(\boldsymbol{k}_1, \boldsymbol{k}), \vartheta_c = 0) \tag{3.38}
\end{aligned}
$$

$$
\begin{aligned}
\Sigma_B^0(\boldsymbol{k}) &= \frac{1}{4} \mathrm{Tr}_2 \left[\gamma^0 \Sigma_B(\boldsymbol{k}) \right] \\
&= \sum_{B_1} \int \frac{d^3 k_1}{(2\pi)^3} 2 f_{B_1}(\boldsymbol{k}_1) F_V^{B_1 B_2}(\sqrt{s}(\boldsymbol{k}_1, \boldsymbol{k}), \vartheta_c = 0) \tag{3.39}
\end{aligned}
$$

$$
\begin{aligned}
\Sigma_B^v(\boldsymbol{k}) &= \frac{1}{4\boldsymbol{k}^2} \mathrm{Tr}_2 \left[\boldsymbol{\gamma}^{(2)} \cdot \boldsymbol{k} \Sigma_B(\boldsymbol{k}) \right] \\
&= \sum_{B_1} \int \frac{d^3 k_1}{(2\pi)^3} 2 f_{B_1}(\boldsymbol{k}_1) \frac{\boldsymbol{k}_1 \cdot \boldsymbol{k}}{E_1(\boldsymbol{k}_1)} F_V^{B_1 B_2}(\sqrt{s}(\boldsymbol{k}_1, \boldsymbol{k}), \vartheta_c = 0) \tag{3.40}
\end{aligned}
$$

It can be nicely seen, that for the Hartree terms of QHD (see sec. 3.3, which are $\Gamma_s = g_s^2/m_s^2$ and $\Gamma_v = g_v^2/m_v^2$, the self energies of the Walecka model, eq.(3.85) and eq.(3.86) with scalar and vector density given by eq.(3.93) and eq.(3.94), are retained.

If we are interested in scattering of identical particles in an isospin-symmetric medium and evaluate the physical, i.e., the antisymmetrized T-matrix, see sec. 1.2.3, the direct self-energy is all we need. The exchange part is implicitly contained in the amplitudes. Considering, however, the interaction of non-identical particles, or evaluating unphysical,

not antisymmetrized amplitudes, as done, e.g. in [Horowitz87], the exchange self-energy has to be calculated explicitly. For the self-energies of non-identical particles, where off-diagonal matrix elements in flavor space, like, e.g., $\langle N\Lambda| T |\Lambda N\rangle$, may contribute to the self-energy, these have the same kinematical structure as the exchange matrix elements of identical particles.
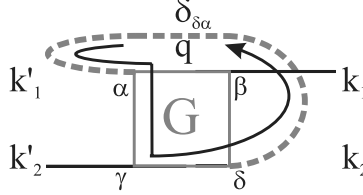
Figure 3.9.: The exchange part of the self-energy. Due to conservation of four-momentum $k_1 - k_2 = -(k_1' - k_2')$. This leads to a scattering angle $\vartheta_c = \pi$.

The kinematics of exchange self-energies is depicted in fig. 3.9. The relations between the four momenta are here $k_2' = k_1$ and $k_2 = k_1'$. This yields, that the relative four momenta differ only by a relative minus sign, $k_1 - k_1' = -(k_2 - k_2')$. As for the direct part, this also translates directly to the relative momenta in the c.m. frame, leading to a scattering angle $\vartheta_c = \pi$. Since the propagator is now contracted with particles $1'$ and 2 (in contrast to $1'$ and 1 for the direct self-energy). The exchange self-energy is thus of the form

$$\Sigma_{B_2}(\boldsymbol{k}_2) = -i \sum_{B_1} \int \frac{d^4 k_1}{(2\pi)^4} \, G^{B_1}_{\delta\alpha} \, T^{B_1 B_2}_{(\alpha\beta(\gamma\delta))} (\sqrt{s}(\boldsymbol{k}_1, \boldsymbol{k}_2), \vartheta_c = \pi). \qquad (3.41)$$

Compared to the direct self-energy there are only two formal changes: the scattering angle is π and the indices of particle 1 and 2 are interchange. The natural expansion of that exchange G-matrix is now in terms of the exchange covariants, $\tilde{S}, \tilde{V}, ...$ in analogy to eq.(3.24)

$$T = \sum_{i=1}^{9} F_i \tilde{\mathcal{K}}_i. \qquad (3.42)$$

By a Fierz transformation the exchange and direct covariants are connected

$$\mathcal{K}^i_{(\alpha\beta)(\gamma\delta)} = \sum_{j=1}^{5} \mathcal{F}_{ij} \mathcal{K}^j_{(\alpha\delta)(\gamma\beta)}, \qquad (3.43)$$

where $\mathcal{F}$ is the Fierz matrix as given in eq.(3.28). These relations allow to combine the direct and the exchange part into a unified expression corresponding to the fully antisymmetrized interaction. Expressing the exchange parts in terms of direct parts has the advantage, that the trace formulas may be used to simplify the integrand as for the direct self-energy. Again, only scalar and vector parts *in the expansion in terms of the direct covariants* survive. This produces the following non-vanishing exchange

self-energies

$$
\Sigma_B^{Xs}(\boldsymbol{k}) = \sum_{B_1} \int \frac{d^3k_1}{(2\pi)^3}\, 2f_{B_1}(\boldsymbol{k}_1) \frac{M_{B_1}}{E(\boldsymbol{k}_1)} \left[F_S^{B_1 B_2}(\pi) + 4F_V^{B_1 B_2}(\pi) \right. \tag{3.44}
$$

$$
\left. + 12F_T^{B_1 B_2}(\pi) - 4F_A^{B_1 B_2}(\pi) + F_P^{B_1 B_2}(\pi) \right]
$$

$$
\Sigma_B^{X0}(\boldsymbol{k}) = \frac{1}{4}\mathrm{Tr}_2\left[\gamma^0 \Sigma_B(\boldsymbol{k}) \right]
$$

$$
= \sum_{B_1} \int \frac{d^3k_1}{(2\pi)^3}\, 2f_{B_1}(\boldsymbol{k}_1) \left[F_S^{B_1 B_2}(\pi) - 2F_V^{B_1 B_2}(\pi) \right. \tag{3.45}
$$

$$
\left. - 2F_A^{B_1 B_2}(\pi) - F_P^{B_1 B_2}(\pi) \right]
$$

$$
\Sigma_B^{Xv}(\boldsymbol{k}) = \frac{1}{4\boldsymbol{k}^2}\mathrm{Tr}_2\left[\boldsymbol{\gamma}^{(2)} \cdot \boldsymbol{k}\, \Sigma_B(\boldsymbol{k}) \right]
$$

$$
= \frac{1}{\boldsymbol{k}^2} \sum_{B_1} \int \frac{d^3k_1}{(2\pi)^3}\, 2f_{B_1}(\boldsymbol{k}_1) \frac{\boldsymbol{k}_1 \cdot \boldsymbol{k}}{E(\boldsymbol{k}_1)} \left[F_S^{B_1 B_2}(\pi) - 2F_V^{B_1 B_2}(\pi) \right. \tag{3.46}
$$

$$
\left. - 2F_A^{B_1 B_2}(\pi) - F_P^{B_1 B_2}(\pi) \right]
$$

For evaluating the off-diagonal parts of self-energies in scattering of non-identical particles the formulas need to be slightly modified. The invariant amplitudes F have now to be taken from the decomposition of the off-diagonal matrix elements and are not those of the direct G-matrix as for scattering of identical particles in a not antisymmetrized basis.

Ambiguities in the calculation of self-energies

It seems obvious at first sight: Evaluating the antisymmetrized T-matrix and mapping the five independent on-shell helicity amplitudes onto the five independent covariants leads to the DBHF self-energy without any ambiguities. Using the σ-ω model, as, e.g. [Horowitz87], the obtained results show no suspicious features. Using, however, a full meson exchange potential, like, e.g., those of the Bonn-model, the momentum dependence of the self-energies becomes tremendous. This leads to problems for particles deeply inside the Fermi sea, since their effective mass goes close to 0, putting the assumed mean-field dynamics in jeopardy.

The source of this strong momentum dependence was traced back to originate from the pion in several publications by C. Fuchs *et al.* [Sehn97, Fuchs98, Gross-Boelting99, Fuchs04]. To understand the mechanism the antisymmetrized T-matrix has to be split up into its direct and exchange part. The self-energy is then given by [Gross-Boelting99]

$$
\Sigma_{\alpha\beta}(\boldsymbol{k}) = \frac{1}{4}\sum_{B_1} \int \frac{d^3k_1}{(2\pi)^3} \frac{f(\boldsymbol{k}_1)}{E(\boldsymbol{k}_1)} \left[(\gamma_\mu k_1^\mu)_{\alpha\beta} \left(4F_V^D - F_S^X + 2F_V^X + 2F_A^X + F_P^X \right) \right.
$$

$$
\left. + M1_{\alpha\beta} \left(4F_S^D - F_S^X - 4F_V^X - 12F_T^X + 4F_A^X - F_P^X \right) \right] \tag{3.47}
$$

F_i are amplitudes obtained from a not antisymmetrized T-matrix. The direct parts are taken at $\vartheta_c = 0$, the exchange parts at $\vartheta_c = \pi$.

Exploring the one meson exchange Born graphs now in more detail, one finds, that, although the invariants constitute a formally complete basis, no pseudovector structure

$$PV = \frac{(k_1 - k_1')_\mu \gamma^{(1)\mu}}{M_1 + M_1'} \gamma_5^{(1)} \otimes \frac{(k_2 - k_2')_\mu \gamma^{(2)\mu}}{M_2 + M_2'} \gamma_5^{(2)} \tag{3.48}$$

is found. $k_i^{(\prime)}$ denote the particle momenta. Since everything is evaluated for the on-shell T-matrix, this, however, does not seem to cause problems. For momenta k_i that fulfill the mass-shell relation

$$\overline{u}_1(\boldsymbol{q}')\overline{u}_2(\boldsymbol{q}') \, PV \, u_{(}\boldsymbol{q})u_2(\boldsymbol{q}) = \overline{u}_1(\boldsymbol{q}')\gamma_5 u_1(\boldsymbol{q}) \, \overline{u}_2(\boldsymbol{q}')\gamma_5 u_2(\boldsymbol{q}) \tag{3.49}$$

(for details an how to evaluate matrix elements of such invariants please see sec. C.1.2. So obviously this is equivalent then to the pseudoscalar invariant P. The pseudovector Lorentz structures are also not forgotten in the covariants, they are hidden in $\mathcal{K}_6$ to $\mathcal{K}_7$, which do not contribute on-shell.

To make the set of invariants look more like the meson vertices actually included, which is nice for reasons of interpretation of the model, one may just exchange P for PV. It is just a different basis of covariants then, which is used. What seems to be only cosmetics leads to severe changes and ambiguities in the calculation of self-energies. When applying this change for the evaluation of self-energies from the antisymmetrized T-matrix, nothing changes. P and PV are identical on-shell and do not belong to the mean-field generating covariants, anyway. For the direct part of the explicitly antisymmetrized self-energy, eq.(3.47), this holds as well. The difference appears in the exchange part, since [Fuchs98]

$$\text{Tr}_1 \left[(\gamma_\mu^{(1)} k_1^\mu + M_!) \tilde{P} \right] = -(\gamma_\mu^{(2)} k_1^\mu - M_1), \tag{3.50}$$

$$\text{Tr}_1 \left[(\gamma_\mu^{(1)} k_1^\mu + M_!) \tilde{PV} \right] = -(\gamma_\mu^{(2)} k_2^\mu - M_1) \left(\frac{k_{1\mu} k_2^\mu}{(M_1 + M_1')(M_2 + M_2')} - \frac{1}{2} \right). \tag{3.51}$$

It was found, that, using the pseudovector covariant instead of the pseudoscalar, one largely removes the problems with a strong momentum dependence. The most recent works on that problem suggest to treat the one pion exchange separately and subtract it from the remaining T-matrix [Gross-Boelting99]. This results in rather stable results which depend only very weakly on the choice of P or PV for decomposing the remaining T-matrix in addition to also removing the strong momentum dependence of the self-energies.

It is well known from pion phenomenology, that there is a subtle difference in coupling the pion as pseudoscalar and pseudovector. Looking at the pion as the Goldstone boson of the spontaneously broken $SU(2)_f^L \otimes SU(2)_f^R$, which is modeled, e.g., in the linear and nonlinear σ models, its coupling has to vanish for vanishing pion momentum. This is exactly fulfilled by the pseudovector coupling. Also the comparison to πN scattering data tells us, that this vertex is realized in nature. One can show, that coupling the pion by a derivative to the nucleon reduces the contributions of antinucleons to the scattering processes. As we are working in the no sea approximation in DBHF theory, i.e., the antinucleons are neglected, a mechanism, which suppresses their admixture is highly

welcome. So using the pseudovector instead of the pseudoscalar invariant is a way to improve the "unitarity" – meant in the sense, that it minimizes a leaking in of degrees of freedom due to the relativistic formalism, which is not explicitly treated. Also the mismatch in the number of covariants and independent helicity matrix elements can be attributed to the fact, that, within a relativistic framework, the BS equation which is restricted to positive energy states is not a closed system [Tjon85].

The ambiguity may, however, also be an artefact of the inversion method used to decompose the T-matrix. A different suggestion to resolve this problem is to use the half off-shell information of the T-matrix. The equation to be inverted instead of eq.(3.30) is in that case

$$[\langle T(q, q_s)\rangle]_q = \sum_\alpha [\Gamma_\alpha(q_S)]_\alpha \, [\langle \mathcal{C}_\alpha(q, q_s)\rangle]_{\alpha q}, \tag{3.52}$$

where the subscripts denote the matrix indices of the linear problem. One has to take as many off-shell momenta as there are independent covariants $\mathcal{C}_\alpha$. This procedure is in the spirit of the coupling renormalization procedure described in sec. 6 and [Lenske04]. In this procedure the assumption enters, that the Γ_α are independent of q. Otherwise the final result would depend on the chosen off-shell momentum grid. This will have to be checked in actual calculations. A similar decomposition was applied in [Lenske04], where the full T-matrix has been mapped onto one boson exhcange Born graphs. The obtained Γ_α are physically reasonable, hinting at the reliability of that method.

3.2. Relativistic mean-field kinematics

The kinematics of DBHF is that of the relativistic mean-field (RMF) theory, see sec. 3.3. A very detailed description of RMF theory is given in [Serot86]. The self-energies calculated from the G-matrix equation enter in the following procedure only as expectation values. That means that the in-medium two particle scattering happens with respect to a static, homogeneous and isotropic background potential and leads to a simple Dirac equation for non-interacting particles, i.e., the potential expressions are no longer operator valued, in the sense, that they are c-numbers with respect to field operators. The Lorentz-structure is preserved.

$$\left[\gamma_\mu k^\mu - M + \Sigma\right]\psi(k) = 0 \tag{3.53}$$

Σ is the self-energy, the relativistic potential. In a homogeneous and isotropic baryonic medium the self-energy has a particularly simple form [Serot86] and can be decomposed in its Lorentz structure

$$\Sigma = \Sigma_s - \gamma_\mu \Sigma^\mu, \tag{3.54}$$

where Σ_s and Σ^μ are the scalar and vector self-energies, respectively. The space-like part of the vector self-energy has under these conditions the form

$$\boldsymbol{\Sigma} = \boldsymbol{k}\Sigma_v \tag{3.55}$$

Plugging eqs.(3.54) and (3.55) into eq.(3.53) yields

$$\left[\gamma_0(k^0 - \Sigma^0) - \boldsymbol{\gamma}\boldsymbol{k}(1 - \Sigma_v) - (M - \Sigma_s)\right]\psi(k) = 0. \tag{3.56}$$

Dividing this by $(1 - \Sigma_v)$ and defining

$$E^*(k) = \frac{(k^0 - \Sigma^0)}{(1 - \Sigma_v)}, \qquad M^*(k) = \frac{(m - \Sigma_s)}{(1 - \Sigma_v)} \tag{3.57}$$

leads to a Dirac equation that is formally identical to the free one

$$[\gamma_0 E^*(\boldsymbol{k}) - \boldsymbol{\gamma k} - M^*] \psi(k) = 0. \tag{3.58}$$

Also the on-shell relation retains the same structure:

$$E^*(k)^2 = \boldsymbol{k}^2 + M^{*2} \tag{3.59}$$

The in-medium spinors can thus be obtained from the free ones, eq. (B.1) by just replacing mass and energy by the respective effective quantities:

$$u(\boldsymbol{q}, \lambda) = \sqrt{\frac{E^* + M^*}{2M^*}} \begin{pmatrix} 1 \\ \frac{2\lambda q}{E^* + M^*} \end{pmatrix} |\lambda\rangle \tag{3.60}$$

To calculate the self-energies later on the relativistic baryon propagator at finite density is needed. The propagator is obtained in a straightforward but a bit lengthy calculation (for details see [Serot86]) from the expectation value of the field operators' time ordered product

$$iG^0_{\alpha\beta}(x' - x) = \langle\Psi_0| T[\psi_\alpha(x')\overline{\psi}_\beta(x)] |\Psi_0\rangle \tag{3.61}$$

α and β are indices in 4-dimensional spinor space. The momentum space propagator is then

$$G^0_{\alpha\beta}(k) = \frac{1}{2E(\boldsymbol{k})} \left\{ (\gamma_\mu K^\mu + M)_{\alpha\beta} \left[\frac{1 - \theta(k_F - |\boldsymbol{k}|)}{k_0 - E(k) + i\epsilon} + \frac{\theta(k_F - |\boldsymbol{k}|)}{k_0 - E(k) - i\epsilon} \right] \right. $$
$$\left. - (\gamma_\mu \tilde{K}^\mu + M)_{\alpha\beta} \left[\frac{1}{k_0 + E(k) - i\epsilon} \right] \right\} \tag{3.62}$$

where

$$\gamma_\mu K^\mu = \gamma_0 E(\boldsymbol{k}) - \boldsymbol{\gamma k}, \qquad \gamma_\mu \tilde{K}^\mu = -\gamma_0 E(\boldsymbol{k}) - \boldsymbol{\gamma k}. \tag{3.63}$$

In this representation the particle-, hole-, and antiparticle-propagation can be nicely identified. For a better manageability in calculations it is, however, better to rewrite eq.(3.62). Collecting the terms not containing a theta function one obtains the well known Feynman propagator describing free baryons and antibaryons

$$G^0_F(k)_{\alpha\beta} = \frac{E(k)}{M} \frac{(\gamma_\mu k^\mu + M)_{\alpha\beta}}{k^2 - M^2 + i\epsilon}, \tag{3.64}$$

$k_\mu = (k_0, \boldsymbol{k})$. For this the formal identity

$$\frac{1}{\omega \pm i\eta} = \mathcal{P}\frac{1}{\omega} \mp i\pi\delta(\omega) \tag{3.65}$$

has to be used, where the δ function needs to be rewritten as

$$\delta(k_0 \mp E(\boldsymbol{k})) = 2E(\boldsymbol{k})\delta^{(\pm)}(k_\nu k^\nu - M^2). \tag{3.66}$$

This is necessary to get the pole structure and prefactors right.

Next one collects the terms proportional to $\theta(k_F - |\boldsymbol{k}|)$. Using again eq.(3.65) one gets the correction to the bare propagator caused by the Pauli principle:

$$G_D^0(k)_{\alpha\beta} = \frac{i\pi}{M} \left(\gamma_\mu k^\mu + M\right)_{\alpha\beta} \, \delta(k_0 - E(k))\theta(k_F - |\boldsymbol{k}|) \tag{3.67}$$

The full non-interacting in-medium propagator is then given by

$$
\begin{aligned}
G^0(k)_{\alpha\beta} &= G_F^0(k)_{\alpha\beta} + G_D^0(k)_{\alpha\beta} \\
&= (\gamma_\mu k^\mu + M)_{\alpha\beta} \left\{ \frac{1}{k_\nu k^\nu - M^2 + i\epsilon} + \frac{i\pi}{E(\boldsymbol{k})} \, \delta(k_0 - E(k))\theta(k_F - |\boldsymbol{k}|) \right\}
\end{aligned}
\tag{3.68}
$$

3.2.1. Reference frames

Due to the nuclear medium boost invariance of the scattering problem is broken. In this situation two favored frames exist, in which the calculations are performed most conveniently:

- the center of momentum (c.m.) frame and

- the nuclear matter rest (n.m.) frame.

As the free T-matrix, the G-matrix is evaluated most conveniently in the c.m. frame. Since the scattering matrix is formulated covariantly it may be easily boosted into other frames. The second frame, the n.m. system, is used for the calculation of self-energies, since they are most easily calculated in that frame. As the scattering matrix also the self-energies are of definite Lorentz structure and may therefore be boosted in a straightforward way.

Let us define $\boldsymbol{\beta}$ such, that it describes a boost from the n.m. frame to the c.m. frame. We shall now determine the relations between the kinematical parameters β and γ and the four vectors P_μ, the in-medium total momentum, and B_μ, the baryon current.

First, we boost P_μ from the c.m. frame to the n.m. frame (please keep in mind, that the definition of $\boldsymbol{\beta}$ is the other way around). In the c.m. frame $P_{cm} = (\sqrt{s^*}, \boldsymbol{0})$ and $(P_{cm})^2 = (P_{nm})^2 = s^*$. By using eqs.(A.27) and (A.28) we find

$$
\begin{aligned}
P_{nm}^0 &= \gamma\sqrt{s^*} \tag{3.69} \\
\boldsymbol{P}_{nm} &= \boldsymbol{\beta}\gamma\sqrt{s^*} \tag{3.70}
\end{aligned}
$$

and therefore

$$\boldsymbol{\beta} = \frac{\boldsymbol{P}_{nm}}{P_{nm}^0}, \quad \text{and} \quad \gamma = \frac{1}{1 - \beta^2} = \frac{P_{nm}^0}{\sqrt{s^*}} \tag{3.71}$$

From this we obtain the useful relations

$$P_{nm}^0 = \gamma\sqrt{s^*}, \quad \text{and} \quad \boldsymbol{P}_{nm} = \boldsymbol{\beta}\gamma\sqrt{s^*} \tag{3.72}$$

Next the baryon current B is boosted from the n.m. frame ($B = (\rho_B, \mathbf{0})$) to the c.m. frame ($B = (B_{cm}^0, \boldsymbol{j})$):

$$B_{cm}^0 \;=\; \gamma \rho_B \tag{3.73}$$

$$\boldsymbol{j} \;=\; -\boldsymbol{\beta}\gamma\rho_B \tag{3.74}$$

In analogy to the above expressions we find

$$\boldsymbol{\beta} = -\frac{\boldsymbol{j}}{B_{cm}^0}, \quad \text{and} \qquad \gamma = \frac{B_{cm}^0}{\rho_B} \tag{3.75}$$

and

$$B_{cm}^0 = \gamma\rho_B, \quad \text{and} \qquad \boldsymbol{j} = -\boldsymbol{\beta}\gamma\rho_B \tag{3.76}$$

3.3. Relativistic mean-field dynamics – saturation

The most important difference between a relativistic and a non-relativistic description of nuclear matter is the saturation mechanism. Using relativistic dynamics, interactions determined in free scattering and applied in many-body frameworks to systems at finite density, yields the correct saturation point (see the discussion in the introduction of this chapter). In contrast to that all non-relativistic descriptions need to introduce phenomenological three-body forces or other empirical recipes.

To understand the relativistic saturation mechanism let us shortly sketch the most simple Walecka model [Serot86]. It is more transparent than DBHF, since almost all expressions can be derived analytically. The Lagrangian contains a fermionic nucleon field and a Lorentz scalar and vector meson, minimally coupled to the nucleons:

$$
\begin{aligned}
\mathcal{L} &= \mathcal{L}_B + \mathcal{L}_m + \mathcal{L}_{int} \\
\mathcal{L}_B &= \overline{\psi}\left(i\gamma_\mu\partial^\mu - M\right)\psi \\
\mathcal{L}_m &= \frac{1}{2}\left(\partial_\mu\sigma\partial^\mu\sigma - m_\sigma^2\sigma^2\right) - \frac{1}{2}\left(\frac{1}{2}F_{\mu\nu}^{(\omega)}F^{(\omega)\mu\nu} - m_\omega^2\omega^2\right) \\
\mathcal{L}_{int} &= -g_\omega\overline{\psi}\gamma_\mu\psi\omega^\mu - g_\sigma\overline{\psi}\psi\sigma
\end{aligned}
\tag{3.77}
$$

$F_{\mu\nu}$ is the field strength tensor of vector particles

$$F_{\mu\nu} = \partial_\mu\phi_\nu - \partial_\nu\phi_\mu \tag{3.78}$$

The corresponding field equations are given by

$$\left[\gamma_\mu\left(i\partial^\mu - g_\omega\omega^\mu\right) - (M - g_\sigma\sigma)\right]\psi = 0 \tag{3.79}$$

$$\left(\partial_\mu\partial^\mu + m_\sigma^2\right)\sigma \;=\; g_\sigma\overline{\psi}\psi \tag{3.80}$$

$$\left(\partial_\mu F^{\mu\nu} + m_\omega^2\omega^\nu\right) \;=\; g_\omega\overline{\psi}\gamma^\nu\psi \tag{3.81}$$

In mean-field approximation the meson field equations, eqs.(3.80) and (3.81), are treated as classical field equations, i.e., the field operators are replaced by their expectation values

$$\sigma, \omega \qquad \rightarrow \qquad \langle\sigma\rangle, \langle\omega\rangle \tag{3.82}$$

$$\overline{\psi}\psi \qquad \rightarrow \qquad \rho_s \equiv \langle\overline{\psi}\psi\rangle \tag{3.83}$$

$$\overline{\psi}\gamma_\mu\psi \qquad \rightarrow \qquad j_\mu \equiv \langle\overline{\psi}\gamma_\mu\psi\rangle \tag{3.84}$$

Considering now a homogeneous and isotropic medium, the meson field equations can be solved algebraically and yield the relativistic scalar and vector single particle potentials. Due to spherical symmetry also the space-like components of the vector fields vanish.

$$V_s \equiv g_\sigma\sigma = \frac{g_\sigma^2}{m_\sigma^2}\rho_s \tag{3.85}$$

$$V_v \equiv g_\omega\omega = \frac{g_\omega^2}{m_\sigma^2}\rho_B \tag{3.86}$$

$\rho_B = j_0$ is the baryon density. Because of translational symmetry the solutions of the Dirac equation in infinite matter are given by plane waves and a 4-component Dirac spinor

$$\Psi_{\boldsymbol{k},\lambda} = \psi(\boldsymbol{k}, \lambda)\exp\left[i(\boldsymbol{kx} - \epsilon(\boldsymbol{k})t),\right] \tag{3.87}$$

normalized as (for $t = 0$)

$$\langle\Psi_{\boldsymbol{k},\lambda}|\Psi_{\boldsymbol{k}',\lambda'}\rangle = \delta_{\lambda\lambda'}\delta(\boldsymbol{k} - \boldsymbol{k}') \tag{3.88}$$

Then eq. (3.79) determines the spinor part by

$$\left[\boldsymbol{\alpha k} + \beta M_{RMF}^*\right]\psi(\boldsymbol{k}, \lambda) = \left[\epsilon(\boldsymbol{k}) - V_v\right]\psi(\boldsymbol{k}, \lambda) \tag{3.89}$$

where $M_{RMF}^* = m - V_s$ is the effective mass of RMF theory (which is different from the definition of the effective mass in DBHF, eq.(3.57)). Squaring eq.(3.89) one finds

$$\epsilon = V_v \pm \underbrace{\sqrt{\boldsymbol{k}^2 + {M_{RMF}^*}^2}}_{\equiv E_{RMF}^*(\boldsymbol{k})} \tag{3.90}$$

Substituting this result in eq.(3.89) we find that that the vector potential drops out from the mean-field Dirac equation! Restricting ourself to the particle solutions $\psi^{(+)}$ we find

$$\psi^{(+)}(\boldsymbol{k}, \lambda) = u_\lambda(\boldsymbol{k}) = N\sqrt{E_{RMF}^* + M_{RMF}^*}\left(\begin{array}{c} 1 \\ \frac{2\lambda q}{E_{RMF}^* + M_{RMF}^*} \end{array}\right)|\lambda\rangle. \tag{3.91}$$

According to the normalization condition, eq.(3.88), $N = 1/\sqrt{2E^*}$. For the Hartree mean-field self-energies, eq.(3.85) and eq.(3.86), the scalar and the baryon densities are needed

$$\overline{u}_\lambda(\boldsymbol{q})u_\lambda(\boldsymbol{q}) = \frac{M_{RMF}^*}{E_{RMF}^*(\boldsymbol{q})} \qquad u_\lambda^\dagger(\boldsymbol{q})u_\lambda(\boldsymbol{q}) = 1. \tag{3.92}$$
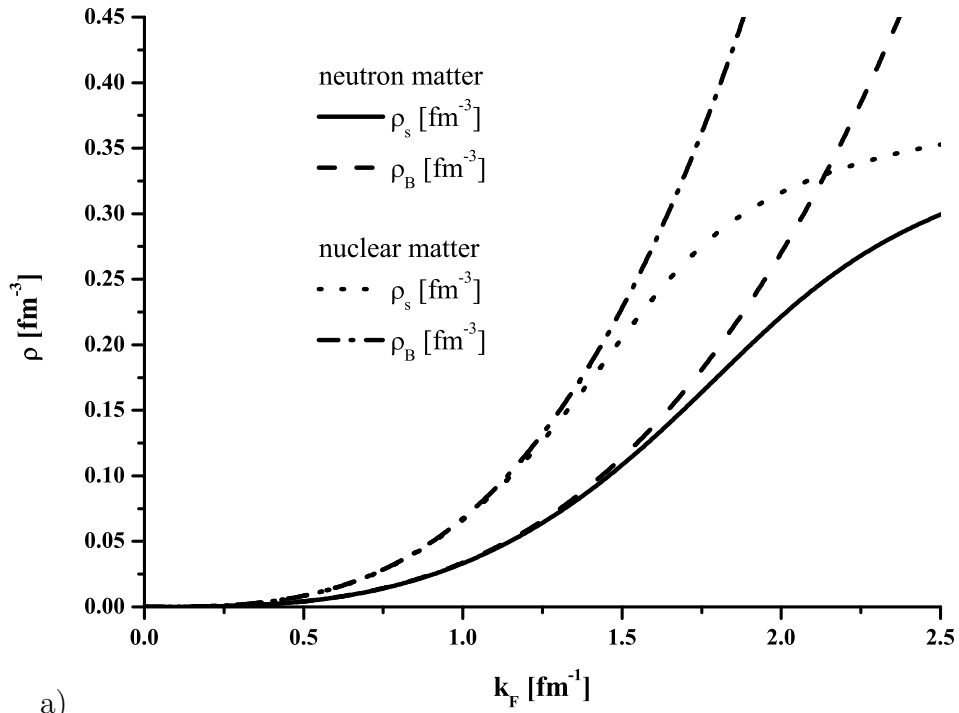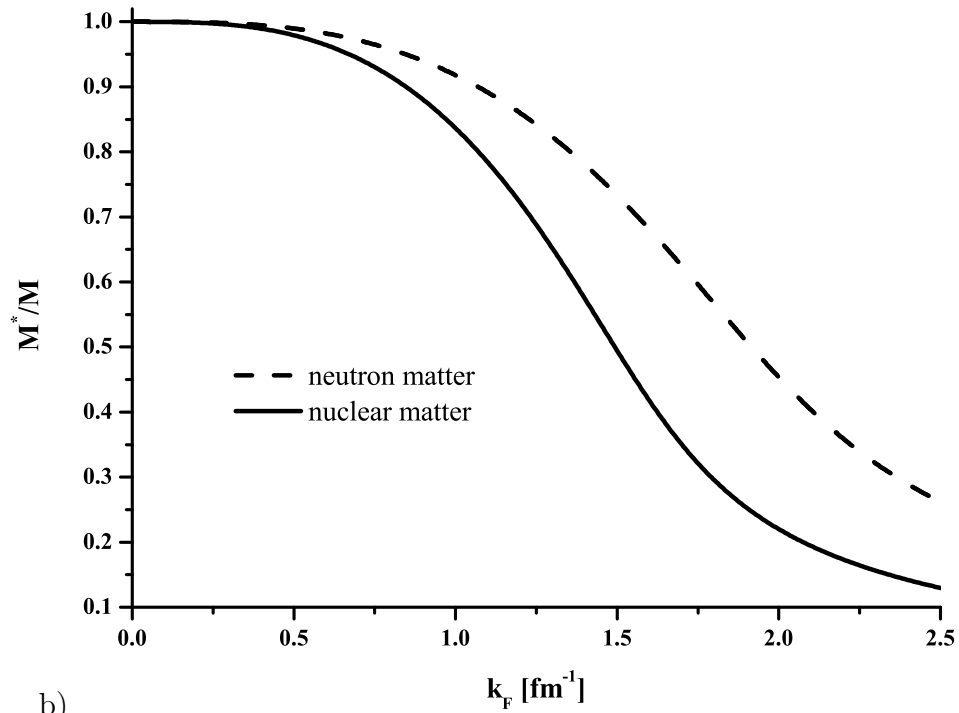
Figure 3.10.: Illustration of the evolution of scalar and vector density in nuclear and neutron matter with increasing baryon density. The different behavior of scalar and vector density is the origin of the relativistic saturation mechanism in nuclear systems.

Because of eq.(3.88) the conserved baryon current is normalized to 1, unlike in the normalization chosen in sec. 3.2, which is the standard choice in scattering theory. Please note, that besides N also the definitions of E^*_{RMF} and M^*_{RMF} differ from those of sec. 3.2!

After these formal developments we can now turn back on the saturation mechanism in relativistic nuclear models. The saturation mechanism works through a delicate cancellation between an attractive scalar and a repulsive vector potential, which are proportional to the scalar and baryon density, respectively. These densities are given by

$$\rho_B = \langle \overline{u}u \rangle = \gamma \int_0^{k_F} \frac{d^3k}{(2\pi)^3} \, \overline{u}u = \frac{\gamma}{6\pi^2} k_F^3 \tag{3.93}$$

$$\rho_s = \langle u^\dagger u \rangle = \gamma \int_0^{k_F} \frac{d^3k}{(2\pi)^3} \, u^\dagger u = \gamma \int_0^{k_F} \frac{d^3k}{(2\pi)^3} \frac{M^*}{E^*}$$

$$= \frac{\gamma}{4\pi^2} M^* \left(k_F E^*(k_F) + M^* \ln\left[\frac{M^*}{k_f + E^*(k_F)} \right] \right) \tag{3.94}$$

γ is the degeneracy factor. For symmetric nuclear matter with $s_z = \pm\frac{1}{2}$ and $T_z = \pm\frac{1}{2}$ $\gamma = 2 \cdot 2 = 4$, whereas for neutron matter with $T_z = +\frac{1}{2}$ $\gamma = 2$. Eq.(3.94) has to be solved iteratively since ρ_s is also hidden in M^*_{RMF}. As can be seen from fig. 3.10, showing the scalar and vector densities and the effective mass as a function of k_F in the QHD-1 model of [Serot86], the baryon density, which is responsible for the repulsion, keeps rising while the scalar density that induces attraction saturates. How fragile this balance is can be seen from fig. 3.11 that shows the corresponding binding energy per nucleon. Although there is no real qualitative difference between the ratio of scalar and vector densities in nuclear and neutron matter, nuclear matter is bound, whereas neutron matter is unbound.

A nice interpretation of the saturation mechanism is that nuclear matter saturates due to an increasing antiparticle contribution in the relativistic wave function, induced by large scalar and vector potentials. Around the saturation point both, scalar and vector potential, are in magnitude of several hundred MeV. The Schrödinger equivalent potential, however, which results from a non-relativistic reduction of the Dirac equation, is about 50 MeV which is just in line with native non-relativistic models. From this number a non-relativistic treatment seems to be justified – if one leaves out the large scalar and vector potential. These lead to large relativistic effects in the wave function, i.e., the lower component and thus the antiparticle content of the wave function grows. Sketching the wave function as $u = (u_1, u_2)$, where, for positive energy, u_1 and u_2 are the particle and ntiparticle content of u, we have $\rho_B \propto |u_1|^2 + |u_2|^2$ and $\rho_s \propto |u_1|^2 - |u_2|^2$. The antiparticle content of the wave function increases the repulsion and decreases the attraction, leading to the saturation of nuclear matter.
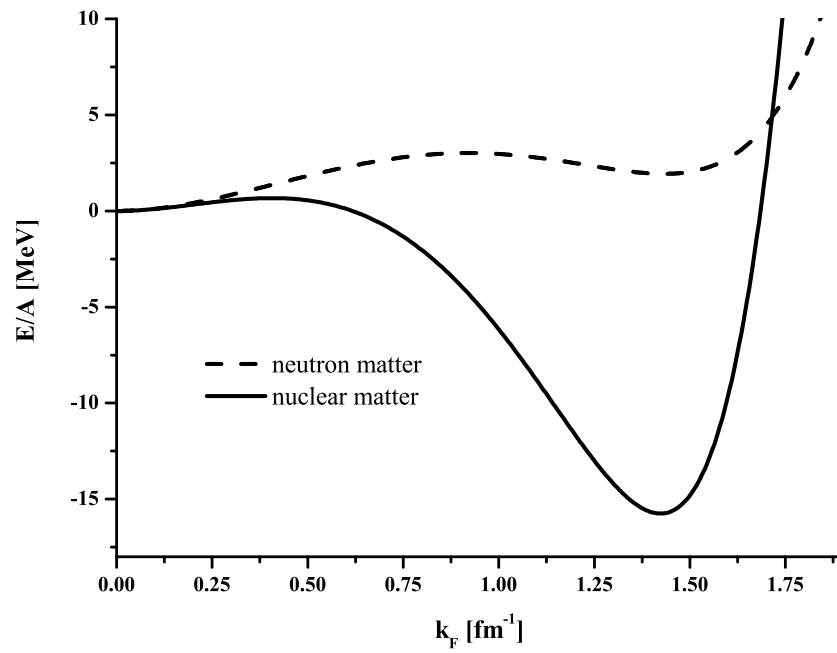
Figure 3.11.: Binding energy per nucleon in the QHD1 model of [Serot86]. The equation of state is shown for symmetric nuclear matter and neutron matter.

4. The Density Dependent Relativistic Hadron Field Theory

The link in our ab initio model, connecting effective interactions in infinite matter with nuclei and hypernuclei is the the density dependent relativistic hadron field theory (DDRH theory) [Fuchs95, Lenske04]. In principle, the relativistic in-medium scattering theory can be formulated for the application to finite systems, and has been applied to small nuclei up to ^{16}O [Muther90]. In heavier systems, however, the computational effort would be by far too high, even for present days computers.

DDRH theory offers here an alternative way to proceed. It is a baryon-meson field theory designed for nuclear structure calculations with medium modified meson-baryon vertices in RMF approximation. This is in contrast to phenomenological RMF models which account for the modification of the in-medium interaction with varying density by self-interactions of the meson fields. The treatment of medium effects by density dependent vertices only is in line with the considerations of DBHF theory, see sec. 3, where the mesons are unaffected by the nuclear medium. To determine the vertices DBHF self-energies are mapped onto DDRH mean-field self-energies in infinite matter. This amounts to an application of DBHF effective interactions to finite nuclei in local density approximation. The meson-baryon vertices are constructed as functionals of baryon field operators and are thus dynamical quantities of the theory. Used in mean-field approximation, they reduce to functions of the local density. Knowing the dynamical content, i.e. the diagrammatic structure, of the used DBHF interactions, one is, however, able to go systematically beyond mean-field and local density approximation by calculating higher order correlations contained in the vertex functionals which vanish in RMF.

Using microscopic interactions DDRH theory was applied very successfully to double magic nuclei [Fuchs95], highly asymmetric nuclei [Hofmann01b] and to hypernuclei [Keil00]. Furthermore DDRH was successfully used to calculate hypermatter in β equilibrium and neutron star properties [Hofmann01a]. An extension of DDRH to also handle momentum dependent coupling functionals has been developed in [Typel03]. Recently DDRH theory was also used for deducing purely empirical density dependent couplings [Typel99, Niksic02a, Niksic02b], which have been applied then in Hartree-Bogolyubov [Niksic02a] and RPA calculations [Niksic02b]. Further extensions of DDRH include the use of additional meson self-interactions [Long04] and at finite temperature [Avancini04].

Although DDRH seems to be very similar to Walecka's QHD models [Serot86], there are important differences. The possibility to use microscopic interactions is a significant advantage. Due to the operator structure of the vertices, however, the dynamics of DDRH is substantially altered. Due to the operator structure, also controlled extensions beyond mean-field are possible, which fails in QHD [Serot86].

4.1. The DDRH formalism

Being a relativistic quantum field theory, DDRH is defined by a Lagrangian density.The DDRH Lagrangian is built from free hadronic and mesonic Lagrangians and the interaction part

$$\mathcal{L}_{\text{DDRH}} = \mathcal{L}_B + \mathcal{L}_M + \mathcal{L}_{int} \tag{4.1}$$

where

$$\mathcal{L}_B \;\; = \;\; \sum_B \overline{\psi}_B \left[i\gamma_\mu \partial^\mu - M_B \right] \psi_B \tag{4.2}$$

$$\mathcal{L}_M \;\; = \;\; \sum_{\alpha_s} \frac{1}{2} \left(\partial_\mu \phi_{\alpha_s} \partial^\mu \phi_{\alpha_s} - m_{\alpha_s}^2 \phi_{\alpha_s}^2 \right)$$

$$-\sum_{\alpha_v} \frac{1}{2} \left(\frac{1}{2} F_{\mu\nu}^{(\alpha_v)} F^{(\alpha_v)\mu\nu} - m_{\alpha_v}^2 \phi_{\alpha_v}^2 \right) \tag{4.3}$$

The central part of DDRH theory is the interaction Lagrangian with operator valued vertex functionals $g(\hat{\rho})$, where

$$\hat{\rho} = \hat{\rho} \left(\overline{\psi}, \psi \right) = \text{Lorentz scalar}. \tag{4.4}$$

This treatment of medium-effects in Lorentz-scalar functionals assures not only the covariance of the model but in addition restores thermodynamical consistency, at least on the mean-field level, which is violated by DBHF theory [Fuchs95]. In the general case, where nucleons as well as hyperons are included, both, g and $\hat{\rho}$ may differ for the different particles.

The vertex functionals replace the conventional coupling constants as they appear in phenomenological RMF models, leading to the interaction Lagrangian

$$\mathcal{L}_{int} \;\; = \;\; \sum_{\alpha,B} g_{\alpha,B} \left(\hat{\rho}_{\alpha,B} \right) \overline{\psi}_B (\Gamma \cdot \phi_\alpha) \psi_B, \tag{4.5}$$

where $(a \cdot b)$ denotes a Lorentz scalar contraction, i.e., ab for scalars and $a_\mu b^\mu$ for vectors. Γ represents the particular vertex structure containing Lorentz, isospin, *etc.* operators. The two most common forms of $\hat{\rho}$ are the so called scalar and vector density dependence, SDD and VDD, respectively [Fuchs95], where

$$\hat{\rho}_{SDD} \equiv \overline{\psi}\psi, \qquad \hat{\rho}_{VDD} \equiv \sqrt{(\overline{\psi}\gamma_\mu \psi)(\overline{\psi}\gamma^\mu \psi)} = \sqrt{j_\mu j^\mu}. \tag{4.6}$$

The dynamics of the theory is now obtained by deriving the field equations from the Lagrangian, eq.(4.1),using the Euler-Lagrange equations

$$\frac{\partial \mathcal{L}}{\partial \Phi} - \partial_\mu \Phi \frac{\partial \mathcal{L}}{\partial (\partial_\mu \Phi)} = 0 \tag{4.7}$$

For the mesons the standard Klein-Gordon and Proca equation are obtained, now with a source term including a vertex functional instead of a simple constant:

$$\left(\partial_\mu \partial^\mu + m_{\alpha_s}^2 \right) \phi_{\alpha_s} \;\; = \;\; \sum_B g_{\alpha_s,B} \left(\hat{\rho}_{\alpha_s,B} \right) \overline{\psi}_B \psi_B \tag{4.8}$$

$$\left(\partial_\mu F^{(\alpha_v)\mu\nu} + m_{\alpha_v}^2 \phi_{\alpha_v}^\nu \right) \;\; = \;\; g_{\alpha_v,B} \left(\hat{\rho}_{\alpha_v,B} \right) \overline{\psi}_B \gamma^\nu \psi_B \tag{4.9}$$

In the Dirac equation additional self-energies appear due to the dependence of the coupling functionals on baryon field operators. From the Euler-Lagrange equation applied to the interaction part of the Lagrangian we obtain

$$
\frac{\partial \mathcal{L}_{int}}{\partial \overline{\psi}_B} = \sum_\alpha \{ g_{\alpha,B}\left(\hat{\rho}_{\alpha,B}\right)\left(\Gamma_\alpha \cdot \phi_\alpha\right)\psi_B + \frac{\partial g_{\alpha,B}\left(\hat{\rho}_{\alpha,B}\right)}{\partial \hat{\rho}_{\alpha,B}} \underbrace{\frac{\partial \rho_{\alpha,B}}{\partial \overline{\psi}_B}}_{\equiv \hat{a}\psi_B} \overline{\psi}_B(\Gamma_\alpha \cdot \phi_\alpha)\psi_B \}
$$

$$
= \left[\Sigma_B + \Sigma_B^{(r)}\right]\psi_B
$$

(4.10)

The normal self-energy is given by

$$
\Sigma_B = \sum_\alpha g_{\alpha,B}\left(\hat{\rho}_{\alpha,B}\right)\left(\Gamma_\alpha \cdot \phi_\alpha\right)
$$

(4.11)

and

$$
\Sigma_B^{(r)} = \sum_\alpha \frac{\partial g_{\alpha,B}\left(\hat{\rho}_{\alpha,B}\right)}{\partial \hat{\rho}_{\alpha,B}} \hat{a}\overline{\psi}_B(\Gamma_\alpha \cdot \phi_\alpha)\psi_B
$$

(4.12)

is the *rearrangement self-energy.* $\hat{a}$ depends on the definition of $\hat{\rho}$. The rearrangement self-energies account for the static polarization of the surrounding medium due to the presence of the baryon that 'feels' the self-energy. These self energies also assure thermodynamical consistency and covariance which would not be given using a formulation based on densities only. A formal proof can be found in [Fuchs95]. In mean-field approximation, Σ_B and $\Sigma_B^{(r)}$ will become Hertree type self-energies.

For the SDD and the VDD prescription we have the following values for $\hat{a}$

$$
\begin{array}{c|cc}
 & \frac{\partial \rho_{\alpha,B}}{\partial \overline{\psi}_B} & \hat{a} \\
\hline
\text{SDD} & \psi_B & 1 \\
\text{VDD} & \frac{\gamma_\mu j^\mu}{\sqrt{j_\mu j^\mu}}\psi_B & \gamma_\mu u^\mu
\end{array}
$$

(4.13)

u^μ is the four velocity related to the baryon current and thus in the n.m. frame, in which nuclear structure calculations are performed, $u_{nm}^\mu = (1, \mathbf{0})$. From the Dirac structure in eq.(4.13) one can easily read off that the SDD prescription adds a correction to the scalar self-energy, i.e., it modifies the effective mass, while the VDD prescription adds a correction to the vector self-energy. Obviously there is an ambiguity in the choice of $\hat{\rho}$. Calculations show [Fuchs95] that VDD yields better predictions than SDD for the bulk properties and low energy single particle excitations in spherical nuclei using DBHF interactions. The rearrangement self-energies lead to a local effect only, as is characteristic for polarizations. They modify mostly the single particle properties but not the bulk properties, while adding corrections to the single-particle potentials, they drops out of the total energy expression. Only through the iteration rearrangement will influence also the total energy as a higher order effect.

For the nuclear structure calculations DDRH is used in RMF approximation. In the common RMF schemes (see sec. 3.3) meson fields are replaced by their expectation values with respect to the according many-body ground-state and treated as classical

fields, which amounts to self energies containing no more field operators. The mean-field approximation arises formally from the expansion of a field operator product Ω according to Wick's theorem [Peskin95]

$$\Omega = \Omega_0 + C(\Omega), \qquad (4.14)$$

where Ω_0 denotes the c-valued, fully contracted product of field operators contained in Ω and $C(\Omega) = \Omega - \Omega_0$ the remaining higher correlations, which always contain at least one normal ordered product of field operators. Taking the expectation value of Ω with respect to a many-body ground state $|X\rangle$, only Ω_0 will survive, since due to its normal ordered parts $\langle X | C(\Omega) | X \rangle = 0$. Using only the expectation values of self-energy expressions in the Dirac equation and of the whole meson equations of motion leads to the mean-field approximation.

This derivation of mean-field theory offers a systematic way of extending the formalism beyond mean-field, especially when deriving the functionals by an approach with a clear diagrammatic structure. Allowing for excitations in the many-body state, also parts of C contribute in expectation values. In the conventional phenomenological RMF models going beyond mean-field will, however, cause problems. The model parameters are determined there by matching calculated properties of nuclei to the respective experimentally observed values. Thus effects of higher correlations present in the experimental data, are absorbed in the couplings of the apparently uncorrelated model. Including now successively higher order effects will due to double counting lead to wrong predictions – the parameters alway have to be fixed for the specific prescription used.

For DDRH the case is different. When using microscopic interactions derived by DBHF theory, DDRH calculations are an ab initio calculations for which the exact dynamical content, i.e., the diagrams contained in the interaction kernel of the BS equation, is known. Extensions beyond mean-field can be studied here systematically, opening a variety of opportunities to perform high accuracy ab initio calculations of nuclei across the nuclear chart and with non vanishing strangeness.

4.2. Microscopic vertices in DDRH

To determine the DDRH vertices a mapping procedure of DBHF self-energies onto infinite matter DDRH self-energies is performed [Fuchs95, Hofmann01b]. The standard meson spectrum of DDRH contains four different mesons, inspired by the mean-field generating Lorentz and isospin contents, a scalar and a vector in each sector. They are the scalar iso-scalar σ, the scalar iso-vector $\boldsymbol{\delta}$, the vector iso-scalar ω and the vector iso-vector $\boldsymbol{\rho}$. The DBHF self-energies have to be transformed into the particle basis to extract iso-scalar and -vector part, Σ_0 and Σ_τ, respectively. As the total self-energy for proton and neutron is

$$\Sigma = \Sigma_0 + \tau_3 \Sigma_\tau, \qquad (4.15)$$

the iso-scalar and -vector component are given by

$$\Sigma_0 = \frac{1}{2}(\Sigma_p + \Sigma_n), \qquad \Sigma_\tau = \frac{1}{2}(\Sigma_p - \Sigma_n). \qquad (4.16)$$
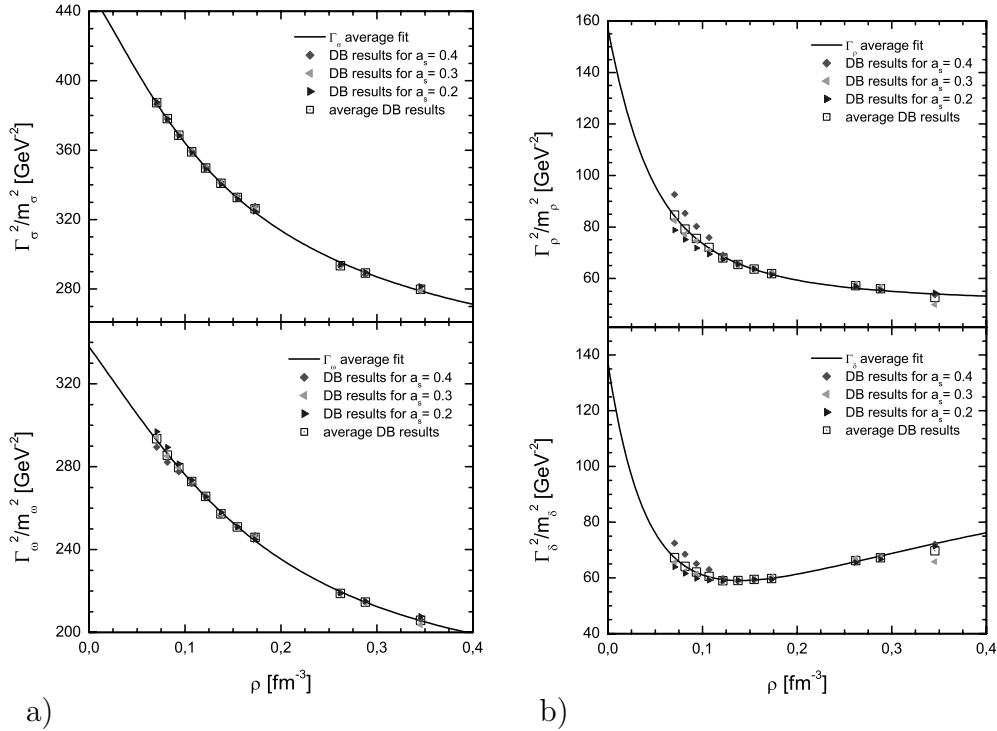
Figure 4.1.: Density dependent vertex functionals as derived from the Groningen NN potential in [Hofmann01b].

The vertex functionals of the respective mesons are then determined by setting equal the DBHF and DDRH infinite matter self energies of corresponding Lorentz and isospin structure. For the σ, e.g., this is

$$\frac{g_\sigma^2(k_F)}{m_\sigma^2}\rho_s \stackrel{!}{=} \Sigma_{DBis}^s \qquad (4.17)$$

As an example we show in fig. 4.1 the mapping of DBHF calculations for asymmetric nuclear matter using the Groningen potential [deJong98] taken from [Hofmann01b].

4.2.1. The structure of the Λ-meson vertex

The Λ is a particularly simple particle to treat in nuclear structure calculations, since it is electrically as well as isospin neutral. There are thus only two coupling parameters and potentials for the Λ. Also experimentally the Λ hypernuclei are those studied best, making it interesting to model single Λ hypernuclei.

In the DDRH calculations for Λ hypernuclei we use a semi-empirical ansatz for the coupling functionals, described in detail in [Keil00], which is consistent with the treatment of the nuclear part. The assumption is made, that the density dependence of the vertices is such, that nuclear and Λ vertices depend only on the respective density. This is motivated by the fact that the main part of the density dependence arises from the Pauli projection operator, which is a product of a nuclear and a Λ projector. In the energy

region relevant in this context we may also neglect the strangeness exchange interactions, contributing in the u-channel, which would spoil the factorization of a nucleonic and a hyperonic part. This factorization leads to the fact, that also the effective interaction may be split in a product of functions depending in the Λ or the nuclear density, which may be attributed to the two vertices then. For a single Λ in nuclear medium the mapping is given by

$$g_{\Lambda\alpha}(\rho_\Lambda)g_{N\alpha}(\rho_N) = m_\alpha^2 \frac{\Sigma_{\Lambda\alpha}}{\rho_N}, \tag{4.18}$$

An especially transparent relation is found when chosing the nucleon density to be equal to the lambda density. Then we can express the Λ-meson coupling functional through [Keil00]

$$g_{\Lambda\alpha}(\rho_\Lambda) = \frac{\Sigma_{\Lambda\alpha}}{\Sigma_{N\alpha}} g_{N\alpha}(\rho_\Lambda). \tag{4.19}$$

The two self-energies in the ratio differ mainly by the couplings and the bare masses, since they are taken at the same density. To simplify this expression we symbolically expand the Λ self-energy around $M = M_N$ with $\Delta M = M_N - M_\Lambda$ and $g = g_N$ where $\Delta g = g_N - g_\Lambda$. g denotes the free coupling here. Defining the meson propagator as D_α we may sketch the solution of the T-matrix

$$T = \frac{g_{B\alpha}g_{B'\alpha}D_\alpha}{1 - g_{B\alpha}g_{B'\alpha}D_\alpha G^{(2)}} \equiv g_{B\alpha}g_{B'\alpha}\tilde{T}, \tag{4.20}$$

$G^{(2)}$ being the two baryon propagator. From the self-energy integral, eq. (3.5),

$$\Sigma = g_{B\alpha}g_{B'\alpha} \int \mathrm{Tr}(\tilde{T}G^{(1)}) \equiv g_{B\alpha}g_{B'\alpha}\tilde{\Sigma}, \tag{4.21}$$

we have

$$g_\Lambda(\rho_B) = \frac{g_\Lambda}{g_N} \left(1 + \frac{\partial_g \tilde{\Sigma}(g, M_N)\big|_{g=g_N}}{\tilde{\Sigma}(g_N, M_N)} \Delta g + \frac{\partial_M \tilde{\Sigma}(g_N, M)\big|_{M=M_N}}{\tilde{\Sigma}(g_N, M_N)} \Delta M + \cdots \right) g_{N\alpha}(\rho_B), \tag{4.22}$$

where g are the bare coupling constants of free-space interactions. For the sake of readability the indices α have been suppressed. The changes of the self-energy with respect to M are surely mild, so that this correction will be small. The variation of Σ with respect to g is somewhat more critical, since resonances in the T-matrix may appear. This needs to be checked if actual DBHF calculations for the Λ-nucleon interaction are available. A very detailed discussion of the general structure of vertex functionals can be found in [Lenske04].

For the time being we use the scaling approach

$$g_{\Lambda\alpha}(\rho_\Lambda) = R_\alpha g_{N\alpha}(\rho_\Lambda), \tag{4.23}$$

which is well motivated by eq.(4.22). R is the ratio of the free Λ and nucleon coupling constants. For investigating single Λ hypernuclei R_σ and R_ω have to be determined empirically, whereas the functional shape is taken from DBHF calculations. The parameter sets which we use in our calculations are given in app. D.

4.3. Mean-field dynamics in Λ hypernuclei

As noted already above, the Λ hyperon is a particle particularly well suited to describe in RMF models, since it is an uncharged iso-singlet. This simplicity makes it highly valuable in collecting information on the coupling mechanism between hyperons and nucleons. There are only two free parameters in the conventional RMF description of Λ hypernuclei, the scalar coupling to the σ and the vector coupling to the ω meson. Also the so called tensor coupling contributes, which will be discussed in detail further down.

In principle, the scalar and the vector self-energies are given by

$$\Sigma_s = g_{\Lambda\sigma}\rho_s, \qquad \Sigma_v = g_{\Lambda\omega}\rho_B, \tag{4.24}$$

where ρ_s and ρ_B are the total scalar and vector densities, respectively. Their influence on the spectral structure of the Λ single particle energies is easiest understood when considering the Schrödinger equivalent potentials [Jaminon87]. They are obtained by a non-relativistic reduction of the Dirac equation. This yields on the one hand side the central potential

$$V_c \propto \Sigma_v + \Sigma_s \tag{4.25}$$

and on the other hand side the spin-orbit potential

$$V_{so} \propto \partial_r(\Sigma_v - \Sigma_s) \tag{4.26}$$

The central potential is responsible for the spectral distribution of the l-shell energies, whereas the spin-orbit potential governs the splitting of these energies. Having a delicate cancellation between large scalar and vector potentials, see sec. 3.3, which lead to a central depth of around 80 MeV in V_c, we get consequently a rather large spin-orbit splitting. For nucleons this is indeed observed in normal nuclei and rather well described by RMF models.

For hypernuclei only very recently a convincing indication of spin-orbit splitting was observed in nuclei with $A \geq 40$, that are heavy enough to be governed mainly by mean-field effects. (This data is discussed extensively in sec. 8.) Only in such systems, showing also a resolved spin-orbit structure, one was really able to constrain the two free parameters of the Λ-nucleus interaction unambiguously. These experiments were essential for resolving the longstanding controversy on Λ spin-orbit interactions. Before, just l-shell energies could be determined, which allow to fix only a range of pairs $(g_{\Lambda\sigma}, g_{\Lambda\omega})$.

4.3.1. The Λ-ω tensor interaction

Now the large spin-orbit splitting, emerging from the strong scalar and vector fields, as discussed above, is in contradiction to predictions by SU(6) spin-flavor symmetry and also, what should be considered more relevant, to recent observations in γ spectroscopy experiments on light hypernuclei, e.g. [May97, Kohri02]. The magnetic vertex between baryons and vector mesons, the second term of eq.(2.2), is responsible for the so called tensor force in non-homogeneous systems, which influences mainly the splitting of the spin-orbit doublets while leaving other observables in the single particle spectrum almost unchanged. It is therefore a candidate to cure the discrepancy between theory and
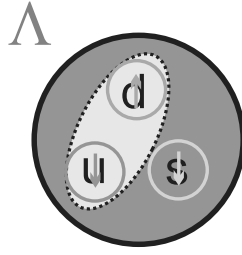
Figure 4.2.: SU(6) spin-flavor symmetry predicts a vanishing spin-orbit splitting of the Λ hyperon, since the up and down quark form a spin singlet in this scheme, so that the Λ spin is carried solely by the strange quark. The mediator of a spin dependent force, the ω meson, cannot have a polarizing effect then, since it does only couple to up and down quarks.

experiment in accordance with SU(6). A detailed derivation of the tensor interaction in RMF models including hyperons is given in [Mares94]. The tensor vertex couples the baryon tensor current with the field strength tensor of the meson:

$$\mathcal{L}_t = \frac{f}{2M}\overline{\psi}\sigma_{\mu\nu}\psi F^{\mu\nu}_{(\omega)} \tag{4.27}$$

The suppression mechanism can, as the scalar and vector self-energies, be understood best, when looking at in the non-relativistic limit, where one finds the tensor potential

$$V_t \propto 2\frac{M^*}{M}\frac{f}{g}\partial_r\Sigma_v. \tag{4.28}$$

In the non-relativistic expansion terms proportional to σ^{00} and σ^{ii} are suppressed. In combination with eq.(4.26) we obtain the full spin-orbit potential

$$V_{so} \propto 2\frac{M^*}{M}\frac{f}{g}\partial_r\Sigma_v + \partial_r(\Sigma_v - \Sigma_s) \tag{4.29}$$

Because of the derivatives this contributes only at the surface, where the densities are low and $M^* \approx M$. Furthermore the derivatives of scalar and vector self-energy are of roughly the same order, so that $\partial_r\Sigma_v \approx -\partial_r\Sigma_s$. Tuning the coupling constant f, we can adjust now the spin-orbit interaction to our will, making it zero for $f/g = -1$ as predicted by SU(6) (see tab. 2.4) or even reverse the order of the doublet states if $f/g < -1$.

The effect of the tensor interaction is studied extensively in the context of single particle spectra of intermediate mass Λ hypernuclei in sec. 8.

5. The Dynamics of Effective ΛN Interactions

In this section we study on the example of the ΛN interaction the influence of changes in the couplings and the mass on the scattering amplitudes, which are characteristic for the scattering of unequal particles as compared to the NN interaction. It is investigated, how a scaling of the bare interaction affects the fully iterated one on a quantitative level, which reveals how well, e.g., SU(3) relations, which are well defined only for the elementary vertices of a theory, hold for effective couplings. In the second part of this chapter we consider the effects of Pauli blocking in the scattering of different particle species. We study the influence of asymmetric media on the scattering amplitudes as well as the influence of different compositions of the medium on the relation between ΛN and NN interaction.

5.1. ΛN interactions in free space

To get a better understanding of the underlying dynamics in ΛN interactions we will now systematically study the dependence of amplitudes and the decomposition into Lorentz covaraints on variations of the particle masses and different values of the g and f couplings. We therefore use the meson exchange framework as derived in sec. 2. To keep the discussion transparent and the covariant decomposition unambiguous, we will apply a model with the following reduced meson exchange kernel as compared to the common meson exchange models:

$$
\begin{array}{c|cc}
\multicolumn{3}{c}{N} \\
\hline\hline
& \omega & \sigma \\
\hline
g & 15.8533 & 10.22145 \\
f/g & 0 & 0 \\
M_{cut} & 1500\ MeV & 2000\ MeV \\
n & 1 & 1
\end{array}
\qquad
\begin{array}{c|cc}
\multicolumn{3}{c}{\Lambda} \\
\hline\hline
& \omega & \sigma \\
\hline
g & 10.568 & 6.8143 \\
f/g & -1 & 0 \\
M_{cut} & 1500\ MeV & 2000\ MeV \\
n & 1 & 1
\end{array}
\qquad (5.1)
$$

The meaning of the parameters is identical to the ones of the Bonn potentials (here we use M_{cut} for the cutoff mass to avoid confusions with the Λ hyperon), given in tab. B.3. For the baryon masses we use $M_N = 939\ MeV$ and $M_\Lambda = 1115\ MeV$. The relation of the Λ to the nucleon vertices is given by SU(3) relations, i.e., g is multiplied by 2/3 and $f/g = -1$ for the $\Lambda\omega$ vertex (see sec. 2.1). Hence, the model uses a ladder kernel as defined by the Born terms of a meson exchange interaction.

By "NN interaction" we will refer to the interaction where we have to nucleon vertices as defined in eq.(5.1) in the Born amplitudes and by "ΛN interaction" we refer to an
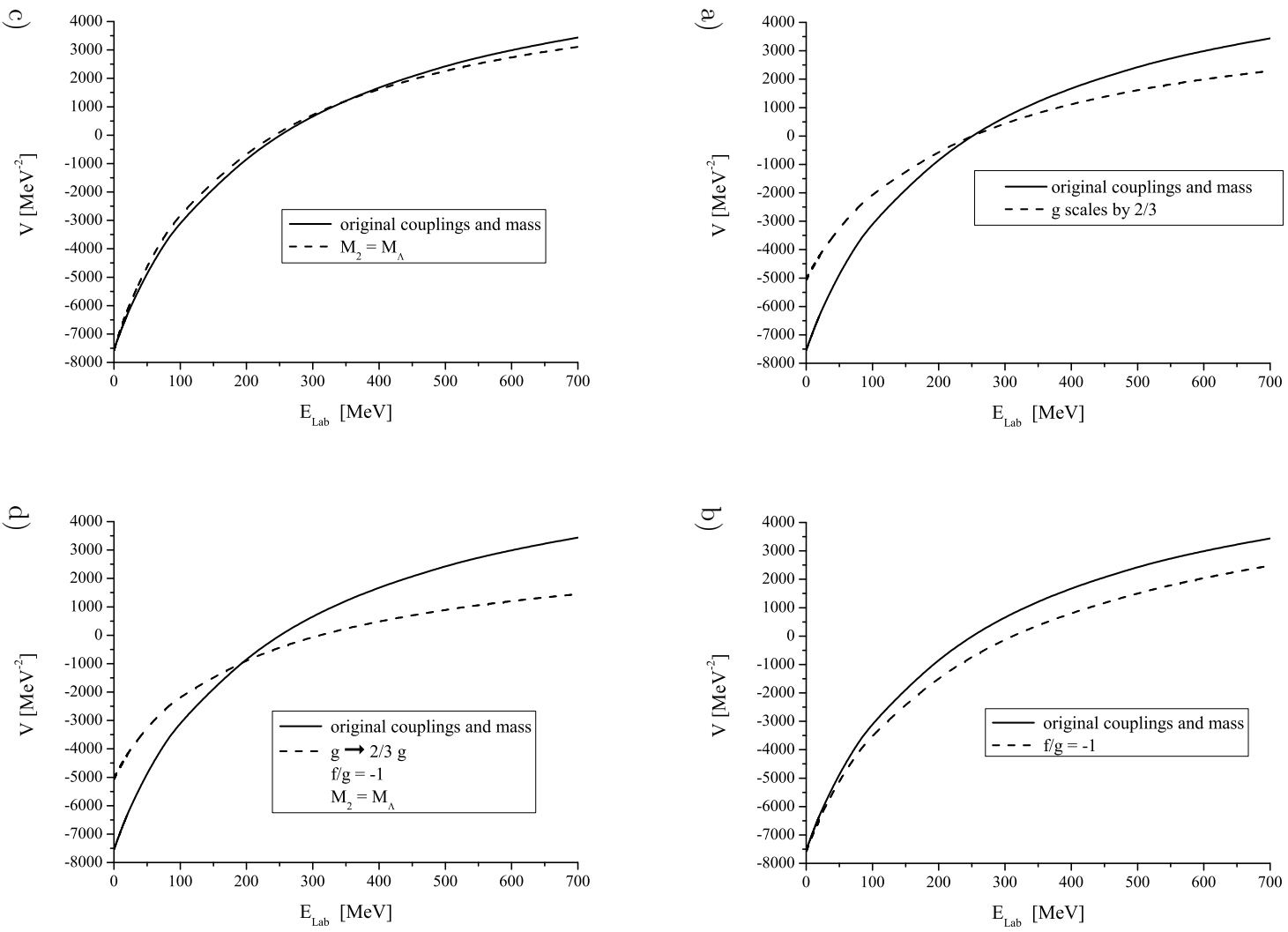
Figure 5.1.: The comparison of kernel amplitudes for the NN parameters and a modified parameter set, related to the ΛN interaction, is shown. The amplitudes displayed are those of the $^1S_0$ partial wave.
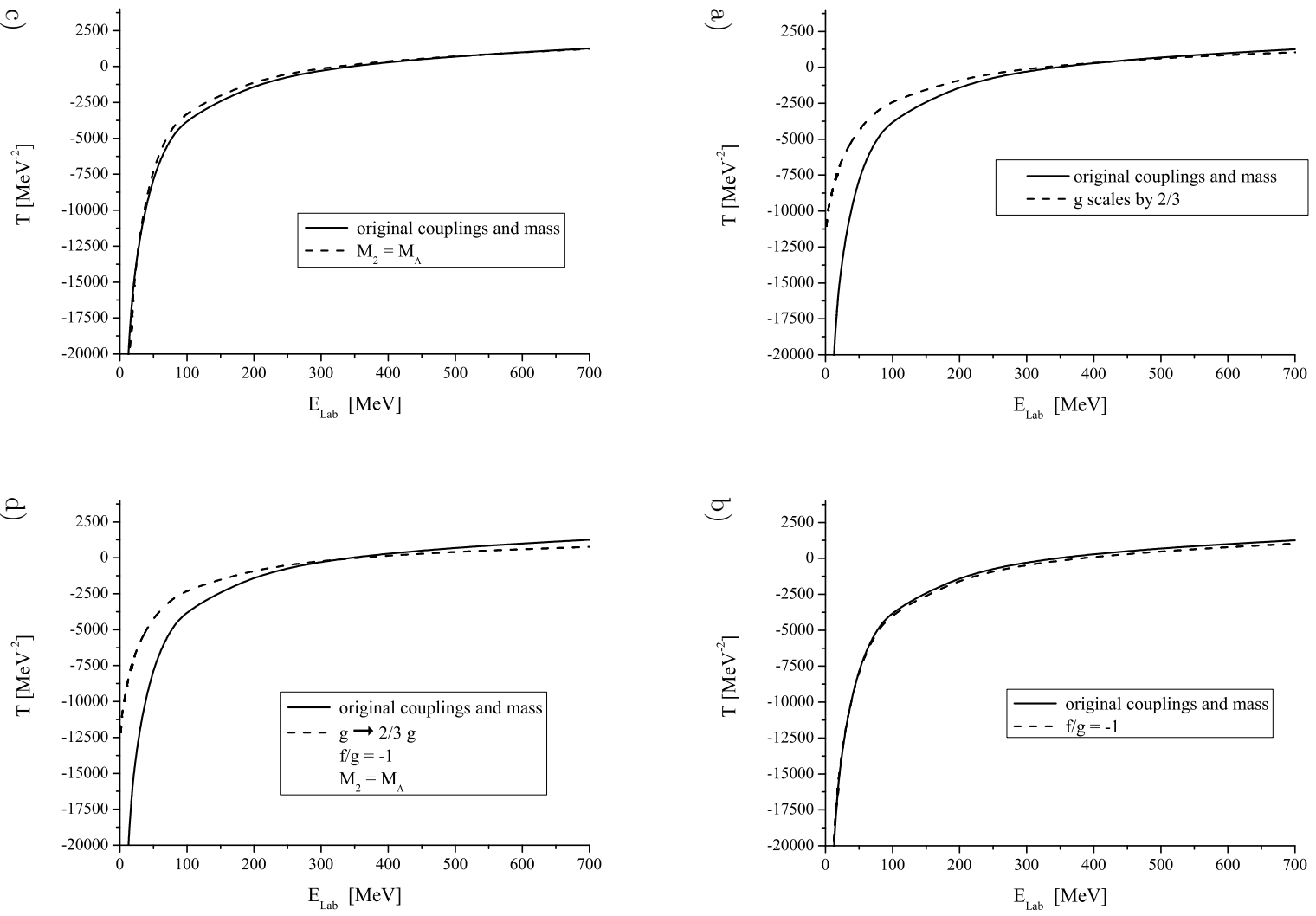
Figure 5.2.: The displayed amplitudes belonging to the iterated interaction corresponding to fig. 5.1.

interaction where one nucleon and one Λ vertex is contained in the kernel elements. No isospin projection will be applied for both interactions. To study the effect of the differing parameters in the Λ and nucleon vertices we first compare the NN interaction with an interaction identical to that one except for one of the parameters, which is set to the value of the ΛN interaction. In panels a)–c) of fig. 5.1 and fig. 5.2 the resulting kernel and T-matrix elements, respectively, in the $^1S_0$ partial wave are displayed for changed mass, g and f. We find, that the influence of a different mass on the kernel as well as on the iterated interaction is only rather small because the baryon mass appears typically in kinematical factors given in terms of $\sqrt{s}/M$. Especially in the full interaction only a slight modification in the intermediate momentum range is found. For the f/g coupling one finds in the kernel a significant modification in the intermediate and especially high momentum range. In the iterated interaction, however, the effect has almost vanished. Only a tiny deviation at higher momenta is left. The most prominent modification arises due to the change of g. In the bare interaction the whole momentum range is significantly altered, while in the full interaction, only the low momentum part shows sizable changes.

Panel d) of fig. 5.1 and fig. 5.2 shows the comparison between NN and the complete ΛN interaction. In summary one can say, that mostly the low momentum changes on the bare potential translate also into effects in the iterated interaction, changes in the high momentum region are clearly suppressed. The most important changes of the interaction are due to the change of g.

Let us now take a closer look on how scaling the bare interaction strength translates to the fully iterated one. To make physically meaningful statements one has to compare the respective Lorentz components of the interaction (see sec. 3.1.2), i.e., compare the scalar and vector invariant of the ΛN interaction to the scalar and vector invariant, respectively, of the unscaled NN interaction. What is used, e.g., in the standard RMF calculations of hypernuclei and hypermatter as effective scalar and vector interactions ("σ and ω exchange") are exactly those Lorentz components of the interaction. So, e.g., the ratio of scalar ΛN over NN invariants gives the scaling factor relating the Nσ vertex to the $\Lambda\sigma$ vertex, which should be used in such calculations (up to effects due to the density which will be discussed in the following section). In panel a) of fig. 5.3 we display the Lorentz scalar and vector amplitudes for the ΛN and NN interaction. It can be seen immediately, that the reduction between both interactions is by far more than 2/3. From panel b), showing the respective ratios of the invariants, we can read off an average reduction factor of 0.1. This is clearly far below the standard SU(3) choice for relating hyperon and nucleon effective vertices.

5.2. ΛN interactions at finite density

To investigate the density dependence of an effective interaction between two different particle species we applied the model defined by eq.(5.1) for three compositions of the
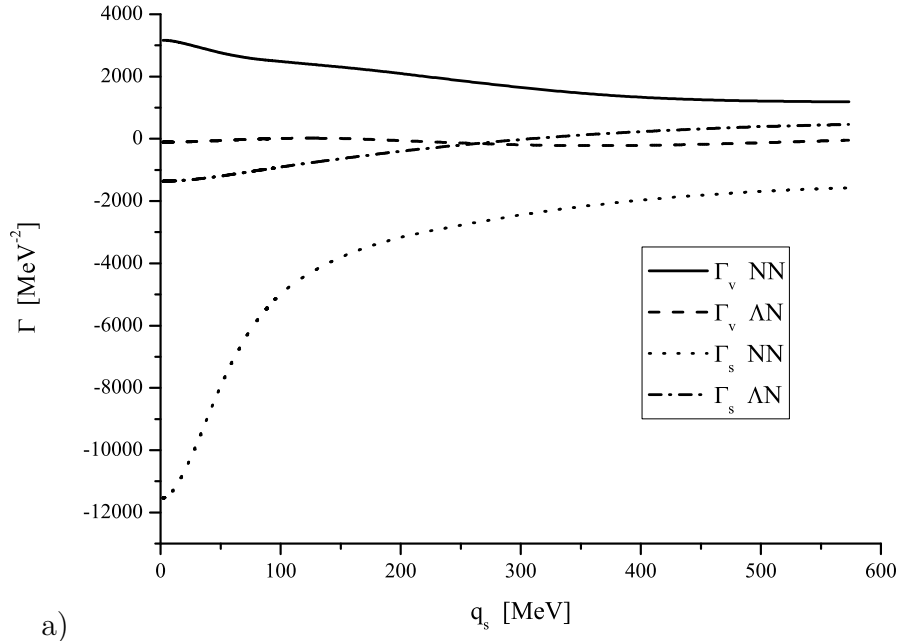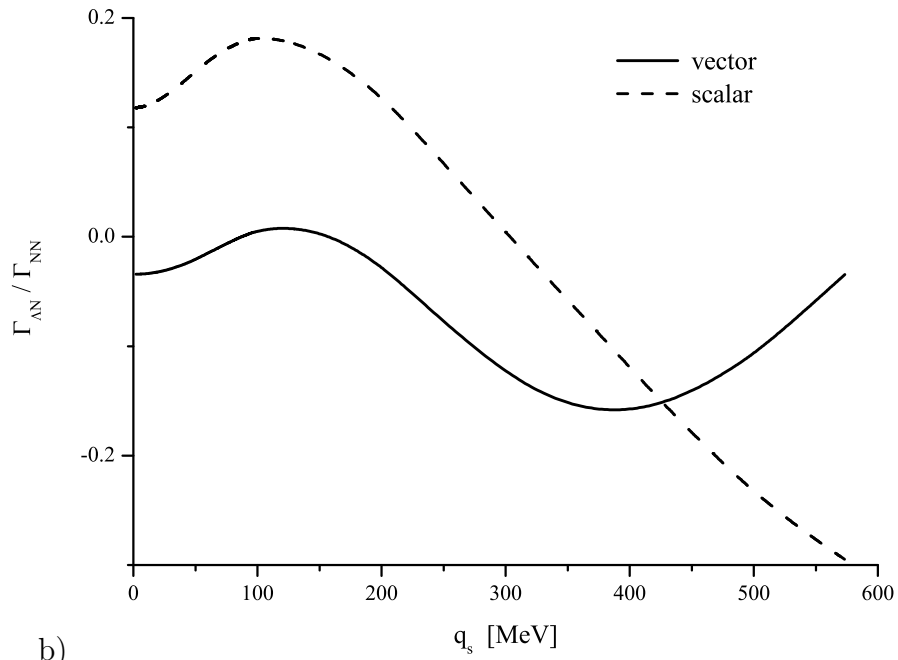
Figure 5.3.: The invariant decompositions of the ΛN and NN interaction are compared. Panel a) shows the invariant amplitudes themselves and panel b) displays the ratios of ΛN and NN amplitudes, which are closely related to the scaling factors of effective interactions, eq.(4.23).
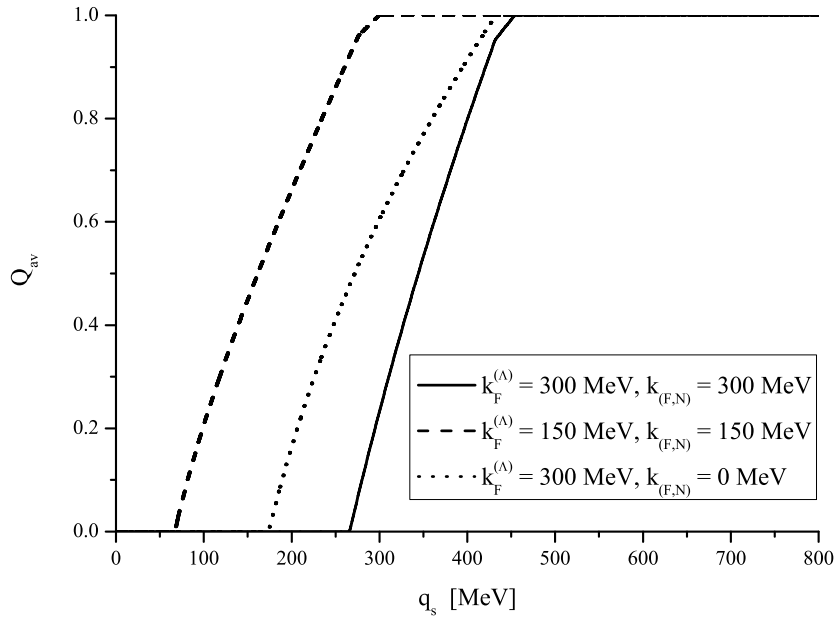
Figure 5.4.: The angle averaged Pauli operator for the different in-mdeium scenarios.

surrounding medium:

$$
\begin{array}{c|cc}
\text{scenario no.} & k_F^{(\Lambda)} & k_F^{(N)} \\
\hline
1 & 300\ MeV & 300\ MeV \\
2 & 150\ MeV & 150\ MeV \\
3 & 0\ MeV & 300\ MeV \\
\end{array}
\tag{5.2}
$$

corresponding approximately to $\rho^{(N)}/\rho^0 \approx 1.4,\ 0.2,\ 1.4$, respectively. The density dependence is accomplished by applying the angle averaged Pauli operator in the scattering equation, as is described in sec. 3.1, but self-energy effects are neglected for this investigation. As average boost $\beta = 0.13$ has been chosen, leaving the particle pair inside the Fermi-sphere for all scenarios. The corresponding angle averaged Pauli operators for the ΛN channel are shown in fig. 5.4. The behavior of Q_{av} is obviously dominated by the larger of the two Fermi momenta. The lower one leads only to slight modifications.

To investigate the effect of the background medium on the ΛN and on the NN interaction let us first focus on the behavior of the respective amplitudes. Fig. 5.5 shows the $^1S_0$ amplitudes, for NN in panel a) and for ΛN in panel b). In the NN interaction scenario 1 and 3 are identical for obvious reasons. Going from lower to higher densities, a suppression of the interaction strength at small momenta is observed. For $k_F = 150\ MeV$ the onset of Pauli blocking, as discussed in sec. 6.2.2 can be nicely seen. The behavior of the ΛN interaction is with respect to the density as well as to the momentum dependence very similar to the NN interaction and seems to be reduced in strength mainly by a constant factor. Even in scenario 3, which is with respect to the conditions imposed by the medium vastly different to the NN scattering, only a slight deviation can be seen. Here the dominance of the larger Fermi momentum, which was found in the angle averaged Pauli operator already, appears again.

a)

b)
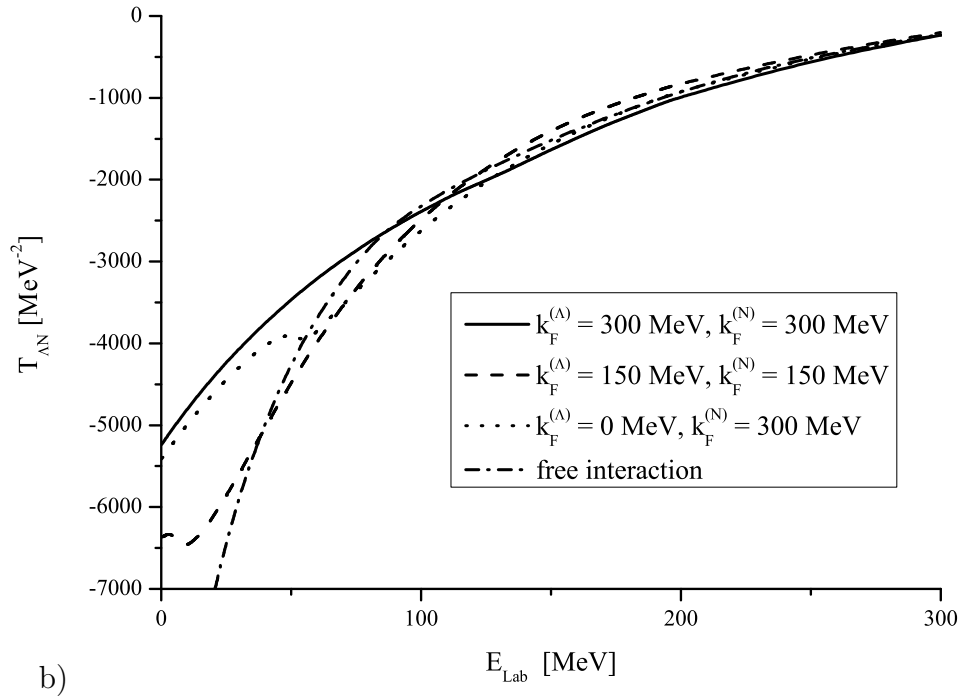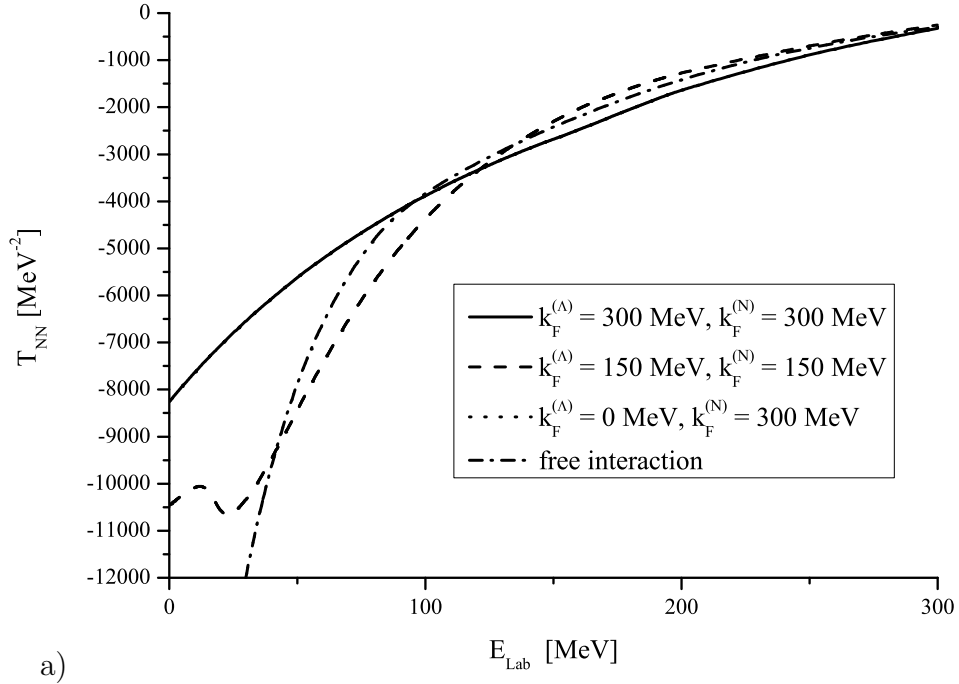
Figure 5.5.: The $^1S_0$ amplitudes of the NN and ΛN interactions are shown for different compositions of the background medium. At low momenta a suppression with respect to the free interaction can be clearly observed.
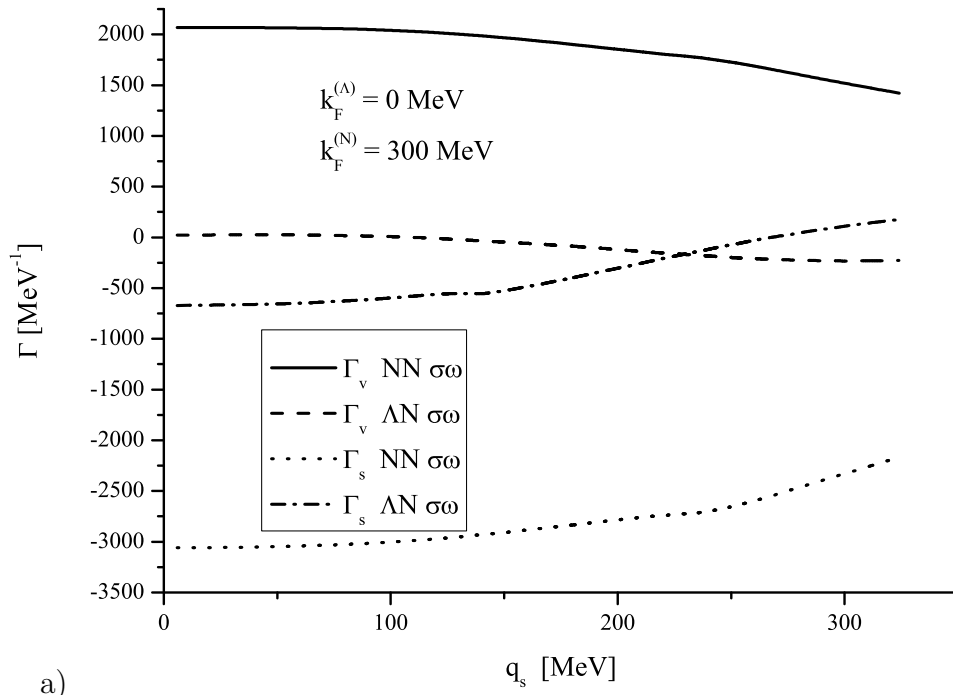
a)
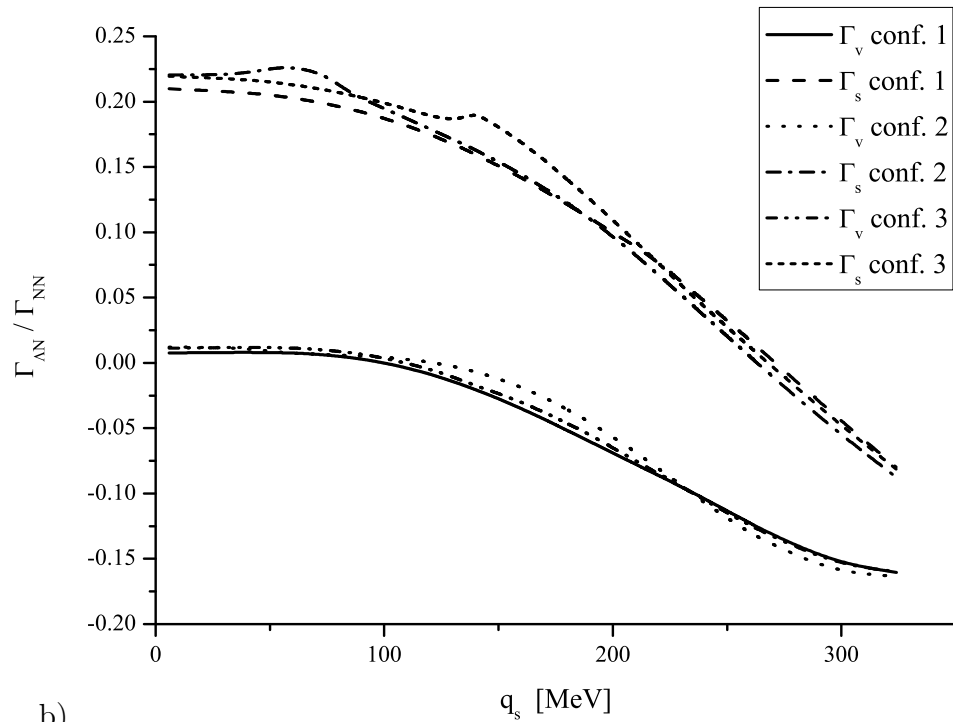
b)

Figure 5.6.: This figure shows the Lorentz components of the effective interactions and their ratios for the different configurations of the medium.

We can make these statements more quantitative by considering the different Lorentz components of the effective interaction, see fig. 5.6. Panel a) compares the ΛN and NN invariants for scenario 3. The ratio between the respective scalar and vector components for all in-medium scenarios are displayed in panel b). Here even less dependence on the different configurations of the medium can be seen than in the amplitudes. Even more, the factor between the ΛN and NN invariants is almost identical to what has been found for free scattering. To obtain the one-body self-energies, an integral over the respective Lorentz components of the interaction is performed, which will smooth most of the small differences in the ratio between ΛN and NN interactions.

5.3. Consequencies

The findings can be summarized as follows:

- The ΛN interaction scales almost exactly with the NN interaction, i.e., The two interactions are approximately related to each other by a constant factor. The scaling is almost independent of the medium.

- The scaling factor is around 0.1, which is far below the scaling factors typically used in hypernuclear calculations.

- The tensor coupling f has almost no influence on the fully iterated interaction and those expected naively from bare SU(3) or SU(6) relations.

So the effective ΛN interaction scales, but not with the SU(3) factors! This may be compared to results we obtained from the extraction of vertex scaling factors by reproducing experimental data using DDRH theory, applied in RMF calculations to hypernuclei. This is described in sec. 8.4. The results obtained with that complementary approach are very similar to what is described above.For the tensor coupling we obtained $f/g = 0$. Also the scaling factor of the σ and the ω vertex turned out to be very small there, values of about 0.25 were found. This is not quite as tiny as the values obtained here, but also considerably smaller than standard scaling factors of effective interactions which are assumed to obey exact SU(3) symmetry. (The deviation may be due to the fact that a simplified interaction was used here).

It seems, that at least when using an interaction with reduced meson spectrum, the effective ΛN interaction scales almost exactly, it is related in very good approximation to the NN interaction by a constant factor. These findings provide an a posteriori numerical justification of the theoretically derived semi-empirical ansatz applied in the calculations of Λ hypernuclei in DDRH theory, as discussed in sec. 4.2.1 and applied in sec. 8 and sec. 9.

6. The Vertex Renormalization Approach

In this chapter we present a new concept for solving the two baryon scattering problem. This method is based on an expansion of the T-matrix in terms of a set of meson exchange operators. This results in scaling factors z_α multiplying the one boson exchange matrix elements, labeled by α, and will in general depend on the three Mandelstam variables s, t and u and on the Fermi momenta $k_{F,i}$. This procedure may be interpreted as a renormalization of the interaction. The factors z_α correspond to a combination of the field strength renormalization, which multiplies the particle field's propagator and a vertex renormalization. From the symbolical solution of the BS equation,

$$T = V + VgT \qquad \longrightarrow \qquad T = \underbrace{(1 - Vg)^{-1}}_{\equiv z} V, \qquad (6.1)$$

it is immediately clear, that an iteration of the infinite ladder series may be interpreted as to introduce a susceptibility that relates the full T-matrix to the kernel by a generalized scaling law.

6.1. Formal developments

Looking back at the discussion about calculating self-energies in sec. 3.1.3, it is obvious, that the T-matrix can be expanded in meson exchange operators, if these include vertex structures corresponding to all covariants. If this is fulfilled we will have in the worst case an over complete basis. In the standard one boson exchange models there is,however, no tensor meson included. Nevertheless, neglecting the tensor interaction should not cause large errors, since the tensor strength of the iterated T-matrix is extremely small anyway (there is no significant contribution due to exchange or iteration). This is found in a decomposition of the scattering matrix into invariants as described in sec. 3.1.2. If $\{V_\alpha\}$ is a set of one boson exchange operators including propagators and vertices, we can express an arbitrary T-matrix, even the exact one, as

$$T = \sum_\alpha z_\alpha(s, t, u, k_F) V_\alpha. \qquad (6.2)$$

By this mapping procedure it is possible to create a connection between arbitrary effective interactions and meson exchange models of the nucleus which use effective microscopic interactions in Hartree approximation, as, e.g., the DDRH theory (see chap. 4). With respect to DDRH theory this treatment is even more advantageous, since it directly

generates the required vertex functionals, so that no detour over the self-energies is necessary as in the procedure described in sec. 4.2.

With the expansion of the T-matrix in terms of a basis of meson exchange operators, eq.(6.2), the calculation of effective interactions is straightforward. Denoting the kernel of the BS equation by K, the scattering equation in terms of the expanded T-matrix, eq.(6.2), is given by

$$\sum_\alpha z_\alpha(s,t,u,k_F)V_\alpha = K + \sum_\alpha \mathcal{P}\int Kgz_\alpha(s,t,u,k_F)V_\alpha \qquad (6.3)$$

for the unknown scaling factors z_α. Solving the BS equation now directly determines the scaling factor z. Although eq.(6.3) holds for arbitrary kernels, the most reasonable choice of K is $K = V$. Eq.(6.3) does, however, not provide any advantages over the original BS equation with respect to solvability the following approximation we find a way to simplify the complicated structure of the BS equation substantially. Chosing an appropriate set of kernel operators V_α, z_α will be in very good approximation independent of t and u. The complex integral equation is transformed in an algebraic equation for z, very similar to eq.(6.1), as $z(s,k_f)$ can be taken out of the integral:

$$\sum_\alpha z_\alpha(s,k_F)V_\alpha = K + \sum_\alpha z_\alpha(s,k_F)\mathcal{P}\int VgV_\alpha. \qquad (6.4)$$

Using the half off-shell T-matrix this system can be easily inverted:

$$
\begin{aligned}
&\sum_\alpha z_\alpha(s,k_F)V_\alpha(q_s,q) = \sum_\alpha V_\alpha(q_s,q) + \sum_\alpha z_\alpha(s,k_F)\mathcal{P}\int d\tilde{q}\, V(q_s,\tilde{q})gV_\alpha(\tilde{q},q) \\
&\Leftrightarrow \sum_\alpha \underbrace{\left(V_\alpha(q_s,q) - \mathcal{P}\int d\tilde{q}\, V(q_s,\tilde{q})gV_\alpha(\tilde{q},q)\right)}_{A_{q\alpha}} \underbrace{z_\alpha(s,k_F)}_{z_\alpha} = \underbrace{\sum_\alpha V_\alpha(q_s,q)}_{B_q}.
\end{aligned}
\qquad (6.5)
$$

q_s is the c.m. relative momentum corresponding to $\sqrt{s}$.

The transformation into a set of algebraic equations for the z_α has, besides easier solvability of the BS equation, another advantage. Since it does not have to be solved for a quantity under the integral any more, one is able to get rid of the partial wave decomposition in solving the scattering equation for an effective interaction. Especially for calculations at finite density there are significant advantages: 1) The full Pauli operator can be used without any problems, we do not have to take an angle averaged one, which preserves the partial wave decomposition. 2) An even bigger advantage arises for the calculation of self-energies. Since the mapping on distinct meson exchange operators, which carry a well defined vertex structure, is implicit in this method, there will be no ambiguities due to under determined inversion schemes for the transformation between different basises of covariant scattering amplitudes.

6.2. A schematic model

To illustrate the vertex renormalization ansatz we will develop a reduced schematic model which is defined by a kernel with a single one boson exchange operator

$$V(\boldsymbol{q}', \boldsymbol{q}) = g^2 \left[(\boldsymbol{q}' - \boldsymbol{q})^2 + m^2\right]^{-1} \tag{6.6}$$

for a boson with mass m. To keep the discussion as transparent as possible, the calculations are done for the uncoupled singlet channel of the lowest partial wave, $^1S_0$, for the scattering of equal mass particles with mass $M.$. The corresponding potential matrix element $^0V^0$ is defined in eq.(1.19). Using that

$$
\begin{aligned}
I_1(q', q) &= \int_{-1}^{1} dt \, [q'^2 + q^2 - 2qq't + m^2] = \frac{1}{2qq'} \log\left[\frac{(q+q')^2 + m^2}{(q-q')^2 + m^2}\right], \tag{6.7}\\
I_2(q', q) &= \int_{-1}^{1} dt \, t[q'^2 + q^2 - 2qq't + m^2] = \\
&\qquad -\frac{1}{qq'} + \frac{q'^2 + q^2 + m^2}{4q'^2q^2} \log\left[\frac{(q+q')^2 + m^2}{(q-q')^2 + m^2}\right], \tag{6.8}
\end{aligned}
$$

the scalar helicity matrix element, eq.(B.20), can be transformed into the partial wave basis by applying eq.(1.8) and the relations of tab. B.2. This yields

$$^0V^0(q', q) = -\frac{g^2}{16\pi^2} \frac{WW'}{M^2} \left[\left(1 + \left\{\frac{qq'}{WW'}\right\}^2\right) I_2(q,'q) - 2\frac{qq'}{WW'} I_1(q', q), \right] \tag{6.9}$$

where $W^{(\prime)} = \sqrt{q^{(\prime)2} + M^2} + M$. Defining now the T-matrix as

$$^0T^0(q', q) \equiv z(q_s) \, ^0V^0(q', q), \tag{6.10}$$

we obtain the BS equation for z

$$z(q_s) \, ^0V^0(q_s, q_s) = \, ^0V^0(q_s, q_s) + z(q_s) \, \mathcal{P} \underbrace{\int dk \, k^2 \, ^0V^0(q_s, k) g^0 V^0(k, q_s)}_{\equiv I_3(q_s)}. \tag{6.11}$$

This can be solved analytically. The q_s dependent scaling factor is then given by

$$z(q_s) = \left[1 - I_3(q_s)/^0V^0(q_s, q_s)\right]^{-1} \tag{6.12}$$

In the model calculation we use the Thompson propagator, eq.(1.55), for equal masses

$$g_{Th}(k, \sqrt{s}) = \frac{M^2}{2E(k)^2} [\frac{1}{2}\sqrt{s} - E(k)]^{-1} = \frac{M^2(\frac{1}{2}\sqrt{s} + E(k))}{2E(k)^2} [q_s^1 - k^2]^{-1}. \tag{6.13}$$

Only the correlation integral has to be solved numerically. This is done using the subtraction method as described in app. F.1.1.
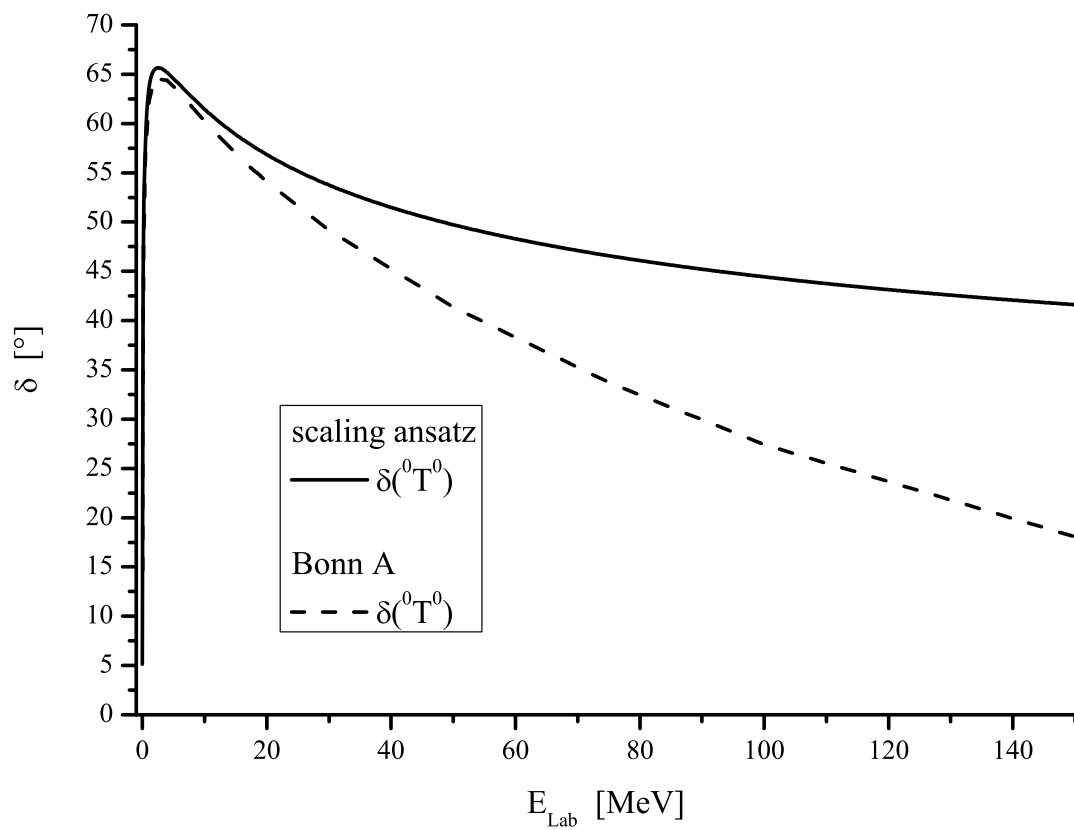
Figure 6.1.: $^0\delta^0$ phase shift in the schematic model as compared to the Bonn A phase shift, which reproduces the experimentally measured one. A matching of the the effective range parameters calculated by the schematic model yields a good agreement in the very low energy region.

6.2.1. Free space scattering

With this model we can now try to mimic at least the very low momentum behavior of the actual NN interaction by adjusting g and m such, that the experimental effective range parameters r and a are reproduced (see sec. 1.4 for the definitions of r and a). Setting the nucleon mass to $M = 939\ MeV$ and cutting the integral off at $\Lambda = 4\ GeV$, we obtain, using

$$m = 173.2\ MeV \tag{6.14}$$
$$g = 2.065, \tag{6.15}$$

the effective range parameters $r = 2.69871\ fm$ and $a = -23.7749\ fm$ as compared to the experimental values $r = 2.75 \pm 0.05\ fm$ and $a = -23.748 \pm 0.01\ fm$. In fig. 6.1 we compare the resulting phase shift with the one calculated by the Bonn A potential, which exactly reproduces experimental data. As expected, only the very low energy range of the schematic model gives a good description of the actual NN potential.

In fig. 6.2 we present the amplitudes of the bare potential V, the full T-matrix and the corresponding phase shifts with respect to the laboratory energy E_{Lab}. An accumulation of strength in the low energy region due to the resummation of all loop diagrams can be observed. The corresponding z-factor is displayed in fig. 6.3. It shows, that besides a strong renormalization of the potential at small momenta, there are almost no more correlations at higher ones. For high laboratory energies the Born terms in the diagrammatic expansion dominate and z goes to 1.

6.2.2. Interactions at finite density

By including the angle averaged Pauli operator, see sec. 3.1.1, in the correlation integral, I_3, medium effect can be studied within our model. The correlation integral has to be generalized to

$$I_3(q_s, k_F, \beta) = \mathcal{P} \int dk\ k^2\ {}^0V^0(q_s, k) g\ Q_{av}(k, q_s, k_F, \beta)\ {}^0V^0(k, q_s) \tag{6.16}$$

To avoid evaluating the correlation integral for all values of β allowed in the Fermi sphere, an average β, defined by

$$\overline{\beta}(k_F) = \frac{\int_0^{k_F} d^3k\ |\boldsymbol{\beta}(\boldsymbol{k})|}{\int_0^{k_F} d^3k}, \tag{6.17}$$

is used, similar to the prescription used in [Horowitz87].

The scattering matrix depends now on two parameters, the on-shell momentum q_s and the Fermi momentum k_F. The whole structure of the resulting scaling factor z is displayed in fig. 6.4. The bump one sees, starting from the origin, has its maximum at $q_s = k_F$. It arises, because the correlation integral I_3 becomes comparable in size or even larger than ${}^0V^0$, leading to a small denominator in eq.(6.12). The strong correlation arises, since, loosely spoken, the step of the Pauli operator lies exactly on top of the pole in the two baryon propagator and cuts away half of it. For a sharp step, i.e., at $\beta = 0$, a logarithmic divergence arises in I_3. For finite β only a bump remains at $q_s = k_F$,
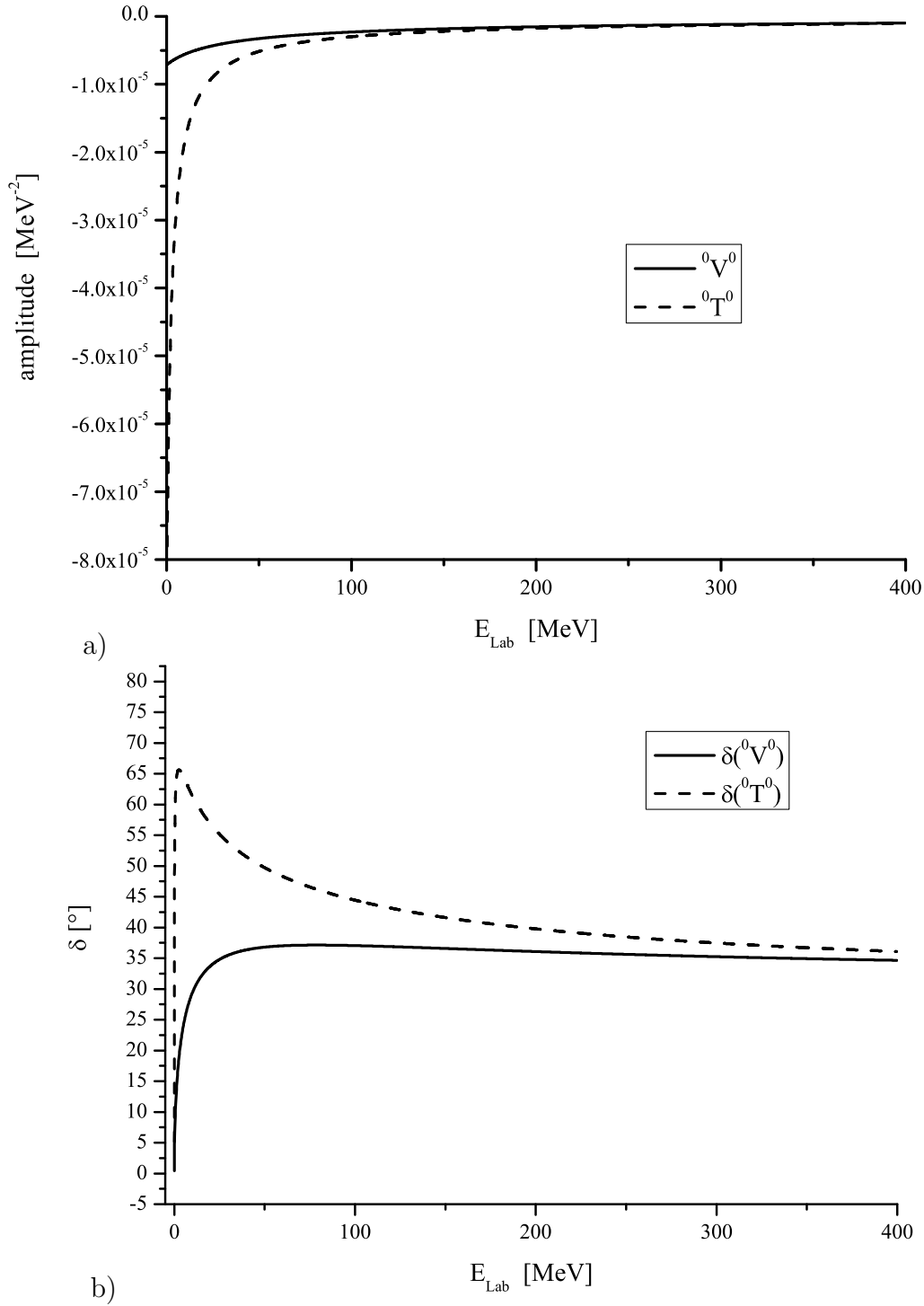
Figure 6.2.: This figure compares the bare and fully iterated interaction in terms of the amplitudes and phase shifts. It can be seen, that strength is redistributed into the low energy region, while with increasing energy the first order Born diagrams dominate. Similar to the exact nucleon-nucleon interaction, the iterated interaction is almost resonant at very low energies.
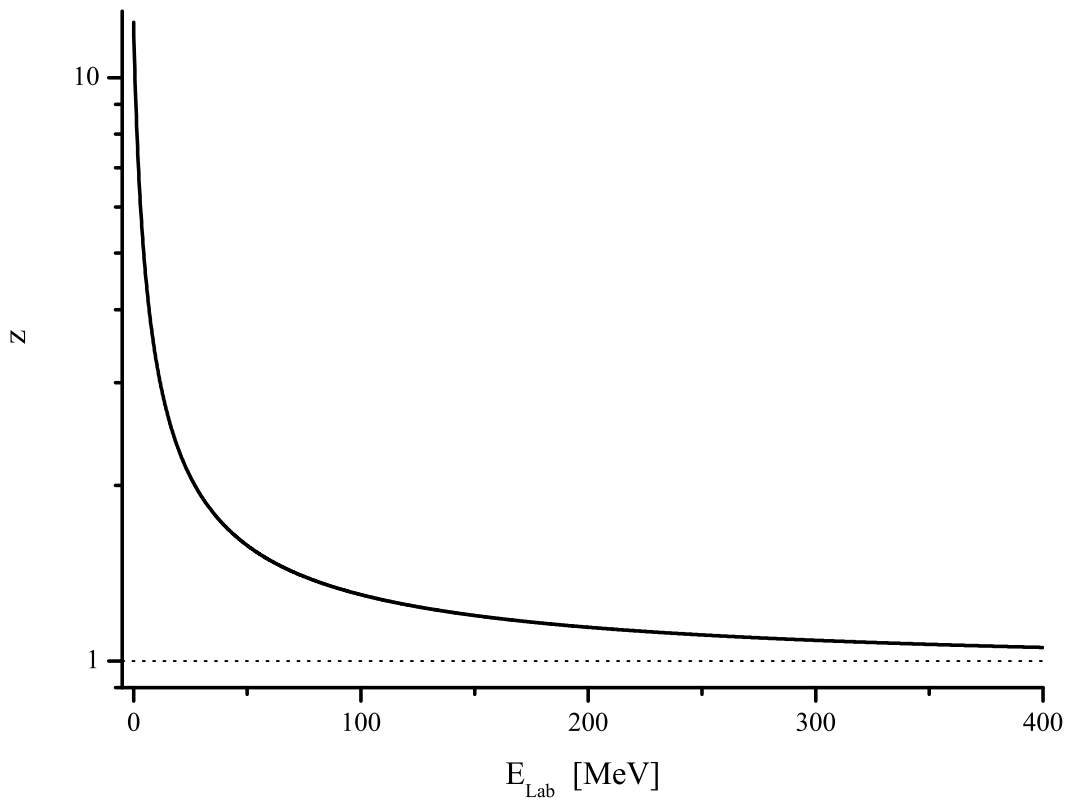
Figure 6.3.: The vertex factor shows a strong effect of the iterated one boson exchange, which gets weaker at higher energy. In the high energy limit the Born graph solves the BS equation, indicated by $z = 1$.
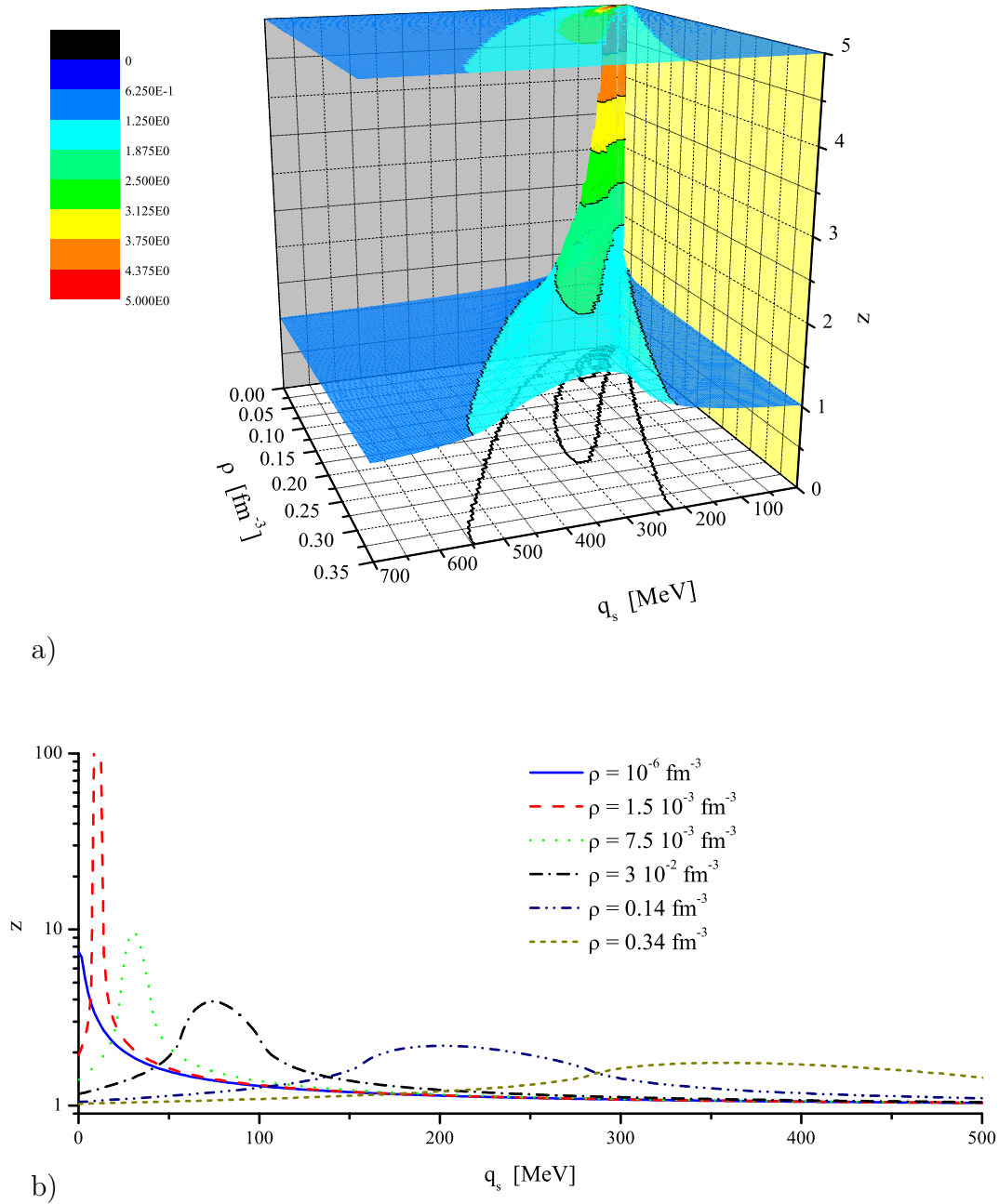
Figure 6.4.: The scaling factor z is at finite density a function of the on-shell momentum and the density. When the on-shell momentum equals the Fermi-momentum the correlation integral gets very strong, leading to the bump in the surface. At very low density it gets, due to almost vanishing β even so large, that a resonant structure appears. In panel b) cuts of the surface at constant ρ are shown, clarifying the details which cannot be seen in panel a). The top of panel a) shows a projection of the contours.

which gets smaller with increasing β, since the step gets washed out. Since an average β, growing with k_F, is used, the effect of a smoother step with increasing density is reflected in the decreasing height of the pronounced structure in fig. 6.4. At very low densities the correlation integral is so strong, that a pole appears. For vanishing density z is again a regular function of q_s, as is known from above, since the pole is suppressed by the q^2 factor of the integral measure. The described behavior of the scaling factor can be seen in the constant-ρ cuts of of fig. 6.4, which are displayed in panel b).

Since the major part of the dynamics in a baryonic medium is governed by processes around the Fermi-surface, it is worthwhile to investigate in some more detail the behavior of the scattering matrix at $q_s = k_F$. This follows exactly the to of the bump in the surface plot of fig. 6.4. In the phase shift one can easily recognize the resonances at low energy. Comparing the scaling factor to the density dependent vertex functionals in DDRH, as shown for example in fig. 4.1, one finds a convincing agreement of the functional form.

6.3. Discussion of the vertex renormalization

The vertex renormalization method provides a new concept in the techniques for solving relativistic scattering equations. As indicated by a mapping of the full Bonn A T-matrix onto a meson exchange kernel, presented in [Lenske04], and by the reasonable behavior of the calculated scattering amplitudes in our schematic model, it seems to be a real alternative for solving the BS equation. Besides a fairly easy solvability as compared to the 3D reduced BS equation, there is the advantage, that no more partial wave decomposition is needed. This allows then, e.g., to use the full Pauli projection operator, which is not possible in a partial wave scheme. Due to the implicit mapping of the interaction on a meson exchange kernel, the ambiguities in a decomposition for evaluating self-energies is no longer present.

There are, however, also some point, that will have to be considered in some more detail. A possible problem becomes apparent, when the scattering amplitude possesses resonances. Since these are of definite angular momentum, the z-factor, having no angular dependence, cannot account for them correctly. This problem arises due to the approximation that z depends only on s and k_F. As described above, solving the scattering problem for a kernel of more than one elements, the off-shell information of the T-matrix is needed. It is assumed there, that z does not depend on the off-shellness, which should also be checked in future works on this concept.
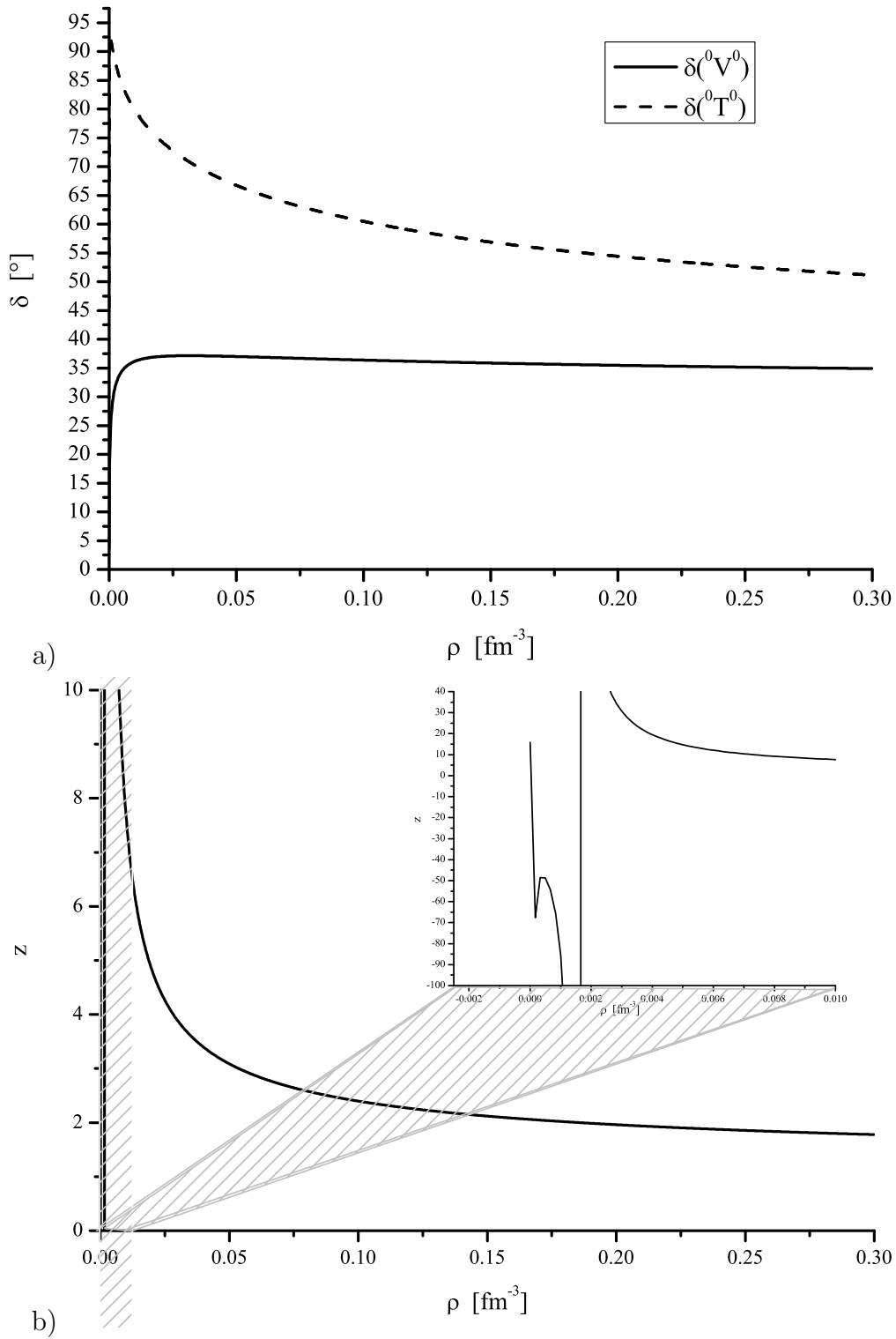
Figure 6.5.: The influence of Pauli blocking is studied in these figures. Panel a) shows the scattering phase shift of the full scattering matrix as compared to the one of the bare potential. The dependence on ρ has to be understood such, that $q = k_F$. In panel b) the vertex renormalization is shown. It nicely coincides with the shape of the vertex functionals used in DDRH, see fig. 4.1.

Part II.

Hypernuclear Structure

7. Hypernuclear Physics

The field of hypernuclear physics was started by the observation of a "strange" event in a balloon based cosmic ray emulsion experiment [Danysz53], where a nuclear decay had been observed which could not be explained by standard nuclear physics known at that time. An explanation of this event was found in the decay of a Λ hyperon, which must have been produced by cosmic rays, inside a normal nucleus. Triggered by the first curiosity, it turned out that hypernuclei are excellent laboratories to study all kinds of nuclear and hadron physics effects related to strangeness in a nuclear environment.

Although the Λ couples weakly to the nucleus, it is still bound. Since there is in addition no Pauli blocking for the Λ, it qualifies as a quasi non-invasive experimental probe of the nucleus, in which it is embedded. From the theoretical side hypernuclei are also very interesting objects to study, since they are an extension of the isospin systematics into the strangeness $S \neq 0$ regime and thus a tool to probe the validity of SU(3) symmetry for the baryon-baryon couplings. Since one expects a global systematics of baryon baryon interactions, their understanding will also help, e.g., in the modeling of nuclei far off stability, for which the coupling mechanisms may not be accessible experimentally. Knowing, however, the global features, it will also reduce the ambiguity in the description of dripline nuclei.
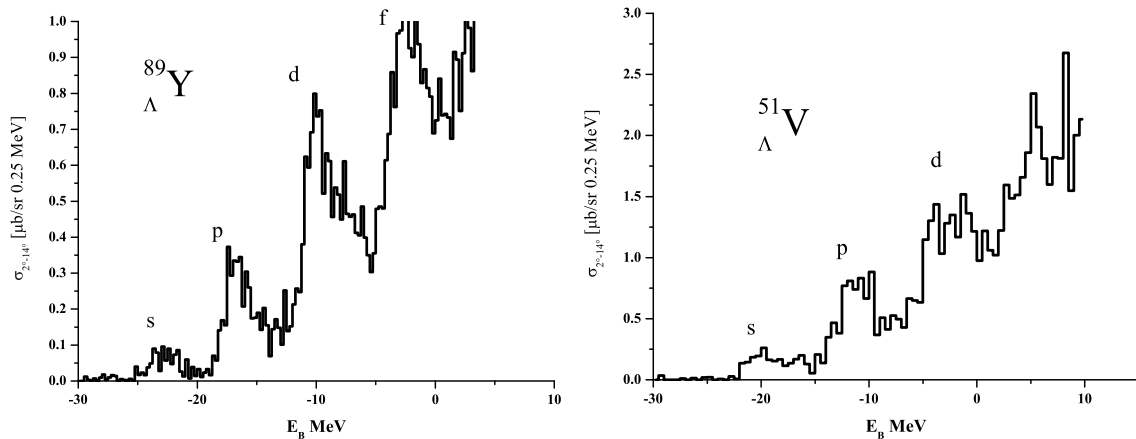
Figure 7.1.: Hypernuclei show down to the s-shell a very clean single particle excitation spectrum. In contrast to the single particle spectra of normal nuclei, in which only the lowest excitations show single particle nature due to strong correlations, the Λ hyperon moves freely in a mean-field, generated by the surrounding nucleus. The figure shows recent $\pi^+(A, _\Lambda A)K^+$ spectra [Hotchi01], obtained in pion induced production of hypernuclei (see sec. 7.1).

In hypernuclear experiments it was soon found, that Λ hypernuclei exhibit an impres-

sive single particle structure of the Λ spectrum as is displayed in fig. 7.1. In the most recent experiments, besides a sharp 1s peak even the spin-orbit splitting can be seen down to the p-shell (see sec. 8). From this observation it can be concluded, that the Λ hyperons occupy almost ideal quasi-particle configurations, produced by the surrounding nucleus. The presence of sharp single particle peaks even at central nuclear density also answers a long standing question about the correct degrees of freedom in nuclear physics: The relevant structures are still the baryons, not the quarks. If the Λ would dissolve at densities below nuclear saturation density already, no s-shell single particle peak or anything like that could appear in experiments.

Another congestion concerning the appropriate degrees of freedom for multibaryon states, especially those involving strangeness, are the strangelets. These quasi-hadronic multi-quark systems, for which the baryon bag model provides some evidence of their actual existence, may, at least theoretically, be the actual ground state of hadronic matter. The argument goes such, that the total energy of a bag of n up, down and strange quarks may be less, than the total energy of a bound hadronic system made up from $n/3$ baryons. Opening a new Fermi-well with the appearance of strange quarks could overcompensate its higher mass by a gain in kinetic energy. The lightest proposed strangelet is the H dibaryon [Jaffe77], a system, which is, concerning its quark content, equivalent to the $\Lambda\Lambda$ system. Thus the observation of double Λ hypernuclei provides direct access to observables, which can prove or disprove the existence of the H. The most recent high precision experiments preformed at KEK (see sec. 7.1) do not provide any evidence for its existence, but can neither rule it out.

A different ground state of baryonic matter from that observed in nuclei, which undoubtedly exists in nature, is hypermatter. When exceeding nuclear saturation density, the appearance of hyperons becomes favorable at some point. That this is not a purely theoretical game is known from astrophysics of compact starts. What is known as neutron stars, and for a long time – even until now – was treated as such, are rather hyperstars, consisting of a mixture of nucleons and hyperons in β equilibrium [Hofmann01a, Schaffner-Bielich00], the heavier ones probably even with a quark matter core [Schertler00]. For the understanding of these compact stellar objects the input of hypernuclear physics is indispensable, since there we find hyperons embedded in a baryonic medium and can study their interactions.

7.1. Hypernuclear experiments

The most common way to produce and study hypernuclei experimentally is by meson induced strangeness exchange or strangeness production reactions on a nuclear target, combined with a missing energy spectroscopy. A sketch of this process is displayed in fig. 7.2. A π^+ or K^- beam of defined energy is shot onto a target, in which it converts a neutron into a Λ hyperon by turning itself into K^+ or π^-, respectively. The elementary processes on the quark level are

$$\pi^+(u\bar{d}) + n(udd) \quad \longrightarrow \quad K^+(u\bar{s}) + \Lambda(uds) \tag{7.1}$$

$$K^-(\bar{u}s) + n(udd) \quad \longrightarrow \quad \pi^-(\bar{u}d) + \Lambda(uds) \tag{7.2}$$
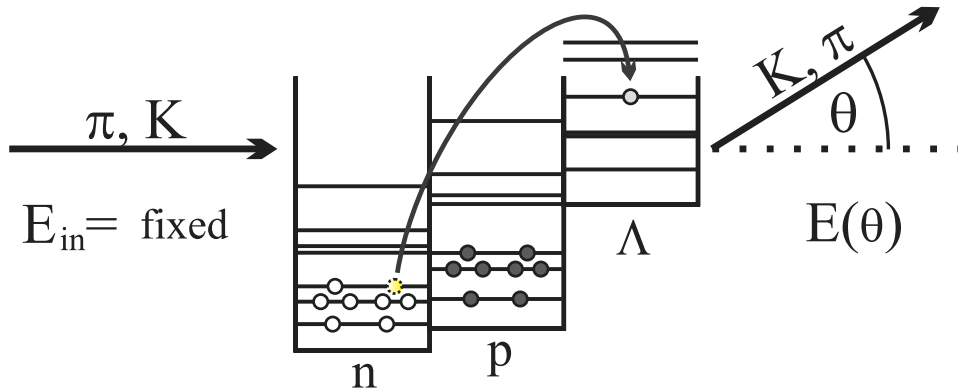
Figure 7.2.: In the mesonic production of hypernuclei a pion (kaon) beam of defined energy is shot onto a nuclear target. On a neutron the meson is scattered inelastically converting it into a Λ hyperon. The outgoing kaon (pion) is then sent through a spectrometer in which a missing energy measurement is performed.

The outgoing debris is searched for kaons or pions of which the momentum is then determined in a spectrometer. The energy of the outgoing kaon is given by

$$E_K = E_\pi + \underbrace{(-|B_n| + M_n)}_{n \text{ anihil.}} + \underbrace{(|B_\Lambda| - M_\Lambda)}_{\Lambda \text{ prod.}}, \tag{7.3}$$

where B is the binding energy of the respective baryon and M is its mass. Gating now on $-30 \, MeV < B_\Lambda < 5 \, MeV$ the whole region of bound Λ states is recorded. According to eq.(7.3) one would have to somehow determine the quantum numbers of the neutron hole in the exit channel. In the actual analysis of such experimental data, it is, however, assumed, that the core nucleus remains in the ground state, i.e., the elementary reactions, eq.(7.1) and eq.(7.2), occur on the valence neutrons only. Therefore

$$- B_\Lambda = M \left({}^{A-1}Z \right) + M_\Lambda - M \left({}^{A}_{\Lambda}Z \right). \tag{7.4}$$

Though this assumption seems wild, the experimental data, showing sharp peaks, seem to support it, see fig. 7.1,

Experiments of this type have been performed at CERN, BNL and KEK (e.g. [Hotchi01, Nagae01, Hasegawa96, Ajimura95, Pile91]). The only remaining active facility which still produces high resolution spectra, see, e.g., [Hotchi01], is the SKS spectrometer at KEK.

Kaon spectrometers, as the SKS, have an energy resolution which is at best slightly below 2 MeV. This is, compared to the typical level spacing in hypernuclei, insufficient. As an improvement, electroproduction experiments of hypernuclei have been started at JLAB [Tang01, Dohrmann]. The elementary reaction

$$e + p(uud) \quad \longrightarrow \quad e' + \Lambda(uds) + K^+(u\overline{s}) \tag{7.5}$$

has two outgoing particles which need to be measured. With an upgrade of their spectrometers the JLAB collaborations promis a resolution of 350 keV and better, which

would be a big step forward. Similar experiments are in preparation at the MAMI-C facility in Mainz.

The state of the art technique in nuclear spectroscopy is to use germanium gamma detectors. This has also been applied in recent experiments to study de-excitations of Λ hypernuclei, supplementing the meson induced spectroscopy. In experiments at KEK and BNL resolutions have been reached as good as several keV, see e.g. [May97, Kohri02]. In these experiments a wealth of information on the fine structure of light hypernuclei has been obtained. In particular a very small spin-orbit splitting has been found for the Λ levels. The spin-orbit splitting problematics in Λ hypernuclei is discussed in detail in sec. 8. A complementary approach to spectroscopy on the internal structure of hypernuclei is the measurement of neutrons, emitted in coincidence with a transition of a Λ inside the hypernucleus. A resolution for the neutron spectroscopy of better than 50 keV is projected for the JLAB experiment [Margaryan00]. It is especially for intermediate and high mass hypernuclei an alternative to γ spectroscopy, because a fairly huge background of gammas has to be expected in these mass regions. The hypernuclear Auger effect is described in detail and discussed with respect to our model calculations in sec. 9.

In the search for double Λ hypernuclei, as e.g. at KEK, the production goes via an intermediate Ξ state,

$$K^-(\overline{u}s) + p(uud) + p(uud) \quad \longrightarrow \quad K^+(u\overline{s}) + \underbrace{\Xi^-(dss) + p(uud)}_{\longrightarrow \quad \Lambda(uds) + \Lambda(uds)} \tag{7.6}$$
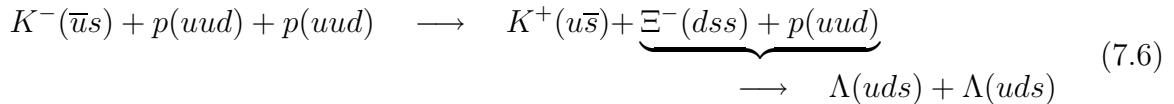
Since the Ξ is produced with a large momentum, it first has to travel through the target before it is captured by a nucleus, which then turns into a double Λ hypernucleus. From the BNL a mass production of $^6_{\Lambda\Lambda}$He was reported [Ahn01], which, however, revealed not much more than the existence of that double Λ hypernucleus. In a very complicated experiment at KEK an electronic tracking and emulsion hybrid detector was used for the exact reconstruction of the production of double Λ hypernuclei [Takahashi01]. One single double Λ hypernucleus was found, again a $^6_{\Lambda\Lambda}$He, from which the $\Lambda\Lambda$ correlation energy could be extracted. For the GSI future facility FAIR the production of double Λ hypernuclei by a $\overline{p}p \to \overline{\Xi}\Xi$ reaction is proposed. The double Λ hypernucleus will then be implanted in a scintillator for a subsequent spectroscopy of de-excitations and decay.

7.2. Hypernuclear theory

The theoretical description of hypernuclei is a strong domain of RMF models for a long time, since these relatively simple calculations yield very good results due to the excellent mean-field characteristics of hypernuclei, as discussed in the previous sections. Also shell model calculations were applied, see, e.g., [Millener01], which are, however, numerically quite involved and rely on the knowledge of two-body mtrix elements involving one or two hyperons. In the meson exchange RMF models the structure of all sorts of hypernuclei, Λ, Σ and multiple strange systems, were studied and the description of data is excellent [Rufa87, Rufa90, Vretenar98, Marcos98, Glendenning93].

A great disadvantage of these RMF models is its use of effective couplings which are largely unknown. In all these calculations SU(3) relations have been applied, which, however, deserve a closer inspection and independent justification, as these are only well defined for the bare couplings, the parameters of the Lagrangian (see the discussion in sec. 9.3). Our own microscopic DDRH approach to hypernuclei [Keil00], that partly cures these problems,will be presented in sec. 4.2.1.

All modern microscopic approaches to hypernuclear structure in the literature are based on the Nijmegen YN interaction models [Rijken99, Stoks99]. Especially several japanese groups are very active in that field, modeling light hypernuclei in different coupled cluster approaches [Hiyama03, Hiyama02, Nemura02, Hiyama00]. Very good results are obtained in these calculations in comparison to data. These models rely, however on an inert cluster structure of the hypernuclei. Besides this, the interaction between clusters themselves and between clusters and hyperons has to be generated in an additional step from the microscopic interaction. These are calculated usually from a phase shift equivalent, separable representation of the original meson exchange potential. Especially for reproducing the spin-orbit splitting, additional interactions have to be introduced, sometimes motivated by quark models. Calculations for light single and double hypernuclei ($a \leq 4$)which are very similar in spirit to the ones just described have been performed in the Fadeev-Yakubovsky framework [Filikhin04, Filikhin02, Nogga02].

Meanwhile also ab initio calculations of light hypernuclei, also based on the Nijmegen potentials, exist, including explicitly the Σ as intermediate state [Nemura02]. In the calculations of $^{5}_{\Lambda}$He it was found, that not only the $\Lambda\Sigma$ mixing plays a important role in leading to a stronger binding, but also the ^{4}He core is substantially affected by the presence of the Λ.

8. Spectra of Hypernuclei with High-Spin Core States

The quality of hypernuclear spectroscopy has significantly improved in the past years, allowing to extract informations on the underlying baryon-baryon interaction on a much more precise level than before. Recent data published from a KEK SKS experiment [Hotchi01] showed Λ single particle peaks in intermediate mass hypernuclei being broader than the experimental resolution. As an explanation the collaboration suggested a fairly large spin-orbit splitting of 1–2 MeV, which is in contrast to experiments performed on, e.g., $^{13}_{\Lambda}$C [Kohri02] that found a Λ 1p shell splitting of 152±90 MeV. Trying to reproduce the extracted Λ excitation spectrum within DDRH calculations by adjusting the $\Lambda\omega$ and $\Lambda\sigma$ coupling constants, the spectral structure turned out to be incompatible with the dynamical model used in our calculations. As a possible source for the conflicting results we have investigated to what extent the Λ spectra are affected by a non-vanishing core spin. This is a particular problem in the popular cases $^{89}_{\Lambda}$Y and $^{51}_{\Lambda}$V, in which the nuclear cores carry ground-state spins of $J^{\pi} = 4^{-}$ and $J^{\pi} = 6^{+}$, respectively [NNDC]. For a further more detailed analysis we took the extremely high core spin[1] of the hypernuclei $^{89}_{\Lambda}$Y and $^{51}_{\Lambda}$V ($J^{\pi} = 4^{-}, 6^{+}$, respectively) into account in a reanalysis of the measured Λ spectrum. This is described in sec. 8.3. It turns out, that the s.o. splitting extracted this way is consistent with the $^{13}_{\Lambda}$C data.

The small spin-orbit splitting suggests, that the tensor interaction, which is required by SU(6) symmetry and reduces the spin-orbit splitting, is at work. Using DDRH calculation, we also tried to reproduce the new spectrum by taking also into account the tensor force, see sec. 8.4, which now works perfectly. It was, however, found, that the tensor force does not play any role!

8.1. The conventional data analysis

In an experiment at the KEK-SKS kaon spectrometer Hotchi *et al.* [Hotchi01] performed a missing energy spectroscopy in the $A(\pi, K)_{\Lambda}A$ reaction, see sec. 7. As targets ^{89}Y and ^{51}V were used, the experimental spectra are displayed in fig. 8.4.

Since the width of the orbital angular momentum shell peaks are broader than the experimental resolution of 1.65 MeV with an increasing width of the peaks for increasing orbital angular momentum, they attributed this to spin-orbit splitting. However, the reliability of this assumption is worth to be discussed. To extract the actual single particle spectrum the following ansatz was chosen: The s-shell peak was modeled by a single

---

[1]With core spin we denote the ground state spin of the strangeness-free core nucleus.

Gaussian, the other orbitals by two gaussians. As width the experimental resolution was taken; the center positions of the Gaussians and the weights were left open. This yields

$$F_1(E) = a_0 G(E - b_0, \sigma_{Exp}) + \sum_l \left(a_l^L G(E - b_l^L, \sigma_{Exp}) + a_l^R G(E - b_l^R, \sigma_{Exp}) \right) \quad (8.1)$$

with the normalized Gaussian

$$G(x, \sigma) = \frac{1}{\sigma\sqrt{2\pi}} \exp{-\frac{x^2}{2\sigma^2}} \quad (8.2)$$

The background between the peaks was interpreted as resulting from core excitations, which should in principle produce a shifted image of the original spectrum with reduced strength, but was only accounted for by additional Gaussian functions filling the gaps

$$F_2(E) = A_0 G(E + \delta B - b_0, \sigma_{Exp}) + \sum_l A_l G(E + \delta B - b_l, \sigma_{Exp}) \quad (8.3)$$

As shift they determined $\delta B = 4.18 \pm 0.07 \ MeV$ for $^{89}_{\Lambda}$Y and $\delta B = 3.3 \pm 0.2 \ MeV$ for $^{51}_{\Lambda}$V. The fit results are displayed in tab. 8.1.

E [MeV]	$^{89}_{\Lambda}Y$	$^{51}_{\Lambda}V$
$1s_{1/2}$	23.11 ± 0.10	19.97 ± 0.13
$1p_{3/2}$	17.10 ± 0.08	11.90 ± 0.17
$1p_{1/2}$	15.73 ± 0.18	10.57 ± 0.15
$1d_{5/2}$	10.32 ± 0.06	3.55 ± 0.14
$1d_{3/2}$	8.69 ± 0.13	1.55 ± 0.11
$1f_{7/2}$	3.13 ± 0.07	
$1f_{5/2}$	1.43 ± 0.07	

Table 8.1.: Single particle energies of $^{89}_{\Lambda}$Y and $^{51}_{\Lambda}$V as extracted by Hotchi *et al.*.

8.2. Hyperon-nucleon coupling constants in medium-mass nuclei

In sec. 4.3 we discussed the systematics of RMF for single Λ hypernuclei. Following that discussion, we are now able to unambiguously fix the scaling factors R_σ and R_ω since the experimentally obtained spectra contain all the necessary fine structure.

To determine the scaling factors R_σ and R_ω from the data, we used a χ^2 procedure, minimizing the sum over the squared deviation of calculated single particle energies E_i^{th} from experimental single particle energies E_i^{ex}, weighted by the inverse square of the respective experimental error ΔE_i^{ex}

$$\chi^2(R_\sigma, R_\omega) = \sum_i \left(\frac{E_i^{ex} - E_i^{th}(R_\sigma, R_\omega)}{\Delta E_i^{ex}} \right)^2 \quad (8.4)$$

It turns out, that R_σ and R_ω are very strongly and exactly linearly correlated. Away from this "valley of best fit" in the R_σ–R_ω plane, the χ^2 value rises instantaneously by orders of magnitude. It is therefore sufficient to keep the following discussion and figures restricted to the behavior of the single particle spectra with respect to R_ω.
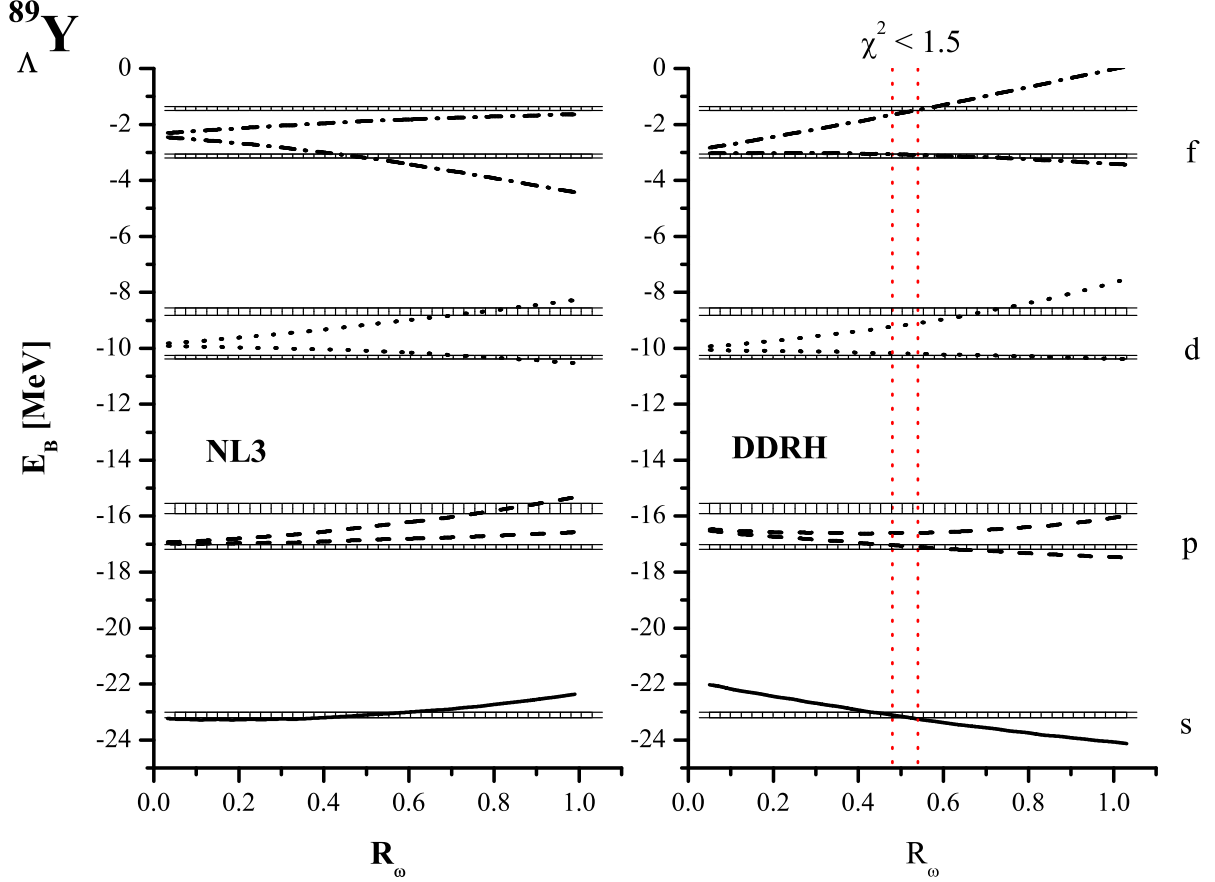
Figure 8.1.: This figure shows the attempt to reproduce the single particle energies of $^{89}_{\Lambda}$Y as deduced by [Hotchi01] from their experimental data in DDRH calculations by adjusting the σ and ω coupling constants. The spectrum extracted by Hotchi *et al.* (ladder lines; the width of each line gives the respective experimental error) obviously has a different systematics in level spacing as compared to our calculations (solid lines). Neither the DDRH nor the NL3 model is able to describe the data.

Trying to fix the scaling factors with respect to the "experimental" spectra, it turned out that neither the gross structure of the spectra, given by the centroids of the spin-orbit doublets, nor their fine structure could be satisfactorily explained in RMF calculations. Calculations have been performed with the DDRH model and also with the phenomenological NL3 model [Lalazissis97], where the latter did even worse. Fig. 8.1 shows the evolution of the Λ single particle spectra with respect to R_ω in comparison to the $^{89}_{\Lambda}$Y data. For the DDRH calculations we show a region in the figure in which $\chi^2 < 1.5$ was obtained, for NL3 we get everywhere $\chi^2 > 3$. Although these numbers do not seem too

bad, the description of the inter-level spacings is completely off. The analysis of Vanadium revealed even poorer results concerning the structural description (The χ^2 are low due to a larger error.). The total finding is shown in tab. 8.2.

$^{89}_{\Lambda}$Y	$R_\sigma(\chi^2_{min})$	$R_\omega(\chi^2_{min})$	χ^2_{min}	$^{51}_{\Lambda}$V	$R_\sigma(\chi^2_{min})$	$R_\omega(\chi^2_{min})$	χ^2_{min}
DDRH	0.51	0.57	1.3	DDRH	0.70	0.81	0.6
NL3	0.55	0.58	2.9	NL3	0.47	0.49	4.9

Table 8.2.: Results of the determination of coupling constants from the original data.

8.3. Reexamination of $^{89}_{\Lambda}$Y and $^{51}_{\Lambda}$V data

Looking more closely at the known substructure of the two hypernuclei, one finds that the core spin is huge. As core nuclei we have ^{88}Y with $J^\pi = 4^-$ and ^{50}V with $J^\pi = 6^+$. Obviously one needs to examine to which extent the high-spin core-states will affect the Λ single particle spectrum. We model the spin dependent part of the interaction
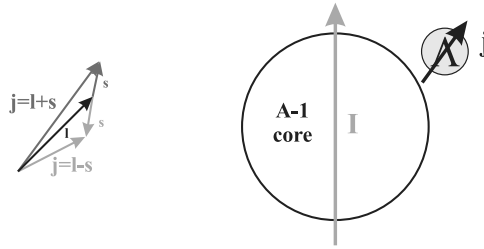
Figure 8.2.: The hypernuclei $^{81}_{\Lambda}$Y and $^{51}_{\Lambda}$V have a rather high core spin of $J^\pi = 4^-$ and 6^+. This leads to an additional splitting of each spin-orbit level, $j = l + 1/2$ and $j = l - 1/2$, proportional to $\boldsymbol{I} \cdot \boldsymbol{j}$, or, if insufficiently resolved, to a broadening of the peaks.

Hamiltonian describing such a system by the following intuitive and simple ansatz:

$$H_j = E_{ls}\boldsymbol{l} \cdot \boldsymbol{s} + E_{Ij}\boldsymbol{I} \cdot \boldsymbol{j} \tag{8.5}$$

which accounts for the Λ-core interactions by a spin-spin interaction. Above, $\boldsymbol{l}$, $\boldsymbol{s}$, $\boldsymbol{j}$ are, respectively, orbital angular momentum, spin and total angular momentum of the Λ state and $\boldsymbol{I}$ denotes the spin of the nuclear core. It is assumed that on top of the usual spin-orbit interaction with a constant interaction matrix element E_{ls} we have an interaction between the single particle state's total angular momentum and the core spin, also with a constant matrix element E_{Ij}. If this assumption is reasonable, it should turn out that the latter is a lot smaller than the spin-orbit interaction matrix element, as is found in other systems.

Following [Hotchi01] we model the broad single particle peaks by a superposition of two Gauss functions. However, in our case we correlate these two gaussians by constraints obtained from the assumed spin dependent matrix element of the interaction Hamiltonian, eq.(8.5):

$$\langle E_j \rangle = E_{ls} \langle \boldsymbol{l} \cdot \boldsymbol{s} \rangle + E_{Ij} \langle \boldsymbol{I} \cdot \boldsymbol{j} \rangle \tag{8.6}$$
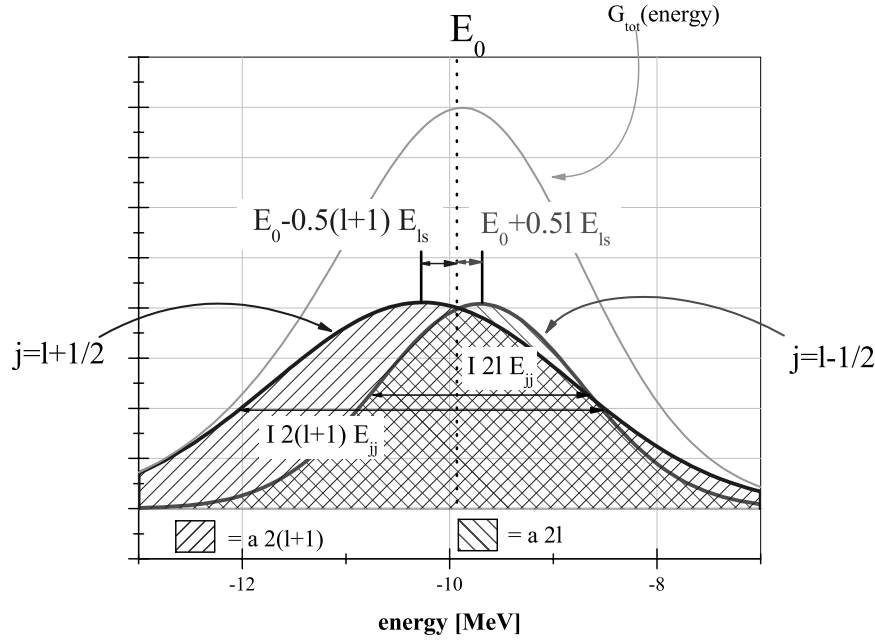
Figure 8.3.: Model construction of an unresolved spin-orbit split single particle peak in which the individual doublet states are broadened due to interaction with the core spin. The relative strength of the peaks is fixed by their degeneracy $2j + 1$.

We shall attribute the spacing of the two Gaussians to the spin-orbit splitting, whereas their width is fixed by the Ij interaction. Using the normalized gaussian, eq.(8.2), we obtain for the description of the spectral structure produced by an angular momentum doublet

$$G_l(x) = \ 2(l + 1)\ G(x - E_{l+}, \sigma_{l+}) + 2l\ G(x - E_{l-}, \sigma_{l-}) \tag{8.7}$$

The relative weights of the two Gaussians are fixed by the degeneracy factors $2j + 1$ of the $j = l + 1/2$ and $j = l - 1/2$ states, denoted by l^+ and l^-, respectively in eq. (8.7). The energies of the l doublet are according to eq. (8.6) given by

$$E_{l+} = E_l - E_{ls}\frac{1}{2}(l + 1); \qquad E_{l-} = E_l + E_{ls}\frac{1}{2}l, \tag{8.8}$$

where $\langle \boldsymbol{l} \cdot \boldsymbol{s} \rangle$ is evaluated through

$$\langle \boldsymbol{j}^2 \rangle = \langle (\boldsymbol{l} + \boldsymbol{s})^2 \rangle = \langle \boldsymbol{l}^2 \rangle + \langle \boldsymbol{s}^2 \rangle + 2 \langle \boldsymbol{l} \cdot \boldsymbol{s} \rangle$$
$$\Leftrightarrow \langle \boldsymbol{l} \cdot \boldsymbol{s} \rangle = \frac{1}{2}\left(j(j + 1) - l(l + 1) - s(s + 1) \right) \tag{8.9}$$

The width of the gaussians is fixed according to the spin-spin matrix element as

$$\sigma_{l+} = E_{Ij}2I(l + 1); \qquad \sigma_{l-} = E_{Ij}2Il \tag{8.10}$$

The expectation value $\langle \boldsymbol{I} \cdot \boldsymbol{j} \rangle$ is evaluated in analogy to eq.(8.9). According to our assumptions E_{ls} and E_{Ij} are the same for each orbit. Furthermore, the elementary

matrix elements E_{ls}^0 and E_{Ij}^0 for spin-orbit and spin-spin interaction, respectively should be identical for all nuclei. Since the spin-orbit interaction is surface dominated, whereas the spin-spin interaction is mainly a volume effect, we model the relation between the elementary matrix elements and those for finite nuclei as

$$E_{ls}(A) = \frac{E_{ls}^0}{A^{2/3}}, \qquad E_{Ij}(A) = \frac{E_{Ij}^0}{A} \tag{8.11}$$

These relations should only be taken as a rough guideline and will only be applied to constrain the fit parameters of Vanadium further, since the structure of this spectrum is not sufficiently pronounced to yield a conclusive fit. In fig. 8.3 an illustration of the spectral structure model for an orbital angular momentum shell is shown.

The complete spectrum is then modeled by a sum over all bound orbitals

$$G_{tot}(x) = \sum_l w_l \, G_l(x) \tag{8.12}$$

with free parameters $\{\{E_l\}, \{w_l\}, E_{ls}, E_{Ij}\}$.

In between the orbital shell peaks there is a signal above background observed. Following [Hotchi01] we also attribute this to a core excitation and model this contribution by adding $w_c G_{tot}(x - E_c)$ to G_{tot}. E_c is the excitation energy of the core, w_c accounts for the excitation strength. This produces an additional image of the Λ single particle spectrum, reduced in strength and shifted by E_c to higher energies.

Fitting the $^{89}_{\Lambda}Y$ spectrum it turns out, that restricting the degrees of freedom in the fit by eq. (8.6) leads to a substantial reduction of uncertainty in the parameters while still keeping a very low mean deviation from the data. This may be taken as an indication that all physics relevant at this level of accuracy is taken into account. In the next step the model parameters of $^{51}_{\Lambda}V$ were extracted. Due to the low statistics it is necessary to introduce additional constraints for the parameters.

By these relations E_{ls} and E_{Ij} are translated from the $^{89}_{\Lambda}Y$ fit result to $^{51}_{\Lambda}V$. There they are used as as fixed constants during fit to reduce uncertainties. The fit results are displayed in fig. 8.4 and the according parameters are given in tab. 8.3. The errors given are the standard errors of the applied Levenberg Marquard algorithm, describing the possible variation of the respective parameter. By the errors one can see that the Yttrium data nicely constrain the parameters while the Vanadium spectrum, due to lower statistics,does not show sufficiently pronounced structures to tightly constrain the model parameters. From the fit parameters the Λ single particle spectra can be reconstructed according to our model assumptions, eq. (8.8) . The final spectra are given in tab. 8.4.

Let us now shortly discuss the reliability of the extraction procedure. Considering the degree of correlation between the model parameters in the fitting procedure yields an estimate if all important relations that may exist between the parameters are taken into account. This is the case describing the spectral function of $^{89}_{\Lambda}Y$. In addition the fit leads to an excellent result, so that we may conclude that the approach accounts for the relevant physical degrees of freedom governing this system. In the case of $^{51}_{\Lambda}V$ the description of the spectrum is also rather well, the parameters are, however, highly correlated. We attribute this to the low statistics in the latter spectrum.
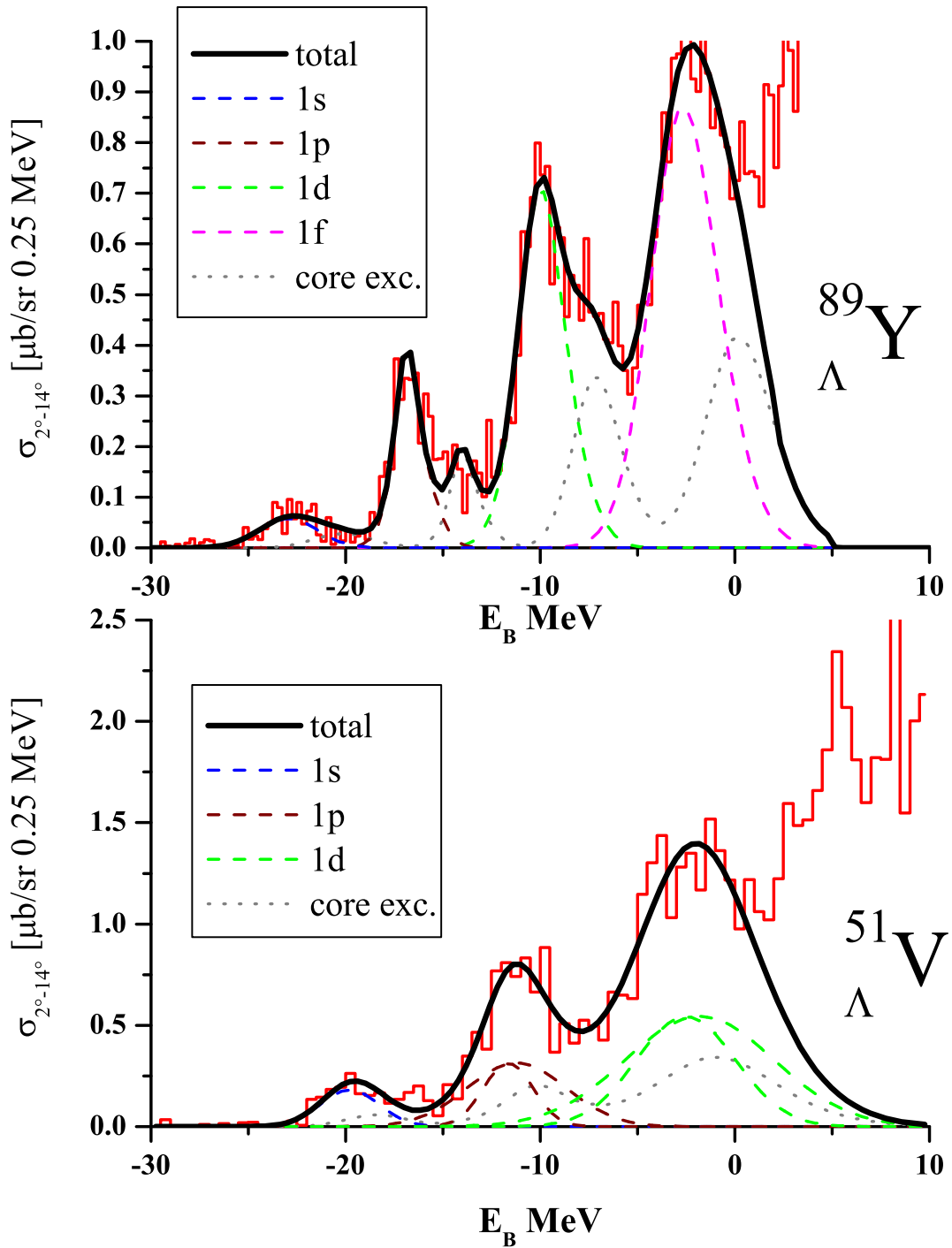
Figure 8.4.: The figure shows our reanalysis of the missing energy spectra obtained by [Hotchi01], taking into account *ls* systematics and the effect of the high core spins in $^{89}_{\Lambda}Y$ and $^{51}_{\Lambda}V$.

	$^{89}_{\Lambda}$Y			$^{51}_{\Lambda}$V	
E_s	-22.94 ±0.66	MeV	-19.79 ± 1.22	MeV
E_p	-16.79 ±0.66	MeV	-11.48 ± 1.11	MeV
E_d	-9.93 ±0.66	MeV	-2.22 ± 1.06	MeV
E_f	-2.60 ±0.66	MeV	-
w_s	0.22± 0.05		0.69± 1.04
w_p	0.25± 0.02		1.02± 1.52
w_d	0.45± 0.02		1.76± 2.61
w_f	0.55± 0.03		-
E_{ls}	222.7±152.7	keV	283.0	keV
E_{Ij}	61.3± 2.5	keV	106.0	keV
E_c	2.83± 0.12	MeV	1.36	MeV
w_c	0.50		0.30

Table 8.3.: Parameters extracted for $^{89}_{\Lambda}$Y and $^{51}_{\Lambda}$V. E_i $(i = s, p, d, f)$ denote the centroid energies of the respective angular momentum shells, E_{ls} and E_{Ij} are the spin interatcion matrix elements and E_c is the energy of the core excitation. The w correspond to the respective excitation strengths.

	$^{89}_{\Lambda}$Y		$^{51}_{\Lambda}$V	
$1s_{1/2}$	-22.94 ± 0.64	MeV	-19.8 ± 1.4	MeV
$1p_{3/2}$	-17.02 ± 0.07	MeV	-11.8 ± 1.3	MeV
$1p_{1/2}$	-16.68 ± 0.07	MeV	-11.4 ± 1.3	MeV
$1d_{5/2}$	-10.26 ± 0.07	MeV	-2.7 ± 1.2	MeV
$1d_{3/2}$	-9.71 ± 0.07	MeV	-1.9 ± 1.2	MeV
$1f_{7/2}$	-3.04 ± 0.11	MeV	
$1f_{5/2}$	-2.26 ± 0.11	MeV	

Table 8.4.: Λ single particle spectrum of $^{89}_{\Lambda}$Y and $^{51}_{\Lambda}$V when taking into account the Λ-core spin-spin coupling effect.

The extracted parameters, which are not connected specific properties of Yttrium and Vanadium have to be be in agreement with other experiments. Especially the two core excited states should appear also in experiments devoted to the core nuclei. For both, ^{88}Y and ^{50}V, data exist and may be found in the NNDC nuclear data base [NNDC]. In both cases there are excitations observed in one neutron stripping reactions starting from the next heavier isotope that lie in the region which was found to produce the background. From this at least a consistency with other nuclear data is assured. The other parameter which should be possible to check is E_{ls}^0. The definition in eq.(8.11) is very rough so only an accuracy within a factor of two should be expected. In translating the strength of the matrix element form Yttrium to Vanadium is not that critical since both nuclei are not very far apart in A and a variation of E_{ls}^0 leads only to slight changes in the final result of the $^{51}_\Lambda$V spectrum. From $^{89}_\Lambda$Y we can extract

$$E_{ls}^0 = 4.44 \pm 3.04 \ MeV. \tag{8.13}$$

This can be compared with the value that corresponds to the observations in high accuracy γ spectroscopy on $^{13}_\Lambda$C [Kohri02]. They found the p-shell splitting in this hypernucleus to be $\Delta E_p = 152 \pm 90 \ keV$. This yields $E_{ls}^0 = 0.56 \pm 0.33 \ MeV$. Scaling the spin dependent interactions with respect to powers af A is a rather crude assumption, especially in light nuclei, where effects beyond mean-field play an important role. Although there is no agreement within the error bars, the outcome may still be considered consistent.

The small spin-orbit splitting we found is, in contrast to what was found in [Hotchi01], in line with the findings in light hypernuclei, as indicated by the γ spectroscopy on $^{13}_\Lambda$C, and the expectations from SU(6) symmetry, which predicts an almost vanishing spin-orbit splitting.

8.4. Determination of the Λ vertices in DDRH theory

From the just determined Λ single particle spectra we will now determine the scaling factors for the scalar and vector couplings, as was already described in sec. 8.2. Since an intriguingly small spin-orbit splitting was found we will in addition introduce the tensor vertex that also couples the Λ to the ω field, see sec. 4.2.1.

To extract the vertices we run a fit of $^{89}_\Lambda$Y and $^{51}_\Lambda$V, where the weights of each single particle level are given by the inverse of the errors as given in tab. 8.4. First, the valleys of best fit are determined independently to get an impression about the consistency of the spectra. As already observed in the fit to the spectra obtained by [Hotchi01], a very strong correlation between R_σ and R_ω is found, which is again used to simplify the representation of our results in figures. The valleys are displayed in fig. 8.5. An exactly linear correlation can be nicely seen. It is also obvious, that both correlations exactly coincide, indicating that the new spectral systematics may be described better by DDRH.

To determine the preferred setof scaling factors an interval of $0.1 \le R_\sigma \le 0.6$ for the electric couplings and $-1.5 \le f/g \le 1$ for the magnetic coupling was scanned. For the comparison with conventional RMF models also a calculation with NL3 was performed.
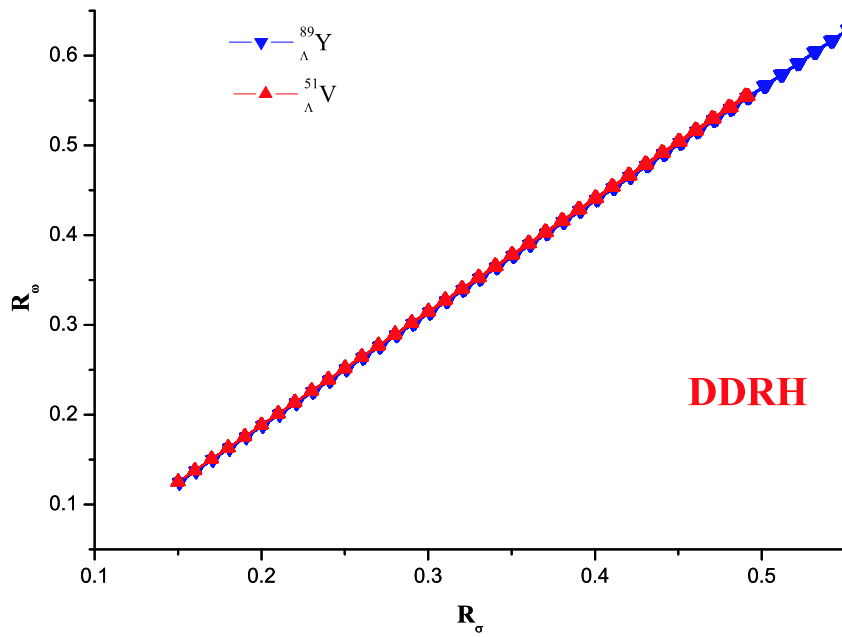
Figure 8.5.: Determining the scaling factors of the Λ by performing a χ^2 fit to hypernuclear data a very sharp and exactly linear correlation between R_σ and R_ω is found. This figure shows the "valleys of best fit" for the fit of $^{89}_{\Lambda}$Y and $^{51}_{\Lambda}$V. One finds a nice agreement of both calculations, indicating a consistent and correct description.
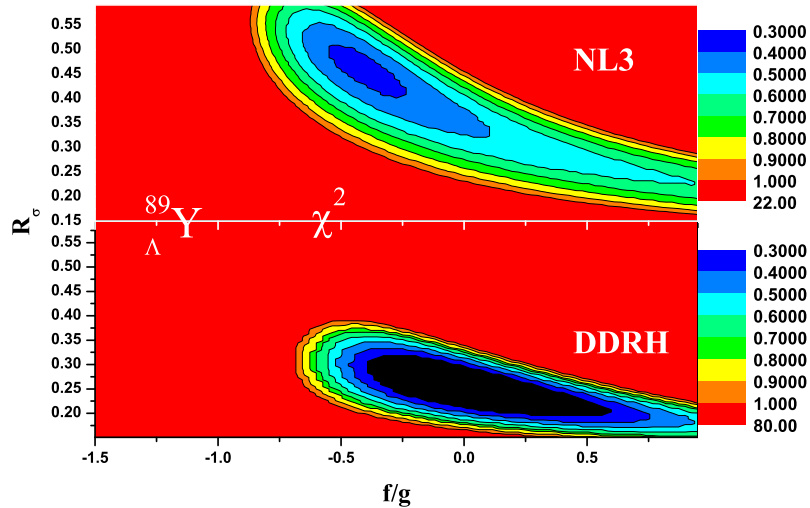
Figure 8.6.: The χ^2 deviation between experimental and calculated Λ single particle spectra are displayed for a range of coupling parameters. Obviously the SU(6) values $f/g = -1$ and $R = \frac{2}{3}$ are ruled out.

The results for both calculations are shown in fig. 8.6 in terms of χ^2 contours in the R_σ–R_ω plane. It seems that DDRH is more appropriate for the description of hypernuclear spectra, it reaches the lower chi-squared and finds a better constrained ideal region in the parameter plane. It is worthwhile noting that both models favor couplings deviating considerably from the commonly SU(6) values $f/g = -1$ and $R = \frac{2}{3}$. DDRH is even consistent with $f/g = 0$. The result we obtained for the best fit parameter set is

$$R_\sigma = 0.2525, \qquad R_\omega = 0.2529, \qquad f/g = 0 \qquad (8.14)$$

In fig. 8.7 we show the evolution of the single particle levels with respect to R_σ. The solid lines represent $f/g = -0.5$, the dashed $f/g = 0$. The effect of the tensor coupling can be easily seen, it simply reduces the spin-orbit splitting. So one might expect that increasing the vector and scalar coupling along the valley of best fit keeps the centroids of the spin-obit pairs in place while only the splitting increases which could be cured by the tensor interaction. However, increasing the σ and ω coupling modifies the relative spacings between the levels, leading to a situation which can not be cured by reducing the splitting when pushing f/g closer to -1. Thus only in sections I-III one obtains excellent agreement with data.

8.5. Consequencies and recommendation

Can we now rule out flavor symmetry relations for the coupling constants of baryon-baryon interaction models? Yes and no. As already discussed in sec. 5, the effective in-medium couplings are just not a place where one should expect that these relations are of any value. Values similar to the scaling factors here were found for the ratios between the respective Lorentz components of the full ΛN and NN in-medium interaction. Furthermore, flavor symmetry in hypernuclei is explicitly broken, since the baryonic medium is not SU(3) saturated. The couplings to which flavor symmetries should apply are the bare couplings which are relevant only in the Born diagrams of the one boson exchange kernel. What is used in RMF calculations is an effective interaction modified by resummations of scattering series and self-energy effects. In the iteration of the T-matrix the different meson exchange channels mix, depending on momentum and the composition of the surrounding medium. It is therefore indispensable to perform microscopic hypernuclear structure calculations to learn about the underlying symmetries.

In fig. 8.8 we present the Λ single particle spectra for the whole mass range of nuclei obtained with the parameter set just extracted. The comparison with experimental data shows a good agreement over almost the complete mass range. Only for the light nuclei, where effects beyond mean-field are likely to become relevant some deviations are seen. Keeping in mind that we use a fully microscopic description of the core nucleus, this result has to be considered as a big success for the DDRH model. In addition to the calculations with the new parameter set we show single particle spectra obtained with our previous parameter sets, derived in [Keil00]. These were obtained by fixing R_σ from a model for correlated $\pi\pi$ and $K\overline{K}$ exchange [Haidenbauer98] and R_ω by mathing hypernuclear single particle spectra. There are two parameter sets, one for the intermediate and heavy mas and one for the low mass nuclei. Comparing the numerical values of the coupling
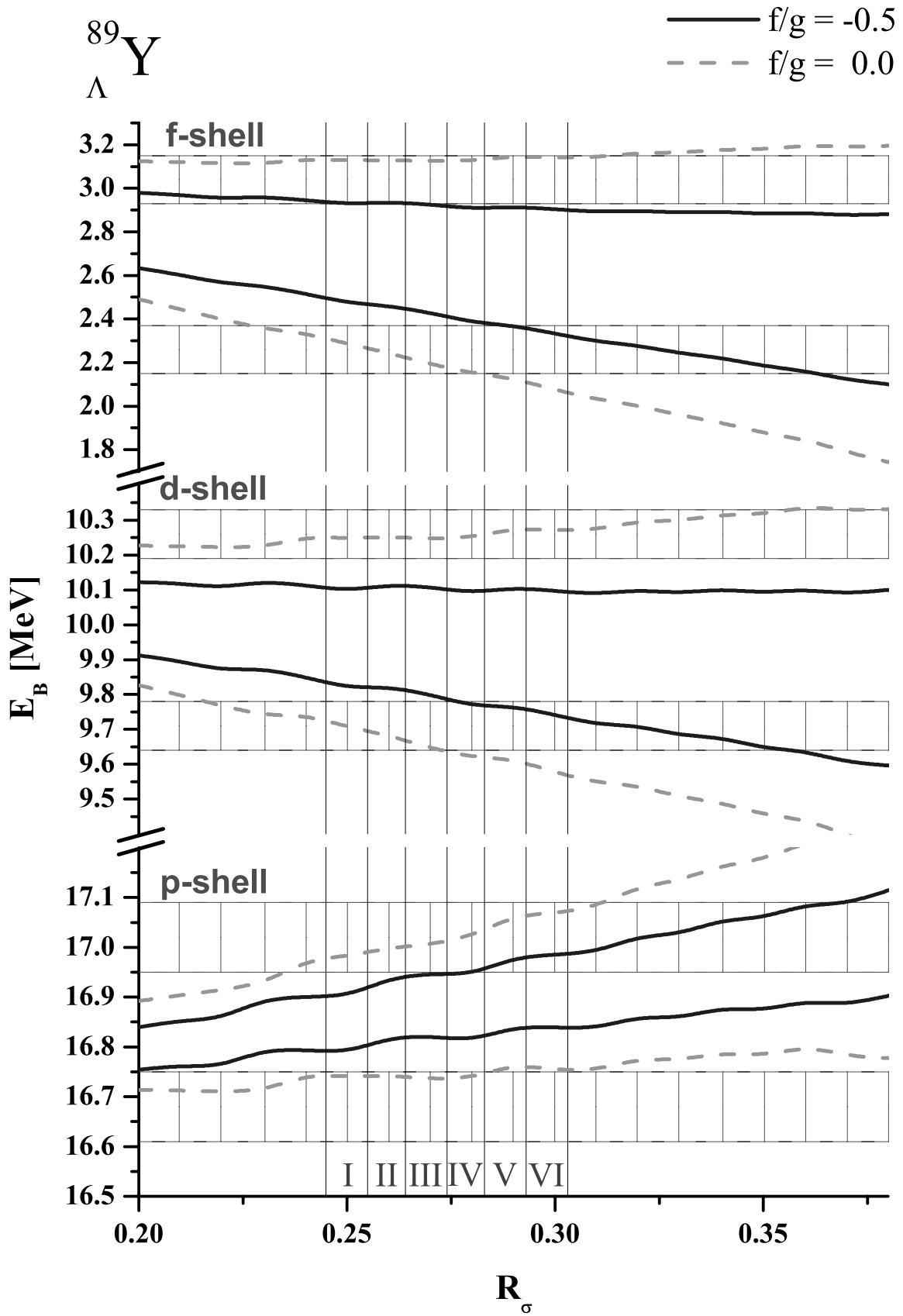
Figure 8.7.: The evolution of the single particle spectrum along the valley of best fit with respect to R_σ is shown for $f/g = -0.5$ and $f/g = 0$.
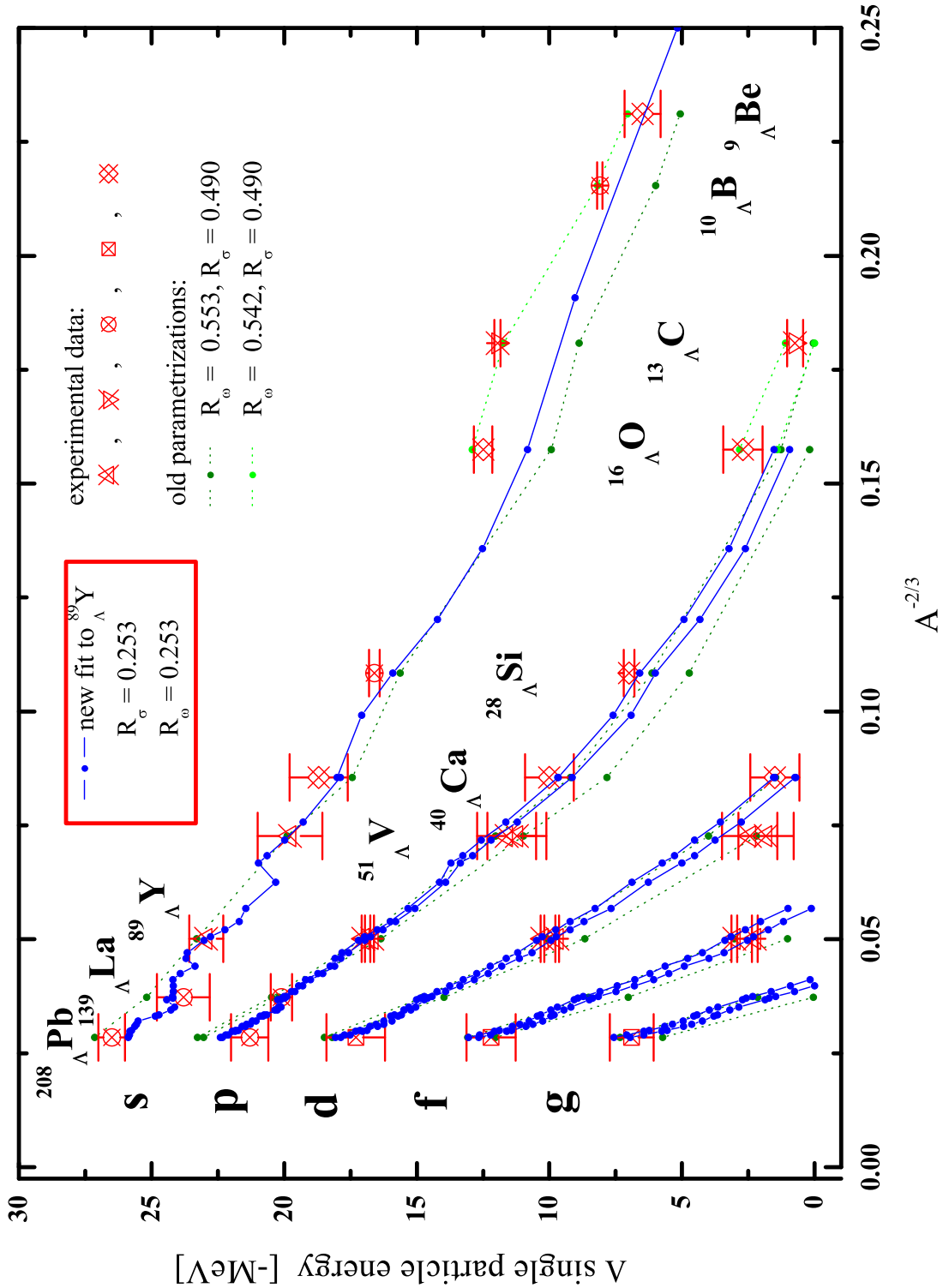
Figure 8.8.: The Λ single particle spectrum for the whole mass region calculated with the parameter set extracted from the data by Hotchi *et al.*. The calculations are compared to the world data set of hypernuclear single particle spectra which were all obtained in meson-nucleus missing energy spectroscopy. For comparison also calculations of our old parametrizations are shown.

constants it is apparent how sensitive these calculations are to the exact interaction strength.

There is another point which we may learn from this fairly complicated analysis: hypernuclei of intermediate and heavy mass are crucial to understand the basic structure of hyperon-nucleon interactions, since they provide a clean, almost nuclear matter environment for a single hyperonic probe, in which blurring finite size effects are mostly absent. However, the nuclei one is going to study should be chosen carefully. In hypernuclei possesing a high core spin, which is the case for the discussed data, additional assumptions have to be made for extracting a single particle spectrum. There is a whole wealth of target nuclei, which also exists in sufficient abundance, where the conversion of a neutron into a Λ yields a 0^+ core nucleus. A list of possible[2] target materials is given in tab. 8.5.

^{A}Z	abund.	^{A}Z	abund.	^{A}Z	abund.	^{A}Z	abund.
^{47}Ti	7.4%	^{53}Cr	9.5%	^{77}Se	7.6%	^{83}Kr	11.4%
^{87}Sr	7.0%	^{91}Zr	11.2%	^{95}Mo	15.9%	^{99}Ru	12.8%
^{101}Ru	17.0%	^{105}Pd	22.3%	^{111}Cd	12.8%	^{113}Cd	22.3%
^{117}Sn	7.7%	^{119}Sn	8.6%	^{128}Te	7.0%	^{129}Xe	26.4%
^{131}Xe	21.2%	^{137}Ba	11.2%	^{143}Nd	12.3%	^{145}Nd	8.3%
^{147}Sm	14.9%	^{149}Sm	13.8%	^{155}Gd	14.8%	^{157}Gd	15.7%
^{161}Dy	18.9%	^{163}Dy	24.9%	^{167}Er	22.9%	^{171}Yb	14.3%
^{173}Yb	16.1%	^{177}Hf	18.6%	^{183}W	14.3%	^{189}Os	16.7%
^{195}Pt	33.8%	^{199}Hg	16.8%	^{201}Hg	13.1%	^{207}Pb	22.2%

Table 8.5.: Target elements for the $A(\pi, K)_\Lambda A$ reaction, which produce hypernuclei with a $J^\pi = 0^+$ nuclear core.

---

[2]possible in the eyes of a theoretical nuclear phycisist.

9. The Hypernuclear Auger Effect

A promising alternative for spectroscopy in medium and heavy mass hypernuclei is the observation of Auger neutrons, emitted during the de-excitation of the hypernucleus after the initial creation of a Λ in an excited single particle level. The hypernuclear Auger process was discussed first by Likar *et al.* [Likar86]. More recently, the idea has been revived and worked out in much more detail for an experiment proposal at JLAB [Margaryan00] and theoretically in [Keil02a].
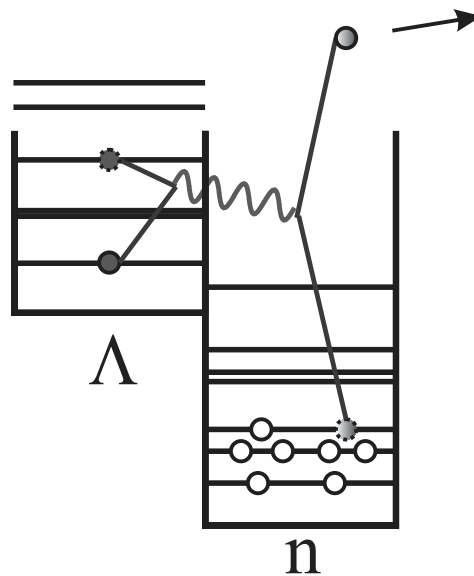
Figure 9.1.: Schematic picture of the hypernuclear Auger effect: A Λ hyperon is de-excited into a lower single particle level,thereby transferring energy and momentum to a valence neutron which is emitted through this process.

The hypernuclear Auger effect is the direct de-excitation of an excited Λ single-particle state in a hypernucleus by the emission of a neutron in close analogy to the well known atomic Auger effect where by the de-excitation of a single particle excitation in the electron cloud an electron is emitted, carrying away the excitation energy. In the hypernuclear Auger effect the energy spectrum of the emitted neutrons reflects the Λ singeparticle level structure, folded with the neutron single-particle spectrum. The mechanism is schematically shown in figure 9.1. In order to occur, the separation energy of at least the Λ 1s-orbit must be larger than the separation energy of the valence neutron. Therefore, due to a much weaker Λ binding, as compared to the nucleons, the hypernuclear Auger effect appears with a strength sufficient for measurements only in intermediate and

heavy mass nuclei where neutron and Λ separation energies of comparable magnitude are available.

Already from this simplified picture, as illustrated in fig. 9.1, it is clear that a single transition of the Λ will yield a wealth of peaks in the neutron's energy distribution, requiring a very careful analysis. For the proposed JLAB experiment [Margaryan00], a neutron energy resolution of better than 50 keV is envisaged. As nuclei to be studied in the experiment Pb and U are proposed.In this mass region it can yield valuable information about the Λ single particle spectra, possibly even resolving finer details as the spin-orbit splitting. One purpose of our studies is to investigate in a realistic model predictions for spectral distributions which may be used to estimate constraints on future measurements.

In this chapter we present our calculations of the hypernuclear Auger spectra within DDRH theory extending our previous work [Keil02a]. Section 9.1 describes the theoretical description of the hypernuclear Auger effect in the relativistic DDRH approach with density dependent meson-baryon vertices. In section 9.2 results are presented and possibilities to extract information from the extremely complex spectra are discussed.

9.1. Modeling the Hypernuclear Auger Effect

The emission of a neutron during the de-excitation of a Λ single particle state in a hypernucleus is described as a decay of an initial Λ single particle state into a 2 particle-1 hole configuration in which the Λ is coupled to a neutron particle-hole core excitation with an energy above the particle emission threshold. The nucleon and hyperon single particle states are obtained in relativistic mean-field (RMF) approximation. Residual interactions among the neutron particle-hole configurations are neglected, i.e. a description in terms of non-interacting quasiparticle description is used.

For the transition operator V, the one-boson-exchange parametrization of the full Dirac-Brueckner (DB) G-matrix with density dependent vertex functionals $\Gamma(\hat{\rho})$ [Fuchs95, Keil00, Lenske04] is used. It is the same interaction as applied in the structure calculation. Since the Λ hyperon is electrically neutral and an iso-scalar particle only the σ and the ω mesons contribute:

$$V = \Gamma_{\sigma\Lambda}(\hat{\rho}_\Lambda)\frac{1}{q^2 - m_\sigma^2}\Gamma_{\sigma N}(\hat{\rho}_N) - \Gamma_{\omega\Lambda}(\hat{\rho}_\Lambda)\frac{1}{q^2 - m_\omega^2}\Gamma_{\omega N}(\hat{\rho}_N) \tag{9.1}$$

Taking $|0\rangle$ to be our many-body ground state, assumed here as the 0^+ ground state of a spherical nucleus, the initial state is in second quantization formulation given by $a_{\Lambda_\alpha}^\dagger |0\rangle$, where $a_{\Lambda_\alpha}^\dagger$ is the creation operator for a Λ state with the set of quantum numbers Λ_α. In the final state the hyperon is attached to a particle-hole excited nuclear core. The excess energy and momentum is carried away by the emitted neutron occupying an unbound single particle continuum state in the nuclear mean-field potential:

$$\left[a_{\Lambda_\beta}^\dagger \otimes A_{n_\beta}^\dagger(j_{n_\beta}j_{n_\beta^{-1}})\right]_{j_\beta m_\beta}|0\rangle = \sum_{m_{\Lambda_\beta}M_{n_\beta}}\langle j_{\Lambda_\beta}m_{\Lambda_\beta}J_{n_\beta}M_{n_\beta}\,|\,j_\beta m_\beta\rangle\, a_{\Lambda_\beta}^\dagger A_{n_\beta}^\dagger(j_{n_\beta}j_{n_\beta^{-1}})|0\rangle \tag{9.2}$$

$A^\dagger_{n_\beta}$ is the particle-hole excitation operator with angular momentum J_{n_β}, M_{n_β} defined through:

$$A^\dagger_n(j, j') = \sum_{m,m'} \langle jmj'm'| \, J_n M_n \rangle \, a^\dagger_{jm} \tilde{a}_{j'm'}, \qquad (9.3)$$

where $\tilde{a} = (-)^{j+m} a_{j,-m}$ denotes a hole creation operator. In eq. 9.2 the $a^\dagger_{\Lambda_\beta}$ and $A^\dagger_{n_\beta}$ are coupled to total angular momentum j_β, m_β.

The differential widths $d\Gamma_{j_{\Lambda_\alpha}}$ describing the decay of an initial Λ_α state is determined by the transition matrix elements of the ΛN interaction V:

$$d\Gamma_{j_{\Lambda_\alpha}} = \frac{1}{32\pi^2} \frac{1}{2j_{\Lambda_\alpha} + 1} \sum_{\{\gamma_1\}} \left| \langle 0| \left[a_{\Lambda_\beta} \otimes A_{n_\beta}(j_{n_\beta}, j_{n_\beta^{-1}}) \right]_{j_\beta m_\beta} V a^\dagger_{\Lambda_\alpha} |0\rangle \right|^2 \frac{|\vec{k}|}{M^2} d\Omega, \qquad (9.4)$$

where $\{\gamma_1\} = \left\{ m_{\Lambda_\alpha}, m_\beta, j_\beta, j_{\Lambda_\beta}, j_{n_\beta}, j_{n_\beta^{-1}} \right\}$ indicates the incoherent summation over degenerate initial and final sub-states, including the appropriate phase space factors [pdg] due to the neutron emerging with momentum $\vec{k}$. M is the mass of the initial hypernucleus. The orthogonality and completeness relations of the Clebsch-Gordan coefficients [Brussaard] allow to convert this expression into the equivalent form of an incoherent sum over matrix elements of uncoupled states:

$$d\Gamma_{j_{\Lambda_\alpha}} = \frac{1}{32\pi^2} \frac{1}{2j_{\Lambda_\alpha} + 1} \sum_{\{\gamma_2\}} \left| \langle 0| a_{\Lambda_\beta} a_{n_\beta} \tilde{a}^\dagger_{n_\beta^{-1}} V a^\dagger_{\Lambda_\alpha} |0\rangle \right|^2 \frac{|\vec{k}|}{M^2} d\Omega \quad , \qquad (9.5)$$

where $\{\gamma_2\} = \left\{ m_{\Lambda_\alpha}, m_{\Lambda_\beta}, m_{n_\beta}, m_{n_\beta^{-1}}, j_{\Lambda_\beta}, j_{n_\beta}, j_{n_\beta^{-1}} \right\}$. From equations (9.4) and (9.5) it is seen that the Auger process is determined by nucleonic particle-hole fluctuations of the nuclear mean-field absorbing the energy-momentum transfer from the Λ transition. This structure becomes even more obvious by expressing the matrix elements in terms of the appropriate non-diagonal elements of Λ and nucleon one-body density matrices in momentum space:

$$\langle 0| a_{\Lambda_\beta} a_{n_\beta} V a^\dagger_{n_\beta^{-1}} a^\dagger_{\Lambda_\alpha} |0\rangle = \int d^4q \, \rho_{\Lambda'\Lambda}(q) V(q) \rho_{n^{-1}n}(q) \quad . \qquad (9.6)$$

Here, the transition densities ρ_{ij} are given by:

$$\rho_{ij}(q) \equiv \int d^4x e^{iqx} \overline{\psi}_i(x) \hat{\Gamma} \psi_j(x)$$

$$= \delta \left((q^0 - (E_i - E_j)) \int d\Omega \, dr \, r^2 \left(\sum_{\mu,\lambda} (-)^\lambda Y^*_{\lambda\mu}(\hat{q}) Y_{\lambda\mu}(\hat{r}) j_\lambda(qr) \right) \overline{\psi}_i(r, \hat{r}) \hat{\Gamma} \psi_j(r, \hat{r}) \right.$$

$$(9.7)$$

$\hat{\Gamma}$ is either $\hat{1}$ or γ^μ for σ- and ω-exchange, respectively. $E_{i,j}$ are the single particle energies of the states $\psi_{i,j}$. In the second line the spatial part of the plane wave is expanded into partial waves. A more detailed description of the evaluation of the matrix elements is given in appendix E.1. The wave functions and single particle energies $E_{i,j}$ are taken from a DDRH calculation which is described are section 4.2.1.

9.2. Results for the hypernuclear Auger effect

In our investigations we consider the hypernuclei $^{91}_{\Lambda}$Zr and $^{209}_{\Lambda}$Pb as representative examples for medium and heavy hypernuclei, respectively. The wave functions and single particle energies used for the evaluation of the matrix elements are calculated self-consistently by solving the DDRH field equations in relativistic mean-field (RMF) approximation. Details of the numerical approach and the model parameters are given in sec. 4.2.1 and [Keil00]. In the present application we need information on knocked-out, unbound neutron states. For that purpose the single particle continuum was discretized by enclosing the system in a huge box of size $R = 150 fm$. Since the spacing of the discretized continuum levels behaves as $\sim \mathcal{O}(1/R^2)$ the use of such a large quantization volume ensures quasi-continuous energy spectra for the neutron scattering states, allowing to resolve single particle resonances and other continuum structures resulting from the calculations.

The continuum wave functions are calculated in the self-consistently obtained ground state mean-field potentials. Thus, final state interactions are taken into account on the level of static mean-field self-energies. The approach assures orthogonality of bound and unbound wave functions thus avoiding the unphysical non-orthogonality contributions inherent to phenomenological approaches.

Since the previous applications of the DDRH theory show that the experimental Λ spectra are reproduced especially accurate in heavy nuclei our approach is well suited for the calculation of the Auger neutron spectra from $^{209}_{\Lambda}$Pb and $^{91}_{\Lambda}$Zr. Numerical values of the single particle energies for occupied neutron states and bound Λ states are displayed in table 9.1.

9.2.1. $^{209}_{\Lambda}$Pb

Because of the high level density and moderate separation energies, heavy hypernuclei are most suitable for the Auger effect. However, at the same time these apparent advantages are, unfortunately, a potential source of problems for experimental work. The huge amount of combinatorial possibilities for transitions, illustrated in table 9.2 and indicated in figure 9.2 for the case of initially populating the $1g^{\Lambda}$-shell in $^{209}_{\Lambda}$Pb, leads to Auger spectra of a rather complicated shape, making in many cases an unambiguous identification of transitions and assignment of quantum numbers almost impossible.

The problem is apparent from figure 9.3 where the complete neutron emission spectrum from the $^{209}_{\Lambda}$Pb hypernucleus is displayed, summed over all energetically open Λ levels. Experimentally, spectra of a similar structure have to be expected. In addition, state-dependent weighting factors from the production vertex of the initial Λ state will be superimposed. From figure 9.3 and figure 9.2 it is obvious that experiments will be confronted with spectra of high complexity. Before observables of physical interest can be accessed the data will have to be analyzed in a more selective approach. From the discussion it is obvious that much of the structure will be produced by incoherent superpositions of contributions from the variety of orbitals in which the Λ was initially produced. By a precise energy tagging of the produced kaon and gating on the outgoing electron (for the case of electromagnetic production of hypernuclei, as will be the case
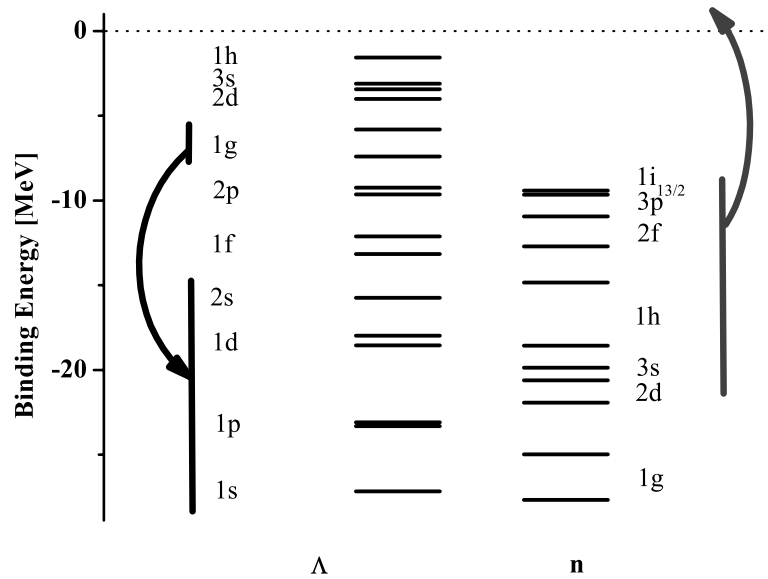
Figure 9.2.: Level schemes of the Λ hyperons and neutrons that are involved in the hypernuclear Auger effect. The levels are displayed in the physical scale as shown in table 9.1. The bars mark the single particle levels involved by the de-excitation of an initial 1g-shell Λ. The maximum energy, released when the Λ drops down to the 1s-orbit, allows to emit neutrons from the $1i_{13/2}$ valence orbit down to the $2d_{3/2}$ or $3s_{1/2}$ shells for the $1g_{7/2}$ and $1g_{9/2}$ initial states, respectively.
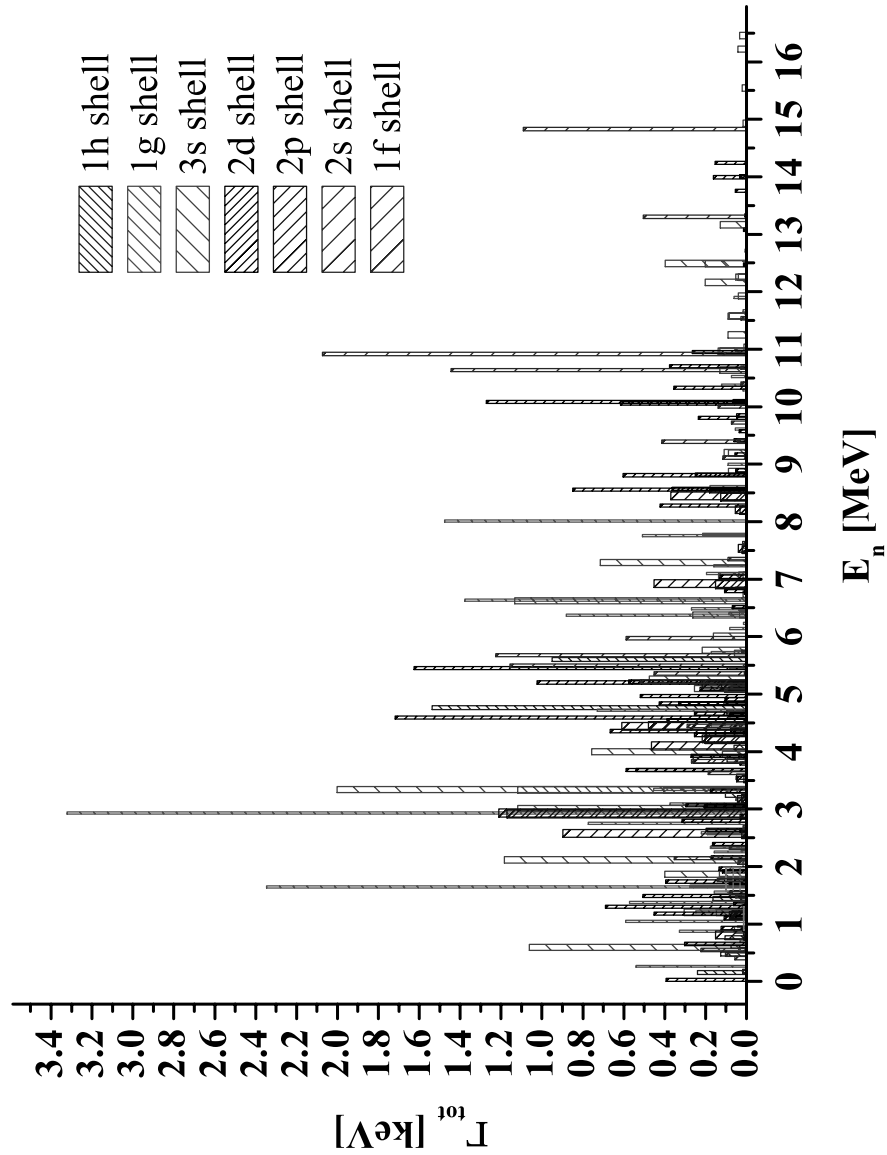
Figure 9.3.: Full spectrum of the Auger transition strengths in $^{209}_{\Lambda}Pb$ including contributions by initial population of the $1h$, $1g$, $3s$, $2d$, $2p$, $2s$ and $1f$ Λ orbitals and their subsequent de-excitation by neutron emission.

$^{209}_{\Lambda}$**Pb**

Λ	E [MeV]	n	E [MeV]
$1s_{1/2}$	-27.16352	$1g_{9/2}$	-27.67206
$1p_{3/2}$	-23.30941	$1g_{7/2}$	-24.97048
$1p_{1/2}$	-23.08789	$2d_{5/2}$	-21.91610
$1d_{5/2}$	-18.53900	$2d_{3/2}$	-20.61122
$1d_{3/2}$	-17.98296	$3s_{1/2}$	-19.86137
$2s_{1/2}$	-15.74262	$1h_{11/2}$	-18.56635
$1f_{7/2}$	-13.15220	$1h_{9/2}$	-14.83666
$1f_{5/2}$	-12.11529	$2f_{7/2}$	-12.70419
$2p_{3/2}$	-9.64314	$2f_{5/2}$	-10.93869
$2p_{1/2}$	-9.25274	$3p_{1/2}$	-10.32673
$1g_{9/2}$	-7.40907	$3p_{3/2}$	-9.64888
$1g_{7/2}$	-5.80963	$1i_{13/2}$	-9.41419
$2d_{5/2}$	-4.00386		
$2d_{3/2}$	-3.42605		
$3s_{1/2}$	-3.09504		
$1h_{11/2}$	-1.56587		

$^{91}_{\Lambda}$**Zr**

Λ	E [MeV]	n	E [MeV]
$1s_{1/2}$	-23.47681	$1f_{5/2}$	-19.36784
$1p_{3/2}$	-17.29138	$2p_{3/2}$	-18.77480
$1p_{1/2}$	-16.60878	$2p_{1/2}$	-17.35511
$1d_{5/2}$	-10.35182	$1g_{9/2}$	-11.59539
$1d_{3/2}$	-8.92933		
$2s_{1/2}$	-7.39805		
$1f_{7/2}$	-3.29197		
$1f_{5/2}$	-1.27159		
$2p_{3/2}$	-1.23856		
$2p_{1/2}$	-0.87765		

Table 9.1.: DDRH results for Λ and neutron single particle energies entering the Auger-calculations.

at JLAB) it might be possible to determine the initial Λ-state accurately enough such that only the Auger-neutrons related to the de-excitation of that specific state can be recorded selectively in a coincidence measurement.

In this context, it is of interest to consider the Auger transitions on the limits of the energetically accessible range of states. Assuming energetically sharp states, i.e. the Λ and neutrons are in good quasiparticle configurations and damping effects are negligible, the present calculation predicts that the Auger process can only take place if the Λ initially is produced in the $2s^{\Lambda}$-orbit or above (see table 9.1), because otherwise the Λ transition energies are less than the lowest neutron separation energy. Next to the $2s^{\Lambda}$-orbit we find the doublet of $1f^{\Lambda}$ states which is of interest because it allows to observe the Λ spin-orbit splitting, at least in principle. Since the energy window available from populating the $1f^{\Lambda}$-orbits is still rather narrow the resulting Auger neutron spectrum is of a comparatively simple structure. In figure 9.4 results for the Auger spectra produced by the $1f_{7/2}$ and $1f_{5/2}$ states are compared. It is seen that in both cases only a small number of final states occurs. Even more, only the transitions to the $1i_{13/2}$ neutron-hole final state yield a significant strength. Thus it is even possible to clearly obtain the spin-orbit splitting of the $1f^{\Lambda}$-shell. The prominent strength of this doublet is also fairly model independent. Considering the kinematically allowed phase space of this transition only, one might expect that wave function effects which are sensitive to the details of the interaction could strongly influence the relative strengths between the emission of the $1i$- or $3p$-shell neutrons, which are in energy almost degenerate (see

final Λ	neutron-hole	$\Gamma_{1g_{9/2}}[10^{-2}keV]$	$\Gamma_{1g_{7/2}}[10^{-2}keV]$
$1s_{1/2}$	$2d_{3/2}$	–	3.2
	$3s_{1/2}$	–	0.6
	$1h_{11/2}$	57.1	77.3
	$1h_{9/2}$	8.7	3.5
	$2f_{7/2}$	16.0	17.8
	$2f_{5/2}$	9.1	12.2
	$3p_{3/2}$	5.5	5.5
	$3p_{1/2}$	1.8	1.7
	$1i_{13/2}$	7.4	6.1
$1p_{3/2}$	$1h_{9/2}$	24.8	22.1
	$2f_{7/2}$	45.3	73.0
	$2f_{5/2}$	8.7	26.9
	$3p_{3/2}$	17.3	19.6
	$3p_{1/2}$	8.6	21.5
	$1i_{13/2}$	137.8	147.6
$1p_{1/2}$	$1h_{9/2}$	4.5	17.6
	$2f_{7/2}$	37.4	17.2
	$2f_{5/2}$	11.2	1.6
	$3p_{3/2}$	8.2	5.4
	$3p_{1/2}$	8.1	2.0
	$1i_{13/2}$	88.1	51.0
$1d_{5/2}$	$2f_{5/2}$	54.1	234.6
	$3p_{3/2}$	32.9	15.7
	$3p_{1/2}$	15.9	332.2
	$1i_{13/2}$	9.4	5.3
$1d_{3/2}$	$2f_{5/2}$	–	59.0
	$3p_{3/2}$	<0.01	27.5
	$3p_{1/2}$	0.5	17.2
	$1i_{13/2}$	1.2	19.2
$2s_{1/2}$	$3p_{1/2}$	–	<0.01

Table 9.2.: Transitions contributing to the de-excitation of the $1g^{\Lambda}$-states. Transition widths for the Λ initial states $1g_{9/2}$ and $1g_{7/2}$ are denoted by $\Gamma_{1g_{9/2}}$ and $\Gamma_{1g_{7/2}}$, respectively.
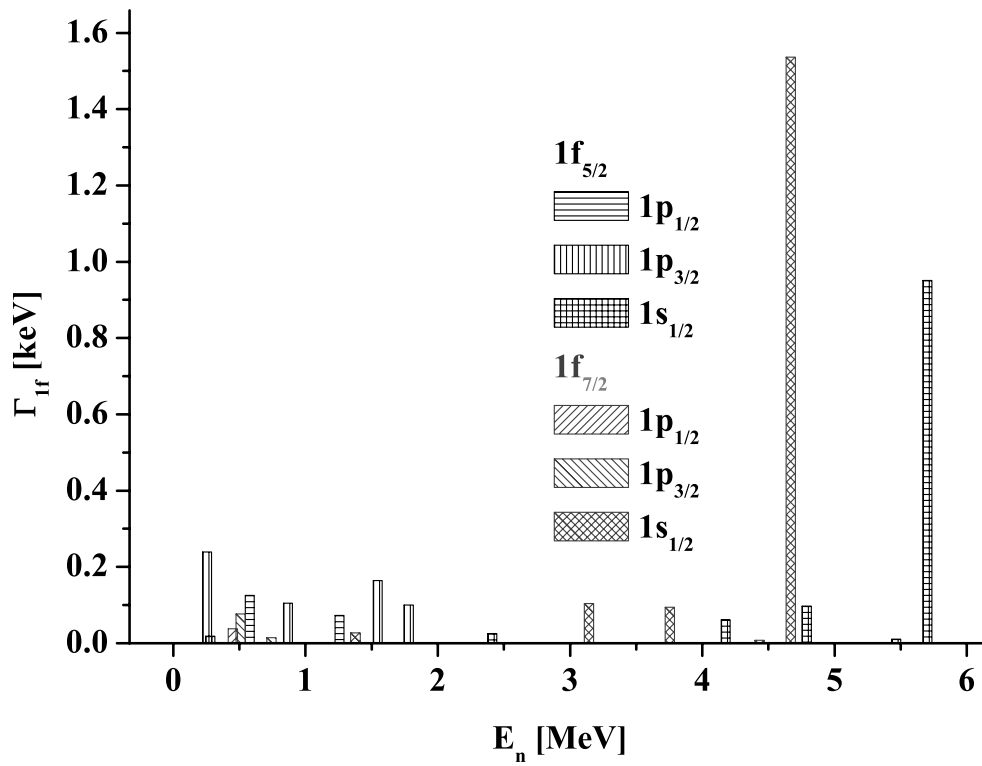
Figure 9.4.: Decay widths of the Auger transition strengths in $^{209}_{\Lambda}Pb$ with an initial 1f Λ state.

table 9.1). Nevertheless, due to the high degeneracy of the $1i_{13/2}$ neutron-orbitals the multiplicity of these neutrons will be greatly enhanced. Therefore one can expect to observe in the de-excitation spectrum of a $1f^{\Lambda}$-state a clear line doublet belonging to the two spin-orbit partners of the $1f^{\Lambda}$ shell falling down to the 1s orbital and thereby knocking out the $1i_{13/2}$ neutron.
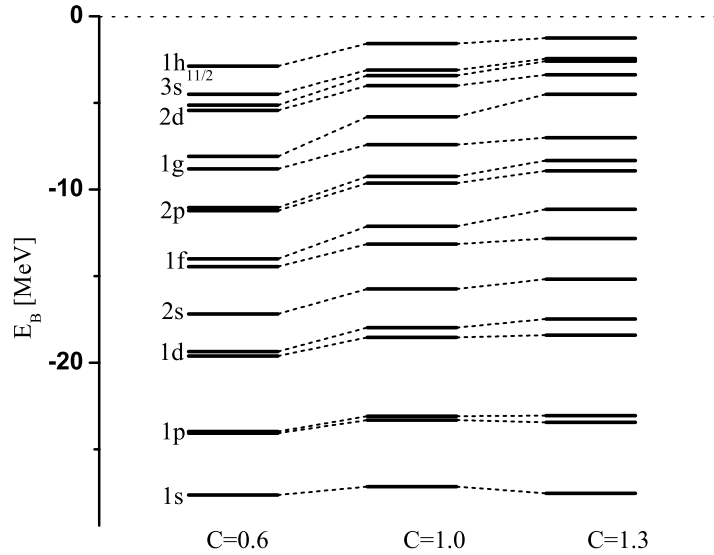
Figure 9.5.: Λ single particle energy spectra in $^{209}_{\Lambda}$Pb for the three different sets of coupling constants discussed in the text.

The general case is, however, more ambiguous. The doublet structure, which one might expect as the signature of the Λ spin-orbit splitting, does not always show up in the spectral distribution, since in many cases the matrix elements depend sensitively on binding energies and other wave function effects. As a representative case, we study the influence of the spin-orbit interaction strength on the Auger neutron spectra in more detail for the $1g^{\Lambda}$ shell of $^{209}_{\Lambda}$Pb. This case is well suited, since the spin-orbit splitting is sufficiently large and the spectrum offers already some complexity. The possible transitions for this configuration together with the corresponding transition rates are shown in table 9.2.

The dependence of the $1g^{\Lambda}$-shell spectra on variations of the spin-orbit strength of the Λ-nucleus potential is investigated by changing the relative and the absolute coupling strength of the σ and the ω meson to the Λ, keeping the overall single particle structure of the Λ spectrum fixed. Numerically, this is realized by observing that in our relativistic mean-field theory with scalar and vector self-energies U_{σ} and U_{ω}, respectively, the leading order non-relativistic Schroedinger-type central potential is given by $U_0 = U_{\omega} - U_{\sigma}$ and the strength of the spin-orbit potential is determined by $U_{ls} = U_{\omega} + U_{\sigma}$ (see sec. 4.3 for details). Hence, we can relate spectral effects from variations of the spin-orbit strength by a factor C to a scaling of the scalar and vector self-energies U_{σ} and U_{ω}, respectively,
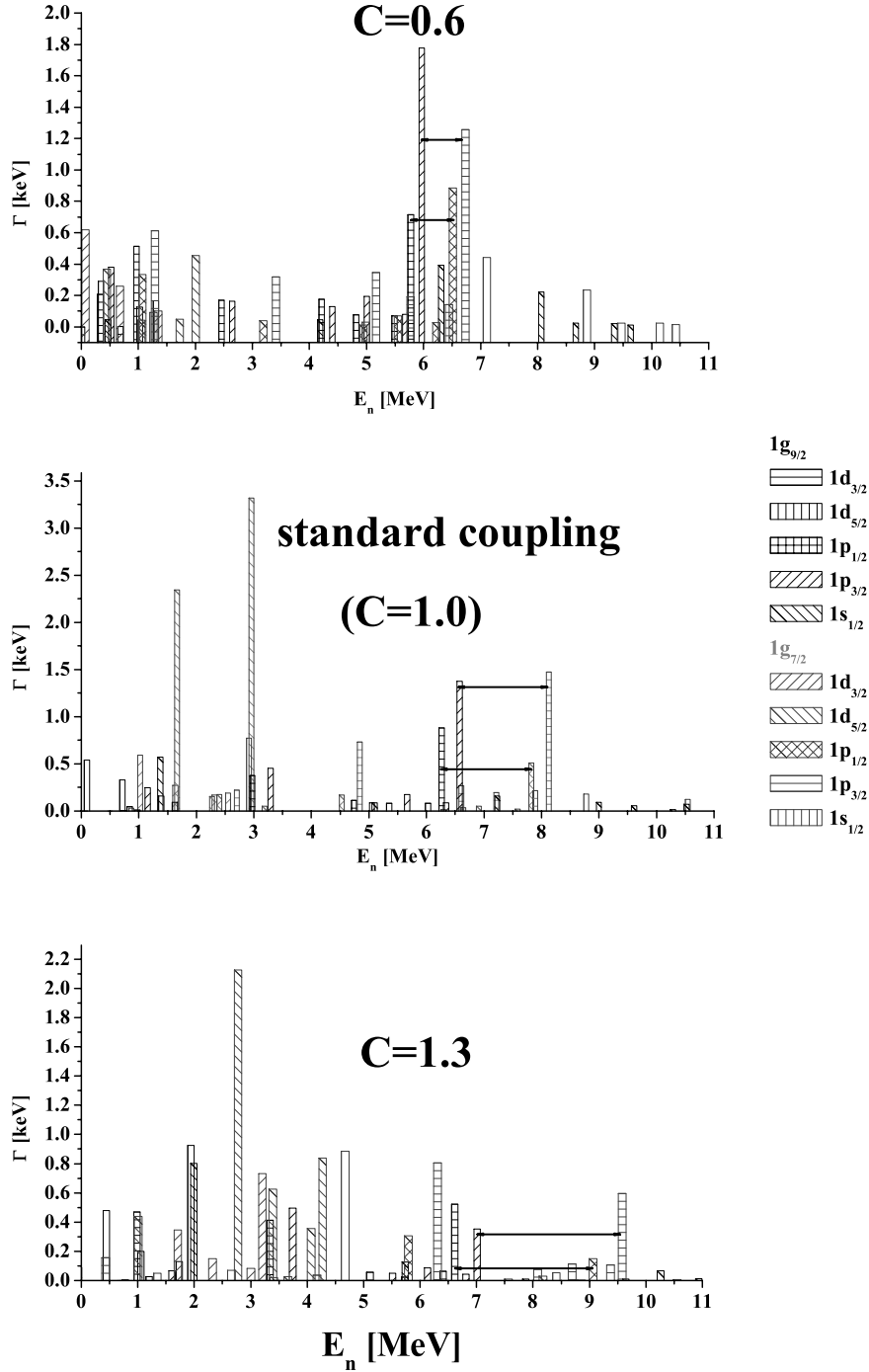
Figure 9.6.: Comparison of the spectral Auger strength distributions produced by transitions from the $1g^\Lambda$ shell for interactions with different spin-orbit splittings. The Auger transition widths Γ are shown as functions of energy E_n of the outgoing neutron. The upper and lower arrows indicate transitions from the $1g_{9/2,7/2}$ to the $1p_{3/2}$ and $1p_{1/2}$ final states, respectively.

127

according to

$$
\begin{aligned}
CU_{ls} &= \beta U_\omega + \alpha U_\sigma \\
DU_0 &= \beta U_\omega - \alpha U_\sigma \quad .
\end{aligned}
\tag{9.8}
$$

We preserve the self-consistency between the nuclear mean-field and the underlying baryon-baryon interactions by scaling the $\Lambda\sigma$ and $\Lambda\omega$ vertices by the same factors α and β, respectively.

Choosing C as our external parameter and using always $D = 1$ as a constraint, the spin-orbit splittings of the Λ levels can be varied over wide ranges while keeping the changes in the overall structure of the Λ single particle spectrum on a minimal level. The Λ single particle spectra obtained for $C = 0.6, 1.3$, corresponding to $(\alpha, \beta) = (0.6, 0.5), (1.3, 1, 4)$, respectively, are compared to the results for $C = 1$ in figure 9.6. For $C = 0.6$ the spin-orbit splittings are reduced by about a factor of 2 and an increase of about the same size is found for $C = 1.3$. These (strong) variations will surely cover the full range of uncertainties about the Λ spin-orbit potential.

The spectral distributions of Auger transitions widths Γ, obtained by putting the initial Λ in $1g_{9/2,7/2}$ orbits are displayed in figure 9.6. Compared to the standard case $C = 1$ the spectral structures and transition strengths are changed drastically when using $C = 0.6$ and $C = 1.3$. As an overall feature the calculations show a concentration of strength in a few states for $C = 1$ and $C = 1.3$ while a more equilibrated distribution is found for $C = 0.6$. The apparent pile-up of strength at low neutron energies for the normal and strong coupling cases are related to the variations in the values of overlap matrix elements due to changes in binding energies and single particle wave functions. Analyzing the dynamical content of the response functions by calculating sum rules for various moments of the excitation energy one finds a disappointing small sensitivity on the spin-orbit interaction strength. Hence, it is unlikely that spin-orbit effects will contribute significantly and on an observable level to the total spectral strength.

On the level of individual transitions there are, however, signals for spin-orbit effects visible. In figure 9.6 the transitions $1g^\Lambda_{9/2,7/2} \rightarrow 1p^\Lambda_{3/2}$ are indicated by the upper arrows while lower arrows denote $1g^\Lambda_{9/2,7/2} \rightarrow 1p^\Lambda_{1/2}$. The length of the arrows corresponds to the $1g^\Lambda_{9/2} \leftrightarrow 1g^\Lambda_{7/2}$ energy splitting which obviously depends directly on the spin-orbit interaction strength. In addition, details of the spectral distributions, e.g. the clustering of strength in certain energy regions, also depends on the overlap of wave functions by which the transition matrix elements and therefore the transition widths Γ are determined (see equations (9.5) and (9.6)).

9.2.2. $^{91}_{\Lambda}$Zr

It might seem somewhat disadvantageous to start out doing Auger experiments with a system of the complexity of a heavy nucleus like lead. However, aiming at resolving the Λ spin-orbit structure in heavy hypernuclei, which is still a controversial question as is discussed in sec. 8, one needs to find hypernuclei that provide a core nucleus of very low spin. In the ideal case this should be $J^\pi = 0^+$ in order to eliminate or at least to suppress effects from Λ angular momentum-core nucleus spin interactions leading
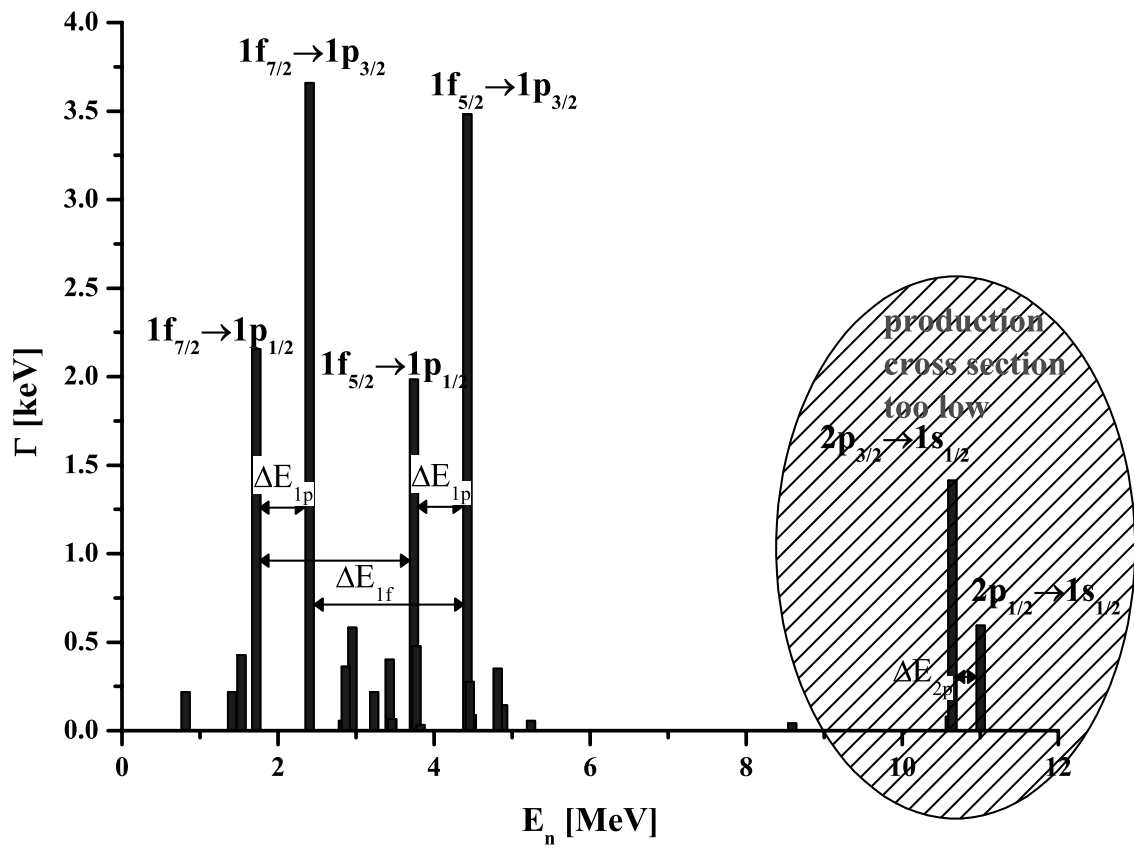
Figure 9.7.: This figure shows the full neutron emission spectrum of $^{91}_{\Lambda}$Zr.

to an additional splitting superimposed on the pure Λ spin-orbit splitting (see sec. 8). Interesting hypernuclei for meson induced production, which fulfill these requirements are listed in tab. 8.5.

As an example of the intermediate mass hypernuclei we have investigated here $^{91}_{\Lambda}$Zr. The Auger rates for the neutron emission of $^{91}_{\Lambda}$Zr are displayed in fig. 9.7. In contrast to the results for lead, the spectrum is very clear. It shows two prominent doublets, belonging to the four combinations of transition from the Λ f-shell to the Λ d-shell. In all four cases the produced neutron hole is in the $1g_{9/2}$-shell. The high multiplicity of this state leads to the strong dominance in the spectrum. In preparation of the experiment proposal our experimental colleagues produced an estimate of the measured Auger neutron spectrum by convoluting the theoretical spectrum with the detector resolution and adding a fairly large constant background [Margaryan04]. The result is shown in fig. 9.8. The four prominent states are still clearly observable, and thereby promis a successful experiment.
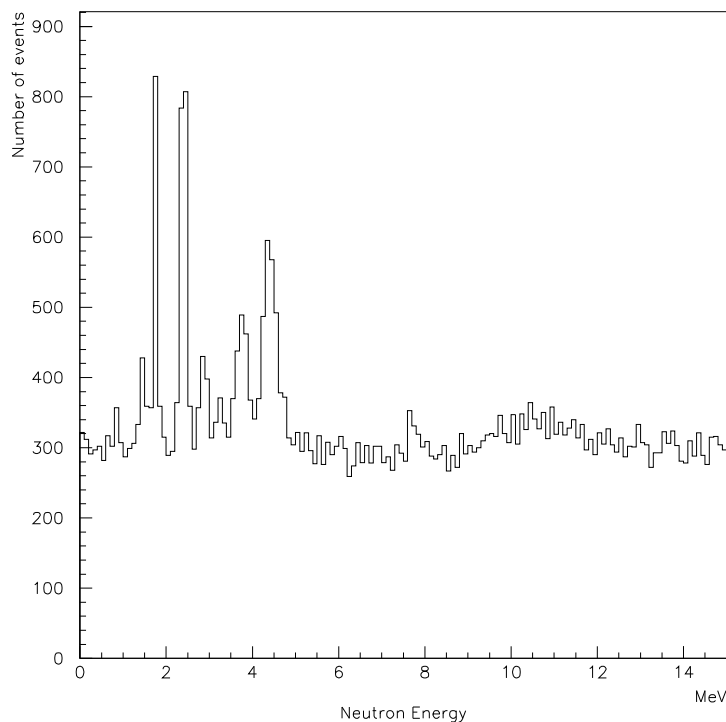
Figure 9.8.: This figure shows the theoretical spectrum of Auger neutrons from $^{91}_{\Lambda}$Zr, convoluted with the estimated experimental resolution and an additionally added background estimate (the figure was provided by A. Margarian [Margaryan04]). The p and f shell splitting is still clearly visible.

However, the experiment will be done by electroproduction of hypernuclei, and would thus have to utilize an ^{91}Nb target, which does not exist in nature. For the electromagnetic production ^{93}Nb would be an almost adequate replacement. In the produced hypernucleus, $^{93}_{\Lambda}$Zr, a new neutron shell, $2d_{5/2}$, is opened. The resulting additional neutron emissions will be slightly suppressed due to smaller multiplicity of the neutron hole states as compared to the $1g_{9/2}$ neutrons. The by 4.2 MeV smaller separation energy

will, however, at least compensate this suppression. Since the two groups of peaks will be shifted in the neutron spectrum by the same amount, they stay nicely separated and observable.

9.3. Resumé on Auger spectroscopy

The Auger-neutron transition rates for the de-excitation of single Λ hypernuclei on the examples of $^{209}_{\Lambda}$Pb and $^{91}_{\Lambda}$Zr have been calculated in relativistic DDRH theory. The initial state was represented by a ground state ^{A}Z core with an attached Λ single particle state, the final state as a neutron particle-hole excited ^{A}Z where the Λ hyperon occupies a lower lying single particle level and the neutron of the particle-hole pair being unbound. Hence the process corresponds to a decay of the initial single Λ configuration into a Λ-neutron-particle-hole configuration.

Due to the fact that the hypernuclear Auger effect appears mainly in heavy and intermediate mass hypernuclei the spectral distribution of the emitted neutrons is extremely complex. For this reason a very detailed reconstruction of each event will have to be done in possible experimental measurements. By focusing on initial states with the Λ in the $1f^{\Lambda}$-orbit our calculations predict a clean doublet structure in the Auger neutron spectrum from which the $1f^{\Lambda}$ spin-orbit splitting can be directly read off, assuming sufficient energy resolution. For a general Λ orbit no definite signature of the spin-orbit splitting will appear due to the huge amount of transitions and the additional broadening of peaks when deeply bound neutrons are involved. The effect of a finite width of the neutron states, increasing with the distance from the Fermi-surface has not been considered in our calculations. For the least bound neutrons it will have almost no effect, but going deeper in binding energy the broadening of the states can no longer be neglected. As described in the previous paragraphs the neutron spectra in which the deeply bound neutrons are also involved are already fairly complex. An additional broadening of the neutron levels will thus wash out most of the spectral structure there. However, in the case of the $1f^{\Lambda}$-shell de-excitation only the valence neutrons close to the Fermi-level are involved so that the spin-orbit splitting signal is going to survive in realistic spectra. Also the conditions of electromagnetic production are ideal here, since the target nucleus, ^{209}Bi is the only stable Bi isotope.

The hypernucleus $^{91}_{\Lambda}$Zr has profen very promising properties for Auger spectroscopy in the intermediate mass region when using meson induced production of hypernuclei. In this case, not even a gating on the initially produced Λ state would be necessary, due to very prominent structures which would also survive the actual experimental background and resolution. Experimentally, this cannot be produced by electroproduction, which is the method used in the proposed JLab experiment. However, as discussed above, $^{93}_{\Lambda}$Zr, for which the stable target nucleus ^{93}Nb exists, is almost equally well suited. Since $^{93}_{\Lambda}$Zr has a $J^{\pi} = 0^{+}$ core, this turns out to be an almost ideal choice.

For the spectroscopy in the intermediate and heavy mass region the hypernuclear Auger effect provides a promising complementary tool to γ spectroscopy, although special care must be taken on the choice of transitions and tagging the energy. For the $^{209}_{\Lambda}$Pb hypernucleus the $1f^{\Lambda}$ shell is such a well suited case. This technique might be the only

way to achieve high resolution information on the hypernuclear fine structure in heavy nuclei since for γ transitions it will be even harder to assign the detected photons to specific transitions.

10. Summary and Outlook

An *ab-initio* description of nuclear and hypernuclear systems was developed using a quantum field theoretical formulation in terms of baryons and mesons which are the relevant dynamical degrees of freedom in hadronic many-body systems close to the ground state. The phrase ab-initio means here, that starting from a given set of parameters describing two-body baryon scattering in free space, other baryonic systems with a non-vanishing density of valence particles can be described unambiguously without introducing any additional parameters. The elementary two-body interactions typically are defined by a set of baryon-meson coupling constants and momentum cut-off parameters defining vertex form factors. A hadron quantum field theory is a well established approach to baryon-baryon interactions being used before by various authors and in a variety of formulations. The advantages are manifold, ranging from the natural treatment of spin statistics and their influence on the structure of the fermionic and mesonic fields over the covariance and proper behaviour under Lorentz transformations of the whole theory to the implementation of internal symmetries into the Lagrangian. For the purpose of this work SU(3) flavor symmetry is of particular importance as very little is known on the interactions of hyperons among themselves and wih nucleons.

The relativistic one boson exchange potential formalism, combined with Dirac-Brueckner-Hartree-Fock (DBHF) theory for calculations at finite baryon density was chosen. The one boson exchange formalism is a well explored and widely used approximation to solve the two particle scattering problem as described by the Bethe-Salpeter equation. The method consists of truncating the full scattering kernel to tree level one meson exchange diagrams and in addition to fix the time-like component of the loop momentum in a covariant way such that the problem is reduced to an integral equation in the three space-like dimensions. The resulting integral equations are very similar to the non-relativistic Lipmann-Schwinger equation, but having the advantage of still incorporating the correct behaviour under Lorentz transformations. The latter point is especially important for in-medium calculations. In the DBHF approach the background medium is accounted for by the Pauli blocking of intermediate two-baryon states in a scattering process and the modification of the kinematics due to one body self-energies. This truncation scheme of the full self-energies is consistent with the restriction to two body interactions in the rest of our formalism.

Since a full DBHF calculation in finite systems is technically not feasible, a further approximation step is needed to calculate nuclear and hypernuclear structure from a microscopic interaction. Thus an effective interaction is calculated for an infinite system of a given density using DBHF theory, which is then applied in local density approximation to calculate finite systems To accomplish this we use the density dependent relativistic hadron (DDRH) field theory. As a relativistic meson exchange theory is used to determine the in-medium interaction, also DDRH theory is a meson-baryon quantum field

theory incorporating many-body effects by means of vertex functionals depending on the field operators. The DDRH formulation guarantees the consistency of the dynamics at all steps of the ab-initio scheme, conserving the Lorentz structur and, by fulfilling the Hugenholtz-van Hove theorem, the thermodynamical consistency of the approach. The mesons are, however, effective mesons, existing in the first place in the t-channel as mediators of the effective long-range van-der-Waals type interactions between the hadronic QCD objects under investigation. Hence, they are distinct from the mesons seen as resonances in s-channel processes although in the one boson exchange kernel masses and quantum numbers are chosen accordingly. The baryon-meson vertices in DDRH theory are functionals that depend on Lorentz scalar contractions of the baryon field operators. These functionals contain all correlation effects appearing at finite density. To determine the coupling functionals, DBHF self-energies are mapped onto DDRH self-energies. As DDRH calculations for finite nuclear systems are performed in Hartree mean-field approximation, the DBHF self-energies are mapped onto the DDRH Hartree mean-field self-energies resulting in an effective microscopic interaction as complete as possible.

As the dynamical content of the used interactions is fully known, it is possible to systematically calculate corrections within our framework. This can be done in two places: 1) the kernel of the scattering equation may be extended to contain other diagrams like, e.g., dynamical polarizations; 2) Since the vertex functionals are constructed from baryon field operators, systematic extensions of DDRH calculations beyond mean-field are possible. In contrast to phenomenological nuclear structure models these corrections are under control, since double counting can be excluded.

As an alternative approach to DBHF theory for the calculation of vertex functionals needed in DDRH theory we constructed a new formalism to solve scattering equations in terms of vertex renormalizations in one boson exchange potentials. In this scheme the full interaction is mapped onto a meson exchange kernel with $\sqrt{s}$ and density dependent vertices. The concept is inspired by renormalization theory. All relevant quantities, like, e.g., self-energies, can be calculated from the tree-level diagrams, since all higher orders are contained in the vertex factors. Especially the ambiguities arising in DBHF theory when calculating self-energies are resolved by this procedure. In a simplified model we studied the density and momentum dependence of vertices within this new approach. Good agreement with density dependent vertex functionals obtained from standard DBHF calculations was found.

Applying DBHF theory without self-energies we have studied changes in the dynamics of baryon-baryon interactions with respect to changes in couplings and mass. It was found that the most important variations in the effective interaction are due to changes in the g couplings. An important question related to the description of hypernuclei and neutron stars in phenomenological models is how reliable flavor symmetry relations are at the level of effective interactions. We found that the effective NN and ΛN interaction are not even approximately related through SU(3) relations if these symmetries are used to relate the bare interactions. It was seen, however, that there is a very simple relation between both effective interactions. Both interactions are related by a simple factor, almost independent of the density, where the relative factor is significantly smaller than the SU(3) factor applied to the bare interaction.

These findings provide a nice explanation for our results obtained in studies of Λ single

particle spectra in intermediate mass hypernuclei. DDRH theory was applied there, using vertex functionals for the Λ-meson vertices constructed from nucleon-meson vertices by scaling them with a constant factor. Fitting the scaling factors to match experimental data with our DDRH calculations, similar small scaling factors violating strongly the commonly used SU(3) relations have been obtained.

The spectra just mentioned were taken from hypernuclei containing a very high core spin. Since these spectra seemed to show an enormous spin-orbit splitting, which is inconsistent with findings in light hypernuclei, we studied the influence of a high core spin on the single particle spectrum of Λ hypernuclei. A significant broadening of the single particle peaks due to a spin-spin interaction between Λ and core washes out the peak structure of the spectra quite strongly, so that the impression of large a spin-orbit splitting arises. After removing these effects from the spectra, values of the spin-orbit strength consistent with the observations in light hypernuclei were found. From these examples it should be learned, that it is very important to reduce unwanted background signals already when choosing the target isotopes to use in an experiment. We strongly recommend to use targets for the production of hypernuclei which will lead to a hypernucleus in which the ground state of the core nucleus is known to be $J^\pi = 0^+$. A list of isotopes fulfilling this requirement was composed.

In preparation of a proposed experiment at JLab we have studied the hypernuclear Auger effect for intermediate and light single Λ hypernuclei using DDRH theory. It was shown, that the spectroscopy of Auger neutrons provides an excellent alternative to γ spectroscopy in that mass region, where the electromagnetic background is rather high. Especially in the intermediate mass region, very clean spectra are envisaged, that cleanly resolve the spin-orbit splitting of the Λ hyperon. Due to a high level density in the heavy mass region additional efforts have to be taken there, e.g. by gating on a specific initially produced Λ single particle state, to obtain clean spectra.

The relativistic ab-initio scheme presented in this work is only the starting point for more extended nuclear and hypernuclear structure calculations. We have seen, that already the ladder + RMF approximation leads to satisfactory and encouraging results. Nevertheless, there are still many pieces to add on the way toward more accurate and complete calculations.

The bare interactions used in meson exchange potentials are highly phenomenological in the sense that they are not derived from an underlying theory with a direct relation to QCD. A whole variety of potential models exists, which reproduce two body observables, e.g., scattering phase shifts, spin observables and the deuteron properties by the same accuracy. An analysis of these realistic models with renormalization group methods shows, however, that the effective low momentum potential $V_{low\,k}$ is the same for all of them [Bogner03]. The differences among these models are hidden in the parts describing short range correlations which are largely unconstrained by the data below the pion threshold, which are primarily used to fix the parameters of potential models. The actual microscopic structure of baryon-baryon interactions is given by low energy QCD, however, in a higly non-pertubative and therefore inaccessible manner. To obtain a solid basis of the microscopic interactions for ab-initio calculations, the methods of chiral effective field theory (χEFT) are a promising tool. Very recently χEFT has been applied to the

description of infinite nuclear matter properties [Kaiser03, Kaiser02] and the calculation of finite nuclei in RMF approximation [Finelli04]. Especially in the calculation of finite nuclei the QCD condensates, which are not well under control in a RMF framework, have to be introduced to account for the main binding effects. In our view it is more reasonable to try to link the very successful χEFT at the very low momenta and a meson-baryon ab-initio approach, as the one developed in this work, to describe the finite density and high momentum region, since the dynamics is there much better under control for conditions other than very low momenta. A very promising link is here the finite density effective field theory and the density functional theory approach to RMF [Furnstahl04]. The DDRH theory, however, is only affected indirectly by such uncertainties because changing the treatment of interactions at the elementary two-body level will not affect the general structure of the DDRH Langrangian but merely alter the description of the vertex functionals.

Besides these very fundamental and probably long term considerations, the dynamics of baryonic matter needs to be studied in much more detail. A very nice example in which hypernuclear structure physics can be used to explore effects that are relevant in normal nuclei is the investigation of dynamical polarizations. Their inclusion is a logical extension of the meson exchange kernel in th DBHF scheme to another class of diagrams. The effect of such corrections will be very cleanly observable in the correlation energy of the two Λ hyperons in double Λ hypernuclei.

For investigations of the interactions between hyperons only very few experimental possibilities besides hypernuclear structure physics are feasible. In view of the very high luminosity high energy heavy ion collisions at RHIC, a promising one is the $\Lambda\Lambda$ Hanbury-Brown-Twiss (HBT) interferometry. In the low momentum region of HBT correlations interaction effects between the Λ particles are visible [Greiner89, Keil02b]. Within the meson exchange framework it is straightforward to calculate these HBT correlations and make predictions for upcoming experimental data.

Appendices

A. Definitions and Conventions

A.1. Space-time metric

We define the space-time metric

$$g_{\mu\nu} = \begin{pmatrix} 1 & 0 & 0 & 0 \\ 0 & -1 & 0 & 0 \\ 0 & 0 & -1 & 0 \\ 0 & 0 & 0 & -1 \end{pmatrix}. \tag{A.1}$$

For the vectors we will use the following conventions:

$$\begin{array}{ll} a_\mu & \text{four-vector} \\ \boldsymbol{a} & \text{three-vector} \\ a = |\boldsymbol{a}| & \end{array} \tag{A.2}$$

A.2. The Dirac equation

The momentum-space Dirac equation for positive energy fermions is given by

$$\begin{aligned} (\gamma_\mu p^\mu - M)\, u(p) &= 0 \\ \overline{u}(p)\, (\gamma_\mu p^\mu - M) &= 0 \end{aligned} \tag{A.3}$$

and the one for negative energy fermions is

$$\begin{aligned} \overline{v}(p)\, (\gamma_\mu p^\mu + M) &= 0 \\ (\gamma_\mu p^\mu + M)\, v(p) &= 0 \end{aligned} \tag{A.4}$$

A.2.1. Dirac matrices and traces

We chose the following representation of the Dirac matrices throughout the calculations:

$$\boldsymbol{\gamma} := \begin{pmatrix} 0 & \boldsymbol{\sigma} \\ -\boldsymbol{\sigma} & 0 \end{pmatrix}, \quad \gamma^0 := \begin{pmatrix} 1 & 0 \\ 0 & -1 \end{pmatrix}, \quad \gamma^5 := \begin{pmatrix} 0 & 1 \\ 1 & 0 \end{pmatrix}, \tag{A.5}$$

where the Pauli matrices are given by

$$\sigma_1 = \begin{pmatrix} 0 & 1 \\ 1 & 0 \end{pmatrix}, \quad \sigma_2 = \begin{pmatrix} 0 & i \\ -i & 0 \end{pmatrix}, \quad \sigma_3 = \begin{pmatrix} 1 & 0 \\ 0 & -1 \end{pmatrix}. \tag{A.6}$$

$$\sigma^{\mu\nu} \equiv \frac{i}{2} \left[\gamma^\mu, \gamma^\nu \right] = i \left[\gamma_\mu \gamma_\nu - g_{\mu\nu} \right], \tag{A.7}$$

The γ and σ matrices obey the following anticommutation relations:

$$\{\gamma_\mu, \gamma_\nu\} = 2g_{\mu\nu} \tag{A.8}$$
$$\{\sigma_i, \sigma_j\} = 2i\epsilon^{ijk}\sigma_k \tag{A.9}$$
$$[\sigma_i, \sigma_j] = 0 \tag{A.10}$$

Further properties of the Pauli and Dirac matrices are

$$(\boldsymbol{\sigma} \cdot \boldsymbol{a})(\boldsymbol{\sigma} \cdot \boldsymbol{b}) = \boldsymbol{a} \cdot \boldsymbol{b} + \boldsymbol{\sigma} \cdot (\boldsymbol{a} \times \boldsymbol{b}) \tag{A.11}$$

$$\gamma_\mu^\dagger = \gamma_0 \gamma_\mu \gamma_0, \tag{A.12}$$
$$\gamma_5^\dagger = -\gamma_0 \gamma_5 \gamma_0 = \gamma_5, \tag{A.13}$$
$$\sigma_{\mu\nu}^\dagger = \gamma_0 \sigma_{\mu\nu} \gamma_0, \tag{A.14}$$

$$a_\mu \gamma^\mu b_\nu \gamma^\nu = a_\mu b^\mu - i\sigma_{\mu\nu} a^\mu b^\nu \tag{A.15}$$
$$\gamma_\mu \gamma^\mu = 4 \tag{A.16}$$
$$\gamma_\mu \gamma_\nu \gamma^\mu = -2\gamma_\nu \tag{A.17}$$
$$\gamma_\sigma \gamma_\mu \gamma_\nu \gamma^\sigma = 4g_{\mu\nu} \tag{A.18}$$

Trace formulas

$$\mathrm{Tr}\,(1) = 4 \tag{A.19}$$
$$\mathrm{Tr}\,(\gamma_{\mu_1}\gamma_{\mu_2}\cdots\gamma_{\mu_{2n+1}}) = 0 \tag{A.20}$$
$$\mathrm{Tr}\,(\gamma_\mu\gamma_\nu) = 4g_{\mu\nu} \tag{A.21}$$
$$\mathrm{Tr}\,(\gamma_\mu\gamma_\nu\gamma_\sigma\gamma_\tau) = 4\left(g_{\mu\nu}g_{\sigma\tau} + g_{\mu\tau}g_{\nu\sigma} - g_{\mu\sigma}g_{\nu\tau}\right) \tag{A.22}$$
$$\mathrm{Tr}\,(\gamma_5) = 0 \tag{A.23}$$
$$\mathrm{Tr}\,(\gamma_5\gamma_{\mu_1}\gamma_{\mu_2}\cdots\gamma_{\mu_{2n+1}}) = 0 \tag{A.24}$$
$$\mathrm{Tr}\,(\gamma_5\gamma_\mu\gamma_\nu) = 0 \tag{A.25}$$
$$\mathrm{Tr}\,(\gamma_5\gamma_\mu\gamma_\nu\gamma_\sigma\gamma_\tau) = 4i\epsilon_{\mu\nu\sigma\tau} \tag{A.26}$$

A.3. Lorentz boost

A Lorentz vector A is boosted with velocity $\boldsymbol{\beta}$ to become the Lorentz vector B by the following transformation

$$B^0 = \gamma\left(A^0 - \boldsymbol{\beta}\boldsymbol{A}\right) \tag{A.27}$$
$$\boldsymbol{B} = \boldsymbol{A} + \gamma\boldsymbol{\beta}\left(\frac{\gamma}{1+\gamma}\boldsymbol{\beta}\boldsymbol{A} - A^0\right) \tag{A.28}$$

with

$$\gamma = \frac{1}{1 - \beta^2} \tag{A.29}$$

B. Meson Exchange Models

In this appendix we will explicitly describe all technical details which are necessary for an actual T-matrix calculation of meson exchange baryon-baryon interactions in a 3D reduced BS equation. This involves the one boson exchange matrix elements, partial wave decomposition and potential parameters.

B.1. Helicity matrix elements of Born diagrams

B.1.1. Definitions and conventions

Spinors

The matrix elements are evaluated with respect to plane wave helicity basis states. This is the basis needed for the partial wave decomposed formalism to solve the BS equation. We use the same conventions as described in [Machleidt91].

$$u(\boldsymbol{q}, \lambda) = \sqrt{\frac{E+M}{2M}} \left(\begin{array}{c} 1 \\ \frac{2\lambda q}{E+M} \end{array} \right) |\lambda\rangle \tag{B.1}$$

$$u(-\boldsymbol{q}, \lambda) = \sqrt{\frac{E+M}{2M}} \left(\begin{array}{c} 1 \\ \frac{2\lambda q}{E+M} \end{array} \right) |\lambda\rangle ,$$

where the covariant normalization

$$\overline{u}(\boldsymbol{q}, \lambda) u(\boldsymbol{q}, \lambda) = 1 \tag{B.2}$$

is chosen with $\overline{u} = u^\dagger \gamma^0$.

Abbreviations

$$
\begin{aligned}
q &\equiv |\boldsymbol{q}| \\
E_{q^{(\prime)}}^{(i)} &\equiv \sqrt{q^{(\prime)2} + M_i^2} \\
W_i^{(\prime)} &\equiv E_{q^{(\prime)}}^{(i)} + M_i \\
C &\equiv \frac{1}{4} \sqrt{\frac{W_1 W_1' W_2 W_2'}{M_1 M_1' M_2 M_2'}}
\end{aligned}
\tag{B.3}
$$

Basic helicity matrix elements

$$
\begin{aligned}
\Gamma_1 &\equiv \overline{u}_1(\boldsymbol{q}',\lambda_1')\gamma_\mu u_1(\boldsymbol{q},\lambda_1)u_2(-\boldsymbol{q},\lambda_2)\gamma^\mu u_2(-\boldsymbol{q},\lambda_2) && \text{(B.4)}\\
&= \overline{u}_1(\boldsymbol{q}',\lambda_1')u_1(\boldsymbol{q},\lambda_1)\overline{u}_2(-\boldsymbol{q}',\lambda_2')u_2(-\boldsymbol{q},\lambda_2) - \\
&\quad \overline{u}_1(\boldsymbol{q}',\lambda_1')\boldsymbol{\sigma_1}u_1(\boldsymbol{q},\lambda_1)\cdot\overline{u}_2(-\boldsymbol{q}',\lambda_2')\boldsymbol{\sigma_2}u_2(-\boldsymbol{q},\lambda_2) \\
&= C\left\{\left(1+\frac{4\lambda_1\lambda_1'qq'}{W_1W_1'}\right)\left(1+\frac{4\lambda_2\lambda_2'qq'}{W_2W_2'}\right)\langle\lambda_1'\lambda_2'|\lambda_1\lambda_2\rangle\right. \\
&\quad \left. -\left(\frac{2\lambda_1q}{W_1}+\frac{2\lambda_1'q'}{W_1'}\right)\left(\frac{2\lambda_2q}{W_2}+\frac{2\lambda_2'q'}{W_2'}\right)\right\}\langle\lambda_1'\lambda_2'|\boldsymbol{\sigma}_1\cdot\boldsymbol{\sigma}_2|\lambda_1\lambda_2\rangle
\end{aligned}
$$

$$
\begin{aligned}
\Gamma_2 &= \overline{u}_1(\boldsymbol{q}',\lambda_1')u_1(\boldsymbol{q},\lambda_1)\overline{u}_2(-\boldsymbol{q}',\lambda_2')u_2(-\boldsymbol{q},\lambda_2) && \text{(B.5)}\\
&= C\left(1-\frac{4\lambda_1\lambda_1'qq'}{W_1W_1'}\right)\left(1-\frac{4\lambda_2\lambda_2'qq'}{W_2W_2'}\right)\langle\lambda_1'\lambda_2'|\lambda_1\lambda_2\rangle
\end{aligned}
$$

$$
\begin{aligned}
\Gamma_3 &= \overline{u}_1(\boldsymbol{q}',\lambda_1')\gamma^0 u_1(\boldsymbol{q},\lambda_1)\overline{u}_2(-\boldsymbol{q}',\lambda_2')u_2(-\boldsymbol{q},\lambda_2) && \text{(B.6)}\\
&= C\left(1+\frac{4\lambda_1\lambda_1'qq'}{W_1W_1'}\right)\left(1-\frac{4\lambda_2\lambda_2'qq'}{W_2W_2'}\right)\langle\lambda_1'\lambda_2'|\lambda_1\lambda_2\rangle
\end{aligned}
$$

$$
\begin{aligned}
\Gamma_4 &= \overline{u}_1(\boldsymbol{q}',\lambda_1')u_1(\boldsymbol{q},\lambda_1)\overline{u}_2(-\boldsymbol{q}',\lambda_2')\gamma^0 u_2(-\boldsymbol{q},\lambda_2) && \text{(B.7)}\\
&= C\left(1-\frac{4\lambda_1\lambda_1'qq'}{W_1W_1'}\right)\left(1+\frac{4\lambda_2\lambda_2'qq'}{W_2W_2'}\right)\langle\lambda_1'\lambda_2'|\lambda_1\lambda_2\rangle
\end{aligned}
$$

$$
\begin{aligned}
\Gamma_5 &= \overline{u}_1(\boldsymbol{q}',\lambda_1')\gamma^0\boldsymbol{\gamma} u_1(\boldsymbol{q},\lambda_1)\overline{u}_2(-\boldsymbol{q}',\lambda_2')\gamma^0\boldsymbol{\gamma} u_2(-\boldsymbol{q},\lambda_2) && \text{(B.8)}\\
&= C\left(\frac{2\lambda_1q}{W_1}-\frac{2\lambda_1'q'}{W_1'}\right)\left(\frac{2\lambda_2q}{W_2}-\frac{2\lambda_2'q'}{W_2'}\right)\langle\lambda_1'\lambda_2'|\boldsymbol{\sigma}_1\cdot\boldsymbol{\sigma}_2|\lambda_1\lambda_2\rangle
\end{aligned}
$$

$$
\begin{aligned}
\Gamma_6 &= \overline{u}_1(\boldsymbol{q}',\lambda_1')\gamma^0\boldsymbol{\gamma} u_1(\boldsymbol{q},\lambda_1)\overline{u}_2(-\boldsymbol{q}',\lambda_2')\boldsymbol{\gamma} u_2(-\boldsymbol{q},\lambda_2) && \text{(B.9)}\\
&= C\left(\frac{2\lambda_1q}{W_1}-\frac{2\lambda_1'q'}{W_1'}\right)\left(\frac{2\lambda_2q}{W_2}+\frac{2\lambda_2'q'}{W_2'}\right)\langle\lambda_1'\lambda_2'|\boldsymbol{\sigma}_1\cdot\boldsymbol{\sigma}_2|\lambda_1\lambda_2\rangle
\end{aligned}
$$

$$
\begin{aligned}
\Gamma_7 &= \overline{u}_1(\boldsymbol{q}',\lambda_1')\boldsymbol{\gamma} u_1(\boldsymbol{q},\lambda_1)\overline{u}_2(-\boldsymbol{q}',\lambda_2')\gamma^0\boldsymbol{\gamma} u_2(-\boldsymbol{q},\lambda_2) && \text{(B.10)}\\
&= C\left(\frac{2\lambda_1q}{W_1}+\frac{2\lambda_1'q'}{W_1'}\right)\left(\frac{2\lambda_2q}{W_2}-\frac{2\lambda_2'q'}{W_2'}\right)\langle\lambda_1'\lambda_2'|\boldsymbol{\sigma}_1\cdot\boldsymbol{\sigma}_2|\lambda_1\lambda_2\rangle
\end{aligned}
$$

$$
\begin{aligned}
\Gamma_8 &= \overline{u}_1(\boldsymbol{q}',\lambda_1')\gamma^5 u_1(\boldsymbol{q},\lambda_1)\overline{u}_2(-\boldsymbol{q}',\lambda_2')\gamma^5 u_2(-\boldsymbol{q},\lambda_2) && \text{(B.11)}\\
&= C\left(\frac{2\lambda_1q}{W_1}-\frac{2\lambda_1'q'}{W_1'}\right)\left(\frac{2\lambda_2q}{W_2}-\frac{2\lambda_2'q'}{W_2'}\right)\langle\lambda_1'\lambda_2'|\lambda_1\lambda_2\rangle
\end{aligned}
$$

$$\Gamma_9 = \overline{u}_1(\boldsymbol{q}', \lambda_1')\gamma^0\gamma^5 u_1(\boldsymbol{q}, \lambda_1)\overline{u}_2(-\boldsymbol{q}', \lambda_2')\gamma^0\gamma^5 u_2(-\boldsymbol{q}, \lambda_2) \tag{B.12}$$

$$= C\left(\frac{2\lambda_1 q}{W_1} + \frac{2\lambda_1' q'}{W_1'}\right)\left(\frac{2\lambda_2 q}{W_2} + \frac{2\lambda_2' q'}{W_2'}\right)\langle\lambda_1'\lambda_2'|\lambda_1\lambda_2\rangle$$

$$\Gamma_{10} = \overline{u}_1(\boldsymbol{q}', \lambda_1')\gamma^0\gamma^5 u_1(\boldsymbol{q}, \lambda_1)\overline{u}_2(-\boldsymbol{q}', \lambda_2')\gamma^5 u_2(-\boldsymbol{q}, \lambda_2) \tag{B.13}$$

$$= C\left(\frac{2\lambda_1 q}{W_1} + \frac{2\lambda_1' q'}{W_1'}\right)\left(\frac{2\lambda_2 q}{W_2} - \frac{2\lambda_2' q'}{W_2'}\right)\langle\lambda_1'\lambda_2'|\lambda_1\lambda_2\rangle$$

$$\Gamma_{11} = \overline{u}_1(\boldsymbol{q}', \lambda_1')\gamma^5 u_1(\boldsymbol{q}, \lambda_1)\overline{u}_2(-\boldsymbol{q}', \lambda_2')\gamma^0\gamma^5 u_2(-\boldsymbol{q}, \lambda_2) \tag{B.14}$$

$$= C\left(\frac{2\lambda_1 q}{W_1} - \frac{2\lambda_1' q'}{W_1'}\right)\left(\frac{2\lambda_2 q}{W_2} + \frac{2\lambda_2' q'}{W_2'}\right)\langle\lambda_1'\lambda_2'|\lambda_1\lambda_2\rangle$$

The spin dependent part of the helicity matrix elements can be expressed in closed form:

$$\langle\lambda_1'\lambda_2'|\lambda_1\lambda_2\rangle = \{|\lambda_1' + \lambda_1|\cos + (\lambda_1' - \lambda_1)\sin\}\{|\lambda_2' + \lambda_2|\cos - (\lambda_2' - \lambda_2)\sin\} \tag{B.15}$$

$$\langle\lambda_1'\lambda_2'|\boldsymbol{\sigma}_1 \cdot \boldsymbol{\sigma}_2|\lambda_1\lambda_2\rangle = -\{(\lambda_1' + \lambda_1)\sin + |\lambda_1' - \lambda_1|\cos\}\{(\lambda_2' + \lambda_2)\sin - |\lambda_2' - \lambda_2|\cos\}$$
$$- \{|\lambda_1' + \lambda_1|\sin - (\lambda_1' - \lambda_1)\cos\}\{|\lambda_2' + \lambda_2|\sin + (\lambda_2' - \lambda_2)\cos\}$$
$$- \{(\lambda_1' + \lambda_1)\cos - |\lambda_1' - \lambda_1|\sin\}\{(\lambda_2' + \lambda_2)\cos + |\lambda_2' - \lambda_2|\sin\} \tag{B.16}$$

$\cos = \cos(\frac{1}{2}\theta)$, $\sin = \sin(\frac{1}{2}\theta)$.

process	mesons	$T = \frac{1}{2}$	$T = \frac{3}{2}$
$N\Lambda \to N\Lambda$	σ, ω	1	0
$N\Sigma \to N\Sigma$	σ, ω	1	1
$N\Sigma \to N\Sigma$	π, ρ	-2	1
$N\Lambda \to N\Sigma$	π, ρ	$\sqrt{3}$	0
$N\Lambda \to \Lambda N$	K, K^*	1	0
$N\Sigma \to \Sigma N$	K, K^*	-1	2
$N\Lambda \to \Sigma N$	K, K^*	$\sqrt{3}$	0

Table B.1.: Isospin factors for the kernel matrix elements involving hyperons and nucleons as calculated in [Holzenkamp88].

Due to isospin invariance the isospin dependent part of the matrix elements, like, e.g., $\langle\tau_1'\tau_2'|\boldsymbol{\tau} \cdot \boldsymbol{\tau}|\tau_1\tau_2\rangle$ factorizes and can be evaluated separately. Isospin invariance allows only a dependence of these isospin factors on total isospin T. For nucleons, where only isoscalar and isovector mesons appear, the matrix elements are

$$\langle T'|T\rangle = \delta_{T'T}$$
$$\langle T'|\boldsymbol{\tau} \cdot \boldsymbol{\tau}|T\rangle = 4\langle T'|\boldsymbol{t} \cdot \boldsymbol{t}|T\rangle \tag{B.17}$$
$$= 2(T(T+1) - \frac{3}{2}))\delta_{T'T} = \begin{cases} -3\delta_{T'T} & \text{for } T = 0 \\ 1\delta_{T'T} & \text{for } T = 1 \end{cases}$$

($\boldsymbol{\tau} = 2\boldsymbol{t}$) For matrix elements involving hyperons, the calculation is a bit more tedious. It has been worked out for YN scattering in [Holzenkamp88]. We list the results obtained there in tab. B.1.

B.1.2. Helicity matrix elements

In the following section the explicit expressions for the Born matrix elements of the different Lorentz structures are given. The functional form of the used form factors is

$$\mathcal{F}_\alpha \left[(\boldsymbol{q}' - \boldsymbol{q})^2\right] = \left[\frac{\Lambda_\alpha^2 - m_\alpha^2}{\Lambda_\alpha^2 + (\boldsymbol{q}' - \boldsymbol{q})^2 - \delta q^0}\right]^{n_\alpha} \tag{B.18}$$

where n_α, Λ_α and m_α are the cutoff exponent, cutoff mass and meson mass, respectively.

$$\mathcal{D}_\alpha \left[(\boldsymbol{q}' - \boldsymbol{q})^2\right] = \frac{i}{(\boldsymbol{q}' - \boldsymbol{q})^2 + m_\alpha^2 - \delta q^0} \tag{B.19}$$

is the meson propagator. For vector mesons there will be the metric tensor $g_{\mu\nu}$ in the numerator. δq^0 is the energy transfer which assures the consistency of the BS equation for different masses in entrance and exit channel, see sec. 2.2.2. It is a constant like the mass, not depending on the loop integrations.

In the matrix elements we include a factor $(2\pi)^{-3}$, which is absorbed from the integral measure as noted following eq.(2.12).

scalar

$$\langle \boldsymbol{q}', \lambda_1', \lambda_2' | V_s | \boldsymbol{q}, \lambda_1, \lambda_2 \rangle = -\frac{g_s^{(1)} g_s^{(2)}}{(2\pi)^3} \overline{u}_1(\boldsymbol{q}', \lambda_1') u_1(\boldsymbol{q}, \lambda_1) \overline{u}_2(-\boldsymbol{q}', \lambda_2') u_2(-\boldsymbol{q}, \lambda_2) \times$$
$$\mathcal{D}_\sigma \left[(\boldsymbol{q}' - \boldsymbol{q})^2\right] \mathcal{F}_1 \left[(\boldsymbol{q}' - \boldsymbol{q})^2\right] \mathcal{F}_2 \left[(\boldsymbol{q}' - \boldsymbol{q})^2\right] \tag{B.20}$$
$$= -\frac{g_s^{(1)} g_s^{(2)}}{(2\pi)^3} \Gamma_2 \mathcal{D}_s \left[(\boldsymbol{q}' - \boldsymbol{q})^2\right] \mathcal{F}_1 \left[(\boldsymbol{q}' - \boldsymbol{q})^2\right] \mathcal{F}_2 \left[(\boldsymbol{q}' - \boldsymbol{q})^2\right]$$

pseudoscalar

$$\langle \boldsymbol{q}', \lambda_1', \lambda_2' | V_{ps} | \boldsymbol{q}, \lambda_1, \lambda_2 \rangle = -\frac{g_{ps}^{(1)} g_{ps}^{(2)}}{(2\pi)^3} \overline{u}_1(\boldsymbol{q}', \lambda_1') \gamma^5 u_1(\boldsymbol{q}, \lambda_1) \overline{u}_2(-\boldsymbol{q}', \lambda_2') \gamma^5 u_2(-\boldsymbol{q}, \lambda_2) \times$$
$$\mathcal{D}_\sigma \left[(\boldsymbol{q}' - \boldsymbol{q})^2\right] \mathcal{F}_1 \left[(\boldsymbol{q}' - \boldsymbol{q})^2\right] \mathcal{F}_2 \left[(\boldsymbol{q}' - \boldsymbol{q})^2\right]$$
$$= -\frac{g_{ps}^{(1)} g_{ps}^{(2)}}{(2\pi)^3} \Gamma_8 \mathcal{D}_{ps} \left[(\boldsymbol{q}' - \boldsymbol{q})^2\right] \mathcal{F}_1 \left[(\boldsymbol{q}' - \boldsymbol{q})^2\right] \mathcal{F}_2 \left[(\boldsymbol{q}' - \boldsymbol{q})^2\right]$$
$$\tag{B.21}$$

vector

In the evaluation of the vector matrix element special care has to be taken because of the derivative appearing in the magnetic part of the coupling. As discussed in sec. 2.2, the structure of the BS equation in 3D form is such, that all the way through the multiple scatterings, the initial $\sqrt{s}$ fixes the zero component of the particles' momenta. It is fixed symmetrically, according to their masses. The energy transfer is then given by $k_1{}^0 - k_1'{}^0 = (x_2 - x_2')\sqrt{s}$, and the three momentum transfer is, in terms of the relative momenta, $(\boldsymbol{q} - \boldsymbol{q}')$. Due to the 3D reduction an explicit $\sqrt{s}$ dependence enters in the case of different masses in entrance and exit channel! An additional i is also obtained by the derivative. Since $\sigma_{\mu\nu}F^{\mu\nu} = 2\sigma_{\mu\nu}\partial^\mu\phi^\nu$, the tensor part of the basic vertex, eq.(2.2), becomes

$$-\frac{f_v^{(i)}}{M_i + M_i'}\overline{u}_i(\boldsymbol{q}', \lambda_i')\sigma_{\mu\nu}u_i(\boldsymbol{q}, \lambda_i)\left[\pm i\left(\begin{array}{c}(x_2 - x_2')\sqrt{s}\\ \boldsymbol{q}' - \boldsymbol{q}\end{array}\right)\right]^\mu \tag{B.22}$$

The $\pm$ takes care of the different signs for the two vertices in the Born amplitude, arising from the direction of the exchanged momentum. A zero is added to the exchanged momentum to make up for two on-shell momentum vectors Q, so that the Dirac equation (A.3) may be exploited for a further evaluation of the matrix element

$$Q_{(i)}^{(')} \equiv \left(\begin{array}{c}E_i^{(')}\\ \pm\boldsymbol{q}^{(')}\end{array}\right) \tag{B.23}$$

$\pm$ again corresponds to the two different vertices, $i = 1, 2$. Eq. (B.22) becomes then

$$\frac{f_v^{(i)}}{M_i + M_i'}\overline{u}_i(\boldsymbol{q}', \lambda_i')\left[\gamma_\mu\gamma_\nu - g_{\mu\nu}\right]u_i(\boldsymbol{q}, \lambda_i)\left[Q_{(i)}'^\mu - Q_{(i)}^\mu + \Delta_E^{(i)}g^{0\mu}\right], \tag{B.24}$$

$$\Delta_E^{(i)} \equiv \pm(x_2 - x_2')\sqrt{s} - (E_{(i)} - E_{(i)}'). \tag{B.25}$$

By commuting the γ_μ to the correct side and exploiting the Dirac equation (A.3) as

$$\gamma_\mu Q_{(i)}^\mu u_i(\boldsymbol{q}, \lambda_i) = M_i u_i(\boldsymbol{q}, \lambda_i), \text{ and } \overline{u}_i(\boldsymbol{q}', \lambda_i')\gamma_\mu Q_{(i)}'^\mu = M_i\overline{u}_i(\boldsymbol{q}', \lambda_i'), \tag{B.26}$$

one finally finds

$$-\frac{f_v^{(i)}}{M_i + M_i'}\overline{u}_i(\boldsymbol{q}', \lambda_i')\sigma_{\mu\nu}u_i(\boldsymbol{q}, \lambda_i)\left[\pm i\left(\begin{array}{c}(x_2 - x_2')\sqrt{s}\\ \boldsymbol{q}' - \boldsymbol{q}\end{array}\right)\right]^\mu =$$
$$f_v^{(i)}\left\{\overline{u}_i(\boldsymbol{q}', \lambda_i')\gamma_\nu u_i(\boldsymbol{q}, \lambda_i) - \frac{1}{M_i + M_i'}\left[(Q_{(i)}' + Q_{(i)})_\nu - \Delta_E^{(i)}(\gamma_0\gamma_\nu - g_{0\nu})\right]u_i(\boldsymbol{q}, \lambda_i)\right\} \tag{B.27}$$

By using the following relations

$$\begin{aligned}\overline{u}_1(\boldsymbol{q}', \lambda_1')\gamma_\mu(Q_{(2)}' + Q_{(2)})^\mu u_1(\boldsymbol{q}, \lambda_1) &= -(M_1 + M_1')\overline{u}_1(\boldsymbol{q}', \lambda_1')u_1(\boldsymbol{q}, \lambda_1)\\ &\quad + \Sigma_E\overline{u}_1(\boldsymbol{q}', \lambda_1')\gamma^0 u_1(\boldsymbol{q}, \lambda_1)\\ (Q_{(1)}' + Q_{(1)})_\mu(Q_{(2)}' + Q_{(2)})^\mu &= (E_{(1)}' + E_{(1)})(E_{(2)}' + E_{(2)})\\ &\quad + (\boldsymbol{q}' + \boldsymbol{q})\\ \overline{u}_1(\boldsymbol{q}', \lambda_1')(\gamma_0\gamma_\nu - g_{9\nu})(Q_{(2)}' + Q_{(2)})^\nu u_1(\boldsymbol{q}, \lambda_1) &= (M_{(1)}' - M_{(1)})\overline{u}_1(\boldsymbol{q}', \lambda_1')\gamma^0 u_1(\boldsymbol{q}, \lambda_1)\\ &\quad - (E_{(1)}' - E_{(1)})\overline{u}_1(\boldsymbol{q}', \lambda_1')u_1(\boldsymbol{q}, \lambda_1),\end{aligned}$$

where $\Sigma_E = E'_{(1)} + E_{(1)} + E'_{(2)} + E_{(2)}$, we find the final expression for the vector matrix element

$$
\begin{aligned}
\langle \boldsymbol{q}', \lambda'_1, \lambda'_2 | \, V_v \, | \boldsymbol{q}, \lambda_1, \lambda_2 \rangle = & \\
\big[(g^{(1)} + f^{(1)})&(g^{(2)} + f^{(2)})\Gamma_1 \\
& - (g^{(1)} + f^{(1)})\frac{f^{(2)}}{M_2 + M'_2}\left\{ -(M_1 + M'_1)\Gamma_2 + \Sigma_E \Gamma_3 + \Delta_E^{(2)}\Gamma_7 \right\} \\
& - \frac{f^{(1)}}{M_1 + M'_1}(g^{(2)} + f^{(2)})\left\{ -(M_2 + M'_2)\Gamma_2 + \Sigma_E \Gamma_4 + \Delta_E^{(1)}\Gamma_6 \right\} \\
& + \frac{f^{(1)}}{M_1 + M'_1}\frac{f^{(2)}}{M_2 + M'_2}\Big\{ \big((E_1 + E'_1)(E_2 + E'_2) + \boldsymbol{q}^2 + \boldsymbol{q}'^2 + 2|\boldsymbol{q}||\boldsymbol{q}'|\cos(\theta_c) \big)\,\Gamma_2 \\
& \qquad\qquad\qquad\qquad + \Delta_e^{(1)}(M'_1 - M_1)\Gamma_3 - \Delta_E^{(1)^2}\Gamma_2 \\
& \qquad\qquad\qquad\qquad + \Delta_e^{(2)}(M'_2 - M_2)\Gamma_4 - \Delta_E^{(2)^2}\Gamma_2 \\
& \qquad\qquad\qquad\qquad - \Delta_E^{(1)}\Delta_E^{(2)}\Gamma_5 \Big\} \\
\big]& \mathcal{D}_v\left[(\boldsymbol{q}' - \boldsymbol{q})^2\right] \mathcal{F}_1\left[(\boldsymbol{q}' - \boldsymbol{q})^2\right] \mathcal{F}_2\left[(\boldsymbol{q}' - \boldsymbol{q})^2\right]
\end{aligned}
$$

(B.28)

Please note, that the first term of $\Delta_E^{(i)}$ comes with opposite signs for $i = 1, 2$ as defined in eq.(B.25).

pseudovector

In analogy to the tensor vertex, also the derivative of the pseudovector vertex, eq.(2.1), has to be evaluated:

$$
\begin{aligned}
& -\frac{f_{ps}}{m_{ps}} \overline{u}_1(\boldsymbol{q}', \lambda'_1)\gamma_5\gamma_\mu u_1(\boldsymbol{q}, \lambda_1)\partial^\mu\phi = \\
& -\frac{f_{ps}}{m_{ps}} \left[-(M_1 + M'_1)\overline{u}_1(\boldsymbol{q}', \lambda'_1)\gamma_5 u_1(\boldsymbol{q}, \lambda_1) - \Delta_E^{(1)}\overline{u}_1(\boldsymbol{q}', \lambda'_1)\gamma^0\gamma_5 u_1(\boldsymbol{q}, \lambda_1) \right]
\end{aligned}
$$

(B.29)

The contraction of both vertices, multiplied by propagator, formfactor, etc., yields the pseudovector matrix element:

$$
\begin{aligned}
\langle \boldsymbol{q}', \lambda'_1, \lambda'_2 | \, V_{pv} \, | \boldsymbol{q}, \lambda_1, \lambda_2 \rangle = & \\
\frac{f_{ps}^{(1)} f_{ps}^{(2)}}{m_{ps}^2} \big[& (M_1 + M'_1)(M_2 + M'_2)\Gamma_8 + \Delta_E^{(1)}\Delta_E^{(2)}\Gamma_9 \\
& - \Delta_E^{(1)}(M_2 + M'_2)\Gamma_{10} - \Delta_E^{(2)}(M_1 + M'_1)\Gamma_{11} \big] \\
& \mathcal{D}_{pv}\left[(\boldsymbol{q}' - \boldsymbol{q})^2\right] \mathcal{F}_1\left[(\boldsymbol{q}' - \boldsymbol{q})^2\right] \mathcal{F}_2\left[(\boldsymbol{q}' - \boldsymbol{q})^2\right]
\end{aligned}
$$

(B.30)

Please note also here, that the first term of $\Delta_E^{(i)}$ comes with opposite signs for $i = 1, 2$ as defined in eq.(B.25).

B.2. Partial wave decomposition

The BS equation is for its numerical solution decomposed into partial waves which reduces the space-like part of the integral into an easily tractable one dimensional integral. One employs here the complete set of Wigner d-functions $d_{\lambda\lambda'}^{J}(\theta)$ which are used to transform (rotate) a particle pair with relative momentum $\boldsymbol{q}$ and relative helicity $\lambda = \lambda_1 - \lambda_2$ into a pair with relative momentum $\boldsymbol{q}'$ and relative helicity $\lambda' = \lambda_1' - \lambda_2'$ where both pairs have a total angular momentum of J [Brink93]. The angle between the two relative momenta will be called θ. The expansion of the full amplitude in partial waves is then given by

$$\langle q' \lambda_1' \lambda_2' | V | q \lambda_1 \lambda_2 \rangle = \frac{1}{4\pi} \sum_J (2J+1) d_{\lambda\lambda'}^{J}(\theta) \langle \lambda_1' \lambda_2' | V^J(\boldsymbol{q}', \boldsymbol{q}) | \lambda_1 \lambda_2 \rangle \qquad (B.31)$$

Using the completeness relation, eq.(B.34), this immediately gives us the rule how to decompose a given matrix element into its different angular momenta:

$$\langle \lambda_1' \lambda_2' | V^J(\boldsymbol{q}', \boldsymbol{q}) | \lambda_1 \lambda_2 \rangle = 2\pi \int_{-1}^{1} d\cos(\theta) d_{\lambda\lambda'}^{J}(\theta) \langle q' \lambda_1' \lambda_2' | V | q \lambda_1 \lambda_2 \rangle \qquad (B.32)$$

With these tools the BS equation can now be decomposed as total into the partial wave representation:

$$\langle \lambda_1' \lambda_2' | T^J(\boldsymbol{q}', \boldsymbol{q}, s) | \lambda_1 \lambda_2 \rangle = \langle \lambda_1' \lambda_2' | V^J(\boldsymbol{q}', \boldsymbol{q}) | \lambda_1 \lambda_2 \rangle +$$
$$\sum_{h_1 h_2} \int dk k^2 \langle \lambda_1' \lambda_2' | V^J(\boldsymbol{q}', \boldsymbol{k}) | h_1 h_2 \rangle \langle h_1 h_2 | T^{J'}(\boldsymbol{k}, \boldsymbol{q}) | \lambda_1 \lambda_2 \rangle$$
$$(B.33)$$

B.2.1. Properties of d functions

Here we list some useful properties of the d functions. Orthogonality and symmetry relations are those of [Brink93], the formulation in terms of Legendre polynomials can be found, e.g., in [Machleidt87].

Orthogonality relations

$$\int_{-1}^{1} d\cos(\theta) \, d_{\lambda\lambda'}^{J}(\theta) d_{\lambda\lambda'}^{J'}(\theta) = \delta_{JJ'} \frac{2}{2J+1} \qquad (B.34)$$

$$\sum_{m''} d_{mm''}^{J}(\theta_1) d_{m''m'}^{J}(\theta_2) = d_{mm'}^{J}(\theta_1 + \theta_2) \qquad (B.35)$$

Symmetry relations

$$d_{mm'}^{J}(\theta) = (-)^{m-m'} d_{m'm}^{J}(\theta) = d_{-m'-m}^{J}(\theta) = d_{m'm}^{J}(-\theta)$$
$$= (-)^{J-m} d_{m-m'}^{J}(\pi - \theta) = (-)^{J+m} d_{m-m'}^{J}(\pi + \theta) \qquad (B.36)$$

Relation to the Legendre polynomials

Since m and m' are always relative helicities, they can only take the values 0 and ± 1.

$$d_{00}^J(\theta) = P_J(\cos(\theta)), \tag{B.37}$$

$$\begin{aligned}
(1 + \cos(\theta))d_{11}^J(\theta) &= P_J + \frac{J+1}{2J+1}P_{J-1} + \frac{1}{2J+1}P_{J+1} \\
&= P_j + \frac{J}{J+1}\cos(\theta)P_J + \frac{1}{J+1}P_{J-1}
\end{aligned} \tag{B.38}$$

$$\begin{aligned}
(1 - \cos(\theta))d_{-11}^J(\theta) &= -P_J + \frac{J+1}{2J+1}P_{J-1} + \frac{1}{2J+1}P_{J+1} \\
&= -P_j + \frac{J}{J+1}\cos(\theta)P_J + \frac{1}{J+1}P_{J-1}
\end{aligned} \tag{B.39}$$

$$\begin{aligned}
\sin(\theta)d_{10}^J(\theta) &= \frac{\sqrt{J(J+1)}}{2J+1}(P_{J+1} - P_{j-1}) \\
&= \sqrt{\frac{J}{J+1}}(\cos(\theta)P_J - P_{J-1})
\end{aligned} \tag{B.40}$$

B.2.2. Partial wave decomposition of helicity matrix elements

$\lambda_1'\lambda_2'\lambda_1\lambda_2$	$\langle\lambda_1'\lambda_2'|\lambda_1\lambda_2\rangle\, d_{m_1,m_2}^J$	$\langle\lambda_1'\lambda_2'|\vec{\sigma}_1\cdot\vec{\sigma}_2|\lambda_1\lambda_2\rangle\, d_{m_1,m_2}^J$
$++++$	$\frac{1}{2}(x+1)P_J$	$\frac{1}{2}(x-3)P_J$
$++--$	$\frac{1}{2}(x-1)P_J$	$\frac{1}{2}(x+3)P_J$
$+-+-$	$\frac{1}{2(J+1)}(P_{J-1}+(1+J+Jx)P_J)$	$\frac{1}{2(J+1)}(P_{J-1}+(1+J+Jx)P_J)$
$+--+$	$\frac{1}{2(J+1)}(P_{J-1}+(J(x-1)-1)P_J)$	$\frac{1}{2(J+1)}(P_{J-1}+(J(x-1)-1)P_J)$
$+++-$	$\frac{1}{2}\sqrt{\frac{J}{J+1}}(P_{J-1}-xP_J)$	$\frac{1}{2}\sqrt{\frac{J}{J+1}}(P_{J-1}-xP_J)$
$+-++$	$\frac{1}{2}\sqrt{\frac{J}{J+1}}(P_{J-1}-xP_J)$	$\frac{1}{2}\sqrt{\frac{J}{J+1}}(P_{J-1}-xP_J)$
$++-+$	$\frac{1}{2}\sqrt{\frac{J}{J+1}}(P_{J-1}-xP_J)$	$\frac{1}{2}\sqrt{\frac{J}{J+1}}(P_{J-1}-xP_J)$
$-+++$	$-\frac{1}{2}\sqrt{\frac{J}{J+1}}(P_{J-1}-xP_J)$	$-\frac{1}{2}\sqrt{\frac{J}{J+1}}(P_{J-1}-xP_J)$

Table B.2.: Elementary spin-operator matrix elements multiplied with $d_{\lambda_1-\lambda_2,\lambda_1'-\lambda_2'}^J$ as it appears in the partial wave decomposition of kernel matrix elements.

In the actual evaluation of eq.(B.32) for decomposing the BS kernel of one boson exchange models we always get integrals of the following types:

$$2\pi \int_{-1}^{1} dx \frac{d_{m_1m_2}^J(x)\,\langle\lambda_1'\lambda_2'|\lambda_1\lambda_2\rangle}{(\vec{q}-\vec{q}')^2 + m^2} F[(\vec{q}-\vec{q}')^2]^2 \tag{B.41}$$

$$2\pi \int_{-1}^{1} dx \frac{d_{m_1m_2}^J(x)\,\langle\lambda_1'\lambda_2'|\vec{\sigma}_1\cdot\vec{\sigma}_2|\lambda_1\lambda_2\rangle}{(\vec{q}-\vec{q}')^2 + m^2} F[(\vec{q}-\vec{q}')^2]^2 \tag{B.42}$$

where $m_{1,2} = \lambda_1 - \lambda_2, \lambda'_1 - \lambda'_2$. The product of d functions with the helicity matrix elements of 1 and $\boldsymbol{\sigma} \cdot \boldsymbol{\sigma}$ may be re expressed by simple Legendre polynomials, which simplifies the numerical evaluation. The respective expressions for the eight independent helicity states are listed in tab. B.2.

B.3. The Bonn potentials

	A	B	C
m_π	138.03 MeV	138.03 MeV	138.03 MeV
f_π	1.00580	0.99562	0.99562
Λ_π	1050 MeV	1200MeV	1300 MeV
n_π	1	1	1
m_η	548.8 MeV	548.8 MeV	548.8 MeV
f_η	2.74099	2.31656	1.79440
Λ_η	1500 MeV	1500 MeV	1500 MeV
n_η	1	1	1
m_σ	550 MeV	550 MeV	550 MeV
g_σ	10.22145	10.07459	10.04398
Λ_σ	2000 MeV	2000 MeV	1800 MeV
n_σ	1	1	1
m_δ	983 MeV	983 MeV	983 MeV
g_δ	3.11246	6.25704	7.98525
Λ_δ	2000 MeV	1500 MeV	1500 MeV
n_δ	1	1	1
m_ω	782.6 MeV	782.6 MeV	782.6 MeV
g_ω	15.8533	15.8533	15.8533
$(f/g)_\omega$	0	0	0
Λ_ω	1500 MeV	1500 MeV	1500 MeV
n_ω	1	1	1
m_ρ	769 MeV	769 MeV	769 MeV
g_ρ	3.52714	3.45515	3.45515
$(f/g)_\rho$	6.1	6.1	6.1
Λ_ρ	1300 MeV	1300 MeV	1300 MeV
n_ρ	1	1	1

Table B.3.: Parameters of the Bonn potentials [Machleidt87]

The one boson exchange model we use here for the nucleon sector is the Bonn meson exchange potential [Machleidt87], mostly Bonn A. The parameters of all three (charge independent) Bonn interactions are given in tab. B.3. In older works the f couplings of the pseudoscalar mesons are often given also by constants called g. The relation between both is

$$g_{ps} = f_{ps}\frac{2M}{m_{ps}}, \tag{B.43}$$

where M denotes the nucleon mass.

In addition to the parameters given, there is an undocumented change to the ${}^3P_1$ kernel applied in the calculation necessary to reproduce the calculation of that partial wave by Machleidt and the experimental data: The attractive parts of the potential are set to 0. This very unpleasant ingredient destroys the meson exchange picture as a link between nuclear and hadron physics.

All three parameter sets have to be used in BS equation where the 3D propagator is the Thompson propagator.

C. G-Matrix: Details

C.1. Decomposition of the G-matrix

As explained already in the main part, sec. 3.1.3, to extract the Lorentz scalar amplitudes, corresponding to a specific set of covariants, the operator valued decomposition equation

$$T = \sum_{i=1}^{N} f_i(|\boldsymbol{q}'|, |\boldsymbol{q}|, \vartheta_c, \sqrt{s})\mathcal{C}_i, \tag{C.1}$$

($\mathcal{C}_i$ stands for the covariants) has to be inverted in terms of a set of N independent helicity amplitudes $\langle \cdots \rangle_h$

$$\langle T \rangle_h = \sum_{i=1}^{N} f_i(|\boldsymbol{q}'|, |\boldsymbol{q}|, \vartheta_c, \sqrt{s}) \, \langle \mathcal{C}_i \rangle_h. \tag{C.2}$$

To obtain f, the matrix equation $\mathcal{C}_{hi} f_i = T_h$ has to be solved, once for each required set of parameters $\{|\boldsymbol{q}'|, |\boldsymbol{q}|, \vartheta_c, \sqrt{s}\}$. To have well defined equations, first kinematic singularities at $\vartheta_c = 0$ and $\vartheta_c = \pi$ have to be removed.

C.1.1. Removal of kinematic singularities in the T-matrix decomposition

As well the helicity matrix elements of the T-matrix, as also those of the covariants become 0 for some h at either $\vartheta_c = 0$ or $\vartheta_c = \pi$ or both. The zeros in $\langle \mathcal{C}_i \rangle_h$ lead to a singular matrix and make an inversion impossible. They, however, coincide exactly with the limiting behavior of $\langle T \rangle$ for $\vartheta_c \to 0, \pi$ and are thus artifacts. To eliminate these spurious singularities we will separate off the angular dependence of both matrix elements.

In the numerical treatment the full T-matrix is obtained by resumming the partial wave components as given in eq.(1.7). The whole angular dependence is hidden in the d functions Their behavior for $\vartheta_c \to 0, \pi$ is independent of J and depends only on the relative helicities $\lambda = \lambda_1 - \lambda_2$, $\lambda' = \lambda'_1 - \lambda'_2$. It can therefore be taken out of the sum. The behavior for the d functions at limiting angles is listed in tab. C.1.

The angular dependence of the covariants' helicity matrix elements is contained in the matrix elements $\langle 1 \rangle_h$ and $\langle \boldsymbol{\sigma} \cdot \boldsymbol{\sigma} \rangle_h$ (for the evaluation of helicity matrix elements see app. B.1). The evaluated helicity matrix elements are listed in tab. C.2. Their limiting

	λ	λ'	$d^J_{\lambda\lambda'}(\vartheta_c \to 0)$	$d^J_{\lambda\lambda'}(\vartheta_c \to 0)$
H_1	0	0	1	$(-)^J$
H_2	0	0	1	$(-)^J$
H_3	1	1	1	$(-)^{J+1}[\frac{1}{8}J(J+1)(\pi-\vartheta_c)^2]$
H_4	-1	1	$\frac{1}{8}J(J+1)\vartheta_c^2$	$(-)^{J+1}$
H_5	1	0	$-\frac{1}{2}\sqrt{J(J+1)}\vartheta_c$	$(-)^{J+1}\frac{1}{2}\sqrt{J(J+1)}(\pi-\vartheta_c)$
H_6	0	1	$\frac{1}{2}\sqrt{J(J+1)}\vartheta_c$	$(-)^{J}\frac{1}{2}\sqrt{J(J+1)}(\pi-\vartheta_c)$
H_7	-1	0	$(-)^J\frac{1}{2}\sqrt{J(J+1)}\vartheta_c$	$\frac{1}{2}\sqrt{J(J+1)}(\pi-\vartheta_c)$
H_8	0	-1	$(-)^{J+1}\frac{1}{2}\sqrt{J(J+1)}\vartheta_c$	$-\frac{1}{2}\sqrt{J(J+1)}(\pi-\vartheta_c)$

Table C.1.: Limiting behavior of the d functions for $\vartheta_c \to 0$ and $\vartheta_c \to \pi$. $\lambda^{(\prime)} = \lambda_1^{(\prime)} - \lambda_2^{(\prime)}$

	λ_1^+	λ_2^+	λ_1^-	λ_2^-	$\langle 1 \rangle$	$\langle \boldsymbol{\sigma}\cdot\boldsymbol{\sigma} \rangle$
$H_1 = \langle ++ \mid ++ \rangle$	1	1	0	0	$\cos^2(\frac{1}{2}\vartheta_c)$	$-1 - \sin^2(\frac{1}{2}\vartheta_c)$
$H_2 = \langle ++ \mid -- \rangle$	0	0	1	1	$-\sin^2(\frac{1}{2}\vartheta_c)$	$1 + \cos^2(\frac{1}{2}\vartheta_c)$
$H_3 = \langle +- \mid +- \rangle$	1	-1	0	0	$\cos^2(\frac{1}{2}\vartheta_c)$	$\cos^2(\frac{1}{2}\vartheta_c)$
$H_4 = \langle +- \mid -+ \rangle$	0	0	1	-1	$\sin^2(\frac{1}{2}\vartheta_c)$	$\sin^2(\frac{1}{2}\vartheta_c)$
$H_5 = \langle ++ \mid +- \rangle$	1	0	0	1	$-\sin(\frac{1}{2}\vartheta_c)\cos(\frac{1}{2}\vartheta_c)$	$-\sin(\frac{1}{2}\vartheta_c)\cos(\frac{1}{2}\vartheta_c)$
$H_6 = \langle +- \mid ++ \rangle$	1	0	0	-1	$\sin(\frac{1}{2}\vartheta_c)\cos(\frac{1}{2}\vartheta_c)$	$\sin(\frac{1}{2}\vartheta_c)\cos(\frac{1}{2}\vartheta_c)$
$H_7 = \langle ++ \mid -+ \rangle$	0	1	1	0	$\sin(\frac{1}{2}\vartheta_c)\cos(\frac{1}{2}\vartheta_c)$	$\sin(\frac{1}{2}\vartheta_c)\cos(\frac{1}{2}\vartheta_c)$
$H_8 = \langle -+ \mid ++ \rangle$	0	1	-1	0	$\sin(\frac{1}{2}\vartheta_c)\cos(\frac{1}{2}\vartheta_c)$	$\sin(\frac{1}{2}\vartheta_c)\cos(\frac{1}{2}\vartheta_c)$

Table C.2.: Helicity matrix elements of the spin-space operators 1 and $\boldsymbol{\sigma}\cdot\boldsymbol{\sigma}$. $\lambda_i^\pm = \lambda_i' \pm \lambda_i$

behavior is given by

$$\cos^2(\frac{1}{2}\vartheta_c) \xrightarrow[\vartheta_c \to \pi]{} \frac{1}{4}(\pi - \vartheta_c)^2 - \frac{1}{24}(\pi - \vartheta_c)^4 + \mathcal{O}([\pi - \vartheta_c]^6) \tag{C.3}$$

$$\sin^2(\frac{1}{2}\vartheta_c) \xrightarrow[\vartheta_c \to 0]{} \frac{1}{4}\vartheta_c^2 - \frac{1}{24}\vartheta_c^4 + \mathcal{O}(\vartheta_c^6) \tag{C.4}$$

$$\cos(\frac{1}{2}\vartheta_c)\sin(\frac{1}{2}\vartheta_c) \xrightarrow[\vartheta_c \to \pi]{} \frac{1}{2}(\pi - \vartheta_c) - \frac{1}{24}(\pi - \vartheta_c)^2 + \mathcal{O}([\pi - \vartheta_c]^5) \tag{C.5}$$

$$\xrightarrow[\vartheta_c \to 0]{} \frac{1}{2}\vartheta_c - \frac{1}{24}\vartheta_c^2 + \mathcal{O}(\vartheta_c^5) \tag{C.6}$$

For the helicities H_1 and H_2, as defined in tab. C.1, there is a mixed behavior. Since both, $\langle 1 \rangle$ and $\langle \boldsymbol{\sigma} \cdot \boldsymbol{\sigma} \rangle$, are contained in the sum over covariants, no singularities appear there. In all other cases kinematical singularities appear at either one or both angles, simultaneously in $\langle 1 \rangle$ and $\langle \boldsymbol{\sigma} \cdot \boldsymbol{\sigma} \rangle$ with identical behavior. This can be nicely separated off.

A comparison between the problematic cases shows, that the behavior of the helicity matrix elements $\langle T \rangle_h$ and of $\langle \mathcal{C}_i \rangle_h$ is the same for each H. In practice the d functions in eq.(1.7) and the matrix elements given in tab. C.2 will have to be replaced by their limiting behaviors with removed 0 if the angle is close to a critical one.

C.1.2. Matrix elements of covariants

In this section the matrix elements of the covariants

$$\gamma^{(2)}{}_\mu Q^{(1)\mu}, \gamma^{(1)}{}_\mu Q^{(2)\mu}, P\gamma^{(2)}{}_\mu Q^{(1)\mu}, P\gamma^{(1)}{}_\mu Q^{(2)\mu}, \tag{C.7}$$

which are not exactly straightforward to read off, are evaluated. We frequently use here the Dirac equations, eq.(A.3) and eq.(A.4), for removing particle four-momenta that are contained in

$$Q^{(i)\mu} = \frac{1}{M_i + M'_i}(p_i + p'_i), \tag{C.8}$$

Taking into account the half off-shell structure of the 3D reduced T-matrix, we always have $p^0_{1,2} = x_{2,1}\sqrt{s}$, i.e., the zero component of the momenta always contains its specific fraction of the on-shell energy s, see sec. 2.2.2. Defining $p_i = (p_i^0, \pm \boldsymbol{q})$ and $q_i = (E_i(q), \pm \boldsymbol{q})$, $\pm$ being for $i = 1, 2$, respectively, we thus have

$$\overline{u}_1(\boldsymbol{q}')\gamma^{(1)}{}_\mu Q^{(2)\mu} u_1(\boldsymbol{q}) = \frac{1}{M_2 + M'_2}\overline{u}_1(\boldsymbol{q}')\left[\gamma^{(1)}{}_\mu(p_2 + p'_2)^\mu\right]u_1(\boldsymbol{q}) =$$

$$\frac{1}{M_2 + M'_2}\overline{u}_1(\boldsymbol{q}')\gamma^{(1)}{}_\mu\left[(q_1 + q'_1)^\mu - g^{\mu 0}(\underbrace{E_1(q) - p_2^0}_{\equiv \Delta E_1} + \underbrace{E_1(q') - p_2'^0}_{\equiv \Delta E'_1})\right]u_1(\boldsymbol{q}) =$$

$$\frac{M_1 + M'_1}{M_2 + M'_2}\overline{u}_1(\boldsymbol{q}')u_1(\boldsymbol{q}) - \frac{\Delta E_1 + \Delta E'_1}{M_2 + M'_2}u_1^\dagger(\boldsymbol{q}')u_1(\boldsymbol{q}) \tag{C.9}$$

Analogously we get the expression for the axial vector, where an additional minus sign appears due to anticommutation of the gamma matrices:

$$\overline{u}_1(\boldsymbol{q}')\gamma_5\gamma^{(1)}{}_\mu Q^{(2)\mu} u_1(\boldsymbol{q}) = \frac{M_1 - M_1'}{M_2 + M_2'}\overline{u}_1(\boldsymbol{q}')u_1(\boldsymbol{q}) - \frac{\Delta E_1 + \Delta E_1'}{M_2 + M_2'}u_1^\dagger(\boldsymbol{q}')u_1(\boldsymbol{q}) \qquad (C.10)$$

This yields the matrix elements

$$\langle K_6 \rangle = \left\langle \gamma^{(2)}{}_\mu Q^{(1)\mu} \right\rangle \qquad (C.11)$$

$$= \left[\frac{M_2 + M_2'}{M_1 + M_1'}\overline{u}_2(\boldsymbol{q}')u_2(\boldsymbol{q}) - \frac{\Delta E_2 + \Delta E_2'}{M_1 + M_1'}u_2^\dagger(\boldsymbol{q}')u_2(\boldsymbol{q}) \right] \overline{u}_1(\boldsymbol{q}')u_1(\boldsymbol{q})$$

$$\langle K_7 \rangle = \left\langle \gamma^{(1)}{}_\mu Q^{(2)\mu} \right\rangle \qquad (C.12)$$

$$= \left[\frac{M_1 + M_1'}{M_2 + M_2'}\overline{u}_1(\boldsymbol{q}')u_1(\boldsymbol{q}) - \frac{\Delta E_1 + \Delta E_1'}{M_2 + M_2'}u_1^\dagger(\boldsymbol{q}')u_1(\boldsymbol{q}) \right] \overline{u}_2(\boldsymbol{q}')u_2(\boldsymbol{q})$$

$$\langle K_8 \rangle = \left\langle P\gamma^{(2)}{}_\mu Q^{(1)\mu} \right\rangle \qquad (C.13)$$

$$= \left[\frac{M_2 - M_2'}{M_1 + M_1'}\overline{u}_2(\boldsymbol{q}')\gamma_5 u_2(\boldsymbol{q}) + \frac{\Delta E_2 + \Delta E_2'}{M_1 + M_1'}u_2^\dagger(\boldsymbol{q}')\gamma_5 u_2(\boldsymbol{q}) \right] \overline{u}_1\gamma_5(\boldsymbol{q}')u_1(\boldsymbol{q})$$

$$\langle K_9 \rangle = \left\langle P\gamma^{(1)}{}_\mu Q^{(2)\mu} \right\rangle \qquad (C.14)$$

$$= \left[\frac{M_1 - M_1'}{M_2 + M_2'}\overline{u}_1(\boldsymbol{q}')\gamma_5 u_1(\boldsymbol{q}) + \frac{\Delta E_1 + \Delta E_1'}{M_2 + M_2'}u_1^\dagger(\boldsymbol{q}')\gamma_5 u_1(\boldsymbol{q}) \right] \overline{u}_2(\boldsymbol{q}')\gamma_5 u_2(\boldsymbol{q})$$

For on-shell amplitudes, $q' = q = q_s$ and identical particles we obtain $\Delta E = 0$. In this case there are only five invariants left, because $\langle K_8 \rangle = \langle K_9 \rangle = 0$ and $\langle K_6 \rangle = \langle K_7 \rangle = \langle K_1 \rangle$. The K_i are defined in eq.(3.23).

D. DDRH Parameter Sets

In this appendix we give the parametrizations and parameters of the vertex functionals used in the DDRH calculations of this work.

D.1. Nucleon-nucleon interactions

For the nuclear sector of our calculations we used the parametrization of [Fuchs95], which is a mapping of DBHF self-energies obtained by Brockmann and Machleidt [Brockmann90] using the Bonn A potential. The σ and the ω couplings are treated density dependent with a polynomial parametrization of $g^2(k_F)$

$$g_\alpha^2(k_F) = g_\alpha^2(k_{F,0}) \left(1 + \sum_i a_{\alpha,i} \left(1 - \frac{k_F}{k_{F,0}} \right)^i \right), \quad \alpha = \sigma,\ \omega. \qquad (D.1)$$

$k_{F,0}$ is the Fermi momentum of the parametrized DBHF calculation at saturation. Here we have $k_{F,0} = 1.4\ fm^{-1}$. The expansion is done up to second order with the parameters:

α	$g_\alpha^2(k_{F,0})\frac{M^2}{m_\alpha^2}$	$a_{1,\alpha}$	$a_{2,\alpha}$
σ	248.395	1.2102	1.6277
ω	179.038	1.2889	1.7771

$$(D.2)$$

The meson masses are: $m_\sigma = 550\ MeV$, $m_\omega = 782.6\ MeV$ and $m_\rho = 770.0\ MeV$ and the density independent coupling $g_\rho = 4.038$.

D.2. Hyperon-nucleon interactions

Set	R_σ	R_ω
I	0.49	0.553
II	0.49	0.542
III	0.2525	0.2529

Table D.1.: Scaling factors of the Λ vertices.

For the hyperon-meson vertices we used a scaled version of the functionals given above

$$g_{\Lambda\alpha}^2(k_F^\Lambda) = R_\alpha^2 g_\alpha^2(k_F^\Lambda) \qquad (D.3)$$

We used three different sets, of scaling factors. Set I and two were derived in [Keil00], starting with a microscopically obtained scaling factor for the Λ-σ vertex by [Haidenbauer98] and fixing the Λ-ω vertex to match hypernuclear single particle spectra. Set I is fixed to describe the intermediate and high mass Λ hypernuclei, whereas Set II is required to describe the low mass hypernuclei. This reflects the different dynamics at work in the two mass regimes. Set III has been derived in sec. 8 from recent high precision data of intermediate mass hypernuclei. The respective scaling factors are given in tab.

E. Hypernuclear Structure

E.1. Matrix Elements for Auger neutron rates

For the evaluation of the matrix elements the transition form-factors, eq. (9.7), are evaluated in the spherical basis of Dirac wave functions:

$$
\begin{aligned}
\rho_{12}(q) &= \int d^3x \, \overline{\psi}_1(\vec{x}) \hat{\Gamma} \psi_2(\vec{x}) \, e^{i\vec{k}\vec{x}} \\
&= \sum_{\lambda\mu} (-)^\lambda Y^*_{\lambda\mu}(\hat{q}) \int d\Omega \, dr \, r^2 \, j_\lambda(kr) Y_{\lambda\mu}(\hat{r}) \left(\begin{array}{c} g_1(r) \, \Omega_{j_1 l_1 m_1}(\theta,\phi) \\ i f_1(r) \, \Omega_{j_1 \tilde{l}_1 m_1}(\theta,\phi) \end{array} \right)^\dagger \\
&\qquad\qquad \gamma^0 \hat{\Gamma} \left(\begin{array}{c} g_2(r) \, \Omega_{j_2 l_2 m_2}(\theta,\phi) \\ i f_2(r) \, \Omega_{j_2 \tilde{l}_2 m_2}(\theta,\phi) \end{array} \right)
\end{aligned}
\tag{E.1}
$$

$\hat{\Gamma}$ is either the 4×4 unit matrix or γ_μ, depending on whether the scalar or the vector potential is evaluated. $\hat{q}$ and $\hat{r}$ denotes the unit vectors in direction of $\vec{q}$ and $\vec{r}$, respectively. The spinors are the usual total angular momentum eigenstates of the Dirac equation with the generalized spin-angle spherical harmonics $\Omega_{jlm}(\theta,\phi)$ obtained by coupling spin and orbital angular momenta [Brussaard]. The numerical solution of the radial Dirac equation was discussed e.g. in [Fuchs95]. The orbital angular momenta l and $\tilde{l}$ are determined by j and the parity π:

$$
l = \left\{ \begin{array}{ll} j + 1/2 & \text{for } \pi = (-)^{j+1/2} \\ j - 1/2 & \text{for } \pi = (-)^{j-1/2} \end{array} \right. \qquad
\tilde{l} = \left\{ \begin{array}{ll} j - 1/2 & \text{for } \pi = (-)^{j+1/2} \\ j + 1/2 & \text{for } \pi = (-)^{j-1/2} \end{array} \right.
\tag{E.2}
$$

For the scalar vertex we get then

$$
\begin{aligned}
\rho^s_{12}(q) = \sum_{\lambda\mu} (-)^\lambda Y^*_{\lambda\mu}(\hat{q}) \quad & \left\{ \left[\int dr \, r^2 \, g_1(r) g_2(r) j_\lambda(qr) \right] \left[\int d\Omega \, \Omega^*_{j_1 l_1 m_1} Y_{\lambda\mu} \Omega_{j_2 l_2 m_2} \right] \right. \\
& \left. - \left[\int dr \, r^2 \, f_1(r) f_2(r) j_\lambda(qr) \right] \left[\int d\Omega \, \Omega^*_{j_1 \tilde{l}_1 m_1} Y_{\lambda\mu} \Omega_{j_2 \tilde{l}_2 m_2} \right] \right\}
\end{aligned}
\tag{E.3}
$$

The radial matrix element is evaluated numerically. The angular integral can be performed analytically. By means of the Wigner-Eckhardt theorem [Brussaard] it can be expressed by Clebsch-Gordan coefficients and reduced matrix elements

$$
\int d\Omega \, \Omega^*_{jlm} Y_{\lambda\mu} \Omega_{j'l'm'} = \langle jlm | Y_{\lambda\mu} | j'l'm' \rangle = (-)^{j-m} \left(\begin{array}{ccc} j & \lambda & j' \\ -m & \mu & m' \end{array} \right) \left\langle l\frac{1}{2}j \left\| Y_\lambda \right\| l\frac{1}{2}j' \right\rangle
\tag{E.4}
$$

For the vector transition form factor we have to evaluate

$$
\rho_{12}^{\nu}(q) = \sum_{\lambda\mu} (-)^{\lambda} Y_{\lambda\mu}^{*}(\hat{q}) \quad \left\{ \left[\int dr \, r^2 \, g_1(r) g_2(r) j_{\lambda}(qr) \right] \left[\int d\Omega \, \Omega_{j_1 l_1 m_1}^{*} Y_{\lambda\mu} \Omega_{j_2 l_2 m_2} \right] \right.
$$

$$
+ \left[\int dr \, r^2 \, f_1(r) f_2(r) j_{\lambda}(qr) \right] \left[\int d\Omega \, \Omega_{j_1 \tilde{l}_1 m_1}^{*} Y_{\lambda\mu} \Omega_{j_2 \tilde{l}_2 m_2} \right],
$$

$$
i \left[\int dr \, r^2 \, g_1(r) f_2(r) j_{\lambda}(qr) \right] \left[\int d\Omega \, \Omega_{j_1 l_1 m_1}^{*} Y_{\lambda\mu} \vec{\sigma} \, \Omega_{j_2 \tilde{l}_2 m_2} \right]
$$

$$
\left. + \left[\int dr \, r^2 \, f_1(r) g_2(r) j_{\lambda}(qr) \right] \left[\int d\Omega \, \Omega_{j_1 \tilde{l}_1 m_1}^{*} Y_{\lambda\mu} \vec{\sigma} \, \Omega_{j_2 l_2 m_2} \right] \right\}^{\nu}
$$

$$
\text{(E.5)}
$$

The σ are the usual Pauli matrices. The reduced matrix element for the angular ρ_{12}^0 matrix element is identical to equation (E.4), for the spatial components it is given by

$$
\begin{aligned}
\langle jlm | Y_{\lambda\mu}\sigma_M | j'l'm' \rangle &= \sum_{IN} \langle \lambda\mu 1M | IN \rangle \langle jlm | \left[Y_{\lambda\mu}\sigma_{1M} \right]_{IN} | j'l'm' \rangle \\
&= \sum_{IN} (-)^{j-m} \langle \lambda\mu 1M | IN \rangle \begin{pmatrix} j & I & j' \\ m & N & m' \end{pmatrix} \left\langle l\frac{1}{2}j \left\| \left[Y_{\lambda}\sigma_1 \right]_I \right\| l'\frac{1}{2}j' \right\rangle \\
&= \sum_{IN} (-)^{j-m} \langle \lambda\mu 1M | IN \rangle \begin{pmatrix} j & I & j' \\ m & N & m' \end{pmatrix} \begin{Bmatrix} l & \frac{1}{2} & j \\ l & \frac{1}{2} & j' \\ \lambda & 1 & I \end{Bmatrix} \\
&\qquad\qquad\qquad\qquad\qquad \langle l \| Y_{\lambda} \| l' \rangle \left\langle \frac{1}{2} \left\| \sigma \right\| \frac{1}{2} \right\rangle \quad \text{(E.6)}
\end{aligned}
$$

Note that the Pauli matrices σ_M, $M = 0, \pm 1$, are used here in the spherical basis [Brussaard]. Explicit expressions for the reduced matrix elements are found e.g. in ref. [Brussaard].

F. Numerics

F.1. Solution of the Bethe-Salpeter integral equation

The partial wave decomposed BS equation is solved by transforming it into a linear system of equations, separately for both parities. Since it is not explicitly needed in this section, the angular momentum index J of the matrix elements will be suppressed. As first step the principal value integral is rewritten as described in sec. F.1.1, following eq.(F.17):

$$
\mathcal{P} \int_a^b dk\, k^2 \frac{g_r(k)}{s_k - s} V(q', k) T(k, q, s) =
$$
$$
\int_a^b dk \left[\frac{k^2 g_r(k)}{s_k - s} V(q', k) T(k, q, s) - \frac{k_s^2 E_1^s E_2^s g_r(k_s)}{s(k^2 - k_s^2)} V(q', k_s) T(k_s, q, s) \right]
$$
$$
+ \underbrace{\frac{k_s E_1^s E_2^s g_r(k_s)}{2s} \log\left(\left| \frac{(b - k_s)(a + k_s)}{(a - k_s)(b + k_s)} \right| \right) V(q', k_s) T(k_s, q, s)}_{\equiv P_1(s)} \tag{F.1}
$$

If treating channels in which a coupling of different two particle states exists, care has to be taken when $q_s^2 < 0$ (see the discussion in sec. 2.2.2). q_s^2 is not a deliberate relative loop momentum, it is connected to s and thus negative for a baryon pair substhreshold. In contrast to the two baryon propagator, a potential matrix element with $q_s^2 < 0$ is unphysical and equals 0. The integral is now discretized for its numerical evaluation. We change the notation to bra-ket $q \to |i\rangle$, $q' \to \langle o|$, $k \to \langle l|, |l\rangle$ in the matrix elements. i, o, l are integer valued indices.

$$
\sum_l^N \left[\frac{k_l^2 g_r(k_l)}{s_l - s} \langle o| V |l\rangle \langle l| T |i\rangle - \frac{k_s^2 E_1^s E_2^s g_r(k_s)}{s(k_l^2 - k_s^2)} \langle o| V |k_s\rangle \langle k_s| T |i\rangle \right] \Delta k
$$
$$
+ P_1 \langle o| V |k_s\rangle \langle k_s| T |i\rangle \tag{F.2}
$$

Defining now

$$
P_2(s) \equiv \frac{k_s^2 E_1^s E_2^s g_r(k_s)}{s} \sum_l^N \frac{1}{k_l^2 - k_s^2} \Delta k, \tag{F.3}
$$

where the sum has to be evaluated *on the same grid as the other sum*, the discretized and regularized integral is

$$
\mathcal{P} \int dk\, k^2 \frac{g_r(k)}{s_k - s} V(q', k) T(k, q, s) =
$$
$$
\sum_l^{N+1} \left[\frac{k_l^2 g_r(k_l)}{s_l - s} (1 - \delta_{l,N+1}) + (P_1(s) - P_2(s)) \delta_{l,N+1} \right] \langle o| V |l\rangle \langle l| T |i\rangle \Delta k \tag{F.4}
$$

The sum was extended to contain one more term, where $k_{N+1} \equiv k_s$. Now the BS equation looks as follows:

$$\langle o | \, T(s) \, | i \rangle = \langle o | \, V \, | i \rangle + \sum_{l}^{N+1} \quad \left[\frac{k_l^2 g_r(k_l)}{s_l - s}(1 - \delta_{l,N+1}) + (P_1(s) - P_2(s))\delta_{l,N+1} \right]$$
$$\langle o | \, V \, | l \rangle \, \langle l | \, T \, | i \rangle \, \Delta k \tag{F.5}$$

and can easily be reformulated to a linear system for T when pulling the *lhs* under the sum:

$$\langle o | \, V \, | i \rangle = \tag{F.6}$$
$$\sum_{l}^{N+1} \left[\delta_{l,o} - \left\{ \frac{k_l^2 g_r(k_l)}{s_l - s}(1 - \delta_{l,N+1}) + (P_1(s) - P_2(s))\delta_{l,N+1} \right\} \langle o | \, V \, | l \rangle \right] \langle l | \, T \, | q \rangle \, \Delta k$$

(which has the side effect, that it fixes the so far unrestricted outgoing momentum to lie on the integration grid or to be q_s) To clarify what are the external variables and which are those integrated over let us reformulate the above equation explicitly in matrix form

$$(A(s))_{ol} \equiv \left[\delta_{l,o} - \left\{ \frac{k_l^2 g_r(k_l)}{s_l - s}(1 - \delta_{l,N+1}) + (P_1(s) - P_2(s))\delta_{l,N+1} \right\} \langle o | \, V \, | l \rangle \right]$$
$$(\langle l | \, T(s) \, | i \rangle)_l \equiv \vec{T}(s, k_i)$$
$$(\langle o | \, V \, | i \rangle)_o \equiv \vec{V}(k_i), \tag{F.7}$$

$$\Rightarrow A(s) \cdot \vec{T}(s, k_i)\Delta k = \vec{V}(k_i) \tag{F.8}$$

So s and the incoming momentum k_i are parameters. Eq. (F.8) defines the full off-shell T-matrix. The equation for the physically relevant half off-shell T-matrix is obtained by choosing $k_i = k_s$.

This scheme can be easily generalized to deal with a multichannel system. Having, e.g., N_B baryon species and N_q momentum steps, using the labels h, b, k for helicity, baryon species and momentum, respectively, the generalized summation index l could be composed as $l = N_q N_B h + N_q b + k$.

It is tempting to assign the lower limit of the angle averaged Pauli operator to a in eq.(F.1). This, however, turns out to be numerically absolutely unstable. The best choice for numerical stability is alway $a = 0$ and $b = \infty$. Calculating in-medium interactions the number of integration steps needs to be set a lot higher than for free scattering due to the step of the Pauli operator.

Numerically the integral discretization is done corresponding to Gauss-integration

$$\int_{-1}^{1} dx \, f(x) = \sum_{i=1}^{N} f(x_i) \, d_i \tag{F.9}$$

This has profen to be a very efficient method in terms of the amount of grid points needed. The original interval $(-1, 1)$ of the Gauss points is stretched to the interval $(0, \infty)$ by

$$k_i = \mathcal{C} \tan\left(\frac{\pi}{4}(x_i + 1)\right) \tag{F.10}$$

and the weights then become

$$w_i = C \frac{\pi}{4} \frac{d_i}{\cos\left(\frac{\pi}{4}(x_i + 1)\right)}. \tag{F.11}$$

In the transformed Gauss points the integral is

$$\int_0^\infty dx \, f(x) = \sum_{i=1}^N f(k_i) \, w_i. \tag{F.12}$$

F.1.1. Numerical evaluation of principle value integrals

The evaluation of principle value integrals is performed in all our numerical treatments by the subtraction method. Knowing the characteristics of the pole, e.g. being $\propto (x - x_0)^{-1}$ or $\propto \log(|x - x_0|)$ as our poles are, it is clear that sufficiently close to the pole the functions will only be $a(x - x_0)^{-1}$ and $a\log(|x - x_0|)$. The constants a are determined and the respective expressions are subtracted from the integrand. This perfectly regularizes the integral. The position of the pole has to be known, however, *as precisely as possible*! To correct for the mistake done by the subtraction the principal value integral over the subtracted expression has to be added again. This part can, in fact, be integrated analytically, which is the merit of that method.

$$\mathcal{P} \int_a^b \frac{f(x)}{x - x_0} dx = \int_a^b \frac{f(x) - f(x_0)}{x - x_0} dx + f(x_0) \, \mathcal{P} \int_a^b \frac{1}{x - x_0} dx \tag{F.13}$$

Here is a list of the principal value integrals used in out numerical treatments:

$$\mathcal{P} \int_a^b \frac{1}{x - x_0} dx = \log\left(\left|\frac{x_0 - a}{x_0 - b}\right|\right) \tag{F.14}$$

$$\mathcal{P} \int_a^b \frac{1}{x^2 - x_0^2} dx = \frac{1}{2x_0} \log\left(\left|\frac{(b - x_0)(a + x_0)}{(a - x_0)(b + x_0)}\right|\right) \tag{F.15}$$

$$\mathcal{P} \int_a^b \log(|x - x_0|) dx = (b - x_0)\left(\log(|b - x_0|) - 1\right)$$
$$- (a - x_0)\left(\log(|a - x_0|) - 1\right) \tag{F.16}$$

The decomposition of a principal value integral, described in eq.(F.13), is especially advantageous if the integral runs from 0 to ∞, since then the last term will vanish, as can be easily seen from eqs.(F.14)–(F.16).

An important case to evaluate for the solution of the BS equation is the following principal value integral:

$$\mathcal{P} \int_a^b dk \frac{f(k)}{s(k) - s_0} \tag{F.17}$$

where $f(k)$ is regular. $s(k)$ is the total energy, the pole momentum k_0 can be evaluated

from eq.(1.32). The integrand can now be rewritten as

$$
\mathcal{P} \int_a^b dk \frac{f(k)}{s(k) - s_0} = \mathcal{P} \int_a^b dk \frac{F(k)}{k^2 - k_0^2}
$$
$$
= \int_a^b dk \frac{F(k) - F(k_0)}{k^2 - k_0^2} + \frac{F(k_0)}{2k_0} \log\left(\left|\frac{(b - k_0)(a + k_0)}{(a - k_0)(b + k_0)}\right|\right)
$$

(F.18)

by defining

$$
F(k) \equiv \frac{k^2 - k_0^2}{s(k) - s_0} f(k)
$$

(F.19)

Now we will evaluate $F(k_0)$ which also shows that this transformation is well defined, i.e., F is also regular:

$$
F(k_0) = \lim_{k^2 \to k_0^2} f(k) \frac{k^2 - k_0^2}{s(k) - s_0} = \frac{\lim_{k^2 \to k_0^2} \partial_{k^2}[f(k)(k^2 - k_0^2)]}{\lim_{k^2 \to k_0^2} \partial_{k^2}(s(k) - s_0)} = f(k_0) \frac{E_1^0 E_2^0}{s_0}
$$

(F.20)

As the final result we then get

$$
\mathcal{P} \int_a^b dk \frac{f(k)}{s(k) - s_0} = \int_a^b dk \left[\frac{f(k)}{s(k) - s_0} - \frac{f(k_0) E_p E_2^0}{s_0(k^2 - k_0^2)}\right]
$$
$$
+ \frac{f(k_0) E_p E_2^0}{2s_0 k_0} \log\left(\left|\frac{(b - k_0)(a + k_0)}{(a - k_0)(b + k_0)}\right|\right)
$$

(F.21)

Bibliography

[Ahn01]　　　　　Ahn, J. K. *et al.* *Production of (lambda lambda)h-4 hypernuclei.* Phys. Rev. Lett. 87, (2001), 132504.

[Ajimura95]　　　Ajimura, S. *et al.* *The lambda hypernuclear spectroscopy with the sks spectrometer at kek 12-gev ps.* Nucl. Phys. A585, (1995), 173c–182c.

[Avancini04]　　　Avancini, S. S., Bracco, M. E., Chiapparini, M., and Menezes, D. P. *On the density dependent hadron field theory at finite temperature and its thermodynamical consistency.* J. Phys. G30, (2004), 27–36. `nucl-th/0311019`.

[Blankenbecler66]　Blankenbecler, R. and Sugar, R. *Linear integral equations for relativistic multichannel scattering.* Phys. Rev. 142, (1966), 1051–1059.

[Blatt52]　　　　Blatt, John M. and Biedenharn, L. C. *Neutron-proton scattering with spin-orbit coupling. i. general expressionsg.* Phys. Rev. 86, (1952), 399–404.

[Bogner03]　　　Bogner, S. K., Kuo, T. T. S., and Schwenk, A. *Model-independent low momentum nucleon interaction from phase shift equivalence.* Phys. Rept. 386, (2003), 1–27. `nucl-th/0305035`.

[Brink93]　　　　Brink, D. M. and Satchler, G. B. *Angular Momentum.* Clarendon Press, Oxford, 1993.

[Brockmann90]　　Brockmann, R. and Machleidt, R. *Relativistic nuclear structure. 1: Nuclear matter.* Phys. Rev. C42, (1990), 1965–1980.

[Brussaard]　　　Brussaard, P.J. and Glaudemans, P.W.M. *Shell-model applications in nuclear spectroscopy* .

[Bryan81]　　　　Bryan, R. *Parametrization of the elastic sector of the nucleon nucleon scattering, matrix. i.* Phys. Rev. C24, (1981), 2659–2666.

[Bryan84]　　　　Bryan, R. *Parametrization of the elastic sector of the nucleon nucleon scattering matrix. ii.* Phys. Rev. C30, (1984), 305–313.

Bibliography

[Coester70]   Coester, F., Cohen, S., Day, B., and Vincent, C. M. *Variation in nuclear-matter binding energies with phase-shift-equivalent two-body potentials.* Phys. Rev. C1, (1970), 769–776.

[Danysz53]   Danysz, M. and Pniewski, J. Phil. Mag. 44, (1953), 348.

[deJong91]   de Jong, Fred and Malfliet, Rudi. *A conserving relativistic many body approach: Equation of state, spectral function and occupation probabilities of nuclear matter.* Phys. Rev. C44, (1991), 998–1011. KVI-865.

[deJong98]   de Jong, F. and Lenske, H. *Asymmetric nuclear matter in the relativistic brueckner hartree fock approach.* Phys. Rev. C57, (1998), 3099–3107. `nucl-th/9707017`.

[deSwart63]   de Swart, J. J. *The octet model and its clebsch-gordan coefficients.* Rev. Mod. Phys. 35, (1963), 916–939.

[Dohrmann]   Dohrmann, F. *et al. Electroproduction of strangeness on light nuclei* Prepared for 9th International Conference on the Structure of Baryons (Baryons 2002), Newport News, Virginia, 3-8 Mar 2002.

[Donoghue92]   Donoghue, J. F., Golowich, E., and Holstein, Barry R. *Dynamics of the standard model*, vol. 2. 1992.

[Erkelenz74]   Erkelenz, K. *Current status of the relativistic two nucleon one boson exchange potential.* Phys. Rept. 13, (1974), 191–258.

[Filikhin02]   Filikhin, I. N. and Gal, A. *Faddeev-yakubovsky calculations for light lambda lambda hypernuclei.* Nucl. Phys. A707, (2002), 491–509. `nucl-th/0203036`.

[Filikhin04]   Filikhin, I., Gal, A., and Suslov, V. M. *Cluster models of (lambda lambda)he-6 and (lambda)be-9 hypernuclei.* Nucl. Phys. A743, (2004), 194–207. `nucl-th/0406049`.

[Finelli04]   Finelli, P., Kaiser, N., Vretenar, D., and Weise, W. *Relativistic nuclear model with point-couplings constrained by qcd and chiral symmetry.* Nucl. Phys. A735, (2004), 449–481. `nucl-th/0307069`.

[Fuchs95]   Fuchs, C., Lenske, H., and Wolter, H. H. *Density dependent hadron field theory.* Phys. Rev. C52, (1995), 3043–3060. `nucl-th/9507044`.

[Fuchs98]   Fuchs, C., Waindzoch, T., Faessler, A., and Kosov, D. S. *Scalar and vector decomposition of the nucleon self-energy in the relativistic brueckner approach.* Phys. Rev. C58, (1998), 20222032.

[Fuchs04]   Fuchs, Christian. *The Relativistic Dirac-Brueckner Approach to Nuclear Matter*, vol. 641 of *Lecture Notes on Physics.* Springer, Berlin, Heidelberg, 2004. ISBN 3-540-21030-X.

164

[Furnstahl04]   Furnstahl, R. J. *Next generation relativistic models.* Lect. Notes Phys. 641, (2004), 1–29. `nucl-th/0307111`.

[Glendenning93]   Glendenning, N. K., Von-Eiff, D., Haft, M., Lenske, H., and Weigel, M. K. *Relativistic mean field calculations of lambda and sigma hypernuclei.* Phys. Rev. C48, (1993), 889–895. `nucl-th/9211012`.

[Greiner89]   Greiner, C. and Muller, B. *Pair correlations of neutral strange particles emitted in relativistic heavy ion collisions.* Phys. Lett. B219, (1989), 199–204.

[Gross-Boelting99]   Gross-Boelting, T., Fuchs, C., and Faessler, Amand. *Covariant representations of the relativistic brueckner t- matrix and the nuclear matter problem.* Nucl. Phys. A648, (1999), 105–137. `nucl-th/9810071`.

[Gross82]   Gross, Franz. *The relativistic few body problem. 1. two-body equations.* Phys. Rev. C26, (1982), 2203–2225.

[GSI01]   *Reise zum urknall.* GSI Sonderheft p. 10.

[Haidenbauer98]   Haidenbauer, J., Melnitchouk, W., and Speth, J. *Meson-exchange model for the y n interaction* `nucl-th/9805014`.

[Hasegawa96]   Hasegawa, T. *et al. Spectroscopic study of (lambda) b-10, (lambda) c-12, (lambda) si-28, (lambda) y-89, (lambda) la-139, and (lambda) pb-208 by the (pi+, k+) reaction.* Phys. Rev. C53, (1996), 1210–1220.

[Hiyama00]   Hiyama, E., Kamimura, M., Motoba, T., Yamada, T., and Yamamoto, Y. *Lambda n spin-orbit splittings in (lambda)be-9 and (lambda)c-13 studied with one-boson-exchange lambda n interactions.* Phys. Rev. Lett. 85, (2000), 270–273.

[Hiyama02]   Hiyama, E., Kamimura, M., Motoba, T., Yamada, T., and Yamamoto, Y. *Four-body cluster structure of a = 7-10 double-lambda hypernuclei.* Phys. Rev. C66, (2002), 024007. `nucl-th/0204059`.

[Hiyama03]   Hiyama, E., Kino, Y., and Kamimura, M. *Gaussian expansion method for few-body systems.* Prog. Part. Nucl. Phys. 51, (2003), 223–307.

[Hofmann01a]   Hofmann, F., Keil, C., and Lenske, H. *Application of the density dependent hadron field theory to neutron star matter.* Phys. Rev. C64, (2001), 025804. `nucl-th/0008038`.

[Hofmann01b]   Hofmann, F., Keil, C., and Lenske, H. *Density dependent hadron field theory for asymmetric nuclear matter and exotic nuclei.* Phys. Rev. C64, (2001), 034314. `nucl-th/0007050`.

Bibliography

[Holzenkamp88]   Holzenkamp, B. *Mesonentheoretisches modell der hyperon-nukleon wechselwirkung (thesis)*. Spezielle Berichte der Kernforschungsanlage Juelich 460.

[Holzenkamp89]   Holzenkamp, B., Holinde, K., and Speth, J. *A meson exchange model for the hyperon nucleon interaction*. Nucl. Phys. A500, (1989), 485–528.

[Horowitz87]   Horowitz, C. J. and Serot, Brian D. *The relativistic two nucleon problem in nuclear matter*. Nucl. Phys. A464, (1987), 613.

[Hotchi01]   Hotchi, H. *et al. Spectroscopy of medium-heavy lambda hypernuclei via the (pi +,k+) reaction*. Phys. Rev. C64, (2001), 044302.

[Hugenholtz58]   Hugenholtz, N. M. and van Hove, L. *A theorem on the single particle energy in a fermi gas with interaction*. Physica 24, (1958), 363–376.

[Jacob59]   Jacob, M. and Wick, G. C. *On the general theory of collisions for particles with spin*. Ann. Phys. 7, (1959), 404–428.

[Jaffe77]   Jaffe, Robert L. *Perhaps a stable dihyperon*. Phys. Rev. Lett. 38, (1977), 195–198.

[Jaminon87]   Jaminon, J., Mahaux, C., and Rochus, P. *Optical-model potential in a relativistic quantum field model*. Phys. Rev. C22, (1987), 2027.

[Joachain75]   Joachain, Charles J. *Quantum collision theory*. North-Holland, Amsterdam, 1975.

[Kaiser02]   Kaiser, Norbert, Fritsch, S., and Weise, W. *Chiral dynamics and nuclear matter*. Nucl. Phys. A697, (2002), 255–276. `nucl-th/ 0105057`.

[Kaiser03]   Kaiser, N., Fritsch, S., and Weise, W. *Nuclear energy density functional from chiral pion nucleon dynamics*. Nucl. Phys. A724, (2003), 47–68. `nucl-th/0212049`.

[Keil00]   Keil, C., Hofmann, F., and Lenske, H. *Density dependent hadron field theory for hypernuclei*. Phys. Rev. C61, (2000), 064309. `nucl-th/9911014`.

[Keil02a]   Keil, C. and Lenske, H. *The hypernuclear auger effect within the density dependent relativistic hadron field theory*. Phys. Rev. C66, (2002), 054307. `nucl-th/0207084`.

[Keil02b]   Keil, C., Lenske, H., and Greiner, C. *In-medium baryon interactions and hypernuclear structure*. J. Phys. G28, (2002), 1683–1688. `nucl-th/0112047`.

[Kohri02]   Kohri, H. *et al.* (AGS-E929). *Study of the (lambda)c-13 hypernu-cleus by the c-13(k-,pi- gamma) reaction.* Phys. Rev. C65, (2002), 034607. `nucl-ex/0110007`.

[Kolb90]   Kolb, E. W. and Turner, Michael S. *The early universe* Redwood City, USA: Addison-Wesley (1990) 547 p. (Frontiers in physics, 69).

[Lalazissis97]   Lalazissis, G. A., Konig, J., and Ring, P. *A new parameterization for the lagrangian density of relativistic mean field theory.* Phys. Rev. C55, (1997), 540–543. `nucl-th/9607039`.

[Lenske04]   Lenske, H. *Density dependent relativistic field theory*, vol. 641 of *Lecture Notes on Physics.* Springer, Berlin, Heidelberg, 2004. ISBN 3-540-21030-X.

[Likar86]   Likar, A., Rosina, M., and Povh, B. *The lambda particle as a probe of deeply bound single particle states in heavy nuclei.* Z. Phys. A324, (1986), 35–41.

[Long04]   Long, Wen-hui, Meng, Jie, Van Giai, Nguyen, and Zhou, Shan-Gui. *New effective interactions in rmf theory with non-linear terms and density-dependent meson-nucleon coupling.* Phys. Rev. C69, (2004), 034319. `nucl-th/0311031`.

[Machleidt87]   Machleidt, R., Holinde, K., and Elster, C. *The bonn meson ex-change model for the nucleon nucleon interaction.* Phys. Rept. 149, (1987), 1–89.

[Machleidt89]   Machleidt, R. *The meson theory of nuclear forces and nuclear struc-ture.* Adv. Nucl. Phys. 19, (1989), 189–376.

[Machleidt91]   Machleidt, R. *ONE-BOSONEXCHANGE POTENTIALS AND NUCLEON-NUCLEON SCATTERING*, vol. Volume 1: Nuclear Structure. Springer-Verlag Berlin Heidelberg, 1991. ISBN 3540535713.

[Machleidt01]   Machleidt, R. *The high-precision, charge-dependent bonn nucleon-nucleon potential (cd-bonn).* Phys. Rev. C63, (2001), 024001. `nucl-th/0006014`.

[Maessen89]   Maessen, P. M. M., Rijken, T. A., and de Swart, J. J. *Soft core baryon baryon one boson exchange models. 2. hyperon - nucleon potential.* Phys. Rev. C40, (1989), 2226–2245.

[Marcos98]   Marcos, S., Lombard, R. J., and Mares, J. *On the binding energy of double lambda hypernuclei in the relativistic mean field theory.* Phys. Rev. C57, (1998), 1178–1183. `nucl-th/9712039`.

Bibliography

[Mares94]   Mares, J. and Jennings, B. K. *Relativistic description of lambda, sigma and xi hypernuclei.* Phys. Rev. C49, (1994), 2472–2478.

[Margaryan00]   Margaryan, Tang L. Majewski S. Hashimoto O., A. and Likachev, V. *Auger neutron spectroscopy of nuclear matter at cebaf.* Letter of intent to JLAB PAC 18 LOI-00-101.

[Margaryan04]   Margaryan, A. *private communications* .

[May97]   May, M. *et al. First observation of the p(lambda) → s(lambda) gamma- ray transition in (lambda)c-13.* Phys. Rev. Lett. 78, (1997), 4343–4346.

[Millener01]   Millener, D. J. *Shell-model description of lambda hypernuclei.* Nucl. Phys. A691, (2001), 93–100. `nucl-th/0103017`.

[Muther90]   Muther, H., Machleidt, R., and Brockmann, R. *Relativistic nuclear structure. 2: Finite nuclei.* Phys. Rev. C42, (1990), 1981–1988.

[Muther00]   Muther, H. and Polls, A. *Two-body correlations in nuclear systems.* Prog. Part. Nucl. Phys. 45, (2000), 243–334. `nucl-th/0001007`.

[Nagae01]   Nagae, T. *Overview of the results on lambda-hypernuclei spectroscopy with the sks.* Nucl. Phys. A691, (2001), 76–84.

[Nagels78]   Nagels, M. M., Rijken, T. A., and de Swart, J. J. *A low-energy nucleon-nucleon potential from regge pole theory.* Phys. Rev. D17, (1978), 768.

[Nemura02]   Nemura, H., Akaishi, Y., and Suzuki, Y. *Ab initio approach to s-shell hypernuclei (lambda)h-3, (lambda)h-4, (lambda)he-4 and (lambda)he-5 with a realistic lambda n - sigma n interaction.* Phys. Rev. Lett. 89, (2002), 142504. `nucl-th/0203013`.

[Niksic02a]   Niksic, T., Vretenar, D., Finelli, P., and Ring, P. *Relativistic hartree-bogolyubov model with density- dependent meson nucleon couplings.* Phys. Rev. C66, (2002), 024306. `nucl-th/0205009`.

[Niksic02b]   Niksic, T., Vretenar, D., and Ring, P. *Relativistic random-phase approximation with density- dependent meson-nucleon couplings.* Phys. Rev. C66, (2002), 064302. `nucl-th/0209016`.

[NNDC]   NNDC. *National nuclear data center, brookhaven national laboratory* `http://www.nndc.bnl.gov`.

[Nogga02]   Nogga, A., Kamada, H., and Gloeckle, Walter. *The hypernuclei (lambda)he-4 and (lambda)h-4: Challenges for modern hyperon nucleon forces.* Phys. Rev. Lett. 88, (2002), 172501. `nucl-th/0112060`.

[pdg]   *see e.g. particle data book, sect. 34, p. 211* .

[Peskin95]   Peskin, Michael E. and Schroeder, D. V. *An Introduction to quantum field theory.* Addison-Wesley, Reading, USA, 1995.

[Pile91]   Pile, P. H. *et al. Study of hypernuclei by associated production.* Phys. Rev. Lett. 66, (1991), 2585–2588.

[Reuber94]   Reuber, A., Holinde, K., and Speth, J. *Meson exchange hyperon - nucleon interactions in free scattering and nuclear matter.* Nucl. Phys. A570, (1994), 543–579.

[Rijken99]   Rijken, T. A., Stoks, V. G. J., and Yamamoto, Y. *Soft-core hyperon nucleon potentials.* Phys. Rev. C59, (1999), 21–40. `nucl-th/9807082`.

[Rufa87]   Rufa, M., Stocker, H., Maruhn, J. A., Greiner, W., and Reinhard, P. G. *Single particle spectra of lambda hypernuclei and the enhanced interaction radii of multistrange objects.* J. Phys. G13, (1987), L143–L148.

[Rufa90]   Rufa, M. *et al. Multi - lambda hypernuclei and the equation of state of hypermatter.* Phys. Rev. C42, (1990), 2469–2478.

[Schaffner-Bielich00]   Schaffner-Bielich, Jurgen, Hanauske, Matthias, Stocker, Horst, and Greiner, Walter. *Hyperstars: Phase transition to (meta)-stable hyperonic matter in neutron stars* `astro-ph/0005490`.

[Schertler00]   Schertler, K., Greiner, C., Schaffner-Bielich, J., and Thoma, M. H. *Quark phases in neutron stars and a 'third family' of compact stars as a signature for phase transitions.* Nucl. Phys. A677, (2000), 463–490. `astro-ph/0001467`.

[Sehn97]   Sehn, L., Fuchs, C., and Faessler, Amand. *Nucleon self-energy in the relativistic brueckner approach.* Phys. Rev. C56, (1997), 216–227. `nucl-th/9701060`.

[Serot86]   Serot, Brian D. and Walecka, John Dirk. *The relativistic nuclear many body problem.* Adv. Nucl. Phys. 16, (1986), 1–327.

[Stoks99]   Stoks, V. G. J. and Rijken, T. A. *Soft-core baryon baryon potentials for the complete baryon octet.* Phys. Rev. C59, (1999), 3009–3020. `nucl-th/9901028`.

[Takahashi01]   Takahashi, H. *et al. Observation of a (lambda lambda)he-6 double hypernucleus.* Phys. Rev. Lett. 87, (2001), 212502.

[Tang01]   Tang, L. *et al. First experiment on spectroscopy of lambda hypernuclei by electroproduction at jlab.* AIP Conf. Proc. 603, (2001), 173–185.

[Ter Haar87]   Ter Haar, B. and Malfliet, R. *Nucleons, mesons and deltas in nuclear matter. a relativistic dirac-bruckner approach.* Phys. Rept. 149, (1987), 207–286.

[Thompson70]   Thompson, R. H. *Three-dimensional bethe-salpeter equation applied to the nucleon-nucleon interaction.* Phys. Rev. D1, (1970), 110–117.

[Tjon85]   Tjon, J. A. and Wallace, Stephen J. *General lorentz invariant representation of n n scattering amplitudes.* Phys. Rev. C32, (1985), 1667–1680.

[Typel99]   Typel, S. and Wolter, H. H. *Relativistic mean field calculations with density dependent meson nucleon coupling.* Nucl. Phys. A656, (1999), 331–364.

[Typel03]   Typel, S., van Chossy, T., and Wolter, H. H. *Relativistic mean field model with generalized derivative nucleon meson couplings.* Phys. Rev. C67, (2003), 034002. `nucl-th/0210090`.

[Ulrych97]   Ulrych, S. and Muther, H. *Relativistic structure of the nucleon self-energy in asymmetric nuclei* `nucl-th/9706030`.

[Vretenar98]   Vretenar, D., Poschl, W., Lalazissis, G. A., and Ring, P. *Relativistic mean-field description of light lambda hypernuclei with large neutron excess.* Phys. Rev. C57, (1998), 1060–1063. `nucl-th/9709046`.

[Woloshyn73]   Woloshyn, R. M. and Jackson, A. D. *Comparison of three-dimensional relativistic scattering equations.* Nucl. Phys. B64, (1973), 269–288.

[Zuber02]   Zuber, K. *Observational cosmplogy and neutrino astrophysics.* Summer school on CP physics, Prerow, 2002 .

Deutsche Zusammenfassung

In dieser Arbeit wird eine *ab-initio* Beschreibung für Kerne und Hyperkerne entwickelt, die auf einer quantenfeldtheoretischen Formulierung für Baryonen und Mesonen basiert, welche die relevanten Freiheitsgrade eines hadronischen Vielteilchenzustandes nahe des Grundzustandes darstellen. Der Begriff ab-initio bedeutet hier, dass ausgehend von einem gegebenen Satz von Parametern, welche die Baryon-Baryon Streuung im freien Raum beschreiben, andere baryonische Systeme mit endlicher Valenzteilchendichte beschrieben werden können, ohne dass Parameter angepasst oder Neue eingeführt werden müssen. Die elementaren Zweiteilchen-Wechselwirkungen sind für gewöhnlich durch einen Satz von Baryon-Meson Kopplungskonstanten und Impuls-Cutoff Parametern, welche Vertex Formfaktoren definieren, festgelegt. Hadronische Quantenfeldtheorien sind eine etablierte Methode, die bereits seit langem von zahlreichen Autoren in verschiedenen Formulierungen benutzt wurde. Die Vorteile einer solchen Beschreibung sind sehr vielfältig. Sie reichen von einer natürlichen Behandlung der Spin-Statistik und deren Einfluss auf die Struktur baryonischer und mesonischer Felder über Kovarianz und ein korrektes Verhalten unter Lorentz Transformation der gesamten Theorie bis zur Implementierung interner Symmetrien in die Lagrangedichte. Bezogen auf diese Arbeit ist die SU(3) Flavor-Symmetrie von großer Bedeutung, da sehr wenig über die Wechselwirkung zwischen Hyperonen und zwischen Hyperonen mit Nukleonen bekannt ist.

Der relativistische Ein-Boson-Austausch Formalismus, kombiniert mit Dirac-Brueckner-Hartree-Fock (DBHF) Theorie für Rechnungen bei endlicher Baryonendichte wird zur Beschreibung effektiver Wechselwirkungen benutzt. Dieser stellt eine gängige Näherung dar, um das durch die Bethe-Salpeter Gleichung beschriebene Zweiteilchen Streuproblem zu lösen. Die Methode besteht darin, den vollen Streukern nach der Tree-Level Ordnung abzuschneiden und zusätzlich die zeitartige Komponente des Loop-Integrals derart kovariant festzulegen, dass sich das Problem auf die Lösung einer Integralgleichung reduziert, welche nur noch von den drei raumartigen Impulsdimensionen abhängt. Die resultierende Streugleichung ist sehr ähnlich zur nichtrelativistischen Lipmann-Schwinger Gleichung, hat gegenüber dieser aber den Vorteil, dass sie das korrekte Verhalten unter Lorentz-Transformation zeigt. Letzteres ist insbesondere bei der Berechnung von In-Medium Wechselwirkungen wichtig. In der DBHF-Theorie wird dem Hintergrundmedium durch Anwendung des Pauli-Prinzips auf die intermediären Zweiteilchenzustände im Streuprozess und über eine veränderte Kinematik aufgrund von Einteilchen-Selbstenergien Rechnung getragen. Diese Beschneidung der Selbstenergien ist konsistent mit der Beschränkung des übrigen Formalismus auf Zweiteilchenwechselwirkungen.

Da die Anwendung der DBHF-Theorie auf endliche Systeme technisch nicht durch-

führbar ist, muss zur Berechnung von Kern- und Hyperkernstruktur mithilfe einer mikroskopischen Wechselwirkung eine weitere Näherung eingeführt werden. Daher wird eine effektive Wechselwirkung in einem unendlichen System bei vorgegebener Dichte berechnet und diese dann in lokaler Dichtenäherung zur Berechnung endlicher Systeme verwendet. Hierfür setzen wir die dichteabhängige relativistische Hadronenfeldtheorie, kurz DDRH-Theorie, ein. Da bereits zur Berechnung der effektiven In-Medium Wechselwirkung eine Baryon-Meson Quantenfeldtheorie verwendet wurde, ist auch die DDRH-Theorie in dieser Art konstruiert. Die Vielteilcheneffekte sind hier in Vertexfunktionalen enthalten, welche von den baryonischen Feldoperatoren abhängen. Der DDRH Formalismus garantiert eine Konsistenz der Dynamik auf allen Stufen des ab-initio Schemas, da er die Lorentz Struktur erhält und, durch Erfüllen des Hugenholtz-van Hove Theorems, die thermodynamische Konsistenz des gesamten Zugangs garantiert. Die hier benutzten Mesonen sind effektive Freiheitsgrade, welche den langreichweitigen van-der-Waals Wechselwirkungen hadronischer QCD-Objekte Rechnung tragen, und existieren vornehmlich im t Kanal, im Unterschied zu den Resonanzen, welche im s Kanal beobachtet werden. Nichtsdestotrotz werden für ihre Massen und Quantenzahlen diejenigen der s Kanal Resonanzen verwendet. Die Baryon-Meson Vertizes in DDRH-Theorie sind Funktionale, die von Lorentz-skalaren Kombinationen der baryonischen Feldoperatoren abhängen. Diese Funktionale enthalten sämtliche Korrelationseffekte, die bei endlicher Dichte auftreten. Um die Form der Kopplungsfunktionale zu bestimmen, werden DBHF Selbstenergien auf DDRH Selbstenergien abgebildet. Da DDRH Rechnungen in endlichen Kernsystemen in Hartree Mean-Field Näherung durchgeführt werden, bildet man die DBHF Selbstenergien auf DDRH Hartree Mean-Field Selbstenergien ab. Dies führt zu einer effektiven Wechselwirkung, die so vollständig wie möglich alle Korrelationen der DBHF Rechnungen enthält.

Da der dynamische Inhalt der benutzten effektiven Wechselwirkungen im vorgestellten Formalismus vollstänig bekannt ist, können systematisch Korrekturen zu den benutzten Näherungen berechnet werden. Dies kann an zwei Stellen geschehen: 1) zum Einen durch Erweiterungen des Kerns der Streugleichung um weitere Klassen von Diagrammen, z.B. dynamische Polarisationen; 2) zum Anderen können systematische Korrekturen der DDRH Rechnungen in Mean-Field Näherung bestimmt werden, da die DDRH Vertexfunktionale aus Feldoperatoren bestehen. Im Gegensatz zu Kernstrukturrechnungen mit phenomenologischen Wechselwirkungen sind diese Korrekturen unter Kontrolle, und eine Doppelberücksichtigung von Diagrammatischen Klassen ist ausgeschlossen.

Als alternativen Zugang zur Berechnung der dichteabhängigen DDRH Vertexfunktionale mithilfe von DBHF-Theorie entwickelten wir eine neue Methode, welche die Bethe-Salpeter Gleichung über die Bestimmung von Vertexrenormierungen der Ein-Boson-Austausch Potentiale löst. In dieser Methode wird die vollständige Wechselwirkung auf einen Meson-Austausch Kern abgebildet, der $\sqrt{s}$ und dichteabhängige Vertizes enthält. Das Konzept basiert auf Ideen der Renormierungstheorie. Alle relevanten Größen, wie zum Beispiel die Selbstenergien, können von den Tree-Level Diagrammen berechnet werden, da diese bereits alle höheren Ordnungen in den Vertexfaktoren enthalten. Insbesondere die Unbestimmtheiten bei der Berechnung von Selbstenergien in der DBHF-Theorie werden hierdurch gelöst. In einem vereinfachten Modell haben wir die Impuls- und Dichteabhängigkeit der Vertizes untersucht. Dabei stellten wir eine gute

Übereinstimmung mit dichteabhängigen Vertexfunktionalen, die aus DBHF Rechnungen extrahiert wurden, fest.

In DBHF-Theorie untersuchten wir, unter Vernachlässigung von Selbstenergieeffekten, die Änderung der Dynamik von Baryon-Baryon Wechselwirkungen bezüglich einer Veränderung in Kopplungskonstanten und Massen. Es zeigte sich, dass die signifikantesten Veränderungen in der effektiven Wechselwirkung durch Veränderungen der g Kopplungen hervorgerufen werden. Eine wichtige Frage, die sich bei Berechnungen von Hyperkernstruktur und Neutronensterneigenschaften in phänomenologischen Modellen stellt, ist, inwieweit die SU(3) Skalierungen, die nur für die elementaren Vertizes wohldefiniert sind, auch für Vertizes effektiver Wechselwirkungen, wie sie in diesen Modellen verwendet werden, gültig sind. Es zeigte sich in unseren Untersuchungen, dass diese Relationen für effektive Wechselwirkungen nicht einmal näherungsweise gelten. ΛN- und NN-Wechselwirkung sind allerdings in guter Näherung, unabhängig vom umgebenden Medium, durch konstante Faktoren miteinander verknüpft, welche signifikant kleiner als die Vorhersagen von SU(6) Spin-Flavor Symmetrie sind.

Diese Resultate liefern eine einleuchtende Erklärung für Ergebnisse, die wir in Untersuchungen an Λ Hyperkernen in der mittleren Massenregion durchgeführt haben. Wir benutzten dort DDRH-Theorie mit Λ-Meson Vertex Funktionalen, welche aus den Nukleonmeson Vertex Funtionalen durch Skalieren gewonnen wurden. Die Skalierungsfaktoren ergaben sich aus dem Anpassen berechneter an experimentelle Λ Einteilchen-Spektren und lieferten ähnlich kleine Werte, welche ebenfalls auf eine starke Verletzung der SU(6) Symmetrie in effektiven Wechselwirkungen hinweisen.

Die eben erwähnten Spektren stammen von Hyperkernen, welche einen Rumpfkern mit sehr hohem Spin im Grundzustand besitzen. Da diese Spektren eine extrem starke Λ Spin-Bahn Aufspaltung zu zeigen scheinen, was im Widerspruch zu Messungen an leichten Hyperkernen steht, untersuchten wir den Einfluss eines hohen Drehimpulses des Rumpfkerns auf das Λ Einteilchenspektrum. Die Wechselwirkung des Rumpfkernspins mit dem Drehimpuls des Λ Einteilchenzustandes führt zu einer signifikanten Verbreiterung der experimentellen Einteilchenpeaks, die dann den Eindruck einer starken Spin-Bahn-Aufspaltung entstehen lassen. Nach dem Bereinigen der Spektren von diesem Effekt erhielten wir Λ Spin-Bahn Aufspaltungen, die im Einklang mit den in leichten Hyperkernen beobachteten sind. Aus diesem Beispiel lässt sich die Wichtigkeit erkennen, geeignete Isotope bei der Durchführung von Experimenten zu benutzen. Es sollten daher Targetkerne verwendet werden, die zu einem Hyperkern mit $J^\pi = 0^+$ Rumpfkern führen. Eine Liste mit entsprechenden Targetisotopen wurde zusammengestellt.

Zur Vorbereitung eines geplanten Experiments am JLab untersuchten wir den Hyperkern-Auger-Effekt in Einfach-Λ-Hyperkernen. Es zeigte sich, dass die Spektroskopie von Auger Neutronen in der mittleren und hohen Masseregion eine ausgezeichnete Alternative zur γ Spektroskopie darstellt, da dort ein hoher elektromagnetischer Untergrund zu erwarten ist. Insbesondere im mittleren Massenbereich erwartet man sehr saubere Spektren, in denen sich deutlich eine Spin-Bahn-Aufspaltung der Λ Orbitale erkennen lassen sollte. Aufgrund der hohen Zustandsdichte bei schweren Elementen sind hier zusätzliche Anstrengungen notwendig, um die Spektren zu säubern, zum Beispiel durch ein Gating auf den anfänglich produzierten Λ Zustand.

Danksagung

Abschließend möchte ich mich noch bei all jenen bedanken, die mich während des Entstehens dieser Arbeit begleitet und dabei wissentlich oder unwissentlich zu ihrem Gelingen beigetragen haben.

An erster Stelle ist hier mein Betreuer Prof. Dr. Horst Lenske zu nennen, auf dessen Unterstützung ich immer zählen konnte. Seine Gesprächsbereitschaft, wann immer ich einen Rat benötigte, und sein stetes, ehrliches Interesse an meiner Arbeit waren eine unentbehrliche Hilfe. Insbesondere möchte ich mich bei ihm für den großzügig gewährten Freiraum bedanken, der es mir ermöglichte, in dieser Arbeit immer wieder eigene Ideen einfließen zu lassen.

Auch Prof. Dr. Ulrich Mosel gilt mein Dank für die Aufnahme an sein Institut und die hervorragenden Arbeitsbedingungen an selbigem. Ich möchte ihm und meinem Betreuer Prof. Dr. Horst Lenske für ihre wohlwollende Förderung meiner Arbeit danken, die es mir möglich machte, an zahlreichen internationalen Tagungen und Workshops teilzunehmen.

Ein besonderes Dankeschön geht noch an Prof. Dr. Carsten Greiner für sein reges Interesse an meiner Arbeit, sowie für seine guten Ratschläge, Ideen, hilfreichen Diskussionen und die Zeit, die er sich trotz großen Arbeitsdrucks immer für sachliche exkurse über die deutsche Politik oder andere weltbewegende Dinge nahm.

Besonderer Dank gilt auch meinen langjährigen Weggefährten am Institut, die glücklicherweise nicht immer nur Physik im Kopf hatten, Dr. Jürgen Lehr, Dr. Thomas Falter, Dr. Sascha Juchem, Dr. Gunnar Martens, Dr. Stefan Leupold, Zhe Xu, Dr. Marcus Post und Dr. Gregor Penner. Ausserdem Danke ich meinen (Ex-) Mitbewohnern des 5. Stocks für zahlreiche Schwätzchen und das gute Arbeitsklime. Besonders ausgedehnte Schwätzchen gingen hier zu Lasten von Frank Frömel, Dr. Sascha Juchem, Dr. Kai Gallmeister und Dr. Peter Watson.

Meinen Lehrmeistern bei der Computer- und Netzwerkadministration Dr. Frank Hofmann und Dr. Klaus Schertler, sowie meinem momentanen Mitstreiter Frank Frömel danke ich für gute Zusammenarbeit.

For interesting and inspiring discussions I would like to thank Prof. Dr. Radhey Shyam, Prof. Dr. Hermann Wolter, Prof. Dr. Josef Pochodzalla, Dr. Michael Bender, Dr. Thomas Bürvenich, Dr. Christian Fuchs, Dr. Thomas Neff, Dr. Jürgen Schaffner-Bielich, Dr. Achim Schwenk and Dr. Stefan Typel. I would especially like to thank Dr. Amour Margaryan for arousing my interest in the hypernuclear Auger effect and fruitful discussions on that topic.

Elke Jung und Christiane Pausch möchte ich für ihre zuvorkommende Hilfe beim alltäglichen Wahnsinn im Umgang mit dem Bibliothekssystem und den administrativen und organisatorischen Dingen danken.

Abschließend möchte ich den mir am nächsten stehenden Menschen, meiner Familie und meiner Freundin Dagmar, danken, für die Unterstützung und Geduld, die sie mir während meiner Arbeit haben zuteil werden lassen. Und auch für alles Andere.

Danke!